Theoretical study of the optical properties of the noble metal nanoparticles: CD and MCD spectroscopy

by

Natalia Vladimirovna Karimova

B.S., Irkutsk State University, 2006
M.S., Irkutsk State University, 2008
Ph.D., Irkutsk State University, 2011

AN ABSTRACT OF A DISSERTATION

submitted in partial fulfillment of the requirements for the degree

DOCTOR OF PHILOSOPHY

Department of Chemistry
College of Arts and Sciences

KANSAS STATE UNIVERSITY
Manhattan, Kansas

2017

Abstract

Gold and silver particles with dimensions less than a nanometer possess unique characteristics and properties that are different from the properties of the bulk. They demonstrate a non–zero HOMO–LUMO gap that can reach up to 3.0 eV. These differences arise from size quantization effects in the metal core due to the small number of atoms. These nanoparticles have attracted great interest for decades both in fundamental and applied research. Small gold clusters protected by various types of ligands are of interest because ligands allow obtaining gold nanoclusters with given sizes, shapes and properties. Three main families of organic ligands are usually used for stabilization of gold nanoclusters: phosphine ligands, thiolate ligands and DNA.

Usually, optical properties of these NPs are studied using optical absorption spectroscopy. Unfortunately, sometimes this type of spectrum is poorly resolved and tends to appear very similar for different complexes. In these cases, circular dichroism (CD) and magnetic circular dichroism (MCD) spectroscopy can be applied. However, the interpretation of experimental CD and MCD spectra is a complicated process.

In this thesis, theoretically simulated CD and MCD spectra were combined with optical absorption spectra to study optical activity for octa– and nona– and undecanuclear gold clusters protected by mono– and bidentate phosphine ligands. Additionally, optical properties of bare and DNA protected silver NPs were studied. Theoretical CD spectra were examined to learn more about the origin of chirality in chiral organometallic complexes, and to contribute to the understanding of the difference in chiroptical activity of gold clusters stabilized by different phosphine ligands and DNA–stabilized silver clusters. Furthermore, optical properties of the small centered gold clusters $Au_8(PPh_3)_8^{2+}$ and $Au_9(PPh_3)_8^{3+}$ were examined by optical absorption and MCD spectra using TDDFT. Theoretical MCD spectra were also used to identify the plasmonic behavior of silver nanoparticles.

These results showed that CD and MCD spectroscopy yield more detailed information about optical properties and electronic structure of the different chemical systems than optical absorption spectroscopy alone. Theoretical simulation of the CD and MCD spectra together with optical absorption spectra can be used to assist in the understanding of empirically measured CD and MCD and provide useful information about optical properties and electronic structure.

Theoretical study of the optical properties of the noble metal nanoparticles: CD and MCD spectroscopy

by

Natalia Vladimirovna Karimova

B.S., Irkutsk State University, 2006
M.S., Irkutsk State University, 2008
Ph.D., Irkutsk State University, 2011

A DISSERTATION

submitted in partial fulfillment of the requirements for the degree

DOCTOR OF PHILOSOPHY

Department of Chemistry
College of Arts and Sciences

KANSAS STATE UNIVERSITY
Manhattan, Kansas

2017

Approved by:

Major Professor
Dr. Christine M. Aikens

Copyright

Abstract

Gold and silver particles with dimensions less than a nanometer possess unique characteristics and properties that are different from the properties of the bulk. They demonstrate a non–zero HOMO–LUMO gap that can reach up to 3.0 eV. These differences arise from size quantization effects in the metal core due to the small number of atoms. These nanoparticles have attracted great interest for decades both in fundamental and applied research. Small gold clusters protected by various types of ligands are of interest because ligands allow obtaining gold nanoclusters with given sizes, shapes and properties. Three main families of organic ligands are usually used for stabilization of gold nanoclusters: phosphine ligands, thiolate ligands and DNA.

Usually, optical properties of these NPs are studied using optical absorption spectroscopy. Unfortunately, sometimes this type of spectrum is poorly resolved and tends to appear very similar for different complexes. In these cases, circular dichroism (CD) and magnetic circular dichroism (MCD) spectroscopy can be applied. However, the interpretation of experimental CD and MCD spectra is a complicated process.

In this thesis, theoretically simulated CD and MCD spectra were combined with optical absorption spectra to study optical activity for octa– and nona– and undecanuclear gold clusters protected by mono– and bidentate phosphine ligands. Additionally, optical properties of bare and DNA protected silver NPs were studied. Theoretical CD spectra were examined to learn more about the origin of chirality in chiral organometallic complexes, and to contribute to the understanding of the difference in chiroptical activity of gold clusters stabilized by different phosphine ligands and DNA–stabilized silver clusters. Furthermore, optical properties of the small centered gold clusters $Au_8(PPh_3)_8^{2+}$ and $Au_9(PPh_3)_8^{3+}$ were examined by optical absorption and MCD spectra using TDDFT. Theoretical MCD spectra were also used to identify the plasmonic behavior of silver nanoparticles.

These results showed that CD and MCD spectroscopy yield more detailed information about optical properties and electronic structure of the different chemical systems than optical absorption spectroscopy alone. Theoretical simulation of the CD and MCD spectra together with optical absorption spectra can be used to assist in the understanding of empirically measured CD and MCD and provide useful information about optical properties and electronic structure.

Table of Contents

List of Figures

List of Tables

Acknowledgements

I would like to acknowledge my advisor, Pr. Christine M. Aikens, for her help and guidance through the past years. I have had a wonderful experience during my PhD because of her assistance and support. She created a great work environment in the group.

Also, I would also like to thank my committee members: Dr. Ryszard Jankowiak, Dr. Viktor Chikan, Dr. Brett Esry and Dr. Placidus B. Amama for their time and attention.

I want to acknowledge the Department of Chemistry and the Graduate School at Kansas State University.

I would also like to thank my group members (both past and present), for their support and friendship. Every member of our group is a smart, kind and very helpful person.

Finally, I would like to thank my family for support, love and courage given to me in each step of my life.

Dedication

To my family.

Chapter 1 - Introduction

In this Introduction some abbreviations are used:

NPs	Nanoparticles
(P^P)	Bidentate phosphine ligands
(PP_3)	Tridentate phosphine ligands
dppm	$Ph_2P–CH_2–PPh_2$
dppe	$Ph_2P–(CH_2)_2–PPh_2$
dppp	$Ph_2P–(CH_2)_3–PPh_2$
dppb	$Ph_2P–(CH_2)_4–PPh_2$
dpppe	$Ph_2P–(CH_2)_5–PPh_2$
dpph	$Ph_2P–(CH_2)_6–PPh_2$
dppo	$Ph_2P–(CH_2)_8–PPh_2$

Small Ligand–Protected Gold NPs

Small gold and silver nanoparticles have attracted great interest for decades both in fundamental and applied research, especially in the fields of heterogeneous medicine, luminescence, catalysis, nanoelectronics, drug delivery, bioanalysis, etc.[1-3] These applications play an important role in our modern life. Therefore, scientists are always keeping trying to develop and synthesize novel gold nanostructures with improved characteristics or new properties. Small gold clusters protected by various types of ligands have held great attention for the few last decades. Ligands allow obtaining the gold nanoclusters with given size, shape and properties. Three main families of organic ligands are usually used for stabilization of the gold nanoclusters: phosphine, thiolate ligands and DNA. These ligands enable the creation of highly stable gold nanoparticles and nanoclusters.[4, 5]

Stability of small gold nanoclusters protected by thiolate (SR) or phosphine (PR_3) and halide ligands can be predicted in the terms of "superatom electronic theory".[6] According to this theory, valence electrons of the metal core can be transferred to suitable ligands, opening the possibility to achieve a noble-gas-like electronic configuration in the formation of stable complexes. The most stable species is associated with a total shell–closing electron count of n*

= 2, 8, 18, 20, 34, 58, 92, 138, … . For a complex with the stoichiometric formula $(L_sA_NX_M)^z$ (where A – gold core, L – weak Lewis base ligands, X – electron–withdrawing ligands, and z – total charge of cluster), the number of core electrons can be calculated with the formula n* = N–M–z.[6] The frontier orbitals of these nanoparticles are commonly named "superatom orbitals". These orbitals look like the *s, p, d* orbitals of the hydrogen atom but are delocalized over the metallic core. They are labeled 1S, 1P, 1D, …

Thiolate–Protected Gold Nanoparticles

Thiolate–stabilized gold NPs are a very interesting class in gold chemistry. In these structures the small gold core is protected by mono– and dimeric protecting units called "staple motifs" such as linear RS-Au(I)-SR and V-shaped RS-Au(I)-SR-Au(I)-SR. Many distinct thiolate–stabilized gold nanoclusters have been synthesized and identified, including the smallest stable thiolated gold $Au_{15}(SR)_{13}$,[7] $Au_{18}(SR)_{14}$,[8] $Au_{25}(SR)_{18}$,[9-12] $Au_{28}(SR)_{20}$,[13] $Au_{30}(SR)_{18}$,[14] $Au_{36}(SR)_{24}$,[15] two clusters of $Au_{38}(SR)_{24}$ with a totally different core structure,[16, 17] $Au_{40}(SR)_{24}$,[18] $Au_{68}(SR)_{34}$,[19] $Au_{102}(SR)_{44}$,[20] $Au_{104}(SR)_{45}$,[21] *etc*.

One the most experimentally and theoretically studied clusters is $Au_{25}(SR)_{18}$[9-12] The symmetry of the entire molecule is approximately T_h.[22] This cluster can exist in three charge states –1, 0 and +1. Ackerson and co–workers considered the structure of the $Au_{25}(PET)_{18}$ cluster (PET=phenylethylthiol) in a "shell–by–shell" representation where the cluster can considered as a composition of four (I – IV) shells of symmetrically related atoms (**Figure 1–1**).[9]

Figure 1–1. A) Structures of the inorganic core and semirings of $Au_{25}(PET)_{18}$, B) is a gold icosahedron, C) a distorted sulfur icosahedron, D) a dodecahedron missing 8 vertices that form the vertices of an inscribed cube and E) is a sulfur octahedron.

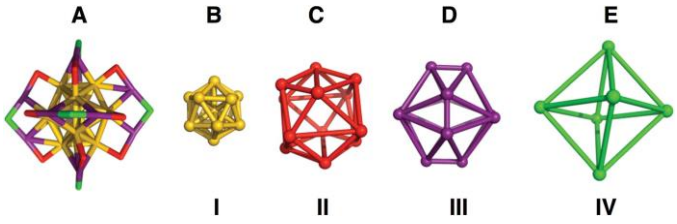

*Reprinted with permission from Ref.[9] (Copyright 2016 The Royal Society of Chemistry).

Figure 1–2. The crystal structures of $Au_{25}(PET)_{18}$ in the +1 A), 0 B), and +1 C) charge states are shown above. Gold is in yellow, and sulfur is in orange.

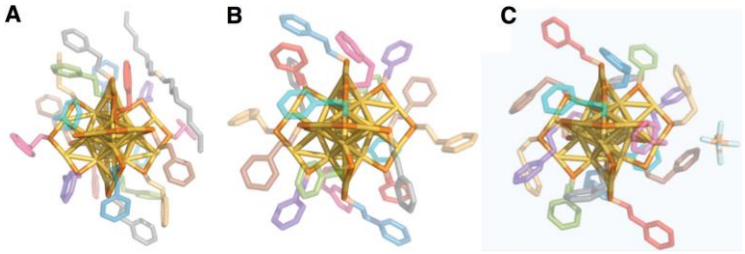

*Reprinted with permission from Ref.[9] (Copyright 2016 The Royal Society of Chemistry 2016).

Phosphine–Protected Gold Nanoparticles

A large group of this class is centered gold species such as $Au_8(PPh_3)_7^{2+}$,[23, 24] $Au_8(PPh_3)_8^{2+}$,[25-28] $Au_9(PPh_3)_8^{3+}$,[24, 28-32] $Au_{11}(PPh_3)_8X_2^+$ (X = Cl, SCN),[33, 34] $Au_{11}(PPh_3)_7Cl_3$,[34] *etc*. Among the phosphine-stabilized gold NPs, the monodentate (TPP – triphenylphosphine and its derivatives)[27, 29, 34-39], bidentate = bisphosphine = (P^P) (dppp – 1,3–bis(diphenylphosphino)propane; BINAP – 2,2'-bis(diphenylphosphino)-1,1'-binaphthyl; DIOP – o-isopropylidene-2,3-dihydroxy-1,4-bis(diphenylphosphino)butane; *etc.*)[40-46] and tridentate phosphines (PP_3 – tris(2–(diphenylphosphino)ethyl)–phosphine)[47, 48] can be used to stabilize small gold nanoclusters.

According to the literature data, phosphine-protected gold clusters with a nuclearity of 3–14, 20, 22, 24, 25, 39 and 55 have been synthesized.[44, 49, 50] The geometrical structures of some of them were determined by X–ray crystallography. These results showed that phosphine–protected gold NPs can have different types of gold core structures such as centered polyhedral, non–centered polyhedral and "core + *exo*" type.[49] The obtained results showed that the shape and charge of the gold core are dependent on the nature of the phosphine ligand used. In this part only small gold NPs with 8, 9 and 11 gold atoms in the inorganic core, with determined X–ray crystal structure, were considered.

Ligand–stabilized gold nanoclusters with eight metal atoms in the core were synthesized using mono– and bidentate phosphine ligands. Three types of octanuclear gold clusters protected by eight, seven and six arylphosphine ligands can be obtained: $[Au_8(PPh_3)_8]^{2+}$,[25, 51, 52] $[Au_8(PPh_3)_7]^{2+}$,[23, 53] and $[Au_8(PMes_3)_6]^{2+}$.[54] In these structures the

octagold core exists in three different shapes (**Figure 1–3**). The charge of the Au_8 core in these structures is +2.

Figure 1–3. Geometrical structure of Au_8 core: coordinates from crystal structures of A) cluster $[Au_8(PPh_3)_8]^{2+}$;[25] B) cluster $[Au_8(PPh_3)_7]^{2+}$;[53] C) cluster $[Au_8(PMes_3)_6]^{2+}$;[54] D) cluster $[Au_8(dppp)_4]^{2+}$;[55] E) cluster $[Au_8(BINAP)_4X_2]^{2+}$;[40] and F) cluster $[Au_8(dppp)_4X_2]^{2+}$.[55] (X = halide or acetylide–ion)

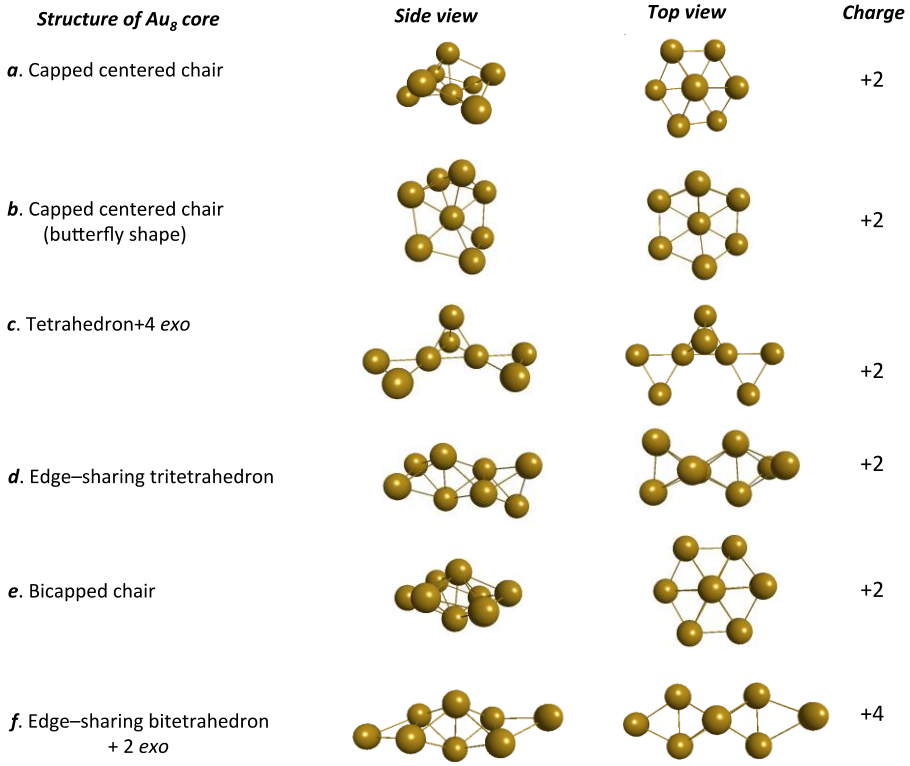

Cluster $[Au_8(PPh_3)_8]^{2+}$ can be prepared in two different ways: by addition of triphenylphosphine to the $[Au_8(PPh_3)_6]^{2+}$ cluster or through a dissociative mechanism of the $[Au_9(PPh_3)_8]^{3+}$ complex.[51, 53, 56]

$$[Au_9(PPh_3)_8]^{3+} + 2PPh_3 \rightarrow [Au_8(PPh_3)_8]^{2+} + [Au(PPh_3)_2]^{+}$$

Four crystal structures with different anions (NO_3, alazarinsulfonate, PF_6 and $SiMo_{12}O_{40}$) have been determined.[23, 51, 53, 57] All these structures display a core of gold atoms in capped centered chair arrangement (**Figure 1–3a**). Each gold atom is bound to a triphenylphosphine ligand. The Au–Au bond distances lie between 2.634 and 2.938 Å.

In the $[Au_8(PPh_3)_8]^{2+}$ cluster, one of the Au–P distances is approximately 0.1 Å longer than the others and can be easily removed by phosphine scavenger $[RhCl(C_8H_{14})_2]_2$.[23] As a result, complex $[Au_8(PPh_3)_7]^{2+}$ is formed. The structure of this cluster can be described as a butterfly shape where four gold atoms create a rectangular plane, another three gold atoms

bridge the opposite atoms of the butterfly part, and an eighth gold atom lies in the center of the cluster (**Figure 1–3b**). The shape of gold core in $[Au_8(PPh_3)_7]^{2+}$ is close to the gold core structure from the $[Au_9(PPh_3)_8]^{3+}$ complex with D_{2h} symmetry. Seven phosphine ligands are linked to the peripheral gold atoms. The Au–Au bond distances in the $[Au_8(PPh_3)_7]^{2+}$ cluster lie between 2.629 and 2.942 Å.[23, 53]

A dicationic octagold cluster protected by six phosphine ligands can be synthesized by reduction of the oxonium salt $[(AuPMes_3)_3O)]BF_4$ in THF in the presence of CO (P = 3 atm).[54] The product of this reaction is the $[Au_8(PMes_3)_6]^{2+}$ complex. The X–ray crystal structure shows that the octagold core has a tetrahedron + 4 *exo* gold atoms (**Figure 1–3c**). Six phosphine ligands are bound to the gold atoms of the unshared vertexes.[54]

Diphosphines (P^P) ligands have also been used for stabilization of octanuclear gold clusters. The $[Au_8(dppp)_4]^{2+}$ cluster has a metal skeleton of an edge–sharing tritetrahedron (**Figure 1–3d**).[55, 58] This cluster was obtained as an intermediate cluster species in the etching reaction:[58]

$$[Au_9(PPh_3)_8]^{3+} + dppp \rightarrow [Au_8(dppp)_4]^{2+} \rightarrow [Au_6(dppp)_4]^{2+}$$

$[Au_8(dppp)_4]^{2+}$ was isolated and identified by mass spectrometry and X–ray diffraction studies.[55] The Au–Au distances in the cluster are in range 2.616–2.752 Å.

Another octagold cluster was obtained with BINAP ligands $[Au_8(BINAP)_3(PPh_3)_2]^{2+}$.[40] $[Au_8(BINAP)_3(PPh_3)_2]^{2+}$ clusters were obtained by adding an excess amount of the borane tertbutylamine complex to a chloroform solution containing equal amounts of $Au(PPh_3)(NO_3)$ and BINAP. In this complex, the geometry of the metal skeleton is a bicapped chair: the gold core does not depart very much from C_{3v} symmetry: six Au–atoms form a "chair–cyclohexane" structure with one gold atom added above and one below the ring (**Figure 1–3e**).[40] The measured Au–Au bond distances are typical for gold systems and are in the range 2.523 to 3.109 Å.

Interaction of the octagold clusters protected by monodentate phosphine ligands with halide or acetilyde–ions promotes the aggregation–induced growth of the cluster core.[55, 59] During interaction of the $[Au_8(dppp)_4]^{2+}$ with halide or acetylide–ion, the $[Au_8(dppp)_4X_2]^{2+}$ (X = Cl, PhCC) cluster can be prepared.[55] The gold cores in these type of clusters have an edge–sharing bitetrahedron + 2 *exo* structure (**Figure 1–3f**). The measured Au–Au bond distances are in the range 2.607 to 3.072 Å.

The Au_9 nanoclusters are protected by eight mono– or by four bidentate phosphine ligands. The gold core in these complexes is less flexible than the octagold core. There are just two possible structures of the Au_9 core that were experimentally detected: bicapped centered chair (also known as butterfly) and centered crown.[60] The core charge in all these complexes is +3 (**Figure 1–4**). The synthesis of these gold clusters is carried out mainly through two reactions: the reduction of a mononuclear gold(I) complex or by an aggregation reaction of the octanuclear cluster with mononuclear gold(I) complex. For example, cluster $[Au_9(PPh_3)_8]^{3+}$ can be prepared in these two ways:

$$Au(NO_3)(PPh_3) + NaBH_4 \rightarrow [Au_9(PPh_3)_8]^{3+}$$

$$[Au_8(PPh_3)_8]^{2+} + Au(NO_3)(PPh_3) \rightarrow [Au_9(PPh_3)_8]^{3+}$$

Figure 1–4. Shape of the Au_9 core: coordinates from crystal structures A) $[Au_9(PPh_3)_8]^{3+}$ (D_{2h}); and B) $[Au_9(PPh_3)_8]^{3+}$ (D_{4d}).[60]

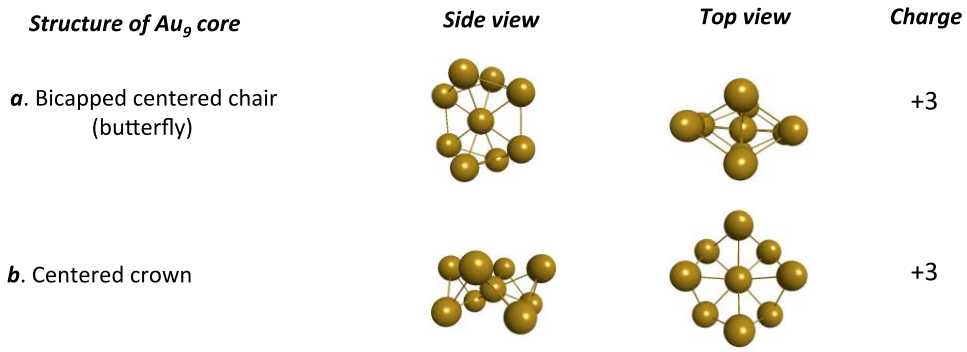

Similar clusters with different ligands and counter anions can be obtained in the same way.[29, 52, 60, 61] Depending on the types of solvents and the concentration, two types of crystals (butterfly and crown) can be prepared with these methods.[60] In some solvent combinations simultaneous growth of both compounds was observed, but they can be obtained selectively, for example, in DMF-acetonitrile and DMF-acetone, respectively.[60]

Small gold clusters with the bicapped centered chair (butterfly) geometry were obtained only with monodentate ligands such as PPh_3, P(*p*Tol)$_3$, P(*p*MeOC$_6$H$_4$)$_3$ and counter anions NO_3, $PW_{12}O_{40}$ and BF_6.[29, 52, 60, 61] The structure of this cluster can be described as a butterfly shape where four gold atoms create a rectangular plane, another four gold atoms bridge the opposite atoms of the butterfly part, and a ninth gold atom lies in the center of the cluster. The symmetry of this Au_9 core is near D_{2h} symmetry (**Figure 1–4a**). Bond distances between gold atoms in the core are in a range of 2.686–2.926 Å.

The centered crown shape of the nonagold core was observed in clusters protected by monodentate phosphine ligands such as $[Au_9(PPh_3)_8](NO_3)_3$, $[Au_9(PPh_3)_8](PW_{12}O_{40})$, $[Au_9(P(pMeOC_6H_4)_3)_8]X_3$ (X = NO_3 and BF_4), and also protected by bidentate ligands $[Au_9(dpph)_4](PW_{12}O_{40})$. The symmetry of this gold core is D_{4d} (**Figure 1–4b**). The measured Au–Au bond distances lie in the range 2.651 to 3.249 Å.[60-63]

Also, for the $[Au_9(PPh_3)_8]^{3+}$ bicapped centered chair complex an electrochemical two–electron redox process has been reported.[64] This process accompanies a skeletal arrangement from toroidal to spherical shape with the formation of the $[Au_9(PPh_3)_8]^{+}$ cluster.

Undecagold clusters can exhibit three main geometrical structures: tetracapped centered chair, capped centered square antiprism and butterfly Au_9 + 2 *exo* gold atoms. The charge of the metal core is +3 in all these systems (**Figure 1–5**).

The Au_{11} core can be protected by seven, eight and ten molecules of monodentate arylphosphine ligands to form clusters such as the neutral $Au_{11}L_7X_3$ complex and charged $[Au_{11}L_8X_2]^{+}$ and $[Au_{11}L_{10}]^{3+}$ clusters (where L = PPh_3, $P(pFC_6H_4)_3$, $P(mCF_3C_6H_4)_3$, $PMePh_2$ and PMe_2Ph; X = Cl, Br, I, SCN or SNC_6H_4).[34, 37, 63, 65-68] In $Au_{11}L_7X_3$ and $[Au_{11}L_8X_2]^{+}$ clusters, the undecagold core is stabilized by phosphine ligands and strong coordinating ions such as halide ions. The shape of the gold skeleton is a tetracapped centered chair (**Figure 1–5a**). The original recipe for preparation of the $Au_{11}L_7X_3$ clusters is the borohydride reduction of monophosphine gold(I) complex AuLX in ethanol using $NaBH_4$ as the reducing agent.[34, 37] Aggregation of strong coordinating ions such as halide– or SCN– ions to the cluster $[Au_9L_8]^{3+}$ gives rise to the cluster $[Au_{11}L_8X_2]^{+}$.[63]

Figure 1–5. Figure 1–5. Shape of the Au_{11} core: coordinates from crystal structures A) $Au_{11}(PPh_3)_7Cl_3$;[37] B) $[Au_{11}(PMePh_2)_{10}]^{3+}$;[68] and C) $[Au_{11}(dppe)_6]^{3+}$.[46]

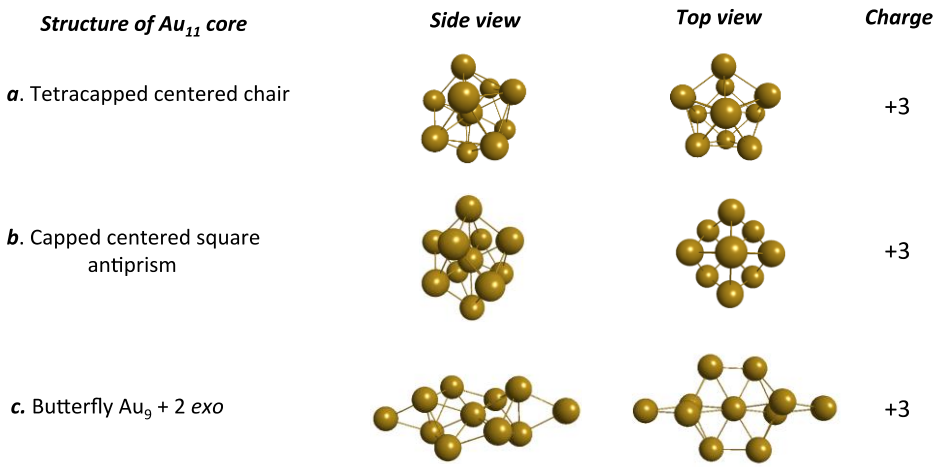

In clusters $[Au_{11}L_{10}]^{3+}$ (L = $PMePh_2$ and PMe_2Ph), the undecagold core is protected only with monodentate phosphine ligands and no strong coordinating ions are used. In these clusters, the metal core has a shape of a capped centered square antiprism (**Figure 1–5b**). The $[Au_{11}L_{10}]^{3+}$ complexes can be prepared via reduction reactions of AuLCl gold complexes with zero–valent titanium reagent.[68]

Also, undecagold clusters can be protected by bidentate phosphine ligands. In this case three types of clusters can be formed: $[Au_{11}(P\text{^}P)_5]^{3+}$,[69] $[Au_{11}(P\text{^}P)_6]^{3+}$,[46] and $[Au_{11}(P\text{^}P)_4X_2]^{+}$.[40] The $[Au_{11}(dppp)_5]^{3+}$ cluster can be obtained via a ligand exchange reaction: the reaction of $Au_{11}[P(p\text{-}ClC_6H_4)_3]_7(SCN)_3$ with 1,3-bis(diphenylphosphino)propane (dppp) in methylene chloride leads to the formation of $[Au_{11}(dppp)_5](SCN)_3$ by a total substitution of the ligands.[69] In this cluster the gold core has a tetracapped centered chair structure. The undecagold cluster $[Au_{11}(dppe)_6]^{3+}$ was prepared from the gold complex $Au_2(dppe)Cl_2$ when the gold salt was reduced by $NaBH_4$ in ethanol solution.[46] This undecagold cluster has a bicapped centered chair (butterfly) shape of Au_9 gold core plus two *exo*-attached gold atoms (**Figure 1–5c**). The gold cluster $[Au_{11}(DIOP)_4X_2]^{+}$ was prepared by the reduction reaction of $Au_2(DIOP)Cl_2$ in an ethanol solution with $NaBH_4$.[40] The gold core structure is a tetracapped centered chair. In all considered undecagold clusters with mono– and bidentate ligands, the Au–Au distances are in the range of 2.608 – 3.216 Å.

DNA Protected Gold and Silver Nanoparticles

Gold and silver nanoparticle structures with a helical arrangement are a very interesting area of research. The most popular methods of synthesis of this type of nanoparticles are based on the assistance of biological molecules such as peptides and DNA molecules. These assemblies have potential applications in photonics and as optical polarizers, sensors, catalysts, *etc*.[70-73] During the interaction of noble metal nanoparticles with biomolecules, formation of two types of nanostructures are possible: (i) metal clusters are nested on the outside of the biomolecule and arrange in external helical chains around these peptide or DNA molecules with production of plasmonic helical metal nanoparticle assemblies (**Figure 1–6**),[70, 72, 74, 75] and (ii) a few to tens of metals atoms are located inside the DNA molecule, between two polynucleotide strands.[76-86]

Figure 1–6. Surface–bound chiral plasmonic nanostructure.

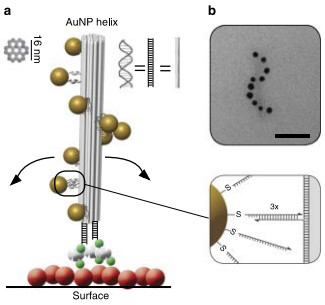

*Reprinted with permission from Ref.[74] (Copyright 2013 Macmillan Publishers Limited).

The second type of noble metal – biomolecule clusters (M:DNA, where M = Au and Ag), where metals atoms are located inside the DNA molecule, are a very interesting class. In particular, Ag:DNA nanoclusters have an extremely wide range of emission colors.[81-84] They exhibit a strong circular dichroism (CD) signal in the visible or near infrared (IR) region, whereas natural helical molecules such as peptides and DNA show CD response in the ultraviolet (UV); this feature makes DNA−metal nanoparticle hybrids very useful for the creation of systems with useful properties.[76, 87] Experimental studies[81, 83-85] have shown that the fluorescent Ag:DNA clusters contain less than 20 silver atoms. However, despite progress in the synthesis and characterization of the optical activity, the structures of these clusters (M:DNA, where M = Au and Ag) remain unclear.

According to some experimental data a few possible structures for Ag:DNA have been proposed.[81, 88] For example, Fygenson and co-workers[88] investigated size, charge and conformation of fluorescent clusters Ag:DNAs using calibrated electrokinetic microfluidics and fluorescence correlation spectroscopy. Two spectrally distinct Ag:DNA emitters stabilized by the same DNA were considered: green emitting Ag_{11}:DNA and red emitting Ag_{13}:DNA. The differential pH dependence of electrophoretic mobility of Ag_{11}:DNA and Ag_{13}:DNA indicated that these two clusters have significant differences in structure. The absence of Ag_{13}:DNA fluorescence at high pH suggests that the emissive Ag_{13} core is more negatively charged with respect to Ag_{11} and has a less compact conformation. Additionally, the nearly 30% difference in diffusivities of the Ag_{11}:DNA and Ag_{13}:DNA clusters was explained by the suggestion that Ag_{11}:DNA is a compact structure, while Ag_{13}:DNA is not. Also, their results showed that Ag_{11}:DNA and Ag_{13}:DNA exhibit similar electrophoretic mobilities at neutral pH, which indicate their nearly identical composition. However, Ag_{13}:DNA is more negative and has 30%

lower diffusivity with respect to Ag_{11}:DNA. To explain this, the authors proposed that the Ag_{13}:DNA cluster can have an extended structure. It can be obtained if the phosphate backbone of both the stem and loop regions are approximately coplanar, in a lollipop- or cigar-like conformation, and in this case the structure could sustain more charge. Also, this cluster could become oriented under electroosmotic flow so as to present less hydrodynamic resistance than when freely diffusing. Finally, two possible structures were proposed for green and red emitting Ag:DNA clusters. The red emitter Ag_{13}:DNA is extended, diffusing more slowly than a disrupted hairpin but migrating more quickly when subject to an electric field (**Figure 1-7**).

Figure 1–7. Schematic and steric illustrations of extremely compact Au_{11}:DNA (top) and extended Au_{13}:DNA (bottom) suggested configurations.

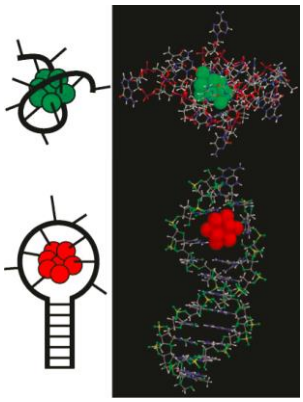

*Reprinted with permission from Ref. [88] (Copyright 2011 American Chemical Society)

However, Shultz and co-workers[81] suggested that silver nanoparticles in the DNA - stabilized clusters have a rod-like shape (not spherical or planar). They used negative ion, high resolution mass spectrometry of compositionally pure solutions to identify the silver cluster charge (Q_{cl}) and total number of silver atoms (N_{Ag}) in fluorescent Ag:DNAs. According to their results, Ag:DNA clusters exhibit charges from Q_{cl} = 6e to 13e with N_{Ag} = 10 to 24 silver atoms in each cluster. Also, the dependence of the excitation and emission wavelength on the number of neutral silver atoms provided evidence that the cluster structure of Ag:DNA complexes is a rod-shape: a neutral, rod-like chain of silver atoms surrounded by a base-bonded Ag frame, such as the pictures shown in **Figure 1–8**. The length of the neutral, rod-like chain in the system appears to be the major control for the color of Ag:DNA. This work was extended by Gwinn and co-workers.[86] They found that the color combinations of Ag:DNA clusters with even numbers of neutral silver atoms are different from magic numbers for spherical clusters: for DNA-stabilized silver clusters, the magic numbers of neutral Ag atoms are 4 and 6, not 2 and 8

as predicted by the spherical "superatom" model. In addition, the peak fluorescence wavelength is dependent on the neutral silver atom number. Molecular dynamics simulations showed that Ag:DNA complexes may exhibit curved shapes due to Coulomb interactions and that addition or subtraction of silver ions near the neutral silver chain can modify the cluster shape.[86]

Figure 1–8. Examples of the Ag:DNA structures. Rod-like, neutral clusters (gray) are shown attached to DNA bases via peripheral Ag (blue) in tetramer B) and trimer C) arrangements.

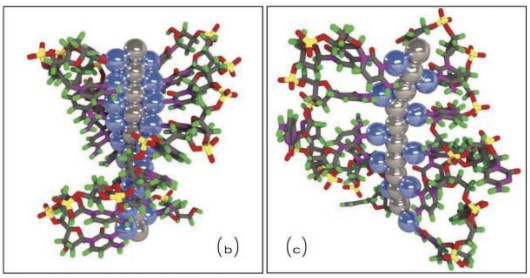

*Reprinted with permission from Ref.[81] (Copyright 2013 Wiley Online Library)

A number of theoretical calculations were performed to help with understanding of structure for small Ag clusters bound to DNA.[89, 90] Theoretical studies of the binding of silver clusters to the DNA bases were performed using DFT.[89-91] Gwinn and co-workers[89] investigated binding of neutral planar Ag_n clusters (n = 1 - 6) with adenine, cytosine, guanine and thymine. Also, the absorption spectra of these Ag:DNA complexes were calculated. These results showed that for clusters of a fixed size, the N-sites of a given base bind more strongly to silver clusters than the O-sites: silver clusters have the strongest binding with cytosine base and weakest with thymine. Binding of clusters to multiple bases results in significant energetic stabilization. Time-dependent DFT calculations show that different base-cluster isomers may have very different absorption spectra. In 2017, Aikens and co-workers[90] studied geometries and binding motifs of bare and guanine-complexed silver clusters Ag_n^z (n=2 – 6; z = 0 – 2). These results showed that neutral systems remain planar in this size range, whereas for cationic and dicationic systems 2D and 3D structures were obtained. Additionally, they showed that neutral and positively charged silver clusters prefer different sites for coordination with the DNA base.

Additionally, the idea about rod–shape structure of Ag:DNA clusters was supported by a combination of experimental and theoretical techniques.[91] Fluorescent, DNA-stabilized silver clusters exhibit ubiquitous features in circular dichroism spectra. As discussed in Chapter 4, TDDFT calculations of CD spectra for bare chains of silver atoms with a helical structure also

exhibit these striking features, indicating electron flow along a chiral, filamentary metallic path as the origin for low-energy Ag_n-DNA transitions (**Figure 1–9**).[91, 92]

Figure 1–9. Calculated circular dichroism spectra for bare, chiral Ag cluster rods show a consistent pattern of positive and negative peaks for different curvatures B) CD data on pure Ag_n-DNA show the same peak pattern as theory.

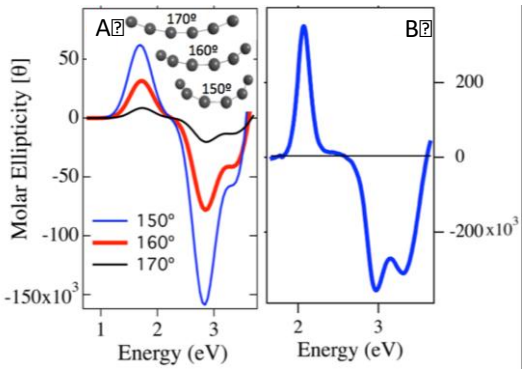

*Reprinted with permission from Ref.[92] (Copyright 2015 MDPI AG)

Berdakin and co-workers studied the electronic and optical properties of Ag:DNA clusters using Molecular Dynamics and DFTB methods.[93] Two model structures of neutral Ag_6 stabilized by DNA were considered: (i) $(dpC_6)_2Ag_6$ where two strings of deoxypolycytosine with six bases protect a rod of six Ag atoms and (ii) $(C_2Ag)_6$ structure without the phosphate and ribose backbone (metal-mediated base pair only) (**Figure 1-10**). The simulation of the absorption spectra of both structures reproduces the main features observed in experimental reports such as a band in the UV spectral region near the absorption band of the DNA moiety and bands in the visible region. The UV absorption band of the $(dpC_6)_2Ag_6$ structure is broadened and blue-shifted, which can be related to the lack of a complete environment and charge description of the system.

Figure 1–10. TD–DFTB optical absorption spectra of A) $(C_2Ag)_6$ and B) $(dpC_6)_2Ag_6$ strauctures.[93]

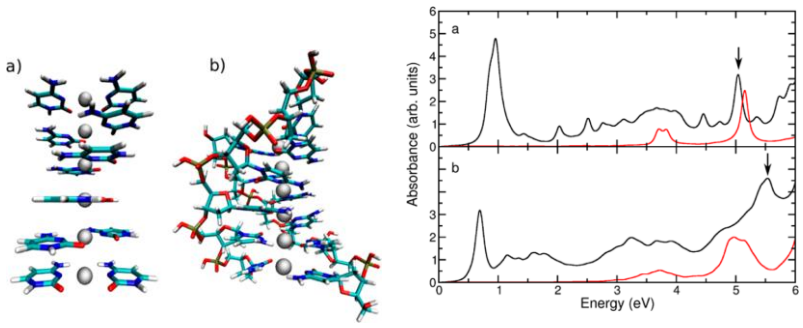

*Adapted with permission from Ref.[93] (Copyright 2017 the Owner Societies)

MCD Spectroscopy for Studying the Optical Properties of Noble Metal NPs

Optical absorption spectroscopy is a simple and widely applied method for investigation of optical properties. Unfortunately, sometimes optical absorption spectra are poorly resolved and tend to appear very similar for different complexes.[94-96] In these cases, MCD and CD spectroscopy can be applied. In general, MCD and CD spectra yield more detailed information than the corresponding optical absorption spectrum.

It is well known that the interpretation of experimental MCD spectra is a complicated process, especially for low–symmetry systems. Therefore, theoretical simulation of the MCD spectra can be used to assist in the understanding of empirically measured MCD spectra and can provide useful information. Theoretically simulated MCD spectra were obtained for investigation of the electronic structures of porphyrins (M = Ca, Ni and Zn),[97] phthalocyanine (M = Mg and Zn),[98] tetraazaporphyrin (M = Mg, Zn and Ni),[98] axially pyridine coordinated metallocorroles,[99] buckybowls,[100] *etc*. All simulated MCD spectra are in good agreement with available experimental findings for considered systems.

Application of MCD Spectroscopy

MCD spectroscopy is an important technique for investigation of the electronic structure and optical properties of different chemical systems. This type of spectroscopy yields more detailed information than a UV-Vis absorption spectrum, which is usually poorly resolved and often tends to appear very similar for different complexes.[94-96] It is well known that in the case of natural circular dichroism (CD) spectroscopy the investigated species need to be optically active to obtain spectral signal and provide information about electronic structure, whereas the MCD signal does not depend on the optical activity of the sample and arises due to interaction of the electronic levels with the magnetic field. This fact makes MCD spectroscopy widely applicable to different groups of organic and inorganic molecules, metal complexes, and biological systems for characterization of metal sites in biological molecules.[26, 30, 31, 94-96, 101-103] For example, MCD spectroscopy in conjunction with *in situ* potentiometric control is ideally suited for deduction of the spin and oxidation state.[104] Haemoproteins have been extensively studied by MCD, which has a capacity to define haem oxidation, state, spin, geometry and axial ligands (number and type) in solution.[105]

Additionally, MCD in combination with absorption spectra can be used for the study of electronic structures of metal complexes with inorganic and organic ligands.[26, 30, 31, 94] Mason and co–workers[96] applied MCD spectroscopy to investigate the electronic structure of noble metal nanoparticles (**Figure 1–11**). Moreover, metal complexes with inorganic ligands that have been studied include square complexes (symmetry D_{4h}) PtX_4^{2-} and AuX_4^- (X = Cl, Br, I),[106, 107] $Pt(CN)_4^{2-}$,[108] $Pt(NH_3)_4^{2+}$,[109] linear complexes (symmetry $D_{\infty h}$) HgX_2 and AuX_2^- (X = Cl, Br, I),[110, 111] *etc*. Metal cluster complexes with organic ligands that have been studied include $Pt_3(CO)_3(P(t–Bu)_3)_3$, $Hg_3(dppm)_3^{4+}$, $Pt(AuPPh_3)_8^{2+}$, $Au_9(PPh_3)_8^{3+}$, $Au_8(PPh_3)_8^{2+}$, *etc*.[26, 30, 31, 94] For some of these complexes, a Hückel molecular orbital treatment was applied to aid in interpretation of MCD spectra. The obtained results evidence that MCD adds important details during consideration of the absorption spectrum and provides significant additional information about the electronic structure for the considered systems.

Figure 1–11. MCD (top) spectra and optical absorption (bottom) spectra for $[Au_9(PPh_3)_8]^{3+}$

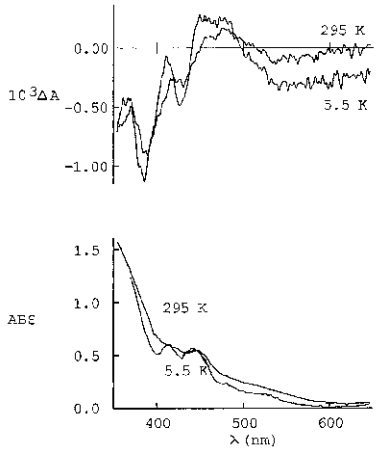

*Reprinted with permission from Ref.[112] (Copyright 2001 American Chemical Society).

MCD Spectra of Plasmonic Silver and Gold NPs

CD spectroscopy is a very useful technique for determination of the plasmon band for colloidal gold and silver NPs.[112, 113] Considerable magneto–optical activity has been observed in aqueous solutions of colloidal noble metal nanoparticles with diameters up to 50 nm when a magnetic field was applied (**Figure 1–12**). The absorption and MCD spectra of gold and silver NPs both exhibit localized surface plasmon resonance (LSPR). MCD spectra show pronounced

Zeeman splitting in the plasmon absorption bands. In other words, the MCD spectral shape is derivative–like.

Figure 1–12. MCD (top) and absorption (bottom) spectra of the surface plasmon band at 523 nm for colloidal gold nanoparticles in water. (A) H = 7.0 T and (B) H = 0.0 T.

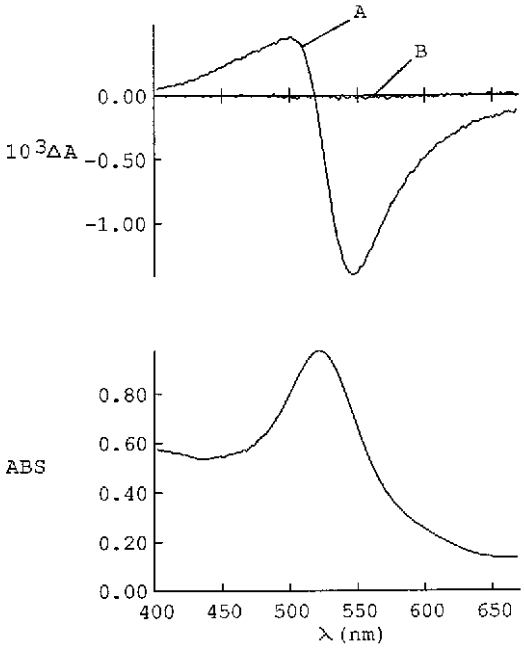

*Reprinted with permission from Ref.[112] (Copyright 2001 American Chemical Society).

Unfortunately, in the literature there are no theoretical studies of properties for small ligand–protected gold nanoclusters using MCD, which would help to get new important information about optical and electronic properties of gold clusters and better understand their behavior.

CD Spectroscopy for Studying Chiral Noble NPs

Chirality is a unique property of some molecules, complexes or clusters that plays an important role in different branches of science such as chemistry, biology, medicine and pharmacology. Some gold nanoclusters can exhibit chiral behavior, and CD signals have been measured in ligand–protected metal clusters and NPs. The first observation of this phenomenon was obtained by Schaaff and Whetten in 2000.[114] In this research, the optical activity of a series of giant metal-cluster compounds, each composed of a gold core and glutathione (GSH) ligands, was investigated. Gold NPs were prepared from Au(I)SG polymers and separated by gel

electrophoresis. Systems with metal core nuclearity in the range of 20 – 80 gold atoms were obtained. Their results showed that the mixture, as obtained simply from the reduction of the precursor Au(I)SG polymer, did not show strong quantum size effects in the optical absorption spectra, nor strong chiroptical effects in the CD. Chiroptical effects in the CD were only revealed when the various cluster compounds were separated (**Figure 1–13**).[114] These results not only provided evidence for the existence of novel optically active nanomaterials, but also indicated that chiral effects are present in matter at the nanoscale.

Figure 1–13. Optical absorption spectrum (lower, left axis) and CD spectrum (upper, right axis) of gold-glutathione (Au:SG) clusters in aqueous solution.

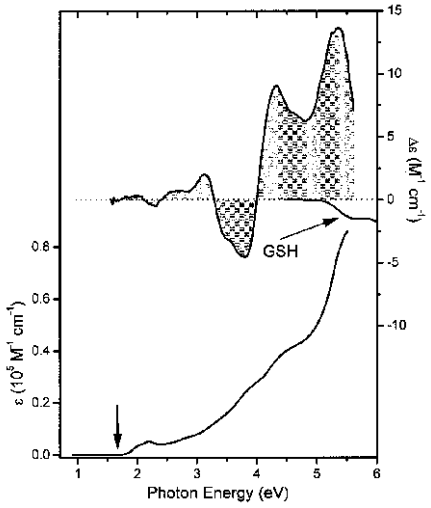

*Reprinted with permission from Ref.[114] (Copyright 2000 American Chemical Society).

The induction of the chirality on a gold cluster surface is important, especially for the development of enantioselective nanocatalysis.[115] Chiral gold NPs can be obtained in a few different ways: (i) via using an intrinsically chiral inorganic core; (ii) via protection of an achiral metal core by chiral ligands; and (iii) via chiral arrangement of the ligands around an achiral core.[114, 116-122]

Chiral Thiolate–Stabilized Gold NPs

Chiral thiolate–stabilized gold NPs have gained significant interest over recent years. Strong Cotton effects of gold nanoclusters protected by chiral ligands have been observed in numerous studies.[13, 18, 114, 120, 123-128] For example, gold NPs (with mean diameters of 0.57, 1.18, and 1.75 nm) protected by *D*- and *L*-penicillamine act as a chiral structures, and exhibit mirror

images in their CD spectra.[120] Another example is the $Au_{25}(SR)_{18}$ structure, which shows no chiroptical activity if protected with achiral SR ligands. However, when achiral ligands are exchanged by chiral thiols, Cotton effects are observed (**Figure 1–14**).[129, 130] Chiral thiolate ligands that have been used include BINAS (R/S-1,1'-binaphthyl-2,2'-dithiol), NILC/NIDC (N-isobutyryl-L/D-cysteine), Capt (captopril), SG (glutathione), chirally modified phenylethanethiol (PET*), *etc*.[129, 130]

Figure 1–14. CD spectra (left) and optical absorption spectra (right) of A) achiral $Au_{25}(PET)_{18}$ cluster; B) chiral $Au_{25}(R–BINAS)_{18}$ cluster, and C) chiral $Au_{25}(S–BINAS)_{18}$ cluster

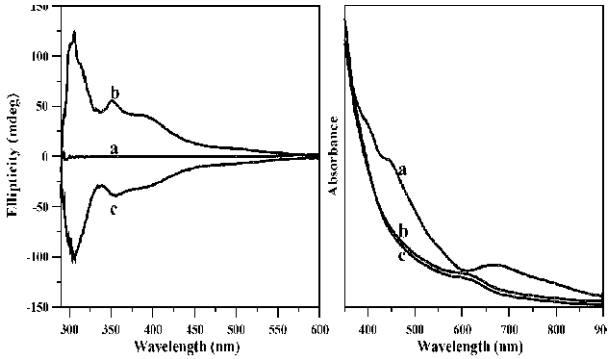

*Reprinted with permission from Ref.[129] (Copyright 2009 American Chemical Society).

Intrinsically chiral gold clusters include $Au_{28}(SR)_{20}$, $Au_{38}(SR)_{24}$, $Au_{40}(SR)_{24}$ and $Au_{102}(SR)_{44}$ systems.[13, 16, 125, 126] The CD spectra of their enantiomers are perfect mirror images. The chirality of the nanoclusters arises from the chiral arrangement of the thiolates on its surface, forming "staple motifs".[123] In these clusters gold cores can be protected either by achiral or chiral ligands, and in both cases they will yield chiroptically active systems.

The crystal structure of $Au_{28}(TBBT)_{20}$ (where TBBT = 4-tert-butylbenzenethiolate) cluster exhibits a rod–like Au_{20} kernel consisting of two interpenetrating cuboctahedra.[13] The gold core is protected by four dimeric $Au_2(SR)_3$ units and eight bridging (–SR–) thiolates.[13] The unit cell of $Au_{28}(TBBT)_{20}$ single crystals contains a pair of enantiomers. Theoretical investigations of the optical properties of the $Au_{28}(TBBT)_{20}$ cluster were performed by Häkkinen and co–workers.[124] They optimized the structure of a model cluster $Au_{28}(SMe)_{20}$ and calculated both absorption and circular dichroism spectra of the right-handed enantiomer using TDDFT. A theoretical analysis of the optimized structure shows that trimeric units $Au_3(SR)_4$ are present (in addition to the known dimers) instead of direct binding of thiolates to the kernel of the cluster. This was the first observation of trimeric units in a cluster of known structure. The

cluster can be reformulated as $Au_{14}(Au_2(SR)_3)_4(Au_3(SR)_4)_2$ (**Figure 1–15**).[13] Experimental and theoretical results showed strong CD signals for $Au_{28}(TBBT)_{20}$ enantiomers. Moreover, the obtained CD spectrum resolved a series of electronic transitions that is not found in the absorption spectrum.[13, 124] Therefore, CD spectroscopy is able to provide more detailed information with respect to optical absorption spectroscopy.

Figure 1–15. A) The two enantiomers of $Au_{28}(TBBT)_{20}$; B) CD spectra of enantiomers; and C) normal optical absorption spectrum.

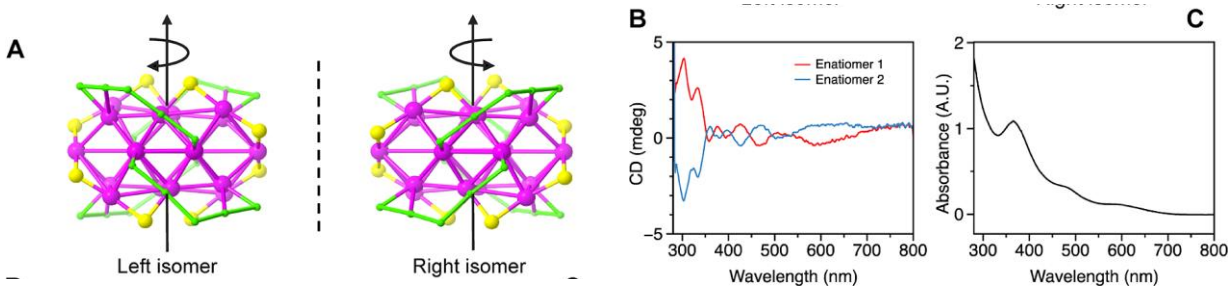

*Adapted with permission from Ref. [13] (Copyright 2013 American Chemical Society).

Figure 1–16. A) Crystal structure of the left–handed enantiomer of $Au_{38}(2–PET)_{24}$ and B) CD spectra of left– and right–handed enantiomers and the racemate of $Au_{38}(2–PET)_{24}$.

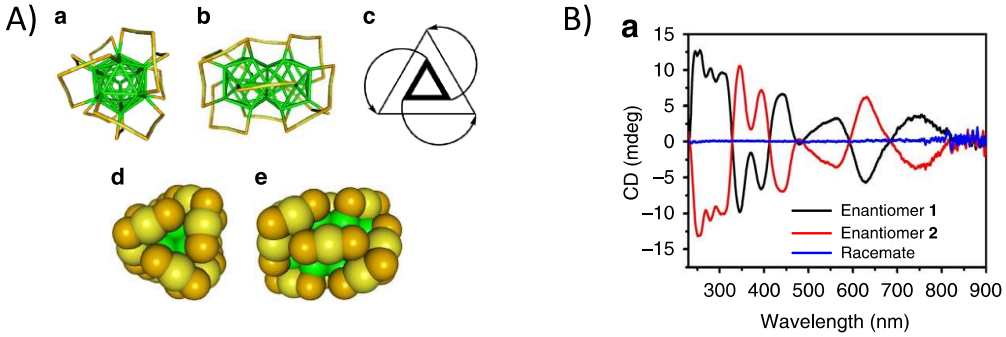

*Adapted with permission from Ref.[123] (Copyright 2012 Macmillan Publishers Limited).

The crystal structure of the $Au_{38}(2–PET)_{24}$ cluster was solved by Qian and co–workers in 2010.[16] However, prior to this work, theoretical studies enabled elucidation of the basic structural features of this cluster.[131] The structure of this cluster consists of a face–fused bi–icosahedral Au_{23} core, which is protected by six dimeric and three monomeric units. The intrinsic chirality of this cluster was studied by Aikens and co–workers.[132] In this study, theoretical and experimental approaches were combined. Geometrical and electronic structures as well as optical properties of $Au_{38}(SR)_{24}$ were investigated by theory for R = CH_3 and C_6H_{13} and by powder X–ray crystallography for R = $C_{12}H_{25}$ clusters. Computationally, two types of

isomers were analyzed: an achiral cluster with symmetry C_{3h} and a chiral cluster with D_3 symmetry. The lowest–energy D_3 isomer has an intrinsically chiral structure due to a special arrangement of the protective $SR(AuSR)_x$ units on the surface of the Au_{23} core. Theoretical absorption and CD spectra of $Au_{38}(SR)_{24}$ are in good agreement with those measured experimentally for $Au_{38}(SG)_{24}$ in the low–energy excitation (NIR–visible light) range.[132] This study showed that chiroptical activity of $Au_{38}(SR)_{24}$ clusters is related to the chiral arrangement of the gold–thiolate ligands around Au_{23} core. Experimentally measured CD spectra for separated enantiomers of the $Au_{38}(2–PET)_{24}$ cluster show perfect mirror image signals (**Figure 1–16**).[123]

Figure 1–17. A) Structures of four low-energy structures A1, A2, B1 and B2 of $Au_{40}(SCH_3)_{24}$, and B) calculated CD spectra of structures A1, A2, B1, and B2 as compared to the experimental CD spectrum (black curve) of $Au_{40}(2\text{-}PET)_{24}$.

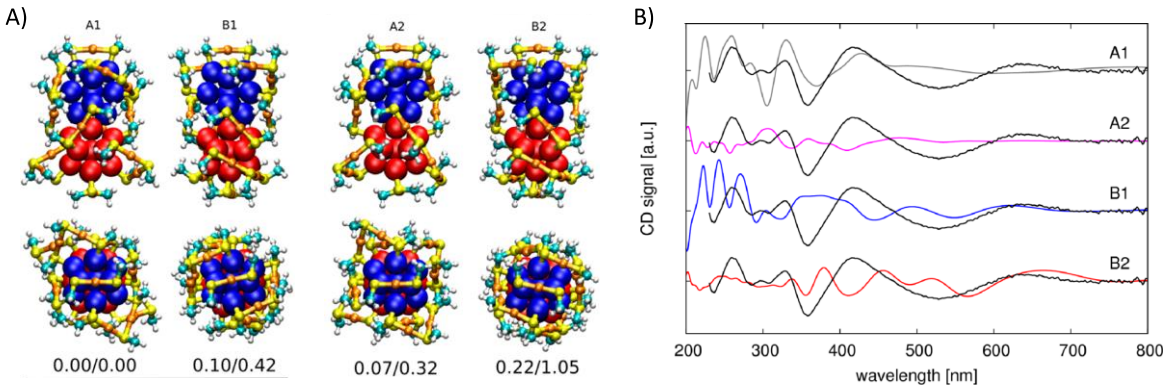

*Adapted with permission from Ref.[18] (Copyright 2012 American Chemical Society).

The next intrinsically chiral gold cluster is $Au_{40}(2–PET)_{24}$.[125, 126] Enantiomers of this cluster were separated via high-performance liquid chromatography (HPLC). The collected fractions exhibit strong chiroptical activity with a mirror–image relationship. Unfortunately, the crystal structure of this cluster is not solved yet. The geometrical structure of the $Au_{40}(SR)_{24}$ cluster is still under debate. A few possible structures were proposed using DFT methods.[18, 133] According to the study of Häkkinen and co–workers,[18] the cluster contains an Au_{26} core that is composed by two icosahedra in edge–to–edge contact with a relative rotation of 90°. This metal core is protected by six monomeric and four dimeric units. In the paper, four low-energy structures A1, A2, B1 and B2 of $Au_{40}(SCH_3)_{24}$ were considered (**Figure 1–17**). The structure with the lowest energy also gives the best match with the measured linear absorption and CD spectra (**Figure 1–17**).[18] One year later, Jiang suggested a different low-symmetry structure for

the $Au_{40}(SR)_{24}$ nanoparticle with two extra Au atoms at the "waist" of a 23-atom biicosahedral core, which is covered by 3 monomer and 6 dimer units.[133]

Bidentate ligands have demonstrated their ability to induce chiroptical activity of thiolate–protected gold nanoclusters.[127] Ligand exchange reactions on $Au_{38}(2–PET)_{24}$ and $Au_{40}(2–PET)_{24}$ clusters with mono– and bidentate chiral thiols such as BINAS and CamSH were performed by Knoppe and co–workers.[127, 128] Their results showed that bidentate ligands lead to slow exchange. Also, even at very low BINAS coverage of the clusters, strong optical activity is induced (**Figure 1–18**). Non–linear behavior between chiroptical activity and the number of chiral ligands is found in the BINAS case for Au_{38} and Au_{40} clusters (**Figure 1–18**).[127, 128] In contrast to BINAP, the CamSH ligands yield weaker optical activity, which demonstrates that the nature of the ligand affects the chiral activity of the gold clusters.

Figure 1–18. Anisotropy factors after 6, 24 and 72 h for A) $Au_{38}(2–PET)_{24–2x}(BINAS)_x$, and B) $Au_{40}(2–PET)_{24–2x}(BINAS)_x$.

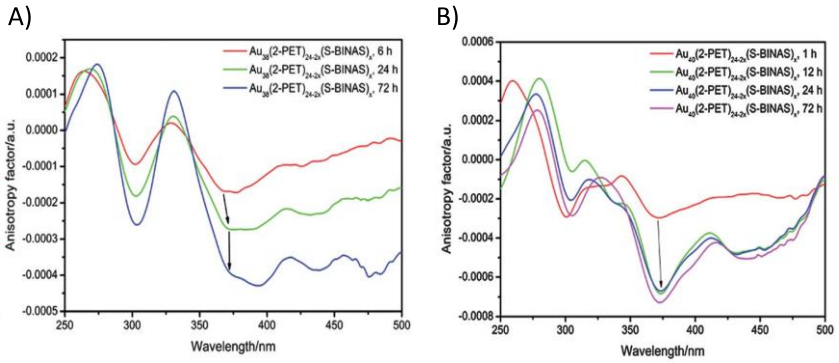

*Reprinted with permission from Ref.[128] (Copyright 2012 The Royal Society of Chemistry)

The influential $Au_{102}(SR)_{44}$ nanoparticle also exhibits intrinsic chirality.[127] Its X–ray crystal structure was successfully determined by Kornberg and co–workers in 2007.[20] Chiral C_5 symmetry was found for the core of the cluster.

Chiral Phosphine–Stabilized Gold NPs

Small gold clusters protected by bi– and tridentate phosphine ligands can also exhibit chiroptical properties. A great number of ultrasmall gold clusters (up to 22 gold core atoms) stabilized by bidentate phosphines have been synthesized and characterized by crystallography and electrospray ionization mass spectrometry, such as $[Au_6(P\text{^}P)_4]^{2+}$, $[Au_8(dppp)_4]^{2+}$, $[Au_8(dppa)_4Cl_2]^{2+}$, $[Au_8(dppp)_4Cl_2]^{2+}$, $[Au_8(BINAP)_3(PPh_3)_2]^{2+}$, $[Au_9(dpph)_4]^{3+}$,

$[Au_{11}(DIOP)_4Cl_2]^+$, $[Au_{11}(BINAP)_4Cl_2]^+$, $[Au_{11}(dppp)_5]^{3+}$, $[Au_{11}(dppe)_6]^{3+}$, $[Au_{13}(dppe)_5Cl_2]^{3+}$, $[Au_{22}(dppo)_6]^0$, and $[Au_{20}(PP_3)_4]^{4+}$.[44, 58, 69, 134-137] Unfortunately, the optical properties of this promising class of small gold nanoclusters protected with bisphosphine (P^P) ligands are not very well studied. There are just a few experimental[40-44] and theoretical[45, 47] papers found in the literature. All these empirical results together with theoretical studies suggest that the bisphosphine (P^P) ligands would affect the core structure and the chiroptical activity of the ultrasmall gold clusters. However, despite these empirical and theoretical studies, the origin of the chiroptical activity of metal clusters protected by optically active organic molecules is still unclear.

Figure 1–19. Optical absorption and CD spectra of $[Au_{11}(S/R–DIOP)_4Cl_2]^+$ (1S/1R) and $[Au_8(S/R–BINAP)_3(PPh_3)_2]^{2+}$ (2S/2R).

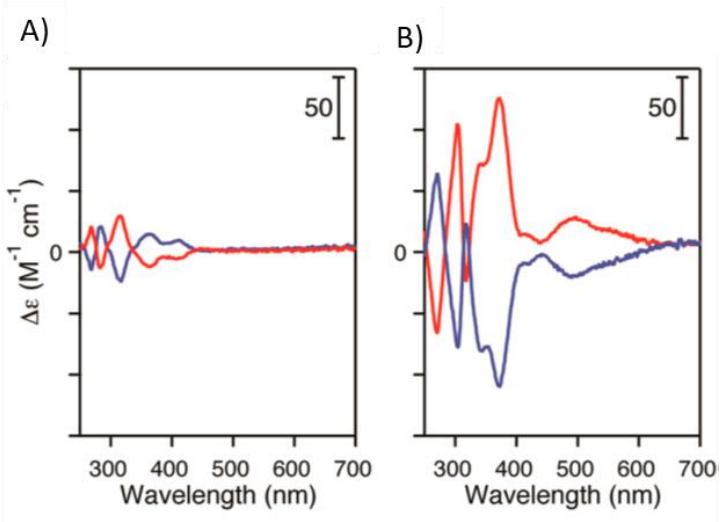

*Reprinted with permission from Ref.[40] (Copyright 2016 American Chemical Society).

Chiroptical activity of undecagold $[Au_{11}(L)_8X_2]^+$ and $[Au_{11}(P^P)_4X_2]^+$ (X = Cl and Br) clusters stabilized by the achiral monodentate (L = 4,4',4'' – phosphinidyne-tris(N-methylbenzamide) (PTMB) and triphenylphosphine (TPP)), and bidentate (P^P = BINAP) phosphine ligands were performed by Tsukuda and co-workers.[41] In that study, the CD spectra of enantiomers $[Au_{11}(R\text{-BINAP})_4X_2]^+$ and $[Au_{11}(S\text{-BINAP})_4X_2]^+$ exhibited intense and mirror image Cotton effects in the 250–500 nm spectral range. However, undecagold clusters stabilized by achiral phosphine ligands did not show chiroptical activity, with CD signals near zero.[41] In this study, these authors initially explained the optical activity in chiral ligand–protected nanoclusters by structural deformation of the metallic core during ligation. It was mentioned that in single crystal X-ray diffraction studies on various phosphine-stabilized Au_{11} clusters, the

Au_{11}^{3+} core geometries (Au–Au distances in gold core) vary significantly with the phosphine ligands used.[41] The flexible nature of the core may be due to the fact that ten out of the eleven atoms are located on the core surface, and are highly unsaturated. Also, the distances of peripheral Au atoms in the undecagold clusters protected by BINAP (2.8–3.3 Å) are much smaller than in the Au_2X_2(BINAP) precursor (initially thought to be ~6.0 Å), which can cause core deformation and generate optical activity associated with the electronic transitions within the core.[41]

Additional interesting and important features of the chiral gold complexes were recently observed by Tsukuda and co–workers (**Figure 1–19**).[40] They found that the gold clusters exhibit CD signals with different intensities when stabilized by BINAP (2,2'-bis(diphenylphosphino)-1,1'-binaphthyl) and DIOP (o-isopropylidene-2,3-dihydroxy-1,4-bis(diphenylphosphino)butane) ligands: BINAP–protected gold clusters have larger anisotropy factors than DIOP–protected species.[40, 41] Single crystal X–ray analysis of the enantiopure samples of $[Au_{11}(S/R\text{–DIOP})_4Cl_2]^+$ (1S/1R) and $[Au_8(S/R\text{–BINAP})_3(PPh_3)_2]^{2+}$ (2S/2R) revealed that both the Au_{11} and Au_8 cores are intrinsically chiral and that the ligand shells are arranged in a chiral geometry. They proposed that the difference in the optical response of gold clusters protected by DIOP and BINAP ligands is enhanced by a chiral arrangement of the π-electron system of BINAP in close vicinity to the Au core. To better understand this phenomenon, application of theoretical methods and approaches are necessary. This work will be described more detailed in Chapter 3.

Theoretical Models of the Origin of Chiroptical Activity in Ligand-Stabilized Gold NPs

There are at least three essential mechanisms for explanation of the origin of chirality in ligand-protected metal NPs that are mentioned in the literature: (i) a chiral core model, (ii) a dissymmetric field model, and (iii) a "chiral footprint" model.

Chiral core model[114, 120] – chirality of the metal clusters is generated by an intrinsic chiral core or as a result of a structural distortion due to interaction with chiral ligands. Initially, Schaaff and Whetten proposed an inherently chiral structure for the metal cluster cores with 20–40 atoms as their main explanation for the intense optical activity observed in L-glutathione-protected gold cluster compounds.[114] However, investigation of the structural fluctuations in the

metal core due to the ligation process using experimental measurement techniques is a very sophisticated and complicated process. Therefore, to study the existence of chiral structures in gold nanoclusters, and provide support to the intrinsically chiral cluster core mechanism as the effect responsible for the chiroptical activity, consistent theoretical calculations and methodologies were required. In 2003, Garzon *et al.*[138-140] performed systematic cluster structure optimizations of bare (in the size range of 12–212 atoms) and methylthiol-passivated gold nanoclusters $Au_{28}(SCH_3)_{16}$ and $Au_{38}(SCH_3)_{24}$ using DFT methods. It was shown that low-symmetry disordered structures are energetically preferably for various clusters. For example, chiral structures were obtained as the lowest energy isomers of bare Au_{28} and Au_{55} clusters, whereas the bare Au_{38} cluster was found to prefer the achiral O_h geometry.

Figure 1–20. Structures of bare and methylthiol-passivated chiral gold nanoclusters.

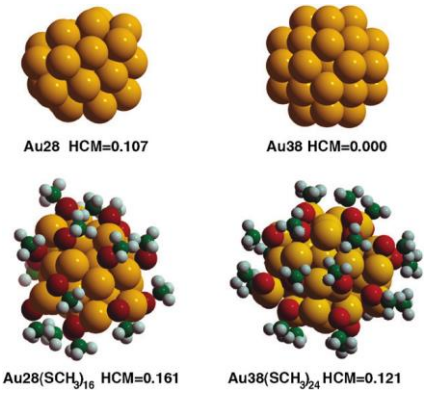

*Reprinted with permission from Ref.[139] (Copyright 2009 The Royal Society of Chemistry)

For determination of chirality in the clusters, the Hausdorff chirality measure (HCM) for bare and ligand–protected gold clusters was used. These results showed that the interaction of the gold core with the thiol ligands could increase the chirality of an intrinsically chiral cluster or induce chirality in an originally achiral cluster (**Figure 1–20**). For small gold clusters, it has been shown both theoretically and experimentally that low-symmetry disordered structures.

Hakkinen and co–workers[141, 142] studied geometrical and electronic structures of the bare anions Cu_n^-, Ag_n^- and Au_n^- with n=53–58 using UV–photoelectron spectroscopy and *ab initio* calculations. They showed that Cu_n^- and Ag_n^- exhibit highly degenerate states, which is a direct consequence of their icosahedral symmetry. However, gold clusters in the same size range show completely different spectra with almost no degeneracy, which indicates that they have structures of much lower symmetry. This behavior is related to strong relativistic bonding effects in gold, as demonstrated by *ab initio* calculations.

Dissymmetric field model[120, 143] – chirality originates when an achiral metal core is surrounded by chiral ligands in an achiral absorption patterns or stabilized by achiral ligands in chiral absorption patterns. According to this model, the induced optical activity in a chiral monolayer-protected cluster could arise from an achiral metal core perturbed by a chiral field originating from the ligands. In other word, the chiral ligands or achiral ligands in chiral absorption patterns induce a chiral perturbation on the core, making it chiroptically active.[143] The dissymmetric environment acts as a perturbing electrostatic field to break down the symmetry of the electronic state of nanoclusters as is observed for chiral *d*-metal complexes.[120]

A dissymmetrically-perturbed particle-in-a-box model was used to study the origin of chirality in Au_{28}(R-methylthiirane)$_6$ and Au_{28}(glutathione)$_6$ NPs.[143] In this model the Au_n core was modeled with non-interacting electrons confined to a cubic box, and the surrounding adsorbates were described using point charges (**Figure 1–21**). The first-order response of the cluster electronic states in a perturbation theory framework can be calculated. Electric and magnetic transition moments could be determined. The obtained transition moments are then used for calculation of the rotational strength and CD spectrum. Their results demonstrated that the induced optical activity of chiral monolayer-protected clusters could arise from symmetric metal cores perturbed by a dissymmetric or chiral field originating from the adsorbates.[143]

Figure 1–21. A) schematic representation of (a) a single molecular adsorbate and adsorbate-Au cluster (i.e. Au_{14}(R-methylthiirane) represented by (b) a system of point charges; and B) optical absorption and CD spectra of Au_{14} and Au_{28} clusters.

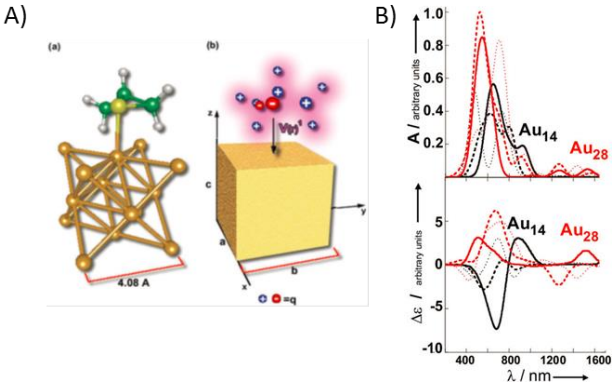

*Adapted with permission from Ref.[143] (Copyright 2006 the Owner Societies)

In addition, the origin of chiroptical activity in gold nanocluster enantiomers protected by a pair of optically active penicillamine (D-Pen or L-Pen) ligands was explained in terms of the dissymmetric field model. These ligands contain chiral centers, so optical activity can be

induced from the dissymmetric field transmission through space and by way of the chemical bonds linking the asymmetric center to the chromophore.[120]

The "chiral footprint" model"[144] – the chirality of metal NPs is generated by a local chiral distortion of the nanoparticle surface atoms involved in the adsorption of the ligand. This model was created after the discovery that chiral molecules on a metal surface create a local chiral environment.[145] In 2001, Hamblot and co-workers[145] studied the absorption process of chiral (R,R)-tartaric acid on the Ni-surface with formation of highly stereoselective catalysts (**Figure 1–22**). A combination of experimental and theoretical methods[145] provided detailed information about chiral induction of the metal surface. The most stable adsorption structure of (R,R)-tartaric acid on the Ni-surface was achieved by a chiral relaxation of atoms in the bulk-truncation Ni(110) surface. The most stable adsorption structure is one in which the adsorption induced stress is alleviated by significant relaxation of surface metal atoms so that a long distance of 7.47 Å between pairs of Ni atoms can be accommodated at the surface. Also, the adsorbed complex destroys all the local mirror planes associated with the clean surface locally. DFT calculations show that only one chiral footprint is favored by the (R,R)-tartaric acid, which mean that, at room temperature, the same local chiral motif is expected to be repeated across over 90% of the metal surface, leading to an overall chiral and very enantiospecific system.[145]

Figure 1–22. Chiral footprint imparted by bitartrate on Ni(100) surface.

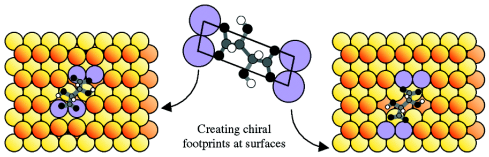

*Reprinted with permission from Ref.[145] (Copyright 2006 the Owner Societies)

This "chiral footprint" model has been employed to explain the origin of chiroptical activity in chiral ligand-protected gold NPs.[144, 146] Optical activity of small gold particles protected with N-isobutyryl-D-cysteine and N-isobutyryl-L-cysteine were investigated with optical absorption and vibrational circular dichroism (VCD) spectroscopy as well as DFT methods.[144] The origin of the chirality of these clusters was explained with "chiral footprint" theory. The results indicate that the carboxylic acid group interacts with the gold particle, and it is proposed that this "two point interaction" leads to a "chiral footprint" on the particle surface, which is the origin of the observed optical activity.

In reality, the origin of chiroptical activity in the gold NPs is a complex problem and cannot be explained in terms of only one of the proposed mechanism such as the chiral metallic core, the dissymmetric field effect, or the chiral footprint model.

Origin of Chiroptical Activity in Ligand-Protected Gold NPs: First Principles Calculation

Understanding the origin of chirality and the impact of the ligand nature on the chiroptical activity of metal clusters protected by optically active organic molecules is very important, in part because it will help to design novel chiral metallic nanostructures with specific properties. One of the main applications for chiral gold nanoparticles is that they can be used as enantioselective nanocatalysts in the pharmaceutical industry and produce chiral molecules on an industrial scale.[147, 148]

The mechanism for the origin of chiral response of thiolate-protected gold clusters with achiral metal cores and ligands was proposed by Aikens and co–workers.[132] Structural, electronic, and optical properties of the thiolate-protected $Au_{38}(SR)_{24}$ cluster were studied by density-functional theory computations (R = CH_3 and R = C_6H_{13}) and by powder X-ray crystallography (R = $C_{12}H_{25}$). Although the alkane thiolate ligands are achiral, the chiral arrangement of the binding motifs yields strong CD signals. Two types of arrangements of Au–S atoms around the Au_{23} gold core were considered: (i) chiral D_3 symmetric structures; and (ii) achiral C_{3h} structures (**Figure 1–23**). Computations showed that $Au_{38}(SR)_{24}$ clusters with a D_3 symmetric structure exhibit strong CD signals, whereas the C_{3h} systems have weak optical response in their CD spectra (**Figure 1–24**).[132]. This study demonstrated that the chiral response for low excitation energies is related to the chiral arrangement of the gold-thiolate ligand shell around the bi-icosahedral Au_{23} core. This mechanism is qualitatively different from the one reported from a theoretical study of $[Au_{25}(SR)_{18}]^-$ clusters.[149]

Figure 1–23. A) Structure of Au_{23} core; B) chiral D_3 arrangement of the Au-S atoms; C) C_{3h} arrangement of the Au–S atoms; and D) Optimal SCH_3 distribution on the low–energy D_3 symmetry structure.

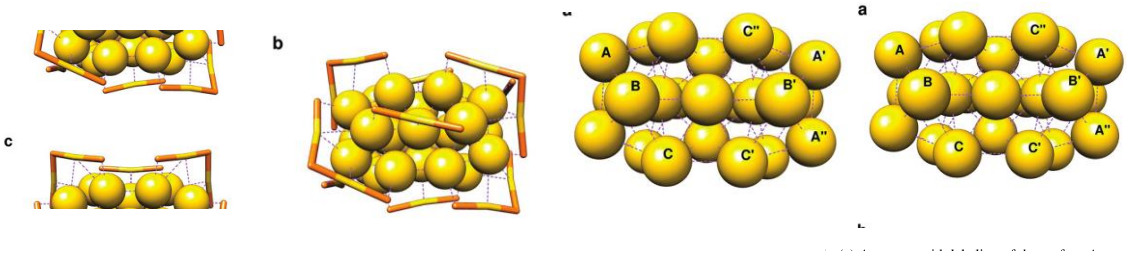

*Reprinted with permission from Ref.[132] (Copyright 2010 American Chemical Society).

Figure 1–24. A) CD spectrum of low–energy $Au_{38}(SCH_3)_{24}$ (D_3 symmetry structure) and B) CD spectrum of low–energy $Au_{38}(SCH_3)_{24}$ (C_{3h} symmetry structure). (Note: folded means convoluted spectrum).

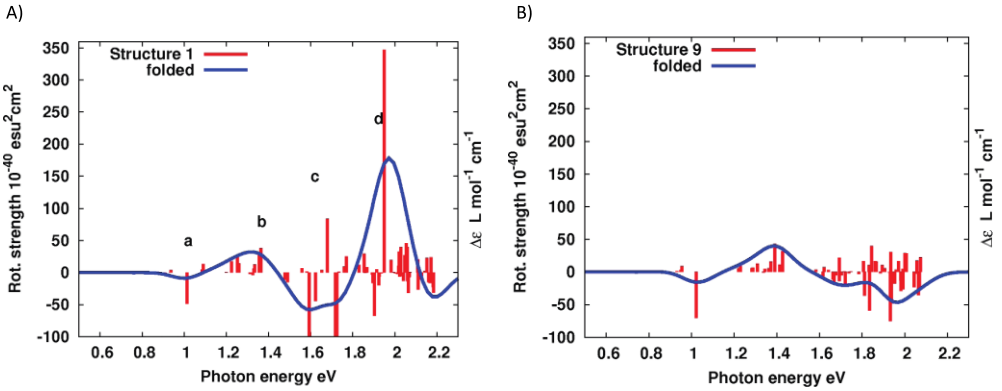

*Reprinted with permission from Ref.[132] (Copyright 2010 American Chemical Society).

Provorse and Aikens[45] applied TDDFT calculations to examine the optical and chiroptical properties of phosphine–protected undecagold $[Au_{11}BINAP_4X_2]^+$ complexes and their Au_2X_2BINAP precursors, where X = Cl, Br. To simulate BINAP ligands in $[Au_{11}BINAP_4X_2]^+$ complexes, the simple model ligand 1,4-diphosphino-1,3-butadiene (dpb) was used. Optical absorption and CD spectra were calculated. The results showed that experimental peak positions are well reproduced in the calculations (**Figure 1–25**). The theoretical CD spectrum of the $[Au_{11}(dpb)_4X_2]^+$ complex has two negative peaks around 480-530 nm and 390-410 nm, which closely match experiment. The third peak in the spectrum at 300-350 nm has the opposite sign from experiment, which can be due to substitution of BINAP by the model ligand dpb. Structural analysis of these systems exhibited that the lowest energy structure of $[Au_{11}BINAP_4X_2]^+$ has a chiral C_2 geometry, whereas monodentate phosphine ligands lead to a C_1 structure. Reduction of the core chiral symmetry from C_2 to C_1 leads to a

decrease in the rotatory strengths by a factor of 2, whereas removal of the ligands results in a decrease of approximately 5-10 for this system. It was clearly shown that the optical activity of the gold core is very sensitive to the existence and chiral arrangement of the surrounding ligands, and bidentate phosphine ligands have both a structural and electronic impact on the system.[45]

Figure 1–25. Theoretical (red) and experimental (blue) A) optical absorption and B) CD spectra of $[Au_{11}L_4Br_2]^+$.

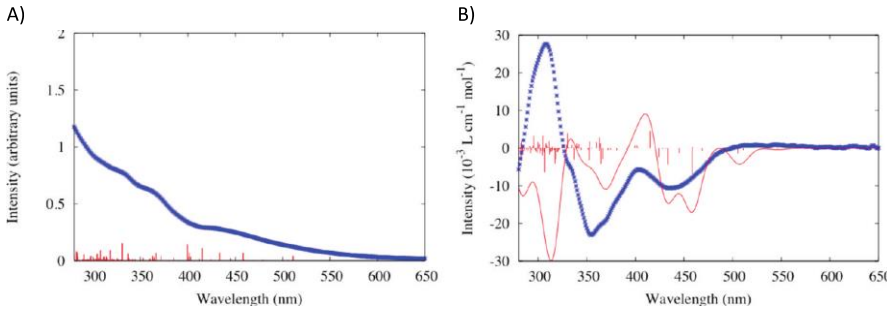

*Reprinted with permission from Ref.[45] (Copyright 2010 American Chemical Society).

Figure 1–26. (Left) Structure of the bare Au_{20} core of the cluster. The triblade 7–atom motif is highlighted in blue. (Center) Structure of the ligand-protected right-handed enantiomer. (Right) Structure of the PP_3 ligand.

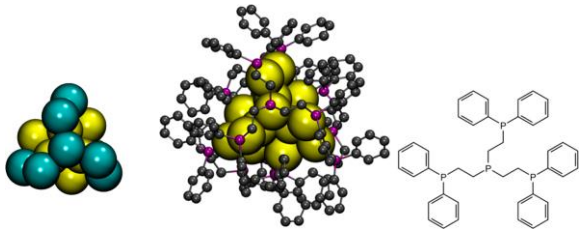

*Reprinted with permission from Ref.[47] (Copyright 2014 American Chemical Society).

Figure 1–27. CD spectra of A) isolated cores $(Au_{20})^{4+}$ (black) and $(Au_{23})^{9+}$ (red). B) clusters $[Au_{20}(PP_3)_4]^{4+}$ (black) and $Au_{38}(SMe)_{24}$ (red).

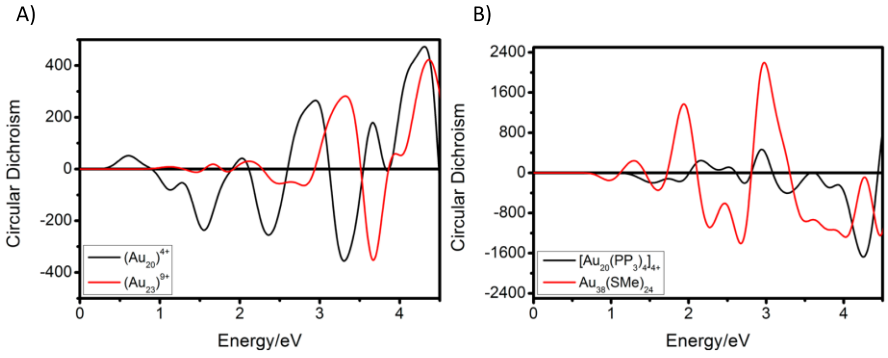

*Reprinted with permission from Ref.[47] (Copyright 2014 American Chemical Society).

Häkkinen and co–workers[47] investigated electronic structure and optical properties of the intrinsically chiral complex $[Au_{20}(PP_3)_4]^{4+}$ where PP_3 is tridentate phosphine ligand = tris(2-(diphenylphophino)ethyl)-phosphine) using DFT and TDDFT methods. Single-crystal structural analysis shows that the Au_{20} core is intrinsically chiral and has C_3 symmetry.[150] The Au_{20} core can be considered as a combination of an icosahedral Au_{13} and a helical Y-shaped Au_7 motif (**Figure 1–26**). This core is stabilized by four peripheral tetraphosphines. Comparison of the computed circular dichroism spectra of ligand–protected clusters $[Au_{20}(PP_3)_4]^{4+}$ vs. $Au_{38}(SMe)_{24}$, and their bare gold cores $(Au_{20})^{4+}$ vs. $(Au_{23})^{9+}$ was performed (**Figure 1–27**). The results showed that the intensity of optical activity in the bare clusters is dictated by the asymmetry of the clusters. However, in the case of $Au_{38}(SMe)_{24}$, the chiral arrangement of the protecting $(SR\text{-}Au)_2\text{-}SR$ units dominates the CD spectra and the phosphine protection has little influence.

Despite all these empirical and theoretical studies, the origin of the chiroptical activity of metal clusters protected by optically active organic molecules still remains unclear due mainly to the lack of structural information about ligand–protected gold NPs. Therefore, theoretical approaches (for example, DFT and TDDFT methods) can be very useful to help better understand this important question.

Overview of This Thesis

This thesis contains eight chapters in total. An introduction to the problems and review of the relevant literature is discussed in Chapter 1. The methods used in the study are then described in Chapter 2. The results from the studies undertaken in this thesis are presented in Chapters 3 – 7. Application of CD spectroscopy to study chiral systems is demonstrated in Chapters 3 and 4. In Chapter 3, the origin of chiral activity in octa– and undecagold clusters is studied. Chapter 4 examines optical properties of bare and DNA protected silver NPs. Chapters 5, 6 and 7 are related to the application of MCD spectroscopy for the study of optical and electronic properties of phosphine–protected AuNPs (Chapter 5 and 6), and for determination of the plasmonic behavior of bare AgNPs (Chapter 7). Finally, Chapter 8 outlines the main conclusions of this study.

Chapter 2 - Theory and Computational Methods

Quantum Chemistry

The Wave Function and Schrödinger Equation

Quantum chemistry applies quantum mechanics to solve different problems in chemistry such as thermodynamic property calculations, helping with interpretation and analysis of different types of molecular spectra, investigation of the mechanisms of chemical reactions, estimation of the relative stabilities of molecules and properties of reaction intermediates *etc*. Laws of quantum mechanics can successfully describe the behavior of microscopic systems like electrons, atoms and molecules.[151, 152] To describe the state of a system in quantum mechanics, the existence of a function of the particle coordinates called the wave function or state function $\boldsymbol{\Psi}$ was postulated. Due to the fact that the state will change with time, the wave function is also a function of time *t*. The wave function contains all possible information about the system it describes. However, $\boldsymbol{\Psi}$ itself does not have a physical meaning. Born postulated that $|\boldsymbol{\Psi}(x,t)|^2 dx$ gives the probability at time *t* of finding the particle in the region of the *x* axis lying between *x* and *x*+*dx*. In other words, $|\boldsymbol{\Psi}(x,t)|^2 dx$ is the probability for finding the particle at various places on the *x* axis.[151, 152]

To find the future state of a quantum–mechanical system from knowledge of its present state, the time–dependent Schrödinger equation (TDSE) is used:

$$i\frac{\partial \Psi(x,t)}{\partial t} = \hat{H}(x,t)\Psi(x,t) \tag{2.1}$$

where $i = \sqrt{-1}$ and $\hat{H}$ is the Hamiltonian operator. The Hamiltonian operator contains five terms: the kinetic energy of the electrons and nuclei, the attraction of the electrons to the nuclei, the interelectronic repulsion and internuclear repulsions.

Many applications of quantum chemistry do not experience any time-dependent external forces, and the time-dependence in the Hamiltonian disappears. In these cases, the time–independent Schrödinger equation (TISE) should be used:

$$\hat{H}\Psi(x) = E\Psi(x) \tag{2.2}$$

The TISE and TDSE cannot be solved exactly for most systems. However, numerous approximation methods are applied to solve the Schrödinger equation that can predict the desirable properties of molecular systems with reasonable accuracy.[152]

The Born-Oppenheimer Approximation

According to the non-relativistic approximation, the full Hamiltonian has the following form:[151]

$$\hat{H} = -\frac{\hbar^2}{2}\sum_{\alpha}\frac{1}{m_\alpha}\nabla_\alpha^2 - \frac{\hbar^2}{2m_e}\sum_i \nabla_i^2 + \sum_\alpha\sum_{\beta>\alpha}\frac{Z_\alpha Z_\beta}{R_{\alpha\beta}} - \sum_\alpha\sum_i\frac{Z_\alpha}{r_{i\alpha}} + \sum_i\sum_{i>j}\frac{1}{r_{ij}} \qquad (2.3)$$

where α and β refer to nuclei, and i and j refer to electrons; $R_{\alpha\beta}$ is the distance between nuclei α and β with atomic numbers Z_α and Z_β; $r_{i\alpha}$ is the distance between electron i and nucleus α; and r_{ij} is the distance between electrons i and j. The first term in equation (2.3) is the operator for kinetic energy of the nuclei, the second term is the operator for kinetic energy of the electrons, the third term is the potential energy of repulsion between the nuclei, and the fourth term is the potential energy of attraction between the electrons and the nuclei.

Solving the full Hamiltonian is a challenge for molecules as it contains terms that are difficult to compute. Born and Oppenheimer showed that to a very good approximation the nuclei in molecules are stationary with respect to the electrons. Mathematically the approximation states that the Schrödinger equation for a molecule may be separated into an electronic and a nuclear equation. This approximation allows us to solve the equation efficiently: considering the nuclei as fixed, we omit the nuclear kinetic-energy terms from the equation (2.3) to obtain the Schrödinger equation for electronic motion.[151, 152]

$$\left(\hat{H}_{el} + V_{NN}\right)\Psi_{el} = U\Psi_{el} \qquad (2.5)$$

$$\hat{H}_{el} = -\frac{\hbar^2}{2m_e}\sum_i \nabla_i^2 - \sum_\alpha\sum_i\frac{Z_\alpha}{r_{i\alpha}} + \sum_i\sum_{i>j}\frac{1}{r_{ij}} \qquad (2.6)$$

$$V_{NN} = \sum_\alpha\sum_{\beta>\alpha}\frac{Z_\alpha Z_\beta}{R_{\alpha\beta}} \qquad (2.7)$$

$$U = E_{el} + V_{NN} \qquad (2.8)$$

where $\hat{H}_{el}$ is the pure electronic Hamiltonian, and V_{NN} is the nuclear repulsion term.

So, to get the total internal energy of a system (U), we need to solve the electronic Schrödinger equation and then add the electronic energy to the internuclear repulsion, as shown in equation (2.8).

Basis Set

The molecular orbitals are usually expanded as linear combinations of atomic orbitals:

$$\Psi_i = \sum_r c_{ri}\,\varphi_r \tag{2.9}$$

where Ψ_i is a molecular orbital, φ_r are atomic orbitals, c_{ri} are coefficients representing the weights of the contributions of the n atomic orbitals to the molecular orbital, and r is an integer number that represents which atomic orbital is combined in the term. These atomic orbitals are referred to as basis functions which are mathematical functions that are convenient to manipulate and in linear combination give useful representations of MOs.[152]

Several types of basis functions can be used to describe the electron distribution around an atom and in the molecule as whole, including hydrogen-like functions based on solutions of the Schrödinger equation for the hydrogen atom, as well as Gaussian and Slater functions.[152]

Gaussian-type orbitals (GTO) can be considered as basis functions. A Cartesian GTO is defined by the equation:[151]

$$\varphi_{\zeta l_x l_y l_z}(x,y,z) = N x^{l_x} y^{l_y} z^{l_z} e^{-\zeta r^2} \tag{2.11}$$

where N is a normalization constant; l_x,l_y,l_z determine the type of orbital; ζ is a positive orbital exponent; and *x,y,z* are Cartesian coordinates. The reason Gaussian orbitals are often used is that the four-index integrals can be expressed analytically which significantly speeds up integral evaluation. However, a Gaussian functions do not have the desired cusp at the nucleus and hence gives a poor representation of an AO for small values of *r*.[151]

Another type of basis function is Slater-type orbitals (STO). STO's are good approximations for atomic wavefunctions and would be a natural choice for basis functions. Also, Slater orbitals describe more accurately with respect to GTO the features of the molecular orbitals and exhibit correct short- and long-range behavior. An STO is defined by the equation

$$\varphi_{\zeta nlm}(r,\theta,\phi) = N Y_{lm}(\theta,\phi) r^{n-1} e^{-\zeta r} \tag{2.10}$$

where N is a normalization constant, $Y_{lm}(\theta,\phi)$ are real or complex spherical harmonics, *r* is the distance of the electron from the atomic nucleus, and the ζ exponent controls the width of the orbitals. A large ζ gives a tight function, and a small ζ gives a diffuse function. Also, these functions are not mutually orthogonal, and their usage can be very time consuming for large molecules due to the calculation of three- and four–center integrals which cannot be performed

analytically and should be performed numerically. The Amsterdam Density Functional (ADF) program used in most of this research uses Slater orbitals.

Now, consider the terminology used to describe basis sets. The simplest one is a ***minimal basis set*** (SZ) that consists of one orbital (STO or GTO) for each atomic orbital (inner- and valence shell) of each atom. A ***double-zeta basis set*** (DZ) is obtained by replacing each orbital (STO or GTO) of a minimal basis set by two basis functions for each AO that differ in their orbital exponents. A ***triple-zeta basis set*** (TZ) replaces each orbital (STO or GTO) of a minimal basis set by three basis functions. A large basis set such as quadruple-zeta (QZ), 5Z, 6Z, *etc*., is obtained by replacing each basis function of a minimal basis set by four, five, six, *etc*. (STO or GTO) functions of different orbital exponents.[151] A split-valence basis uses only one (STO or GTO) basis function for each core AO, and a two (or more) for each valence AO.

Also, the quality of the basis set can be improved by addition of diffuse and polarization functions.[151, 152] ***Diffuse functions*** have small ζ exponents; this means the electron is held far away from the nucleus. These functions are necessary for anions, Rydberg states, and very electronegative atoms with a lot of electron density. ***Polarization functions*** are very important for modeling chemical bonding, because the bonds are often polarized. To polarize a basis function with angular momentum l, it is mixed with basis functions of angular momentum $l + 1$.

Density Functional Theory (DFT)

Density functional theory is based on the electron density function, designated by $\rho(x,y,z)$, instead of the wavefunction. A wavefunction for an N election system contains 4N variables (three spatial and one spin coordinate) for each electron, whereas the electron density function is a function of only the three spatial coordinates x, y and z.[152] The complexity of a wavefunction increases exponentially with the number of electrons, but the electron density has the same number of variables, independent of the system size. The electron density function is a probability per unit volume.[152] DFT calculates all the properties of atoms and molecules (geometries, energies, optical properties, *etc*.) from the electron density. The main problem of DFT is that although each different density yields a different ground state energy, the functional connecting these two quantities is not known.[153] To use DFT methods, functionals connecting the electron density with energy should be designed first.

Nowadays DFT calculations are based on the two Hohenberg–Kohn theorems and Kohn–Sham approach.

The Hohenberg-Kohn Theorems

The first Hohenberg–Kohn theorem says that all properties of molecule in a ground electronic state are determined by the ground state electron density function $\rho_0(x,y,z)$. So, if we know $\rho_0(x,y,z)$ we can calculate any ground state property. In other words, any ground state properties of a molecule are functions of the ground state electron density function. For example, for the energy:[152]

$$E_0 = E[\rho_0] \tag{2.12}$$

where E_0 is the ground state energy and E is a functional of the ground state electron density. This theorem says that a functional exists, but does not tell us how to find it.

The second Hohenberg–Kohn theorem says that any trial electron density function will give an energy higher than or equal to (if exact, it is the true electron density function) the true ground state energy (this theorem is analogous to the wavefunction variation theorem):[152]

$$E_v[\rho_t] \geq E_0[\rho_0] \tag{2.13}$$

where ρ_t is the trial electronic density, ρ_0 is the true electronic state, $E_0[\rho_0]$ is the true ground state energy, and $E_v[\rho_t]$ is the electronic energy from the trial electron density (it is an energy of the electrons moving under the potential of the atomic nuclei). DFT calculations use approximate functionals (because the exact functional is unknown) and can give an energy below the true energy. Thus, approximate DFT is not variational.

The Kohn-Sham Method

The Hohenberg–Kohn theorem states that we can calculate any molecular properties from the electron density. But, it does not tell us how to find electron density and calculate the functional. Kohn and Sham (KS) suggested a practical method to find ρ_0 and E_0. In order to evaluate the density of the interacting system, Kohn and Sham considered a fictitious system of N non–interacting electrons that move under the potential of the atomic nuclei. This nuclear potential is called the "external potential" $v(\mathbf{r})$.[152] Since the electrons are not interacting, the electronic Hamiltonian can be expressed as a sum of one–electron operators, has eigenfunctions

that are Slater determinants of the individual one–electron eigenfunctions, and has eigenvalues that arise from the sum of the one–electron eigenvalues.[154]

There are two basic ideas behind the KS approach: (i) the molecular energy can be expressed as a sum of terms and only one term is relatively small and involves the unknown functional; and (ii) the initial guess of the electron density ρ is used in the KS equations to calculate an initial guess of the KS orbitals, which is then used to refine the orbitals in a Self–Consistent–Field (SCF) manner. The final KS orbitals are used to calculate an electron density that in turn is used to calculate energy.

The ground state electronic energy of a molecule is a sum of expectation values of:[151, 152]

$$E_0 = E[\rho_0] = \langle T[\rho_0]\rangle + \langle V_{Ne}[\rho_0]\rangle + \langle V_{ee}[\rho_0]\rangle \tag{2.14}$$

where $T[\rho_0]$ is the electron kinetic energy, $V_{Ne}[\rho_0]$ is the nucleus–electron attraction potential energy, and $V_{ee}[\rho_0]$ is the electron–electron repulsion potential energy. The first term of equation (2.14) can be expressed as a sum of the kinetic energy contribution to the ground state of the non–interacting system and the kinetic energy difference between the real and non–interacting system (note: the subscript *s* denotes the non-interacting system):[151, 152]

$$\langle T[\rho_0]\rangle = \langle T_s[\rho_0]\rangle + \Delta\langle T[\rho_0]\rangle \tag{2.15}$$

The second term of equation (2.14) is known and can be calculated by:

$$\langle V_{Ne}[\rho_0]\rangle = \int \Psi \sum_{i=1}^{2n} v(\boldsymbol{r}_i)\, \Psi dt = \int \rho_0(\boldsymbol{r}) v(\boldsymbol{r}) d\boldsymbol{r} \tag{2.16}$$

The third term of (2.14) is electron–electron repulsion:

$$\langle V_{ee}[\rho_0]\rangle = \frac{1}{2}\iint \frac{\rho_0(\boldsymbol{r_1})\rho_0(\boldsymbol{r_2})}{r_{12}} d\boldsymbol{r_1} d\boldsymbol{r_2} + \Delta\langle V_{ee}[\rho_0]\rangle \tag{2.17}$$

where the first part of equation (2.17) represents the charge–cloud Coulomb repulsion energy, and r_{12} is the distance between coordinates r_1 and r_2. The term $\Delta\langle V_{ee}[\rho_0]\rangle$ is all non–classical corrections to the electron–electron repulsion energy between the real system and the non-interacting system.

Using equations (2.15) – (2.17), equation (2.14) can be written as:[151, 152]

$$E_0 = \langle T_s[\rho_0]\rangle + \int \rho_0(\boldsymbol{r}) v(\boldsymbol{r}) d\boldsymbol{r} + \frac{1}{2}\iint \frac{\rho_0(\boldsymbol{r_1})\rho_0(\boldsymbol{r_2})}{r_{12}} d\boldsymbol{r_1} d\boldsymbol{r_2} + \Delta\langle T[\rho_0]\rangle + \Delta\langle V_{ee}[\rho_0]\rangle \tag{2.18}$$

The last two terms of the equation (2.18) are unknown correction terms. Their sum is called the exchange correlation energy functional or the exchange–correlation energy, E_{XC}:

$$E_{XC} = \Delta\langle T[\rho_0]\rangle + \Delta\langle V_{ee}[\rho_0]\rangle \quad (2.19)$$

Since the functional E_{XC} is unknown, different types of approximations have been developed. These approximations vary from very simple to very complex. The accuracy of DFT calculations strongly depends on the approximation of the exchange–correlation functional. There is no single universal functional. The functional to choose depends on the system and properties investigated. The DFT functionals are classified as follows:

- Local Density Approximation (LDA) – is the lowest rung of approximation for the exchange–correlation part. In the LDA, the exchange–correlation energy density depends only on the density at a given point and it applies well to a uniform electron gas. This is the simplest density functional. For example, the Xα method is a special case of the LDA in which the correlation part of the exchange–correlation functional is neglected and the exchange functional depends on an empirical parameter α. This Xα method gives reasonable bond distances. The Local Spin Density Approximation (LSDA) is obtained by an elaboration of the LDA: electrons of α and β spin in the uniform gas are assigned different spatial KS orbitals and different electron density functions ρ^{α} and ρ^{β} are used. This method can be used for systems with one or more unpaired electrons.
- Generalized Gradient Approximation (GGA) – is the next rung of functionals used in DFT calculations. These functionals use both the electron density and its gradient (first derivatives with respect to position $\nabla\rho$) at each point. GGA functionals are more accurate than LDA. They significantly reduce the bond dissociation energy errors and generally improve transition barriers.
- *meta*–GGA – additionally depends on higher order derivatives of the electron density, with the Laplacian ($\nabla^2\rho$) being the second–order term.
- Hybrid functionals – this type of functional mixes exact Hartree–Fock exchange energy with GGA or *meta*-GGA. Inclusion of exact Hartree–Fock exchange energy is often found to improve the calculation results. These functionals are often more accurate; however, they are more costly to compute.

Relativistic Effects

The electron mass increases when electrons move with a velocity comparable to the speed of light. This has a significant effect on the radial distribution of the electrons of elements with high atomic numbers. The effective mass of an electron is given by:[155]

$$m = \frac{m_0}{\left(1 - (v/c)\right)^{1/2}} \tag{2.20}$$

where m_0 is the rest mass of the electron, c is the speed of light, and v is the velocity of the electron.

For a nonrelativistic hydrogenlike atom, the average orbital velocity of a 1s electron is approximately Z a.u.:

$$v = \frac{Zc}{137} \approx Z \text{ a. u.} \tag{2.21}$$

where Z is the nuclear charge, and c = 137 is the speed of light in atomic units (a.u.). However, for an electron in Au atom with Z = 79, the ratio $v/c \approx 79/137$ or 0.58. Therefore, the 1s electron in a gold atom moving with this speed has a mass of $1.23m_0$. This increased mass of the electron has a considerable effect on the radial distribution of the electron. For example, the ratio between the relativistic 1*s* radius to its nonrelativistic counterpart is approximately $(1.23\ m_0)^{-1}/m_0^{-1}$, or 0.81. This implies that relativistic effects have decreased the 1*s* orbital size in Au by about 20%. The result is a lowering of the energies of all *s* orbitals. Additionally, due to this higher shielding of the inner *s* electrons, the more diffuse *d* and *f* orbitals become higher in energy. These relativistic effects can strongly affect the geometries, optical properties, and physical properties of heavy metal complexes. In this work, we focus mainly on silver and gold NPs. So, it is very important to take these effects into account.

The ADF program used in this research uses the zeroth order regular approximation (ZORA). The ZORA equation is the zeroth order regular approximation to the Dirac Hamiltonian. The relativistic and nonrelativistic Kohn-Sham DFT equations can be written as:[156]

$$(T + V^{KS})\Psi_i = \varepsilon_i \Psi_i \tag{2.22}$$

where V^{KS} is the effective molecular Kohn-Sham potential and T is the kinetic energy operator. This kinetic energy operator T is different for each relativistic method: nonrelativistic (NR), Dirac, ZORA and scalar relativistic SR-ZORA.[156]

$$T^{NR} = \frac{p^2}{2} \tag{2.23}$$

$$T^{Dirac} = \sigma p \frac{c^2}{(2c^2 + \varepsilon_i - V^{KS})} \sigma p \tag{2.24}$$

$$T^{ZORA} = p \frac{c^2}{(2c^2 - V^{KS})} p + \frac{c^2}{(2c^2 - V^{KS})^2} \sigma(\nabla V^{KS} \times p) \tag{2.25}$$

$$T^{SR-ZORA} = p \frac{c^2}{(2c^2 - V^{KS})} p \tag{2.26}$$

where p is the momentum ($p = -i\nabla$), c is the velocity of the light, and σ are Pauli spin matrices:

$$\sigma_x = \begin{pmatrix} 0 & 1 \\ 1 & 0 \end{pmatrix}$$
$$\sigma_y = \begin{pmatrix} 0 & -i \\ i & 0 \end{pmatrix} \tag{2.27}$$
$$\sigma_z = \begin{pmatrix} 1 & 0 \\ 0 & -1 \end{pmatrix}$$

The ZORA kinetic energy operator T^{ZORA} depends on the molecular Kohn–Sham potential. The scalar relativistic SR-ZORA kinetic energy operator $T^{SR\text{-}ZORA}$ is the ZORA kinetic energy operator without spin–orbit coupling. This operator can be used in cases where spin–orbit coupling is not important. ZORA is a computationally efficient method for relativistic calculations.

Time–Dependent Density Functional Theory (TDDFT)

The Runge-Gross Theorem

This theorem is a time–dependent analogue of the first Hohenberg–Kohn theorem. It states that the exact time–dependent (TD) electron density $\rho(r,t)$ determines the time–dependent external potential $v(\boldsymbol{r},t)$, up to a spatially constant, time–dependent function $C(t)$ and thus time–dependent wavefunction $\Psi(\boldsymbol{r},t)$, up to a time–dependent phase factor.[157] In other words, this means that the external potential can be expressed as functional of the electron density and all properties of the system can be obtained.

The Time-dependent Kohn-Sham (TDKS) Equations

Similar to ground state DFT, it is assumed that a TD non–interacting reference system exists with an external one–particle potential $v_s(\boldsymbol{r},t)$ of which the electron density $\rho_s(\boldsymbol{r},t)$ is

equal to the exact electron density $\rho(\boldsymbol{r},t)$ of the real interacting system.[157] This potential is not known and approximations must be used.[157, 158] The non–interacting system is represented by a single Slater determinant $\Psi(\boldsymbol{r},t)$ consisting of the TD single–electron orbitals $\psi_i(\boldsymbol{r},t)$. The time–dependent electron density is given by a sum over these occupied orbitals:[157, 158]

$$\rho(r,t) = \rho_s(\boldsymbol{r},t) = \sum_i^n |\psi_i(\boldsymbol{r},t)|^2 \tag{2.28}$$

These TD single–electron orbitals are then given as a solution of the TDKS equation, which is similar to the time–independent one:[157, 158]

$$i\frac{\partial}{\partial t}\psi_i(\boldsymbol{r},t) = h^{KS}(\boldsymbol{r},t)\psi_i(\boldsymbol{r},t) \tag{2.29}$$

$$h^{KS}(\boldsymbol{r},t) = -\frac{1}{2}\nabla_i^2 + v_s[\rho](\boldsymbol{r},t) \tag{2.30}$$

The TD external potential $v_s[\rho](\boldsymbol{r},t)$ of the non–interacting system consists of the Hartree potential (Coulomb), the external potential, and an effective exchange–correlation potential, all of which are time–dependent:[158]

$$v_s[\rho](\boldsymbol{r},t) = v_{ext}[\rho](\boldsymbol{r},t) + v_{Hartree}[\rho](\boldsymbol{r},t) + v_{XC}[\rho](\boldsymbol{r},t) \tag{2.31}$$

The first term of the equation (2.31) is $v_{ext}[\rho](\boldsymbol{r},t)$, which includes the nuclear and any other external potentials. The second term is the Hartree potential, which is written as:[157, 158]

$$v_{Hartree}[\rho](\boldsymbol{r},t) = \int d^3r_1 \frac{\rho(r_2,t)}{r_{12}} \tag{2.32}$$

The exchange–correlation part $v_{XC}[\rho](\boldsymbol{r},t)$ can be expressed as:

$$v_{XC}[\rho](\boldsymbol{r},t) = \frac{\partial A_{XC}[\rho]}{\partial \rho(\boldsymbol{r},t)} \tag{2.33}$$

The $A_{XC}[\rho]$ is the so–called exchange–correlation part of the action integral $A[\rho]$. The quantum mechanical action integral $A[\rho]$ is a functional of the density. This action integral is a prescription of how the exact density can be obtained. The exact electron density $\rho(\boldsymbol{r},t)$ can be found from the Euler equation:[157, 158]

$$\frac{\partial A[\rho]}{\partial \rho(\boldsymbol{r},t)} = 0 \tag{2.34}$$

when appropriate boundary conditions are applied.

The final TDKS equation can be written as:[157, 158]

$$i\frac{\partial}{\partial t}\psi_i(\boldsymbol{r},t) = \left(-\frac{1}{2}\nabla_i^2 + v_{ext}[\rho](\boldsymbol{r},t) + \int d^3r_1 \frac{\rho(r_2,t)}{r_{12}} + \frac{\partial A_{XC}[\rho]}{\partial\rho(\boldsymbol{r},t)}\right)\psi_i(\boldsymbol{r},t) \qquad (2.35)$$

This TDKS equation is a single–particle equation in which each electron is treated individually in the field of all others.[158] The TD exchange–correlation action functional (called the XC kernel, f_{XC}) is not known and approximations to this functional have to be applied. The first approximation for the action functional is the adiabatic approximation, where the TD exchange–correlation functional is replaced by a time–independent equation. This is a good approximation if the probability density changes slowly with time.

To obtain excitation energies and oscillator strengths using the TDKS equation, different strategies can be applied. One of them is linear response TDDFT or LR–TDDFT. In the LR–TDDFT, the change of the density is described by first order perturbation theory under the assumption that the perturbation is turned on slowly (adiabatic approximation) and that the system initially resides in the ground state with the corresponding density ρ_0. The non-Hermitian LR–TDDFT equation should be used:[158]

$$\begin{bmatrix} A & B \\ B^* & A^* \end{bmatrix}\begin{bmatrix} X \\ Y \end{bmatrix} = \varepsilon \begin{bmatrix} 1 & 0 \\ 0 & -1 \end{bmatrix}\begin{bmatrix} X \\ Y \end{bmatrix} \qquad (2.36)$$

where *A* and *B* are matrix elements with dimensions of number of occupied orbitals. They can be defined as:[157, 158]

$$A_{ia,jb} = \delta_{ij}\delta_{ab}(\epsilon_a - \epsilon_i) + (ia|jb) + (ia|f_{XC}|jb) \qquad (2.37)$$

$$B_{ia,jb} = (ia|bj) + (ia|f_{XC}|bj) \qquad (2.38)$$

where the two-electron integrals are given in Mulliken notation, *i* and *j* denote occupied orbitals, and *a* and b are virtual KS orbitals. The solution of equation (2.36) yields the transition energies ε and eigenvectors |X> and |Y>. Oscillator strengths, which determine the magnitude of the absorption peaks, are calculated from the solution vectors |X> and |Y>.[157, 158]

CD Spectroscopy

CD spectroscopy is based on the measurement of the difference in absorption between left and right circularly polarized light:

$$\Delta A = A_- - A_+ = A_{lcp} - A_{rcp} \qquad (2.39)$$

The CD signal can be either positive or negative. The CD sign is positive when absorption of the left circularly polarized light is greater than absorption of the right circularly polarized light.

The simulation of the CD spectra is based on the relations:[159, 160]

$$CD = 4\alpha \sum_m R_m E_m \sigma_m(E) \tag{2.40}$$

$$\alpha = \frac{4\pi^2 N_A}{3 \cdot \ln(10) 10^3} \frac{2\pi}{hc} \tag{2.41}$$

$$\sigma_m(E) = \frac{1}{\sigma\sqrt{2\pi}} \exp(-\frac{1}{2\sigma^2}(E - E_m)^2) \tag{2.42}$$

where CD is the circular dichroism signal in arbitrary units (a.u.), α is a set of constants, N_A is Avogadro's number in units of mole^{-1}, h is the Planck constant in units of J·s, c is the speed of light in units of cm/s, R_m is rotatory strength in units of esu^2·cm^2, E is the energy of the incident light in eV, and E_m is the excitation energy to state M in eV. CD spectra were fitted with a Gaussian function, where $\sigma_m(E)$ is the Gaussian band shape factor and σ is the exponential half-width.

MCD Spectroscopy

MCD spectroscopy is based on the measurement of the difference in absorption between left and right circularly polarized light, which is induced in the sample by a strong magnetic field oriented parallel to the direction of light propagation.[161, 162]

$$\Delta A = A_- - A_+ = A_{lcp} - A_{rcp} = \triangle \varepsilon_M clB \tag{2.44}$$

where $\Delta\varepsilon_M$ is the differential molar absorptivity per Tesla of field, analogous to the ε molar absorptivity in the CD case, c is the molar concentration of the absorbing species, and l is the path length (in centimeters), B is the magnetic field. MCD data can be plotted in a few different ways: as the absorption difference (ΔA), as the absorption coefficient difference (Δk), as molar absorptivity ($\Delta\varepsilon_M$) and as molar ellipticity ($[\theta]_M$).[162-165] Molar absorptivity ($\Delta\varepsilon_M$) is related to molar ellipticity ($[\theta]_M$) by the following equation:[163]

$$\frac{[\theta]_M}{10^4 Gauss} = \frac{3298.2 \triangle \varepsilon_M}{Tesla} \tag{2.45}$$

where molar ellipticity is expressed in deg L m^{-1} mol^{-1} G^{-1}.

There are three main sources of MCD intensity, which are referred to as the A, B and C terms.[162, 165, 166] Which term will be dominant depends on the type of investigated molecule: the

A term is found only for molecules with degenerate excited states, and it has a derivative shape in the MCD spectrum; the *B* term arises in MCD spectra for systems with excited states close enough in energy to allow mixing; and the *C* term is present for paramagnetic molecules whose ground state is degenerate, and this term is temperature dependent.[163] MCD intensity is often interpreted in terms of the equation:[162, 165]

$$\mathrm{MCD}(\hbar\omega) = \chi\hbar\omega \mathrm{B} \sum_J \left[A_J \left(-\frac{\partial f_J(\hbar\omega - \hbar\omega_J)}{\partial \hbar\omega} \right) + \left(B_J + \frac{C_J}{\kappa T} \right) f_J(\hbar\omega - \hbar\omega_J) \right] \qquad (2.46)$$

where $\hbar\omega$ is the energy of incident light, $\hbar\omega_J$ is the excitation energy to state *J*, B is the amplitude of the applied magnetic field, *T* is the temperature, κ is Boltzmann's constant, χ is a collection of constants and experimental parameters that depend on what quantity is measured and units, f_J is a bandshape function and A_J, B_J and C_J are magnetic circular dichroism terms.[163]

In this research, the theoretical simulation of MCD spectra is based on the implementation in the Amsterdam Density Functional (ADF) program in which a magnetic perturbation of the TDDFT was applied for calculation of the MCD terms.[158]

Using our calculated A_J, B_J and C_J parameters and the MCD intensity equation (2.46) we can calculate MCD spectra in terms of molar ellipticity $[\theta]_M$, which is independent of the major experimental parameters such as the concentration of absorption species (*c*), the path length (*l*) and magnetic field (B):[162, 165]

$$[\theta]_M = \chi\hbar\omega \sum_J \left[A_J \left(-\frac{\partial f_J(\hbar\omega - \hbar\omega_J)}{\partial(\hbar\omega)} \right) + \left(B_J + \frac{C_J}{\kappa T} \right) f_J(\hbar\omega - \hbar\omega_J) \right] \qquad (2.47)$$

where χ is the collection of constants which is approximately equal to 0.0014803.[165] To get molar ellipticity $[\theta]_M$ in the units (deg L m^{-1} mol^{-1} G^{-1}), the energy of incident light ($\hbar\omega$) and excitation energy to state *J* ($\hbar\omega_J$) should be in a.u.

The bandshape functions chosen are normalized Gaussian functions and their derivatives:[162]

$$f_J(\hbar\omega) = \frac{1}{\sqrt{\pi} W_J} e^{-((\hbar\omega_J - \hbar\omega)/W_J)^2} \qquad (2.48)$$

$$\frac{\partial f_J(\hbar\omega)}{\partial(\hbar\omega)} = \frac{2(\hbar\omega_J - \hbar\omega)}{\sqrt{\pi} W_J^3} e^{-((\hbar\omega_J - \hbar\omega)/W_J)^2} \qquad (2.49)$$

The bandwidth parameters W_J were chosen to reproduce the observed bandwidths.

Chapter 3 - Chiroptical Activity in BINAP– and DIOP– Stabilized Octa– and Undecagold Clusters

Abstract

In order to learn more about the origin of chirality in chiral organometallic complexes and to contribute to the understanding of the difference in chiroptical activity of metal clusters stabilized by different phosphine ligands, we examined the optical properties of the undecagold (Au_{11}^{3+}) and octagold (Au_8^{2+}) clusters protected by bisphosphine ligands of different natures. The chirality of pairs of clusters $[Au_{11}(BINAP)_4Cl_2]^+$, $[Au_{11}(DIOP)_4Cl_2]^+$ and $[Au_8(BINAP)_3(PPh_3)_2]^{2+}$, $[Au_8(DIOP)_3(PPh_3)_2]^{2+}$ were investigated with density functional theory (DFT) and time–dependent density functional theory (TDDFT). To simulate BINAP and DIOP ligands, which possess a great number of atoms, small model ligands are used. The obtained results showed that the shapes of the octa– and undecagold cores in the model clusters are similar to the gold cores of the crystal structures. Theoretical optical absorption and CD spectra of the model clusters are in good agreement with experimental data. Three main hypotheses to explain the different chiroptical activity of the clusters were suggested: (i) the CD activity originates from core deformation due to ligation; (ii) the nature of the chiral ligands can play a crucial role in the optical activity of the achiral core and (iii) Cl atoms positions can affect the CD intensity. It was shown that the gold core geometry deformation due to ligation and the nature of ligand play the most important roles in the chiroptical activity of the gold clusters. Additionally, the connectivity of ligands determines a gold core structural deformation and mainly affects the high-energy region of the CD spectra, whereas the gold core exhibits a significant effect on the shape and sign of the CD spectra in the low energy region above ~350 nm.

Introduction

Gold nanoclusters with dimensions less than a nanometer possess unique characteristics and properties, which enable applications in luminescence, sensing, catalysis, *etc*.[55, 167-169] Therefore, scientists continue to try to develop and synthesize novel gold nanostructures with improved characteristics or new properties. Small gold clusters protected by various types of

ligands have received great attention for the few last decades. Ligands allow researchers to obtain gold nanoclusters with given sizes, shapes and properties.

A very interesting and promising class of gold nanoclusters is chiroptically active gold nanostructures. Chirality is an exceptional property of some molecules, complexes or clusters that plays an important role in different branches of science such as chemistry, biology, medicine, and pharmacology. One of the important applications for chiral gold nanoparticles is that they can be used as enantioselective nanocatalysts in the pharmaceutical industry and produce chiral molecules on an industrial scale.[147, 148] Metal surfaces with chiral characteristics have been successfully obtained with many different approaches: (i) by adsorbing chiral organic molecules (such as DNA, glutathione, penicillamine, cysteine, *etc.*) onto an achiral metal core; (ii) by adsorbing achiral ligands in a "chiral pattern" onto an achiral metal core or (iii) by synthesis of left and right handed symmetries of metal nanoparticles.[114, 116-122] In this project, we focus on chiroptically active gold nanoparticles that are obtained by combination of an essentially achiral metal core with chiral organic molecules.

In gold nanocluster chemistry, phosphines are one of the most common types of ligands.[26, 34, 40, 43, 45, 94, 170] There are two categories of phosphine–ligands: monodentate phosphines (including triphenylphosphine and its derivatives)[34, 35, 171] and bidentate phosphines (bisphosphine (P^P)–ligands).[40, 41, 45, 172] Bidentate phosphines are a very interesting class of ligands. These organic molecules are chiral and their combination with gold clusters can yield chiral gold nanostructures. A great number of ultra-small gold clusters (up to 13 core gold atoms) stabilized by bidentate phosphines have been synthesized and characterized by crystallography and electrospray ionization mass spectrometry.[44, 58, 69, 134, 135] Unfortunately, the optical properties of this promising class of small gold nanoclusters protected with bisphosphine (P^P) ligands are not very well studied. There are just a few experimental[40-44] and theoretical[45] papers found in the literature. These results suggest that the bisphosphine ligands affect the core structure and the chiroptical activity of the ultra-small gold clusters. However, despite all these empirical and theoretical studies, the origin of the chiroptical activity of metal clusters protected by optically active organic molecules is still unclear.

One of the interesting and important features of chiral gold complexes was observed by Tsukuda and co–workers.[40] They found that the gold clusters exhibit circular dichroism (CD) signals with different intensities when stabilized by BINAP (2,2'-bis(diphenylphosphino)-1,1'-

binaphthyl) and DIOP (o-isopropylidene-2,3-dihydroxy-1,4-bis(diphenylphosphino)butane) ligands; they also ascertained that BINAP–protected gold clusters have larger anisotropy factors than DIOP–protected species (**Figure 3–1**).[40, 41] Investigation of this phenomenon will help to better understand the origin of cluster chirality and the impact of the nature of the ligand on the chiroptical activity of metal clusters protected by optically active organic molecules, which is very important to design novel chiral metallic nanostructures with specific properties.

Figure 3–1. UV–vis spectra of A) $[Au_{11}(DIOP)_4Cl_2]^+$, B) $[Au_{11}(BINAP)_4Cl_2]^+$ and C) $[Au_8(BINAP)_3(PPh_3)_2]^{2+}$ and CD spectra of D) $[Au_{11}(DIOP)_4Cl_2]^+$, E) $[Au_{11}(BINAP)_4Cl_2]^+$ and F) $[Au_8(BINAP)_3(PPh_3)_2]^{2+}$ clusters in CH_3CN at room temperature.

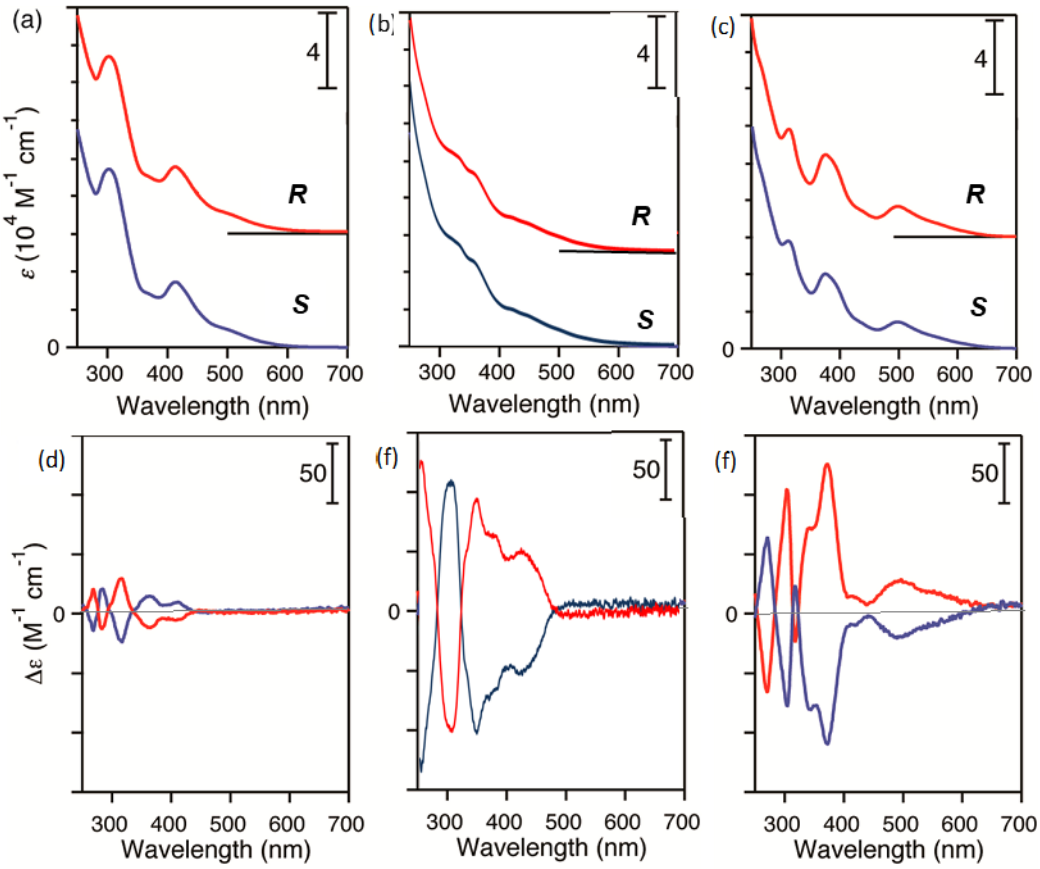

* Figures A, D, C and F were adapted with permission from Ref. [40]. (Direct link: <http://pubs.acs.org/doi/abs/10.1021%2Facs.jpclett.6b02294>, Note: further permissions related to the material excerpted should be directed to the ACS). Figures B and F were plotted using empirical data from Dr. Tsukuda and co–workers.

In order to learn more about the origin of chirality in chiral organometallic complexes and to contribute to the understanding of the difference in chiroptical activity of metal clusters stabilized by different phosphine ligands, we examined the optical properties of the undecagold

(Au_{11}^{3+}) and octagold (Au_8^{2+}) clusters protected by bisphosphine ligands of different nature. The chirality of pairs of clusters $[Au_{11}(BINAP)_4Cl_2]^+$, $[Au_{11}(DIOP)_4Cl_2]^+$ and $[Au_8(BINAP)_3(PPh_3)_2]^{2+}$, $[Au_8(DIOP)_3(PPh_3)_2]^{2+}$ were investigated with density functional theory (DFT) and time–dependent density functional theory (TDDFT). To simulate BINAP and DIOP ligands, which possess a great number of atoms, small model ligands are used. These model ligands cut computational costs while preserving essential features of the systems of interest, which are necessary to get the answers to our questions. Three main hypotheses to explain the different chiroptical activity (more intense CD signal of BINAP–protected gold nanoparticles with respect to the DIOP–stabilized clusters) of the $[Au_{11}(BINAP)_4Cl_2]^+$, $[Au_{11}(DIOP)_4Cl_2]^+$ and $[Au_8(BINAP)_3(PPh_3)_2]^{2+}$, $[Au_8(DIOP)_3(PPh_3)_2]^{2+}$ clusters were suggested: (i) the flexible nature of the Au_{11}^{3+} gold core means that deformation inside the gold core due to ligation can be a source of the CD activity; (ii) the nature of the ligands suggests that the presence of the double bonds could be a reason for the dramatic difference in the chiroptical activity of the organometallic clusters; and (iii) in the case of the undecagold clusters, the chlorine atom positions could also affect the CD intensity.

Computational Details

The Amsterdam Density Functional (ADF) program was employed for performing DFT and TDDFT calculations.[158] Scalar relativistic effects were included by utilizing the zero–order regular approximation (ZORA).[173] The geometries used in the TDDFT calculations were obtained with Becke-Perdew (BP86) functional.[174, 175] For calculation of the optical absorption and CD spectra, TDDFT was employed with the asymptotically correct van Leeuwen–Baerends (LB94) functional.[176] For both DFT and TDDFT calculations, the double-ζ (DZ) Slater–type basis set with frozen core (up to 4f for gold, 2p for phosphorus and 1s for carbon atoms) was used. Implicit solvation effects on the geometry and optical spectra were considered by employing the COSMO model[177] with parameters for chloroform using the LB94 functional.

Equations used for calculation of the CD spectra have been already discussed and can be found in **Chapter 2** (equations 2.40 – 2.42). Optical absorption and CD spectra were convoluted with an exponential half–width of $\sigma = 35$ nm.

Results and Discussion

Model Ligands

In order to theoretically investigate the cause of the dramatic difference in chiroptical activity of the undecagold clusters protected by DIOP and BINAP ligands, calculation of the most stable geometrical structures and simulation of the optical absorption and CD spectra are necessary for $[Au_{11}(BINAP)_4Cl_2]^+$, $[Au_{11}(DIOP)_4Cl_2]^+$ and $[Au_8(BINAP)_3(PPh_3)_2]^{2+}$, $[Au_8(DIOP)_3(PPh_3)_2]^{2+}$ clusters. Unfortunately, these systems contain a large number of atoms and calculations with the full ligands will be very time consuming. Furthermore, single crystal structures are known only for $[Au_{11}(DIOP)_4Cl_2]^+$ and $[Au_8(DIOP)_3(PPh_3)_2]^{2+}$ clusters, which means that we need to find the most energetically preferable structures for the $[Au_{11}(BINAP)_4Cl_2]^+$ and $[Au_8(BINAP)_3(PPh_3)_2]^{2+}$ systems by performing geometry optimizations for every possible isomer, which are difficult to perform for systems of this size. Therefore, simplifications of the original systems $[Au_{11}(BINAP)_4Cl_2]^+$, $[Au_{11}(DIOP)_4Cl_2]^+$, $[Au_8(BINAP)_3(PPh_3)_2]^{2+}$ and $[Au_8(DIOP)_3(PPh_3)_2]^{2+}$ are necessary.

Provorse and Aikens[45] used simple model ligands to simulate BINAP molecules for investigation of the chiroptical effects in the undecagold particles protected by BINAP. Their results showed that this model allowed trimming the computational cost and at the same time was good enough to qualitatively simulate the essential properties of the original large systems. In this project, simple model ligands for *S*-DIOP and *S*-BINAP were used. For modeling *S*-DIOP the 1,4–bis(diphosphino)butan ligand (L1) was applied, whereas for simulation of *S*-BINAP the 1,4–bis(diphosphino)buta–1,3–dien ligand (L2) was used (**Figure 3–2**). The triphenylphosphine ligands in $[Au_8(BINAP)_3(PPh_3)_2]^{2+}$ and $[Au_8(DIOP)_3(PPh_3)_2]^{2+}$ clusters were substituted with PH_3 groups.

Figure 3–2. A) *S*-DIOP ligand is modeled by L1 = *S*–1,4–bis(diphosphino)butan; B) *S*-BINAP ligand is modeled by L2 = *S*–1,4–bis(diphosphino)buta–1,3–dien.

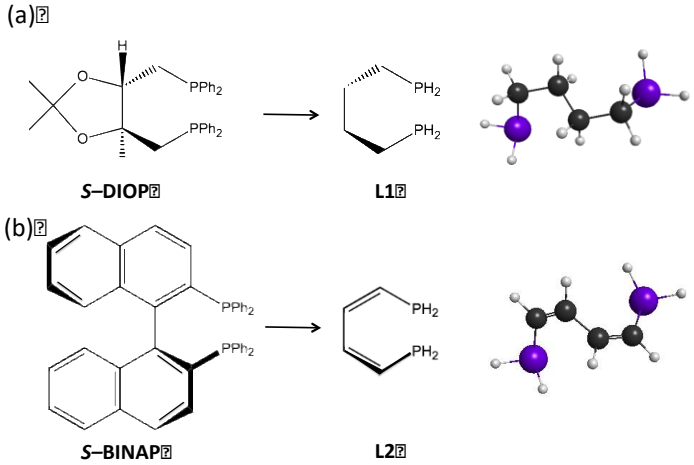

Geometrical Structure of $[Au_{11}X_4Cl_2]^+$ and $[Au_8X_3(PH_3)_2]^{2+}$ (X = L1, L2)

X–ray crystal structures are known only for $[Au_{11}(DIOP)_4Cl_2]^+$ and $[Au_8(BINAP)_3(PPh_3)_2]^{2+}$ clusters, which means that we need to determine structures of $[Au_{11}(BINAP)_4Cl_2]^+$ and $[Au_8(DIOP)_3(PPh_3)_2]^{2+}$ to calculate the optical properties of these systems. For simulation of these structures, the $[Au_{11}X_4Cl_2]^+$ and $[Au_8X_3(PH_3)_2]^{2+}$ (X = L1, L2) systems with small model ligands were used. The most stable isomers of the model systems were found in gas phase and in chloroform; comparison of the geometrical structure of the gold core fragment, chlorine atoms positions and bridging ligand arrangement was performed for the known experimental structures and their theoretical models such as $[Au_{11}(DIOP)_4Cl_2]^+$ vs. $[Au_{11}(L1)_4Cl_2]^+$, $[Au_{11}(BINAP)_4Cl_2]^+$ vs. $[Au_{11}(L2)_4Cl_2]^+$ and $[Au_8(BINAP)_3(PPh_3)_2]^{2+}$ vs. $[Au_8(L2)_3(PH_3)_2]^{2+}$.

$[Au_{11}X_4Cl_2]^+$ (X = L1, L2) clusters: chlorine atoms positions. To identify the most stable isomers of $[Au_{11}X_4Cl_2]^+$ (X = L1, L2) clusters we need to find a preferable arrangement of the four bridging ligands L1 and L2 around the Au_{11} gold core and the position of the two chlorine atoms, each of which is attached to one gold atom.

The geometrical structure of some undecagold clusters has previously been investigated experimentally[34, 40] and theoretically.[45] Crystal structures were determined for undecagold clusters protected by achiral[19] and chiral[14] ligands: $[Au_{11}(PPh_3)_8Cl_2]^+$ and $[Au_{11}(DIOP)_4Cl_2]^+$. The obtained results showed that the structure of the Au_{11} fragment in both types of clusters

(with mono– and bidentate ligands) is an incomplete icosahedral structure: a central gold atom (yellow color) is located between a pentagonal pyramid (6 gold atoms in dark purple color) and a rectangular gold ring (4 gold atoms in blue) (**Figure 3–3**). The distances between the central gold atom and the gold atoms of the shell are 2.639–2.700 Å for the cluster stabilized by PPh_3 ligands, and 2.641–2.695 Å in the case of chiral DIOP ligands. Average distances between gold atoms and phosphine groups are ~2.280 and 2.282 Å for $[Au_{11}(PPh_3)_8Cl_2]^+$ and $[Au_{11}(DIOP)_4Cl_2]^+$, correspondingly (**Table A–1**). The position of the two chlorine atoms near the Au_{11} core is different for clusters protected by PPh_3 and DIOP ligands (**Figure 3–3**). For the monodentate phosphine system $[Au_{11}(PPh_3)_8Cl_2]^+$, the two chlorine atoms are attached to two opposite gold atoms on a 5-fold ring of the pentagonal pyramid base (denoted as the 5,5–position) (**Figure 3–3b**),[19] whereas in the case of $[Au_{11}(DIOP)_4Cl_2]^+$ one chlorine atom is attached to gold atom on the pentagonal ring and the second one is connected to the opposite gold atom from the 4–fold ring (denoted as the 4,5–position), so that they are located on the same axis (**Figure 3–3a**).[14]

Figure 3–3. A), B) Structures of the $Au_{11}Cl_2$ fragment of clusters $[Au_{11}(DIOP)_4Cl_2]^+$ and $[Au_{11}(PPh_3)_8Cl_2]^+$ from the corresponding x-ray crystal structures[34, 40]; C) structure of the $Au_8(PH_3)_2$ fragment (with H substituted for Ph rings) from the crystal structure[40] of $[Au_8(BINAP)_3(PPh_3)_2]^{2+}$. Gold atoms – yellow, blue and dark purple; chlorine atom – green; phosphorous – light purple; hydrogen – white.

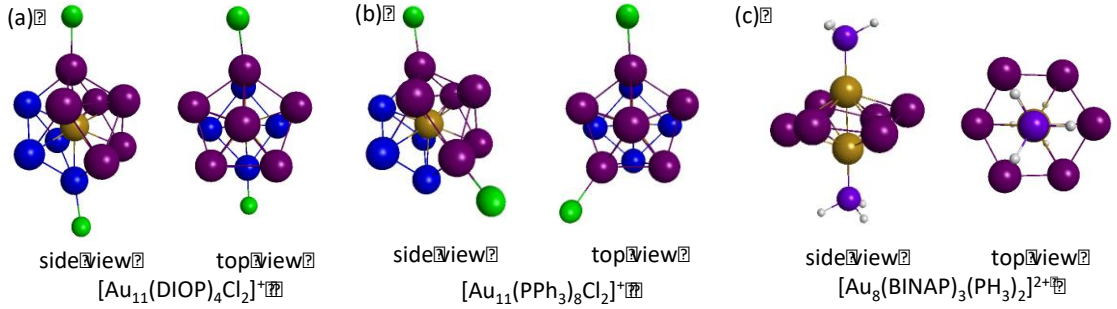

A previous theoretical investigation[45] of the geometrical structure was performed for $[Au_{11}(PH_3)_8Cl_2]^+$ and $[Au_{11}(L2)_4X_2]^+$ (where X = Cl, Br) using the Xα local density approximation (LDA) functional with a TZP frozen core basis set. For the cluster protected by monodentate ligands, the obtained theoretical results are very close to the experimental data for the $[Au_{11}(PPh_3)_8Cl_2]^+$ cluster: the geometrical structure of the gold core and the chlorine atoms positions are similar (5,5–position) for experiment and theory. For the simulation of $[Au_{11}(BINAP)_4X_2]^+$ clusters, only systems with chlorine atoms positions near opposite gold

atoms on a 5-fold ring were reported (5,5–position). In order to determine the position of the chlorine atoms in the $[Au_{11}X_4Cl_2]^+$ (X = L1, L2) model clusters, all possible positions of the chlorine atoms should be considered.

To identify preferable chlorine locations in the $[Au_{11}X_4Cl_2]^+$ (X = L1, L2) model clusters, all possible positions of the two Cl atoms were first considered for the undecagold cluster protected by simple phosphine ligands $[Au_{11}(PH_3)_8Cl_2]^+$. During the geometry optimization procedure, three main geometrical structures of $[Au_{11}(PH_3)_8Cl_2]^+$ were obtained with energy differences up to 1.6 kcal/mol in the gas phase (**Figure 3–4**). The results showed that the most stable isomer is $[Au_{11}(PH_3)_8Cl_2]^+$ (**1**) where the Cl atoms are attached in the 4,5–position, and the next most stable structure is $[Au_{11}(PH_3)_8Cl_2]^+$ (**2**) with the 5,5–position for chlorine atoms. The geometries of the undecagold cores in the $[Au_{11}(PH_3)_8Cl_2]^+$ structures (**1**) and (**2**) are similar to each other and to the crystal structure of $[Au_{11}(PPh_3)_8Cl_2]^+$ system. The least stable isomer (**3**) is obtained when one chlorine atom is attached to a gold atom of the pentagonal pyramid base and a second one to the top gold atom of this pyramid (denoted the 5,5'–position). During the geometry optimization procedure for $[Au_{11}(PH_3)_8Cl_2]^+$ (**3**), the Au_{11} fragment was significantly deformed, and exhibits a very different structure with respect to the experimental core. The energy difference between $[Au_{11}(PH_3)_8Cl_2]^+$ (**1**) and (**2**) is small (~1.0 kcal/mol in the gas phase) and the gold core fragments are similar in both isomers, which makes it very difficult to say which chlorine ion positions will be preferred in real clusters with various ligands. Therefore, two types of chlorine atom positions (4,5– and 5,5–positions) will be tested during geometry optimizations of the $[Au_{11}X_4Cl_2]^+$ (X = L1, L2) clusters.

Figure 3–4. Structures and relative energies of $Au_{11}(PH_3)_8Cl_2^+$ isomers. Method: BP86/DZ.fc (gas phase).

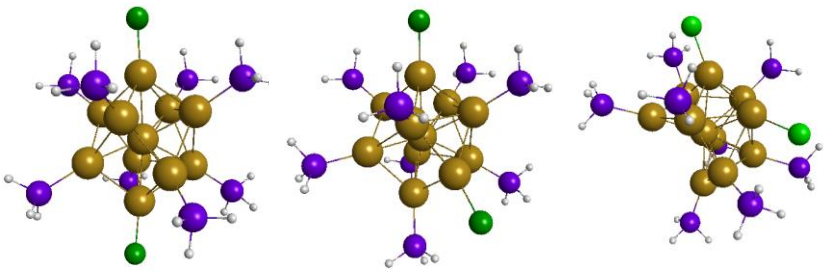

$[Au_{11}X_4Cl_2]^+$ (X = L1, L2): ligand arrangement. In order to find the geometries of $[Au_{11}X_4Cl_2]^+$ (X = L1, L2) clusters, the eight achiral PH_3 groups in $[Au_{11}(PH_3)_8Cl_2]^+$ (**1**) and (**2**)

clusters were substituted by four model bridging ligands L1 and L2 (**Figure 3–4**) in different ways. The possible structures were limited by the bond lengths and angles in the bisphosphine ligands. The geometries of all considered isomers were optimized in the gas phase first, followed by further optimization of the most energetically preferable in continuum solvent (using COSMO) as described below. All obtained isomers and their relative energies in the gas phase can be found in **Appendix A** (**Figures A–1** and **A–2)**. The most energetically stable gas phase isomers of $[Au_{11}X_4Cl_2]^+$ (X = L1, L2) are $[Au_{11}(L1)_4Cl_2]^+$ (**4**), $[Au_{11}(L2)_4Cl_2]^+$ (**5**), $[Au_{11}(L1)_4Cl_2]^+$ (**6**) and $[Au_{11}(L2)_4Cl_2]^+$ (**7**) (shown in **Figure 3–5a)**. In the gas phase, these clusters exhibit bond distances between the central gold atom and the shell atoms of the undecagold core in the range of 2.663–2.802 Å, chlorine atoms are attached to the Au atoms with bonds of 2.450–2.458 Å, and phosphine atoms are coordinated around the gold core with distances of 2.440–2.449 Å (**Table A–1**). In complexes $[Au_{11}(L1)_4Cl_2]^+$ (**4**) and $[Au_{11}(L2)_4Cl_2]^+$ (**5**) the chlorine atoms are in the 4,5–position, whereas in $[Au_{11}(L1)_4Cl_2]^+$ (**6**) and $[Au_{11}(L2)_4Cl_2]^+$ (**7**) the Cl atoms are attached to the gold core in the 5,5–position. The theoretically calculated relative energies in the gas phase for these isomers show that structures with chlorine atoms in the 4,5–position are more preferable energetically in both cases (L1 and L2 ligands) (**Figure 3–5a**).

In the next step, the geometries of these most energetically stable (in the gas phase) isomers of $[Au_{11}X_4Cl_2]^+$ (X = L1, L2) were reoptimized including solvent effects. Comparison of the geometries for the $[Au_{11}(L1)_4Cl_2]^+$ (**4**), $[Au_{11}(L2)_4Cl_2]^+$ (**5**), $[Au_{11}(L1)_4Cl_2]^+$ (**6**) and $[Au_{11}(L2)_4Cl_2]^+$ (**7**) clusters in the gas and liquid phases shows similarities and differences. For example, the shape of the Au_{11} gold core is very close in the gas phase and in chloroform. However, there are some differences in the bond lengths: distances between the central Au atom and the shell Au atoms (connected to the chlorine ions) became shorter in chloroform by ~0.04 Å, whereas the distances between the central Au atom and shell Au atoms (connected to the phosphine ligands) and the Au–Cl bonds became longer by ~0.05 Å (**Table A–1**). The structure of the Au_{11} core, the positions of the two chlorine ions and the arrangement of the four bridging ligands in the experimental structure $[Au_{11}(DIOP)_4Cl_2]^+$ and theoretically predicted model structure $[Au_{11}(L1)_4Cl_2]^+$ (**4**) in chloroform are very similar. For example, overlay of the Au_{11} fragments of theoretical and experimental clusters showed that the shape of these undecagold cores is very close (**Figure 3–6a**). However, the Au–Au, Au–Cl and Au–P bonds are longer in

the optimized cluster $[Au_{11}(L1)_4Cl_2]^+$ (**4**) with respect to the experimental structure $[Au_{11}(DIOP)_4Cl_2]^+$ by up to 0.091, 0.127 and 0.161 Å, correspondingly; these types of bond elongations are typical for the BP86 exchange-correlation functional used in the DFT optimizations.

Figure 3–5. A) Geometries of the most stable isomers of $[Au_{11}X_4Cl_2]^+$ (X = L1, L2) clusters with 4,5– and 5,5–position of chlorine–ions (in chloroform). Energy differences between isomers are calculated for systems in the gas phase (ΔE_{gas}) and in chloroform solution (ΔE_{solv}) using their respective optimized geometries; B) geometrical structure of $[Au_8X_3(PH_3)_2]^{2+}$ (X = L1, L2) clusters (COSMO).

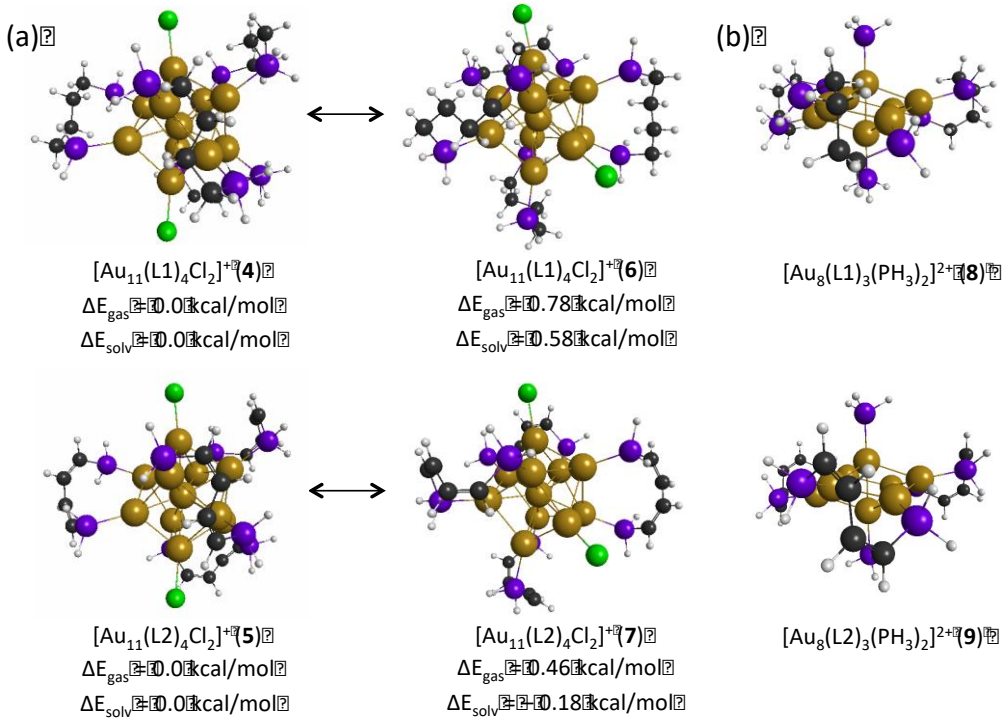

Figure 3–6. Superposition of experimental and theoretical gold cores (in chloroform): A) Au_{11} core and B) Au_8 core. Color key: experiment – blue and theory – yellow.

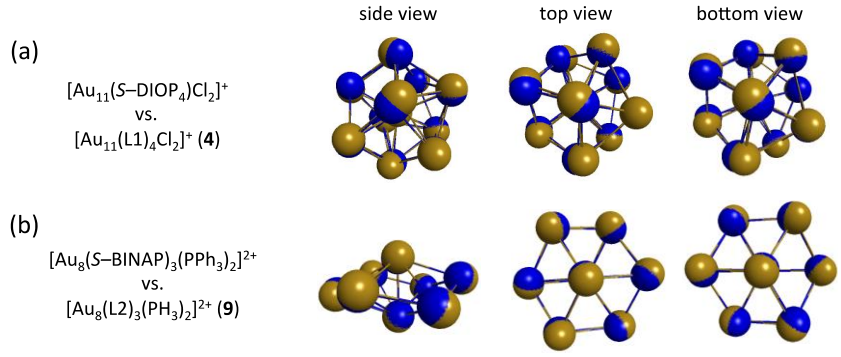

Theoretically calculated relative energies for gas phase structures of $[Au_{11}(L1)_4Cl_2]^+$ (**4**), $[Au_{11}(L2)_4Cl_2]^+$ (**5**), $[Au_{11}(L1)_4Cl_2]^+$ (**6**) and $[Au_{11}(L2)_4Cl_2]^+$ (**7**) clusters showed that structures

with chlorine atoms in the 4,5–position are energetically more preferable for both L1 and L2 ligands (**Figure 3–5a**). However, solvent effects change this for systems protected by L2 ligands: the $[Au_{11}(L2)_4Cl_2]^+$ (**7**) cluster with the 5,5–chlorine atom position is more energetically stable by 0.18 kcal/mol with respect to the $[Au_{11}(L2)_4Cl_2]^+$ (**5**) cluster. Due to the small differences in the relative energies between the isomers, optical absorption and CD spectra were calculated for $[Au_{11}(L1)_4Cl_2]^+$ (**4**), $[Au_{11}(L2)_4Cl_2]^+$ (**5**), $[Au_{11}(L1)_4Cl_2]^+$ (**6**) and $[Au_{11}(L2)_4Cl_2]^+$ (**7**) clusters both in gas phase and in chloroform.

$[Au_8X_3(PH_3)_2]^{2+}$ (X = L1, L2). The x–ray crystal structure of $[Au_8(BINAP)_3(PPh_3)_2]^{2+}$ was determined by Tsukuda and co–workers.[40] Their results showed that the Au_8 gold core does not depart very much from C_{3v} symmetry: six Au atoms (dark purple) form a "chair–cyclohexane" structure with one gold atom added above and one below the ring (**Figure 3–3c**). The measured Au–Au bond distances in the crystal structure are typical for gold systems and are in the range of 2.523 to 3.109 Å (**Table A–2**). Two achiral triphenylphosphine ligands are attached to the top gold atoms above and below the 6–fold ring with a distance of 2.303 Å and they create a central axis (Ph_3P–Au–Au–PPh_3) in the $[Au_8(BINAP)_3(PPh_3)_2]^{2+}$ cluster. Three BINAP ligands are bound to the octagold core through six equatorial surface atoms (atoms of the hexagonal ring) with an average distance of 2.305 Å (**Table A–2**).

To simulate $[Au_8(BINAP)_3(PPh_3)_2]^{2+}$ and $[Au_8(DIOP)_3(PPh_3)_2]^{2+}$ clusters, the theoretical models $[Au_8X_3(PH_3)_2]^{2+}$ (X = L1, L2) were used. The DIOP and BINAP ligands were substituted by the L1 and L2 model ligands and PPh_3 groups were exchanged for simple PH_3. In theoretical clusters $[Au_8X_3(PH_3)_2]^{2+}$ (X = L1, L2), positions of the PH_3 groups and the model bridging ligands are similar to the known experimental structure $[Au_8(BINAP)_3(PPh_3)_2]^{2+}$: two monodentate phosphine ligands (PH_3) are coordinated on the top and the bottom of the gold core, and bridging ligands L1 and L2 are bound to the octagold core through gold atoms of "chair–cyclohexane" ring (dark purple atoms in **Figure 3–3c**). Therefore, model clusters $[Au_8(L1)_3(PH_3)_2]^{2+}$ (**8**) and $[Au_8(L2)_3(PH_3)_2]^{2+}$ (**9**) were considered (**Figure 3–5b**).

Comparison of the Au_8 fragment geometry of the experimental structure $[Au_8(BINAP)_3(PPh_3)_2]^{2+}$ and the theoretically predicted model structure $[Au_8(L2)_3(PH_3)_2]^{2+}$ (**9**) are very close (**Figure 3–6b, Table A–2**). Gold–gold distances are longer in the theoretical structure by up to 0.16 Å with respect to experimental gold core in both gas phase and chloroform; again, this is typical of the BP86 functional employed in the optimizations.

Experimental DIOP and BINAP ligands have shorter Au-P bonds than the Au-P bonds present in optimized clusters containing the L1 and L2 model ligands, with differences of 0.127–0.193 Å. Full geometry optimization was performed only for the $[Au_8(L2)_3(PH_3)_2]^{2+}$ (**9**) structure because dramatic changes happened in the gold core during optimization of $[Au_8(L1)_3(PH_3)_2]^{2+}$. To obtain the $[Au_8(L1)_3(PH_3)_2]^{2+}$ (**8**) structure shown in **Figure 3–5b**, the Au_8 fragment was frozen during optimization (i.e. the gold core geometry was used from the optimized $[Au_8(L2)_3(PH_3)_2]^{2+}$ (**9**) cluster), and only optimization of the L1 shell was performed.

Optical Properties of Octa– and Undecagold Clusters

Optical absorption and CD spectra were calculated for $[Au_{11}X_4Cl_2]^+$ and $[Au_8X_3(PH_3)_2]^{2+}$ (X = L1, L2) clusters in the gas phase and in chloroform. Simulated CD spectra are presented in **Figure 3–7**. The gas phase CD spectra are less intense and redshifted with respect to the spectra obtained in implicit chloroform solvent. More detailed information about the calculated optical spectra in gas phase can be found in **Appendix A Figure A-5**. In the main paper, we will primarily focus on discussion of the data obtained using implicit solvent.

Figure 3–7. CD spectra for $[Au_{11}(L1)_4Cl_2]^+$ (4), $[Au_{11}(L2)_4Cl_2]^+$ (5), $[Au_{11}(L1)_4Cl_2]^+$ (6) and $[Au_{11}(L2)_4Cl_2]^+$ (7) clusters in A) gas phase and B) chloroform; CD spectra for $[Au_8(L1)_3(PH_3)_2]^{2+}$ (8) and $[Au_8(L2)_3(PH_3)_2]^{2+}$ (9) clusters in C) gas phase and D) chloroform.

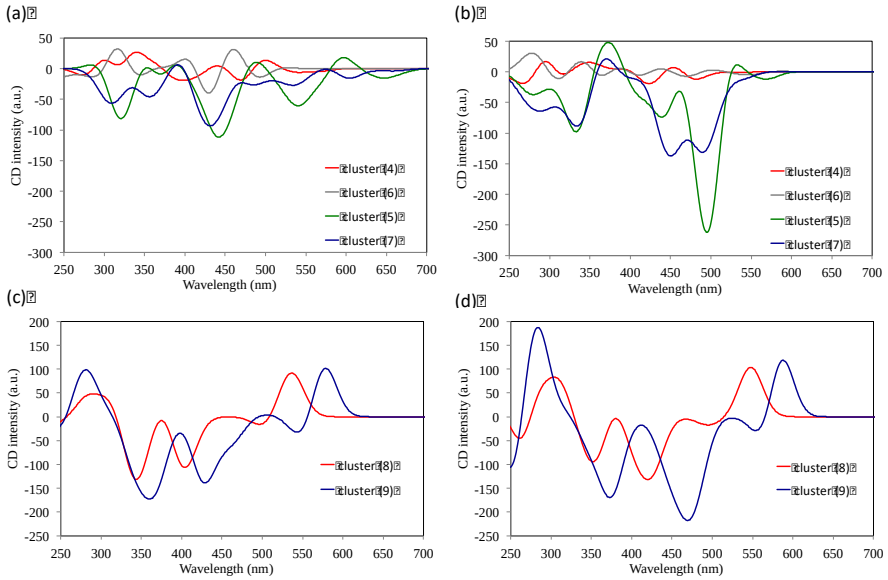

UV–vis and CD spectra of $[Au_{11}X_4Cl_2]^+$ (X = L1, L2). Optical absorption and CD spectra were calculated for $[Au_{11}(L1)_4Cl_2]^+$ (**4**), $[Au_{11}(L2)_4Cl_2]^+$ (**5**), $[Au_{11}(L1)_4Cl_2]^+$ (**6**) and $[Au_{11}(L2)_4Cl_2]^+$ (**7**) clusters in gas phase and chloroform (**Figure A–3 to A–6**, **Figure 3–8**, **Table 3–1** and **Table 3–2**). In this paper, we will focus only on excitations in the theoretical absorption and CD spectra with wavelengths between 280 and 700 nm. The absorption spectrum of the $[Au_{11}(L1)_4Cl_2]^+$ (**4**) cluster in chloroform increases in intensity with decreasing wavelength and exhibits four peaks at 459, 412, 351 and 301 nm (**Table 3–1**). The theoretical CD spectrum for this cluster has eight peaks. The first calculated CD band 1 with a peak minimum at 533 nm is a negative peak that arises primarily from a combination of three excitations at 539, 515 and 500 nm. This theoretical CD peak 1 does not have analog in the absorption spectra of the $[Au_{11}(L1)_4Cl_2]^+$ (**4**) cluster in chloroform (**Figure 3–8, Table 3–1**). The next two predicted CD peaks 2 and 3 at 481 and 453 nm have negative and positive signs, respectively. These two peaks are formed by excitations with wavelength from 480 to 450 nm and correspond to shoulder peak I in the theoretical absorption spectrum at 459 nm. Calculated CD peaks 4 (at 423 nm) and 5 (at 385 nm) are related to the strong absorption peak II at 412 nm. The next CD peak 6 is positive; it is located at 349 nm and arises due to excitations with wavelengths from 351–340 nm. This peak can be compared with shoulder peak III at 351 nm in the absorption spectrum. The last two considered CD bands 7 and 8 at 316 and 294 nm are negative and positive peaks. These two peaks are correlated to peak IV at 301 nm in the optical absorption spectrum. The intensities of the CD signals in the region 280 – 700 nm for $[Au_{11}(L1)_4Cl_2]^+$ (**4**) are in the range from –19.36 to 16.59 a.u. (**Figure 3–8, Table 3–1**).

Calculated optical absorption and CD spectra were also calculated for the $[Au_{11}(L1)_4Cl_2]^+$ (**6**) cluster. Due to the difference in the Cl atom positions, the optical absorption and CD spectra of the $[Au_{11}(L1)_4Cl_2]^+$ (**4**) and (**6**) clusters are slightly different (**Figure 3–8, Table 3–1**). The absorption spectrum of structure (**6**) in chloroform exhibits four peaks I–IV in the range of 280 – 700 nm: 480, 418, 348 and 301 nm (**Table 3–1**). The CD spectrum has seven bands 1–7: at 493, 460, 430, 400, 345, 316 and 284 nm. The first CD peak 1 of $[Au_{11}(L1)_4Cl_2]^+$ (**6**) is blueshifted by 35 nm with respect to the peak 1 position obtained for complex (**4**). The correlation between the absorption and CD bands can be found in **Table 3–1**. The intensities of the signals of this portion of the CD spectrum of the $[Au_{11}(L1)_4Cl_2]^+$ (**6**) cluster are in the range from –40.24 to 32.25 a.u. (**Figure 3–8, Table 3–1**). The intensities of the CD signals of

$[Au_{11}(L1)_4Cl_2]^+$ clusters (**4**) and (**6**) are not significantly different. So, the position of the chlorine atoms near undecagold core does not significantly affect the strength of the circular dichroism response, although it does change the overall shape.

Table 3-1. Optical absorption and CD spectra data for $[Au_{11}(L1)_4Cl_2]^+$ (4) and (6) clusters. Method LB94/DZ.fc (in chloroform).

$[Au_{11}(L1)_4Cl_2]^+$ (**4**)					$[Au_{11}(L1)_4Cl_2]^+$ (**6**)				
Abs		CD			Abs		CD		
no	peak, nm	no	peak, nm	CD (a.u.)	no	peak, nm	no	peak, nm	CD (a.u.)
–	–	1	533	–0.80	I	~480[s]	1	493	–13.82
I	~459[s]	2	481	–12.01			2	460	31.31
		3	453	6.81	II	418	3	430	–40.24
II	412	4	423	–19.36			4	400	15.33
		5	385	4.6	III	~348[s]	5	345	–10.11
III	~351[s]	6	349	15.17			6	316	32.25
IV	301	7	316	–3.8	IV	301	7	284	–13.48
		8	294	16.59					

[s] – shoulder peak. Maximum of this peak type was chosen to be equivalent to the wavelength of the strongest excitation in the region of the peak.

Table 3-2. Optical absorption and CD spectra data for $[Au_{11}(L2)_4Cl_2]^+$ (5) and (7) clusters. Method: LB94/DZ.fc (in chloroform).

$[Au_{11}(L2)_4Cl_2]^+$ (**5**)					$[Au_{11}(L2)_4Cl_2]^+$ (**7**)				
Abs		CD			Abs		CD		
no	peak, nm	no	peak, nm	CD (a.u.)	no	peak, nm	no	peak, nm	CD (a.u.)
I	~552[s]	1	568	–11.98	I	~558[s]	1	540	–12.45
		2	533	10.98	II	~499[s]	2	490	–131.28
II	~497[s]	3	495	–262.4	III	457	3	450	–137.54
III	452	4	440	–74.18	IV	~413[s]	4	408	–12.96
IV	~420[s]	5	405	–31.61	V	~369[s]	5	369	20.82
V	378[s]	6	373	47.86	VI	~330[s]	6	333	–88.83
VI	300	7	333	–97.86	VII	294	7	287	–64.20

[s] – shoulder peak. Maximum of this peak type was chosen to be equivalent to the wavelength of the strongest excitation in the region of the peak.

Figure 3–8. UV–vis and CD spectra of A) $[Au_{11}(L1)_4Cl_2]^+$ (4); B) $[Au_{11}(L1)_4Cl_2]^+$ (6); C) $[Au_{11}(L2)_4Cl_2]^+$ (5); D) $[Au_{11}(L2)_4Cl_2]^+$ (7); E) $[Au_8(L1)_3(PH_3)_2]^{2+}$ (8) and F) $[Au_8(L2)_3(PH_3)_2]^{2+}$ (9) structures. Method LB94/DZ.fc (in chloroform).

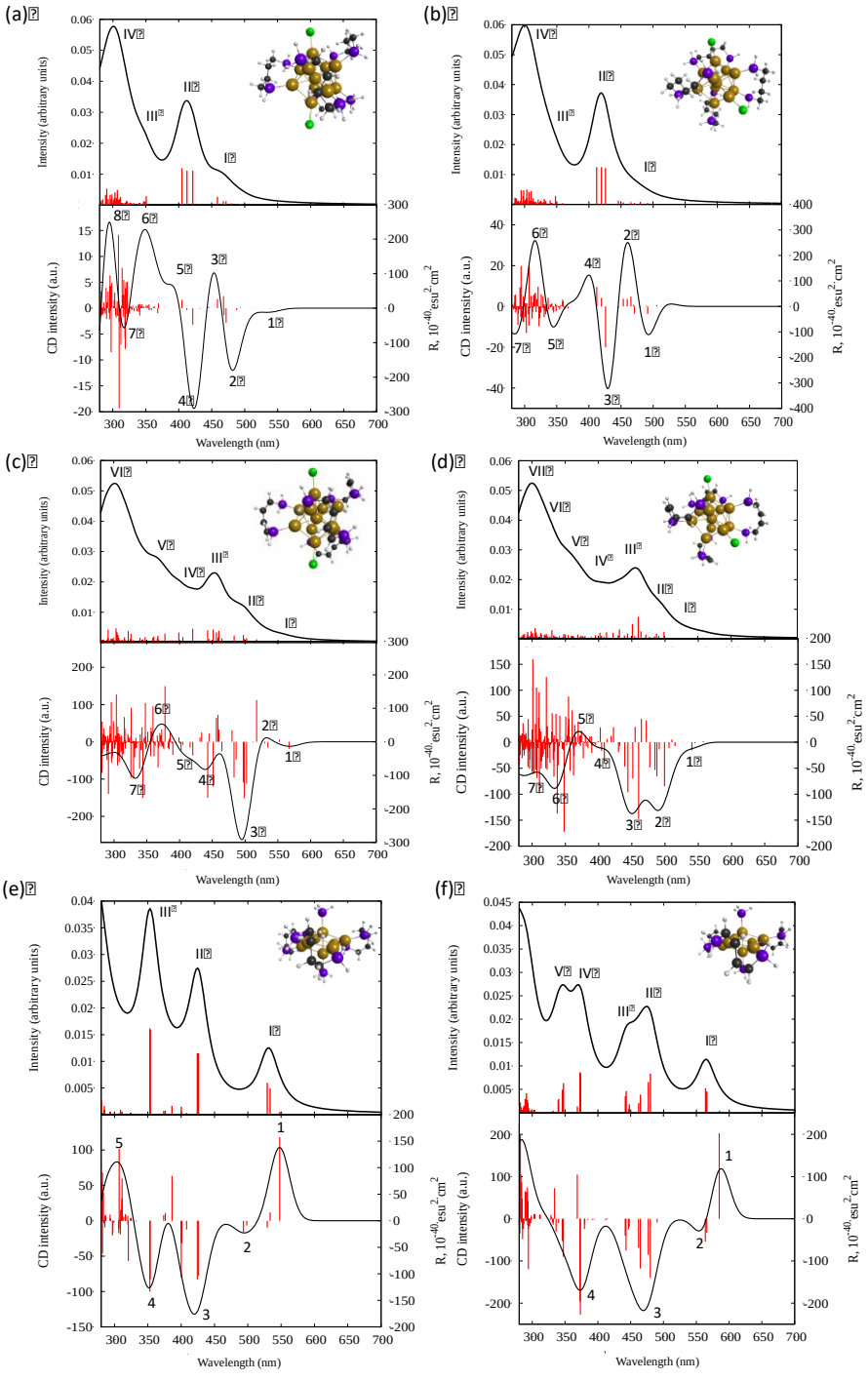

The absorption spectrum of the $[Au_{11}(L2)_4Cl_2]^+$ (**5**) cluster in chloroform increases in intensity with decreasing wavelength and exhibits six peaks at 552, 497, 452, 420, 378 and 300 nm (**Figure 3–8**, **Table 3–2**). The calculated CD spectrum for this cluster has seven peaks. The

first two CD peaks 1 and 2 at 568 and 533 nm have negative and positive sign, respectively. These two peaks are formed by excitations with wavelength from 567 to 530 nm and correspond to shoulder peak I in the theoretical absorption spectrum at 552 nm. The next three CD peaks 3, 4 and 5 are negative with minima at 495, 440 and 405 nm, respectively. The CD band 5 is a weak positive band with a maximum at 373 nm. CD peak 7 is negative and located at 300 nm. These CD peaks 3–7 can be associated with absorption bands II–VI, respectively (**Table 3–2**). The intensity of the CD signal in the region 280 – 700 nm for $[Au_{11}(L2)_4Cl_2]^+$ (**5**) is in the range from –262.4 to 47.86 a.u. (**Table 3–2**).

The optical and CD spectra of the $[Au_{11}(L2)_4Cl_2]^+$ (**7**) cluster with the 5,5–position of chlorine atoms were also calculated. The optical absorption and CD spectra for this structure are redshifted with respect to $[Au_{11}(L2)_4Cl_2]^+$ (**5**) (**Table 3–2**). The first absorption peak I was detected at 558 nm. This peak is shifted to a lower wavelength by 67 nm with respect to structure (**5**). Absorption peaks II–VII are located at 499, 457, 413, 369, 330 and 294 nm. The CD spectrum of $[Au_{11}(L2)_4Cl_2]^+$ (**7**) also contains seven peaks. The first three CD peaks 1–3 at 540, 490 and 450 nm exhibit negatively signed amplitude with different intensity. For cluster (**7**), peak 1 is less intense than peaks 2 and 3. The next CD peak 4 in the CD spectrum of $[Au_{11}(L2)_4Cl_2]^+$ (7) is a weak negative peak at 408 nm. The fifth CD peak 5 is located at 369 nm; this is a weak positive peak. The last two CD peaks in the CD spectrum of $[Au_{11}(L2)_4Cl_2]^+$ (**7**) are negative with minima at 333 and 287 nm, respectively. The intensities of the CD signals in the region 280 – 700 nm for $[Au_{11}(L2)_4Cl_2]^+$ (**7**) are in the range of –137.54 ± 20.82 a.u. (**Table 3–2**).

A comparative analysis of theoretical and experimental spectral data was performed. Provorse and Aikens[45] have already shown that removal of the aromatic groups during replacement of BINAP by the model ligand affects the CD spectrum at wavelengths shorter than 350 nm. Therefore, only the region above 350 nm in the optical spectra will be analyzed. The experimental optical absorption and CD spectra of $[Au_{11}(S\text{–DIOP})_4Cl_2]^+$ and $[Au_{11}(S\text{–BINAP})_4Cl_2]^+$ clusters are presented in **Figure 3–1a** and **Figure 3–1b**. In **Figure 3–9**, these experimental optical absorption and CD data are compared with theoretical results of the most stable isomers of the model systems: $[Au_{11}(S\text{–DIOP})_4Cl_2]^+$ vs. $[Au_{11}(L1)_4Cl_2]^+$ (**4**) and $[Au_{11}(S\text{–BINAP})_4Cl_2]^+$ vs. $[Au_{11}(L2)_4Cl_2]^+$ (**7**).

Figure 3–9. Comparison of the theoretical and experimental spectral data. Optical absorption spectra of A) $[Au_{11}(S–DIOP)_4Cl_2]^+$ vs. $[Au_{11}(L1)_4Cl_2]^+$ (4); B) $[Au_{11}(S–BINAP)_4Cl_2]^+$ vs. $[Au_{11}(L2)_4Cl_2]^+$ (7); and C) $[Au_8(S–BINAP)_3(PPh_3)_2]^{2+}$ vs. $[Au_8(L2)_3(PH_3)_2]^{2+}$ (9). CD spectra of D) $[Au_{11}(S–DIOP)_4Cl_2]^+$ vs. $[Au_{11}(L1)_4Cl_2]^+$ (4); E) $[Au_{11}(S–BINAP)_4Cl_2]^+$ vs. $[Au_{11}(L2)_4Cl_2]^+$ (7); and F) $[Au_8(S–BINAP)_3(PPh_3)_2]^{2+}$ vs. $[Au_8(L2)_3(PH_3)_2]^{2+}$ (9). Method LB94/DZ.fc (in chloroform). The shift of the theoretical data was determined from the average difference in the positions between the first two theoretical and experimental absorption peaks.

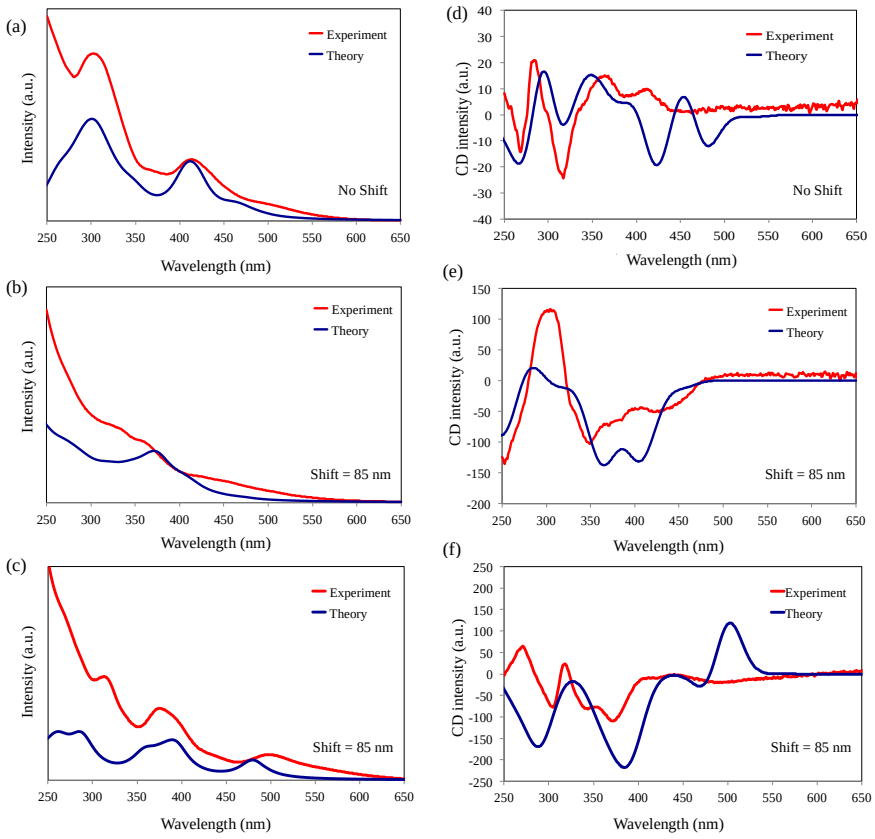

The experimental optical absorption spectrum of the $[Au_{11}(S–DIOP)_4Cl_2]^+$ cluster above 350 nm has three peaks: one strong maximum at 417 nm and two shoulder peaks about 550–475 nm and 380–350 nm (**Figure 3–9a**). The theoretically predicted optical absorption spectrum of the model cluster $[Au_{11}(L1)_4Cl_2]^+$ (**4**) is in great agreement with empirical results: (i) the shape of the calculated spectrum is similar to the experimental spectrum, and (ii) the maximum of the strongest peak in the considered region (from 650–350 nm) is located at 412 nm (**Figure 3–9a**). The difference in the position of first maximum in the theoretical and experimental absorption spectra is just 5 nm. Therefore, offsetting the theoretically predicted CD peaks is not necessary during comparison of the theoretical data of $[Au_{11}(L1)_4Cl_2]^+$ (**4**) with the empirical results of $[Au_{11}(S–DIOP)_4Cl_2]^+$. The experimental CD spectrum of $[Au_{11}(S–DIOP)_4Cl_2]^+$ exhibits two

positive peaks at 411 and 364 nm in the considered spectral region above 350 nm (**Figure 3–9d**).[40] The calculated CD spectrum of $[Au_{11}(L1)_4Cl_2]^+$ (**4**) in the region 300 – 700 nm is more complex with respect to the experimental one. Main differences between experimental and theoretical CD spectra are observed in the low energy region (430–700 nm): the empirical CD spectrum do not exhibit any strong peaks in this area, whereas the theoretical results predicted peaks at 533, 481, 453 and 423 nm. However, the high-energy parts (300–430 nm) of the theoretical and experimental CD spectra look very similar to each other: the theoretical CD exhibits two positive peaks at 385 and 349 nm, which can be assigned with positive bands at 411 and 364 nm in the empirical CD spectrum.

In the case of the BINAP-stabilized undecagold cluster $[Au_{11}(S\text{–BINAP})_4Cl_2]^+$, the experimental CD spectrum shows two negative peaks at 428 and 349 nm.[40, 41] In the simulated CD spectrum of the $[Au_{11}(L2)_4Cl_2]^+$ (**7**) cluster, the first strong negative peak occurs at 490 nm and the second appears at 450 nm. It is well known that metal–metal transitions in gold nanoparticles are usually underestimated by about 0.15–0.35 eV.[45] Furthermore, substitution of the DIOP/BINAP molecules by model ligands L1/L2 can potentially lead to an additional redshift in the simulated CD spectra. As shown in **Figure 3–9,** offsetting the theoretically predicted peaks by 85 nm in the case of $[Au_{11}(L2)_4Cl_2]^+$ (**7**) leads a very good agreement with the experimental data.

Kohn–Sham orbitals involved in the excitations with wavelengths between 700–280 nm for the $[Au_{11}(L1)_4Cl_2]^+$ (**4**) and $[Au_{11}(L2)_4Cl_2]^+$ (**7**) clusters are represented in **Figure 3–10**. For the Au_{11}^{3+} gold core, we have 8 electrons with an expected occupation of $1S^2 1P^6 1D^0 2S^0$…, where S, P, and D represent superatom orbitals that are formed from a linear combination of the valence 6s electrons of the gold atoms. Orbitals between HOMO–11 and LUMO+14 were considered. In the case of the $[Au_{11}(L1)_4Cl_2]^+$ (**4**) cluster, the HOMO, HOMO–1 and HOMO–2 orbitals are essentially P superatom orbitals (**Figure 3–10a**). The highest occupied molecular orbitals from HOMO–3 through HOMO–11 are a mixture of Cl *p* and Au *d* orbitals. The five lowest unoccupied molecular orbitals (LUMO, LUMO+1, LUMO+2, LUMO+3 and LUMO+4) exhibit significant superatom D character. The next lowest unoccupied molecular orbitals (between LUMO+5 and LUMO+12) are a mixture of atomic gold and phosphorous orbitals. LUMO+13 and LUMO+14 are composed primarily of atomic *s* and *p* orbitals on the L1 ligands. According to these results, we can conclude that the optical absorption and CD spectra in the

region 700–350 nm for the undecagold core protected by DIOP or L1 model ligands occur due to electronic transitions within the Au_{11}^{3+} gold core framework only (from occupied superatom P orbitals to unoccupied superatom D orbitals) (**Table A–3**). The bands in the high–energy part of the spectra (wavelengths below 350 nm) for $[Au_{11}(L1)_4Cl_2]^+$ (**4**) occur due to electron transitions primarily from the occupied Cl *p* and Au *d* orbitals orbitals to gold–phosphorous and atomic *s* and *p* orbitals on the L1 ligands. The HOMO–LUMO gap for $[Au_{11}(L1)_4Cl_2]^+$ (**4**) is 2.26 eV.

Figure 3–10. Kohn–Sham orbitals of (a) $[Au_{11}(L1)_4Cl_2]^+$ (4) and (b) $[Au_{11}(L2)_4Cl_2]^+$ (7). Method LB94/DZ.fc (in chloroform).

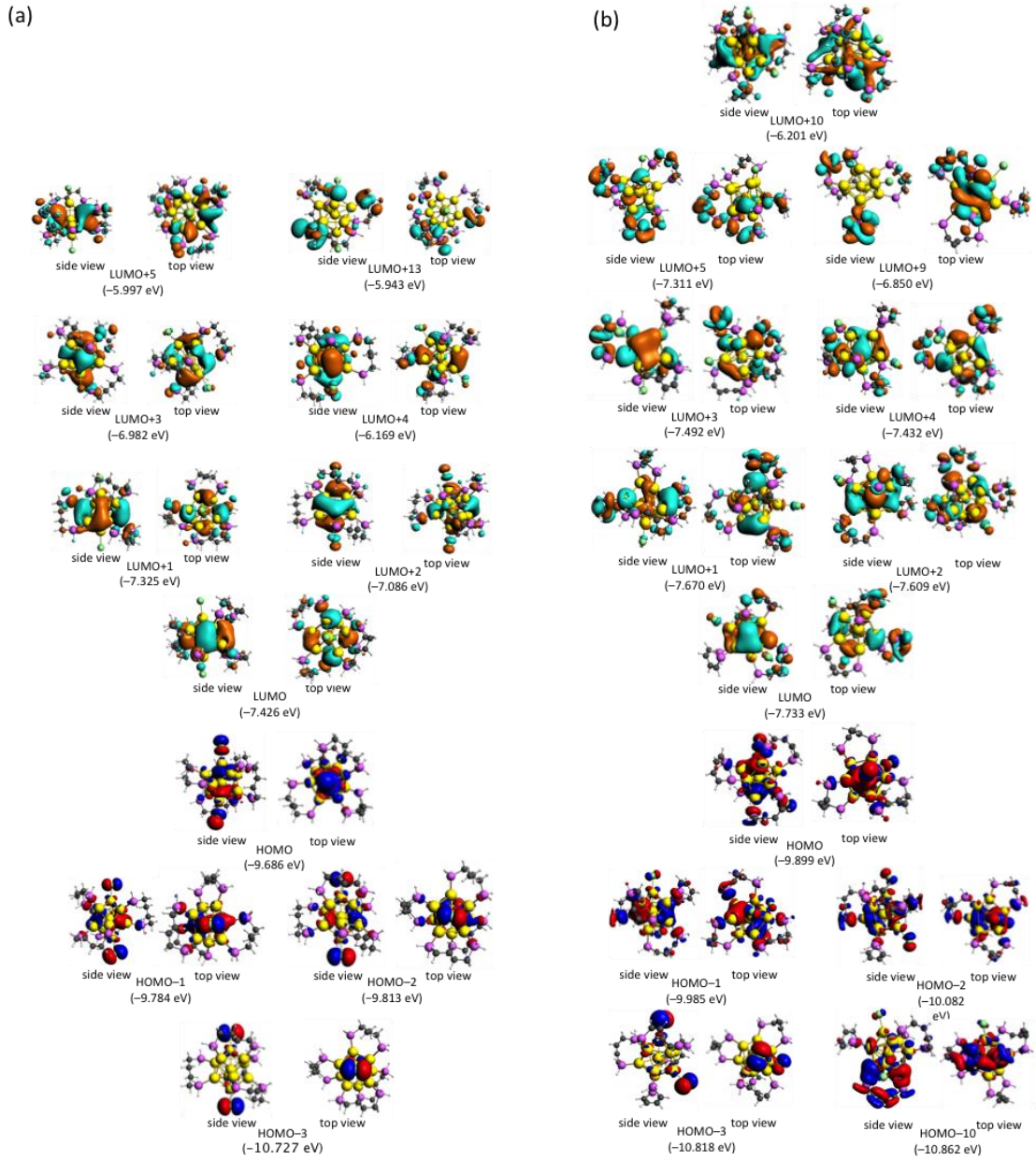

In the case of the undecagold core protected by model ligands containing double bonds (i.e. $[Au_{11}(L2)_4Cl_2]^+$ (**7**)), the character of the orbitals from HOMO–2 through LUMO+4 are identical to those for the system protected by ligands with single bonds only (i.e. $[Au_{11}(L1)_4Cl_2]^+$ (**4**)); HOMO, HOMO–1 and HOMO–2 are P superatom orbitals, and LUMO, LUMO+1, LUMO+2, LUMO+3 and LUMO+4 are D superatom orbitals (**Figure 3–10b**). The highest occupied molecular orbitals from HOMO–3 through HOMO–7 are a mixture of Cl *p* and Au *d* orbitals, whereas the orbitals starting at HOMO–8 and below are a mixture of Cl *p*, Au *d* orbitals and π orbitals of the L2 model ligands. The LUMO+5, LUMO+6, LUMO+7 and LUMO+8 are a mixture of Au *d* orbitals and π* orbitals of the L2 model ligands. The LUMO+9 through LUMO+12 orbitals are primarily π* orbitals of the model ligands only. Orbitals above LUMO+13 are a mixture of atomic gold and phosphorous orbitals. These data show that the first strong negative band (in the experimental spectrum at 428 nm and in the theoretical spectrum at 490 nm without offsetting the peaks) arises due to electronic transitions within the undecagold core framework only. However, the second negative peak (in the experimental spectrum at 349 nm and at 450 nm in the theoretical spectrum without offsetting) occurs because of electronic transitions within the undecagold core framework and from electronic transitions from P occupied orbitals to the π* orbitals of the L2 model ligands (**Table A–6**). The HOMO–LUMO gap for $[Au_{11}(L2)_4Cl_2]^+$ (**7**) is 2.17 eV. Therefore, in the region of the spectrum above 350 nm for the undecagold core protected by ligands with double bonds (L2), the orbitals of the ligands are actively involved in the electronic transitions in addition to transitions within the gold core, whereas for undecagold clusters protected by ligands with single bonds (L1), only electronic transitions within the gold core framework were detected. In both the experimental and theoretical clusters, the absorption spectra for systems with single bonds (**Figure 3–1a**, **Figure 3–8a**, and **Figure 3–8b**) are more well-defined than the absorption spectra for systems with double bonds (**Figure 3–1b**, **Figure 3–8c**, and **Figure 3–8d**).

UV–vis and CD spectra of $[Au_8X_3(PH_3)_2]^{2+}$ (X = L1, L2). Optical absorption and CD spectra were calculated for $[Au_8(L1)_3(PH_3)_2]^{2+}$ (**8**) and $[Au_8(L2)_3(PH_3)_2]^{2+}$ (**9**) clusters in the gas phase and chloroform (**Figure 3–8ef**, **Table 3–3**). Both of these clusters have an identical Au_8^{2+} gold core because of the constrained optimization for $[Au_8(L1)_3(PH_3)_2]^{2+}$ (**8**). The results showed that the shapes of the optical absorption and CD spectra of $[Au_8(L1)_3(PH_3)_2]^{2+}$ (**8**) and $[Au_8(L2)_3(PH_3)_2]^{2+}$ (**9**) clusters are very similar (**Figure 3–8ef**). However, the peak positions

and intensities of the CD signals are different. The optical absorption spectrum of the $[Au_8(L1)_3(PH_3)_2]^{2+}$ (**8**) complex exhibits three strong peaks (I-III) in the region above 280 nm at 530, 425 and 353 nm (**Table 3–3**). The CD spectrum of this complex has five peaks (1–5). The first absorption band I at 530 nm can be assigned with the first two CD peaks: the strong positive peak 1 with a maximum at 548 nm and the small negative CD peak 2 at 495 nm. The second and third absorption bands (II and III) at 425 and 353 nm are correlated with two strong negative CD peaks (3 and 4) at 420 and 352 nm, respectively. The last CD peak 5 is positive with a maximum at 304 nm. This peak is related to the strong absorption band around 274 nm (**Table 3–3**).

Both optical absorption and CD spectra for $[Au_8(L2)_3(PH_3)_2]^{2+}$ (**9**) are shifted to longer wavelengths by about 40 nm with respect to $[Au_8(L1)_3(PH_3)_2]^{2+}$ (**8**). Moreover, the intensities of the CD signals of the octagold core protected by model ligands with double bonds (i.e. $[Au_8(L2)_3(PH_3)_2]^{2+}$ (**9**)) are much stronger than for the cluster with ligands that contain only single bonds ($[Au_8(L1)_3(PH_3)_2]^{2+}$ (**8**)) (**Table 3–3**). The optical absorption spectrum of structure (**9**) exhibits five peaks (**Figure 3–8**). The first absorption peak of $[Au_8(L2)_3(PH_3)_2]^{2+}$ (**9**) is located at 565 nm. The next two absorption peaks II and III of structure (**9**) can be associated with the second band in the absorption spectrum of cluster (**8**), which becomes split when L2 ligands are used. Similar splitting is observed in the case of peaks IV and V in the absorption spectrum of structure (**9**). These two peaks can be associated with band III in the absorption spectrum for the cluster with L1 ligands (**8**). Overall, the optical absorption spectra of (**8**) and (**9**) exhibit three main peaks, albeit with some splitting for (**9**), which are in good agreement with the three peaks evident in the experimental optical absorption spectrum of $[Au_8(BINAP)_3(PPh_3)_2]^{2+}$ (**Figure 3–1c**). The CD spectrum of $[Au_8(L2)_3(PH_3)_2]^{2+}$ (**9**) has a shape very similar to the CD spectrum of structure (**8**). Four main peaks in the CD spectrum are observed at 587, 553, 470 and 372 nm.

Comparison of the theoretical data with experiment is shown in **Figure 3–9c** for $[Au_8(S–BINAP)_3(PPh_3)_2]^{2+}$ vs. $[Au_8(L2)_3(PH_3)_2]^{2+}$ (**9**) (theoretical data are shifted by 85 nm). For the experimental $[Au_8(S–BINAP)_3(PPh_3)_2]^{2+}$ complex, the CD spectrum above 350 nm has two strong negative bands at 490 and 407 nm.[40] As shown in **Figure 3–9c,** offsetting the theoretically predicted peaks of $[Au_8(L2)_3(PH_3)_2]^{2+}$ (**9**) by 85 nm leads a reasonable agreement with the experimental data in the region between 475 and 350 nm wavelength range: theoretical

negative CD peaks at 553 and 470 nm (before shift) can be assigned with experimental peaks at 490 and 407 nm, respectively. However, the theoretical CD spectrum exhibits a strong positive band at 587 nm, whereas the experimental CD signal is negative above 350 nm. This theoretical positive band occurs due to an excited state at 548 nm, which is very weak in the absorption spectrum (oscillator strength f = 0.030) and became strong in CD (R = 157.52 10^{-40} esu^2 cm^2). This excited state arises due to electron transitions out of the HOMO to LUMO and HOMO+1 to LUMO+1, so it is not a charge transfer state. To check the method and basis set effect on the results, the CD spectrum of $[Au_8(L2)_3(PH_3)_2]^{2+}$ (**9**) was recalculated with the SAOP/TZP method. Moreover, the sensitivity of the CD spectrum to the hydrogen atom position in the PH_3 groups was also tested. However, all obtained CD spectra of $[Au_8(L2)_3(PH_3)_2]^{2+}$ (**9**) exhibit this positive band. Thus, it does not appear to be a charge transfer artifact or a model functional or basis set problem. It could be related to the replacement of BINAP by the model ligand, vibrational effects, or even to experimental instrument accuracy.

Table 3-3. Optical absorption and CD spectra data for $[Au_8(L1)_3(PH_3)_2]^{2+}$ (8) and $[Au_8(L2)_3(PH_3)_2]^{2+}$ (9) clusters. Method LB94/DZ.fc (in chloroform).

$[Au_8(L1)_3(PH_3)_2]^{2+}$ (**8**)					$[Au_8(L2)_3(PH_3)_2]^{2+}$ (**9**)				
Abs		CD			Abs		CD		
no	peak, nm	no	peak, nm	CD (a.u.)	no	peak, nm	no	peak, nm	CD (a.u.)
I	530	1	548	103.39	I	565	1	587	118.29
		2	495	–17.18			2	553	–28.88
II	425	3	420	–132.08	II	474	3	470	–217.72
III	353	4	352	–94.87	III	450			
IV	274	5	304	83.14	IV	371	4	372	–169.62
					V	346			

Kohn–Sham orbitals involved in the excitations with wavelength between 700–280 nm for the $[Au_8(L1)_3(PH_3)_2]^{2+}$ (**8**) and $[Au_8(L2)_3(PH_3)_2]^{2+}$ (**9**) clusters are represented in **Figure 3–11**. For the Au_8^{2+} gold core, we have 6 electrons with an expected occupation of $1S^2 1P^4 1D^0 2S^0$…, where S, P, and D are superatom orbitals that are formed from a linear combination of the valence 6s electrons of the gold atoms. Orbitals between HOMO–9 and LUMO+17 were considered. In the case of $[Au_8(L1)_3(PH_3)_2]^{2+}$ (**8**), the HOMO and HOMO–1 are essentially P superatom orbitals (**Figure 3–11a**). The HOMO–2 is a mixture of H *s*, P *s*, and Au *d* orbitals. Molecular orbital HOMO–3 is formed by a contribution of H *s*, P *s*, and Au *s* and *d* orbitals. The highest occupied molecular orbitals from HOMO–4 to HOMO–9 are primarily

Au *d* orbitals with some contributions from interactions between gold and phosphorous atoms. The LUMO, LUMO+1, LUMO+3 and LUMO+4 orbitals exhibit significant superatom D character, whereas the LUMO+2 is a P superatom orbital. The other lowest unoccupied molecular orbitals (between LUMO+5 and LUMO+17) arise essentially from *s* and *p* atomic orbitals from the ligand atoms . The HOMO–LUMO gap for $[Au_8(L1)_3(PH_3)_2]^{2+}$ (**8**) is 2.06 eV.

Figure 3–11. Kohn–Sham orbitals of A) $[Au_8(L1)_3(PH_3)_2]^{2+}$ (8) and B) $[Au_8(L2)_3(PH_3)_2]^{2+}$ (9). Method LB94/DZ.fc (in chloroform).

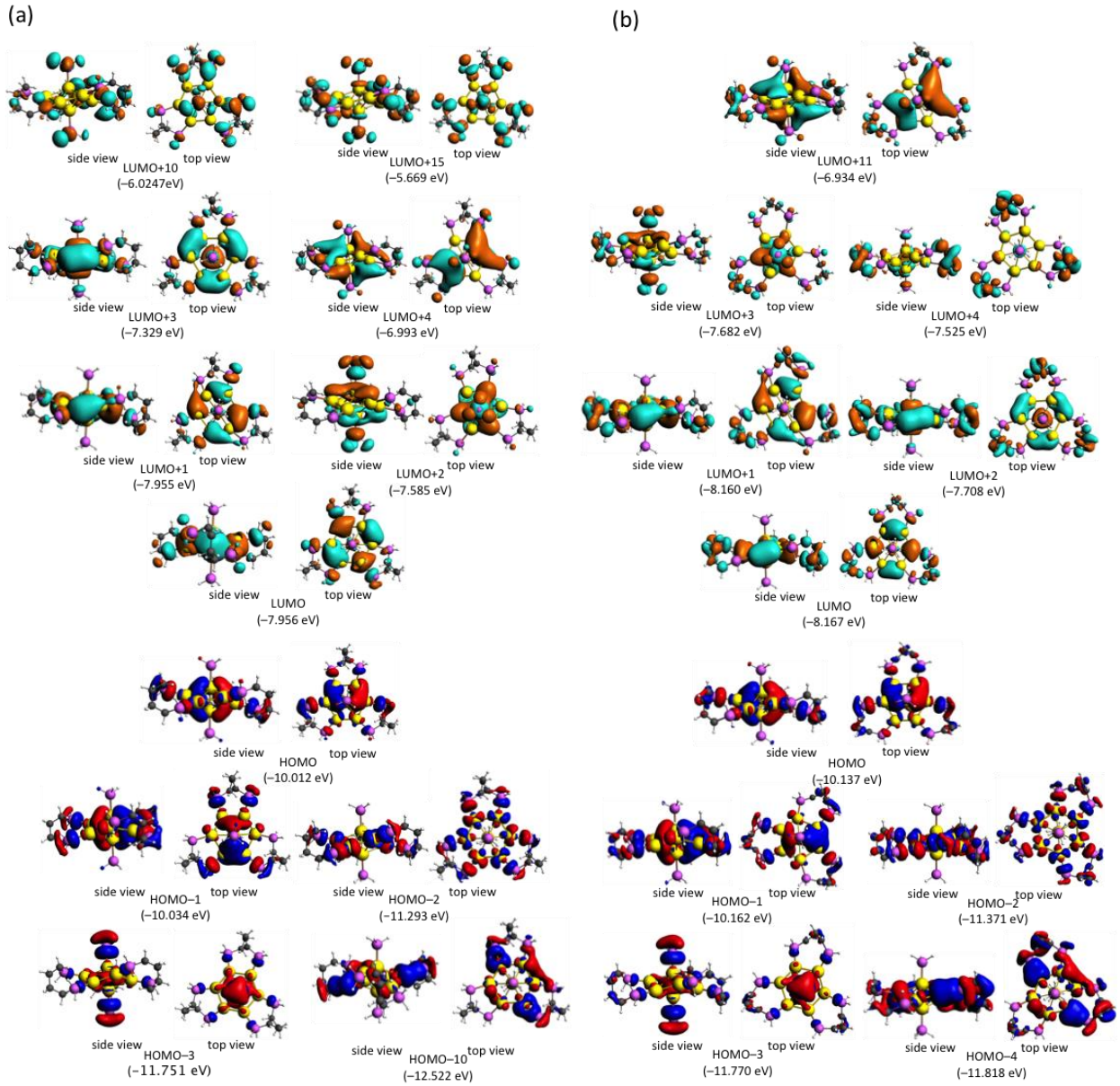

In the case of the octagold core protected by model ligands that contain double bonds (i.e. $[Au_8(L2)_3(PH_3)_2]^{2+}$ (**9**)), the HOMO and HOMO–1 are P superatom orbitals as well

(**Figure 3–11b**). The other highest occupied molecular orbitals are similar to the same orbitals for $[Au_8(L1)_3(PH_3)_2]^{2+}$ (**8**), but include contributions from C *p* and π orbitals of the L2 model ligands. The LUMO, LUMO+1, and LUMO+2 have D character, whereas the LUMO+3 is a P superatom orbital. The orbitals LUMO+4 to LUMO+17 are not supertaom orbitals and essentially arise from a mixture of P *s*, Au *s* and/or *d* orbitals, and/or π* orbitals of the model ligands (**Figure 3–11b**). The results showed that the first three bands (1–3) of the CD spectrum of the $[Au_8(L2)_3(PH_3)_2]^{2+}$ (**9**) cluster occur because of electronic transitions within the octagold core framework and from electronic transitions from occupied P orbitals to the π* orbitals of the L2 model ligands (**Table S8**). Similar results were obtained for the $[Au_{11}(L2)_4Cl_2]^{+}$ (**7**) system. The HOMO–LUMO gap for $[Au_{11}(L2)_4Cl_2]^{+}$ (**7**) is 1.97 eV.

Factors influencing chiroptical activity in gold clusters. The obtained results showed a reasonable agreement between the simulated absorption and CD spectra of octa– and undecagold clusters protected by model ligands L1 and L2 with experimental data for DIOP and BINAP stabilized clusters (**Figure 3**–**9**). For both octa– and undecagold clusters, the CD signals are much weaker for systems stabilized by L1 ligands (model ligand for DIOP) than for systems with L2 ligands (model ligand for BINAP). Tsukuda and co–workers observed similar differences in the intensities of their CD signals: BINAP–protected gold clusters have larger anisotropy factors than DIOP–protected species (**Figure 3–1**).[40, 41] In this article, three main hypotheses for explanation of the observed differences in the chiroptical activity of the gold cluster clusters are considered: (i) geometrical deformation of the gold core due to ligation; (ii) nature of ligands; and (iii) chlorine atom positions in the undecagold clusters.

Figure 3–12. CD spectra of A) Au_{11}^{3+} core of clusters $[Au_{11}(L1)_4Cl_2]^{+}$ (4) and $[Au_{11}(L2)_4Cl_2]^{+}$ (5); and B) isolated model ligands L1 and L2.

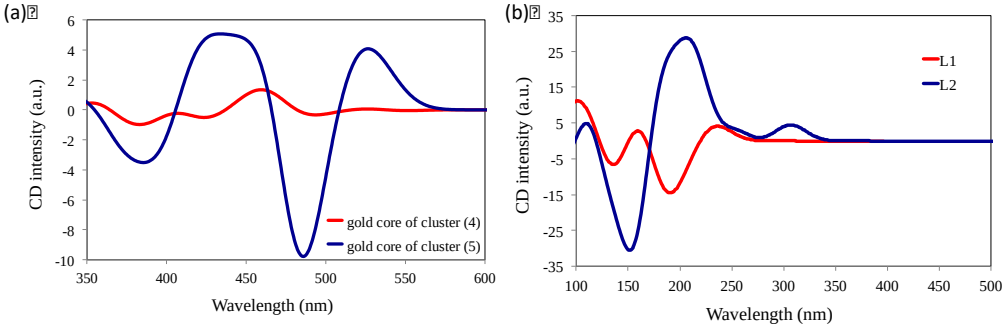

First, geometrical deformation of the gold core due to ligation can be a source of the CD activity. To check the influence of geometrical deformation of the gold core on the intensities of the CD signals, Au_{11}^{3+} fragments from $[Au_{11}X_4Cl_2]^+$ (X = L1, L2) clusters were isolated and used for calculation of the CD spectra of the gold cores in chloroform (**Figure 3–12a**). To eliminate the effect of the Cl atom positions on the shape and intensities of the CD spectra of the gold core, a pair of undecagold clusters with almost identical positions of chlorine atoms were chosen: $[Au_{11}(L1)_4Cl_2]^+$ (**4**) and $[Au_{11}(L2)_4Cl_2]^+$ (**5**). In these clusters, the chlorine atoms are located in the 4,5 position and the bond angle between these two atoms ($\angle ClAu_{(1)}Cl$, where $Au_{(1)}$ is the central gold atom) is 167° in both cases. For clusters with the 5,5 position of chlorine atoms structures (**6**) and (**7**), the difference in the angle is more significant: the $\angle ClAu_{(1)}Cl$ angles are equivalent to 121° and 123°, respectively.

The calculated CD spectra of the Au_{11}^{3+} fragment of $[Au_{11}(L1)_4Cl_2]^+$ (**4**) and $[Au_{11}(L2)_4Cl_2]^+$ (**5**) clusters are presented in **Figure 3–12a**. The results showed that the CD spectrum of the core of the undecagold cluster protected by L2 ligands (ligand with double bonds) is much stronger than the CD spectrum of the cluster protected by L1 ligands (single bonds only). Therefore, we can conclude first that deformation in the gold core under ligation can be one of the reasons for the origin of chirality in metal clusters protected by chiral ligands and second that the ligation of gold clusters by different types of organic molecules initiates different forms of geometry perturbation in the gold core, which can be a cause of significant differences in the intensities of the CD signals (**Figure 3–12a**). It is important to notice that the amplitude of the CD spectrum of an isolated gold core is in the range from –10 to 5 a.u. This is ~20 times weaker than the CD signals for $[Au_{11}(L2)_4Cl_2]^+$ (**6**), which shows that ligands can contribute dramatically to the origin and intensity of the CD spectrum.

Second, the nature of ligands themselves affects the CD spectrum. The theoretical results presented above showed that the presence of double bonds in a ligand could be a reason for dramatic differences in the chiroptical activity of organometallic clusters. For example, octagold clusters $[Au_8(L1)_3(PH_3)_2]^{2+}$ (**8**) and $[Au_8(L2)_3(PH_3)_2]^{2+}$ (**9**) have an identical Au_8^{2+} core. The calculated optical absorption and CD spectra for these structures exhibit very similar shapes (**Figure 3–8**). However, both types of spectra for structure (**9**) stabilized by ligands with double bonds are redshifted and the intensities of the CD signals of this cluster are stronger with respect to $[Au_8(L1)_3(PH_3)_2]^{2+}$ (**8**) (**Table 3–3**). Furthermore, analysis of the orbitals for octa–

and undecagold clusters showed that in the region of the spectra above 350 nm for the gold cores protected by ligands with double bonds (L2), π* orbitals of the L2 ligands are actively involved in electronic transitions, whereas gold clusters protected by L1 model ligands only exhibit electronic transitions within the gold core framework.

Calculated CD spectra for isolated molecules L1 and L2 in the gas phase are presented in **Figure 3–12b**. The intensity of the CD signals for the L2 molecule is also much stronger. Moreover, the first peak for the L2 molecule is detected at 305 nm, whereas for L1 ligands the first peak is located at 237 nm. Therefore, L2 ligands should have a stronger effect in the UV–Vis part of the spectra for gold nanoparticles.

The third factor to consider is whether the position of the chlorine atom in the undecagold clusters can potentially affect the CD spectra. In the results shown in this work, simulated CD spectra for $[Au_{11}(L1)_4Cl_2]^+$ (**4**), $[Au_{11}(L2)_4Cl_2]^+$ (**5**), $[Au_{11}(L1)_4Cl_2]^+$ (**6**) and $[Au_{11}(L2)_4Cl_2]^+$ (**7**) clusters showed that the position of the chlorine atoms around the undecagold core does not affect the strength of the circular dichroism signals dramatically either in the gas phase or in chloroform (**Figure 3–7a** and 3–**7b**). The intensities of the CD signals are very close for the pairs $[Au_{11}(L1)_4Cl_2]^+$ (**4**) – $[Au_{11}(L1)_4Cl_2]^+$ (**6**) and $[Au_{11}(L2)_4Cl_2]^+$ (**5**) – $[Au_{11}(L2)_4Cl_2]^+$ (**7**).

Figure 3–13. A) S–L1 ligands arrangement in the clusters $[Au_{11}(S–L1)_4Cl_2]^+$ (4) and (10) (bidentate ligands were highlighted in different colors, marked gold atoms by green circle are from bottom layer); B) CD spectra of $[Au_{11}(S–L1)_4Cl_2]^+$ (4) and (10) clusters in gas phase. Method LB94/DZ.fc.

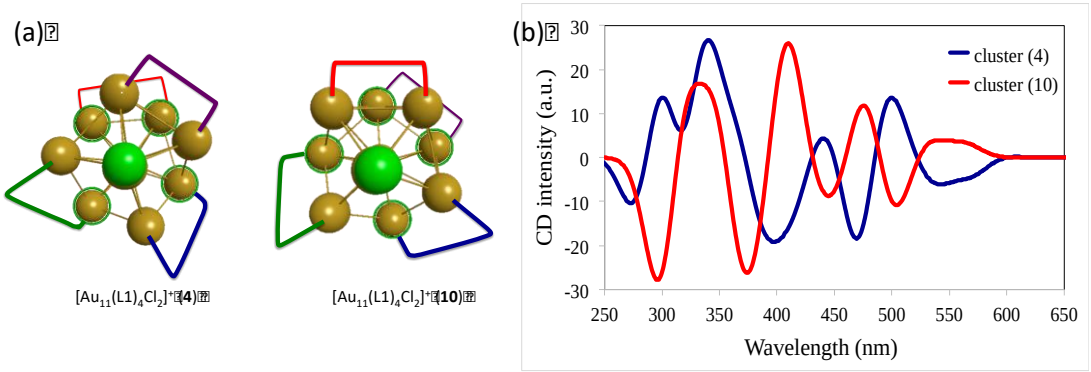

Additionally, interesting results were observed regarding the connectivity of the bidentate ligands around the undecagold core. The geometry of the $[Au_{11}(S–L1)_4Cl_2]^+$ (**4**) cluster was taken as a basis for a new structure $[Au_{11}(S–L1)_4Cl_2]^+$ (**10**). In creating this cluster, first the *y* Cartesian coordinates for gas phase structure (**4**) were multiplied by –1, yielding a

$[Au_{11}(R\text{–L1})_4Cl_2]^+$ cluster. Then, the *R*–L1 ligands in this complex were substituted by *S*–L1 to form a new cluster $[Au_{11}(S\text{–L1})_4Cl_2]^+$ (**10**) (**Figure 3–13a**). Subsequently, the geometry of this new structure (**10**) was optimized in the gas phase. The obtained structure (**10**) is 2.6 kcal/mol higher in energy than structure (**4**) in the gas phase. Thus, the undecagold core in the complex $[Au_{11}(S\text{–L1})_4Cl_2]^+$ (**10**) has a structure related to the core of the $[Au_{11}(R\text{–L1})_4Cl_2]^+$ enantiomer, but it is stabilized by *S*–L1 ligands. In consequence, the gold core of cluster $[Au_{11}(S\text{–L1})_4Cl_2]^+$ (**10**) is an approximate mirror image of the gold core of cluster $[Au_{11}(S\text{–L1})_4Cl_2]^+$ (**4**) (**Figure 3–13a**). It is well known that the CD spectra of enantiomeric pairs (R/S–ligands) are mirror images of each other. In our case we have two clusters (**4**) and (**10**) with *S*–ligands. However, the calculated CD spectrum of the $[Au_{11}(S\text{–L1})_4Cl_2]^+$ (**10**) cluster is an approximate mirror image of the $[Au_{11}(S\text{–L1})_4Cl_2]^+$ (**4**) cluster in the region with wavelengths above 350 nm (**Figure 3–13b**). It was shown earlier that CD spectra in the 350–700 nm region for the undecagold systems protected by DIOP or L1 model ligands occur due to electronic transitions within the Au_{11}^{3+} gold core framework only. So, the CD signals in this spectral region will be determined essentially by the structure of the metal core, and the mirror image CD signals can be correlated to the essentially mirror image cores present in clusters (**4**) and (**10)**. We can thus conclude, that the ligand arrangement can determine the preferred structural deformations of the gold core, and then the gold core structure defines the intensity and sign of the CD spectrum in the region above ~350 nm.

Conclusion

To contribute to an understanding of the origin of chirality and the differences in chiroptical activity of gold clusters stabilized by different phosphine ligands, we examined the optical properties of undecagold (Au_{11}^{3+}) and octagold (Au_8^{2+}) clusters protected by bisphosphine–ligands of different nature. The chiroptical properties of $[Au_{11}(BINAP)_4Cl_2]^+$, $[Au_{11}(DIOP)_4Cl_2]^+$, $[Au_8(BINAP)_3(PPh_3)_2]^{2+}$, and $[Au_8(DIOP)_3(PPh_3)_2]^{2+}$ clusters were investigated with density functional theory (DFT) and time–dependent density functional theory (TDDFT). To reduce the size of the calculated complexes, the ligands BINAP and DIOP were substituted with model ligands: BINAP was simulated by the L2 ligand (1,4-bisdiphosphino-1,3-butadiene) and DIOP was modeled by the L1 ligand (1,4-bisdiphosphinobutane). Model

clusters $[Au_{11}X_4Cl_2]^+$ and $[Au_8X_3(PH_3)_2]^{2+}$ (X = L1, L2) were considered for simulation of the experimental systems.

The obtained results showed that the shapes of the octa– and undecagold cores in the model clusters are similar to the gold cores of the crystal structures. Theoretical optical absorption and CD spectra of the model clusters are in good agreement with experimental data. For both octa– and undecagold clusters, CD signals are much weaker for systems stabilized by L1 ligands (model ligand for DIOP, which contains only single bonds) than those for systems with L2 ligands (model ligand for BINAP, which contains double bonds). Tsukuda and co–workers observed similar phenomena for gold clusters protected by DIOP and BINAP ligands.[40, 41] Moreover, the calculated spectra exhibit CD spectral shapes very close to experimental CD. However, the simulated spectra are redshifted by up to 85 nm with respect to the empirical data.

Three main hypotheses to explain the different chiroptical activity of the $[Au_{11}(BINAP)_4Cl_2]^+$, $[Au_{11}(DIOP)_4Cl_2]^+$ and $[Au_8(BINAP)_3(PPh_3)_2]^{2+}$, $[Au_8(DIOP)_3(PPh_3)_2]^{2+}$ pairs of clusters were suggested: (i) the flexible nature of the Au_{11}^{3+} gold core can lead to deformation inside the gold core due to ligation that can be a source of the different CD activity; (ii) the nature of the ligands, specifically the presence of double bonds, can be a reason for the dramatic difference in the chiroptical activity of organometallic clusters; and (iii) in the case of the undecagold clusters, chlorine atom positions can also affect the CD intensity. The results showed that the gold core geometry deformation due to ligation and the nature of ligand play the most important roles in the chiroptical activity of the gold clusters considered in this work.

Additionally, it was shown that connectivity of ligands determines the gold core structural geometries and the ligands themselves mainly affect the high-energy region of the CD spectra, whereas the gold core itself yields a significant effect on the shape and sign of the CD spectra in the low-energy region with wavelengths above ~350 nm.

Acknowledgement

This material is based on work supported by the National Science Foundation under Grant CHE-1507909. The computing for this project was performed on the Beocat Research Cluster at Kansas State University, which is funded in part by NSF grants CNS-1006860, EPS-

1006860, and EPS-0919443. The authors are grateful to Prof. Tatsuya Tsukuda (University of Tokyo) for interesting discussions and for providing experimental spectral data.

Chapter 4 - Time–Dependent Density Functional Theory Investigation of the Electronic Structure and Chiroptical Properties of Curved and Helical Silver Nanowires

Natalia V. Karimova, Christine M. Aikens, *J. Phys. Chem. A* **2015**, 119, 8163–8173

Abstract

Time–dependent density functional theory methods are employed to examine the evolution of the absorption and circular dichroism (CD) spectra of neutral bare silver helical nanostructures as a function of their geometrical parameters. Calculations of excited states to determine optical absorption and CD spectra were performed using the SAOP/TZP level of theory. In our model, the geometry of the helical silver chain is dependent on the Ag−Ag−Ag bond angle and the Ag−Ag−Ag−Ag dihedral angle. The influence of different geometrical structures on the optical absorption and CD spectra were studied for helical and planar Ag_8. Silver nanowires Ag_n (n = 4, 6, 8, 10, 12) were examined to determine the effect of the helical chain length on the electronic properties. The results show that when the metal atomic chain loses planarity, strong CD signals arise; the intensities of the CD peaks for these structures are strongly affected by the shape and length of the silver nanowires. The theoretically predicted CD spectra of the nonplanar Ag_4 and Ag_6 model systems show good agreement in spectral shapes and reasonable agreement in peak locations compared to experimental data for silver−DNA clusters. However, the theoretical and experimental results for the longer Ag_{12} wire show larger differences in the peak locations, which could potentially be caused by effects such as the presence of DNA and cationic silver atoms in the experimental system.

Introduction

Metal nanoparticles with a chiral geometry exhibit unusual optical properties such as a strong circular dichroism (CD) signal in the visible or near infrared (IR) region, whereas natural helical molecules such as peptides and DNA show CD response in the (UV) or IR range; this feature makes DNA-metal nanoparticle hybrids very useful for the creation of new materials.[71-73] The most popular methods of synthesis of chiral nanoparticles are based on the assistance of

biological molecules such as peptides and DNA molecules.[70] The interaction of biomolecules with metal nanoparticles can produce plasmonic helical metal nanoparticle assemblies, in which metal clusters are nested on the outside of the biomolecule and arrange in external helical chains around these peptide or DNA molecules.[70, 72, 74, 75] Gold and silver nanoparticle structures with a helical arrangement are a very interesting area of research. These assemblies have potential applications in photonics and as optical polarizers, sensors, catalysts, *etc*. The CD spectra for these synthetic chiral plasmonic gold, silver, and gold/silver peptide–[73] and DNA–based[72, 74, 75] nanostructures show a bisignate shape. The theoretical investigation of these structures demonstrates that helix pitch, helix radius, nanoparticle size, interparticle distance, composition of a cluster, and the number of metal particles in a helix chain can have an effect on the optical properties of these structures.[72, 73, 178-184]

Another very interesting type of metal – biomolecule clusters are DNA-stabilized metal clusters (M:DNA, where M = Au and Ag), where a few to tens of metals atoms are located inside the DNA molecule, between two polynucleotide strands.[76-86] These DNA-templated noble metal clusters are a fluorescent species. In particular, Ag:DNAs nanoclusters have an extremely wide range of emission colors.[81-84] Experimental studies[81, 83-85] have shown that the fluorescent Ag:DNA clusters contain less than 20 silver atoms, but some metal clusters can produce both dark and fluorescent active DNA-stabilized complexes. Knowledge of what factors determine the colors of Ag:DNA complexes is significant for strategic development of sensing and signaling schemes. Schultz and co-workers[81] used negative ion, high resolution mass spectrometry of compositionally pure solutions to identify the silver cluster charge (Q_{cl}) and total number of silver atoms (N_{Ag}) in fluorescent Ag:DNAs. Furthermore, those authors showed that silver nanoparticles in the DNA - stabilized clusters have a rod-like shape (not spherical or planar). According to their results, Ag:DNA clusters exhibit charges from Q_{cl} = −6e to −13e with N_{Ag} = 10 to 24 silver atoms in each cluster. In addition, the dependence of the excitation and emission wavelength on the number of neutral silver atoms provided evidence that the cluster structure of Ag:DNA complexes is rod-shape (a neutral, rod-like chain of silver atoms surrounded by a base-bonded Ag frame, such as the pictures shown in **Figure 1**). The length of the neutral, rod-like chain in the system appears to be the major control for the color of Ag:DNA.

Figure 4–1. Examples of the Ag:DNA structures. Rod-like, neutral clusters (gray) are shown attached to DNA bases via peripheral Ag□□(blue) in tetramer (b) and trimer (c) arrangements.

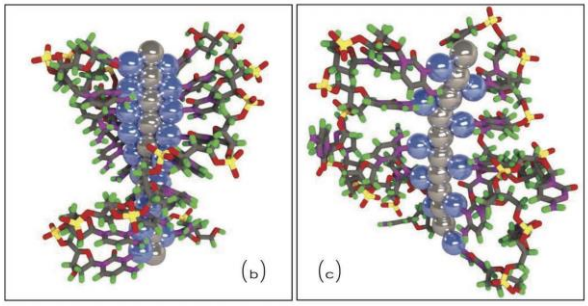

*Adapted with permission from Ref. [81]. (Copyright 2013 Wiley Online Library)

Copp and co-workers then extended this work by focusing on how the determination of magic numbers in Ag:DNA fluorescent clusters leads to "magic colors".[86] In addition, they performed molecular dynamics calculations to simulate the structure of these complexes.

Figure 4–2. Peak fluorescence wavelength histogram for Ag:DNAs.

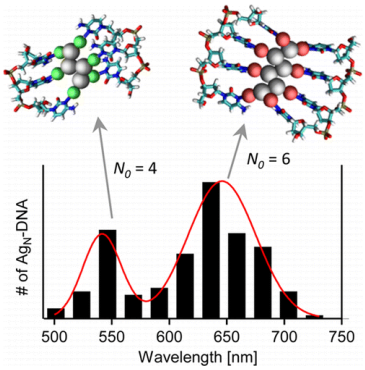

*Reproduced from Ref. [86]. (Copyright 2014 American Chemical Society).

They found that the color combinations of Ag:DNA clusters with even numbers of neutral silver atoms are different from magic numbers for spherical clusters: for DNA-stabilized silver clusters, the magic numbers of neutral Ag atoms are 4 and 6 (**Figure 4–2**), not 2 and 8 as predicted by the spherical “superatom” model. In addition, peak fluorescence wavelength is dependent on neutral silver atom number. The existence of such “magic colors” has implications for the palette available to colorimetric assays and could be exploited in sensing applications where transitions between green and red emissive clusters act as signals for desired processes. Molecular dynamics simulations using AMBER showed that Ag:DNA complexes may exhibit curved shapes due to Coulomb interactions, and addition or subtraction of silver ions near the neutral silver chain can modify the cluster shape.

The chiral structures of DNA-stabilized fluorescent silver clusters have also been studied by using the experimental CD and optical absorption spectroscopy and a theoretical time-dependent density functional theory (TDDFT) approach.[91] In this work, neutral and cationic structures Ag_n:DNAs (n = 4–12) were considered. For all these structures the CD spectra exhibit a low-energy positive peak and a highly anisotropic negative dichroic peak. Experimental and theoretical results are in good agreement.

In this work, we used time-dependent density functional theory to examine the evolution of the absorption and circular dichroism spectra with geometrical parameters such as bond and dihedral angles for neutral silver nanowires of helical shape. When a metal atomic chain loses a planar structure and forms a helical structure, strong CD signals arise. The intensity of the CD peaks for these structures are strongly affected by the shape of the helix.

Computational Method

We investigated the electronic structure, optical absorption, and circular dichroism spectra of neutral planar (curved) and nonplanar (helical) silver wires Ag_n (n = 4, 6, 8, 10, 12). The nonplanar silver chains complete a full turn around a cylindrical surface only with certain dihedral (Ag−Ag−Ag−Ag) and bond (Ag−Ag−Ag) angle combinations. According to the definition of a helix,[185] a curve is a cylindrical helix if and only if the ratio of torsion angle to curvature is constant. Thus, in the present paper all modeled nonplanar silver wires will be called helices or helical structures because they completely satisfy these conditions, notwithstanding that some of them do not show a full helical turn.

For systems with eight silver atoms in the chain, we considered planar and helical Ag8 structures with different combinations of dihedral (0−70°) and bond (180−90°) angles. Clusters Ag_4, Ag_6, Ag_{10}, and Ag_{12} have been considered only with 170° and 160° Ag−Ag−Ag bond angles and a dihedral Ag−Ag−Ag−Ag angle of 10°. In this paper, structures are denoted B-D, where B is the Ag−Ag−Ag bond angle and D is the Ag−Ag−Ag−Ag dihedral angle. The Ag−Ag bond length is constant for all calculations and is set equal to 2.7 Å. Geometries of these model structures were not optimized because without ligands the curved structure is not a local minimum. The coordinates of the model structures are presented in the **Appendix B**.

The calculated optical absorption spectra for the planar and helical silver chains considered show that the first three peaks are very sensitive to the geometrical parameters of the

structure, whereas the high-energy region is not significantly affected by changing the geometry of the systems. Thus, our investigation will be primarily focused on the first three peaks in the low energy region of spectra.

The Amsterdam Density Functional (ADF) program[158] was used for all calculations. Scalar relativistic effects were included by utilizing the zero-order regular approximation (ZORA).[173] Time-dependent density functional theory (TDDFT) was employed to calculate excited states to determine optical absorption and circular dichroism (CD) spectra. For these calculations the asymptotically correct SAOP functional was used.[186] This functional was combined with a triple-ζ plus polarization (TZP) Slater type basis set. The SCF convergence is tightened to 10^{-8}; the tolerance was set to 10^{-8}; and the orthonormality was set to 10^{-10}. The first 200 dipole-allowed transitions were evaluated for each optical absorption and CD spectrum.

The process of single–photon absorption is characterized by a transition dipole moment (μ_{ij}) and oscillator strength (f_{ij}).[151, 187] These two characteristics enable us to predict which excited state transitions are the most probable. The probability of absorption is proportional to the transition dipole moment, and the strength of an electronic transition (intensity of a transition) can be express in terms of the oscillator strength.

The circular dichroism spectroscopy is used extensively to study chiral molecules of all types and sizes. These species show a difference in absorption of the left and right circularly polarized light. The simulation of the CD spectra is based on the relations:[159, 160]

$$\Delta e = 4\alpha \sum_m R_m E_m \sigma_m(E)$$

$$\alpha = \frac{4\pi N_A}{3\ln(10)10^3}\frac{2\pi}{hc}$$

$$\sigma_m(E) = \frac{1}{\sigma\sqrt{2\pi}}\exp\left(-\frac{1}{2\sigma^2}(E - E_m)^2\right)$$

where Δε is molar circular dichroism or molar differential dichroic absorptivity in units of $L\cdot mole^{-1}\cdot cm^{-1}$, α is a set of constants, N_A is Avogadro's number in units of $mole^{-1}$, h is the Planck constant in units of J·s, c is the speed light in units of cm/s, E is the energy of the incident light in eV, E_m is the excitation energy to state M in eV, $\sigma_m(E)$ is the Gaussian band shape factor and σ is the exponential half-width (we used $\sigma = 0.2$ eV), R_m is rotatory strength in units of $esu^2\cdot cm^2$. Rotatory strength is the important property that allows a quantitative

description of CD spectra.

In literature CD spectra can be expressed by two terms: molar circular dichroism (Δε) and molar ellipticity [Θ]. Molar circular dichroism is related to molar ellipticity by the following equation[188]

$$[Q] = 3298.2D\epsilon$$

where [Θ] is molar ellipticity, expressed in deg·cm^2·dmole^{-1}.

Results and Discussion

Planar Structures

To show how bond angle changes affect the optical properties of silver nanowires, we first calculated absorption and circular dichroism spectra for a linear chain of eight silver atoms and compared results with data for other planar Ag_8 structures. These structures are constructed by decreasing the Ag−Ag−Ag bond angle in the linear chain from 180° to 140°, whereas the dihedral angle Ag−Ag−Ag−Ag was kept constant at 0° (**Figure 4–3**).

Figure 4–3. Structures of planar Ag_8 with bond angles 180°, 170°, 160°, 150° and 140° and their absorption spectra

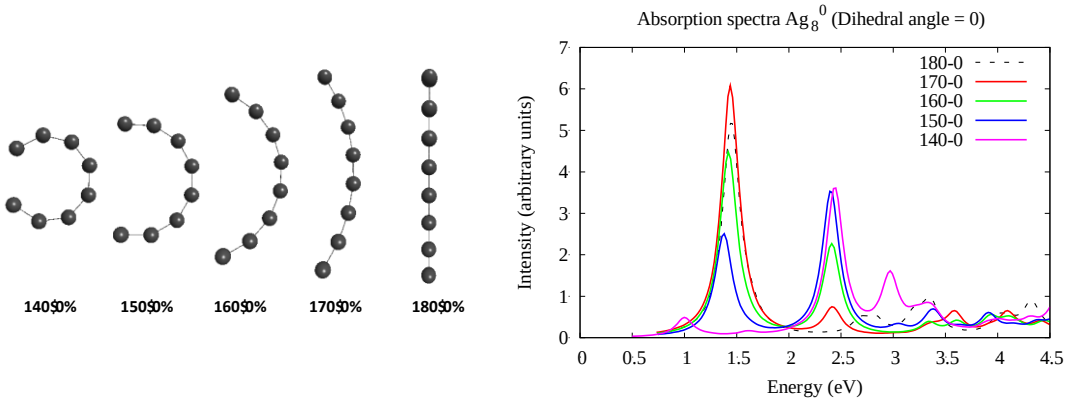

The excitation spectra of neutral and charged linear atomic silver and gold chains have been studied by Guidez and Aikens using the SAOP/DZ and BP86/DZ levels of theory.[189] These linear clusters exhibit two strong peaks: a longitudinal peak which is located in the low-energy region of the spectrum and arises from the highest occupied molecular orbital to lowest unoccupied molecular orbital (HOMO−LUMO) transition, and a transverse peak which occurs in the high-energy region of the spectrum.[189] In the current research, the calculated optical absorption spectrum for the linear Ag_8 structure **180-0** shows the same characteristics as

described in ref.[189]. In the low energy region, the extinction spectrum has one narrow and strong (longitudinal) peak at 1.45 eV with an oscillator strength of *f*=1.61. This peak arises primarily from the HOMO to LUMO electronic transition (**Figure 4–4**), where the HOMO–LUMO gap is 0.63 eV.

Figure 4–4. Kohn-Sham orbitals for linear structure 180-0 and planar structure 140-0

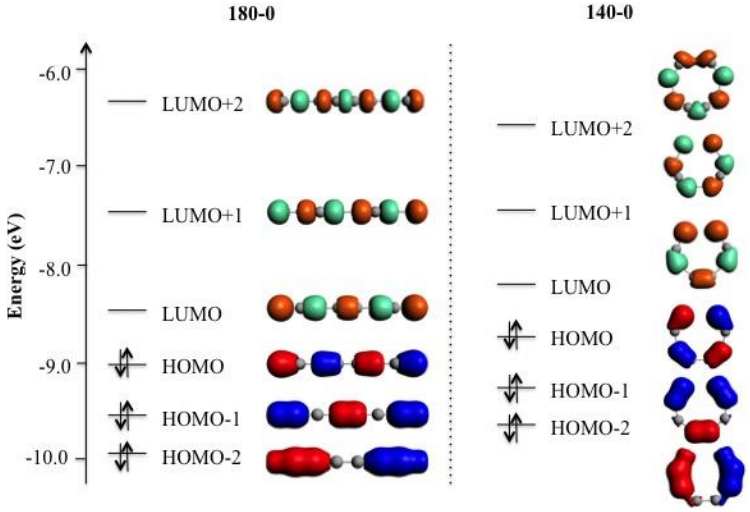

Absorption spectra for planar structures with Ag−Ag−Ag angles of 170°, 160°, and 150° exhibit two peaks, whereas the spectrum for the system with 140° angles has three relatively strong peaks. The lowest-energy peak shifts to the red and loses intensity as the bond angle becomes smaller. This peak is located at 1.44 (f = 1.87), 1.42 (f = 1.39), 1.38 (f = 0.77), and 0.99 (f = 0.14) eV for the structures with 170°, 160°, 150°, and 140°, respectively. The transition responsible for it corresponds to a HOMO → LUMO transition (**Figure 4–4**), so this is the same as for the linear chain. For structures with angles 170°, 160°, and 150°, the HOMO−LUMO gaps are 0.54 eV, whereas the gap for the system with 140° angles equals 0.43 eV.

A second peak appears for structures **170-0**, **160-0**, **150-0**, and **140-0** and is located at 2.41 (f = 0.13), 2.41 (f = 0.61), 2.40 (f = 1.09), and 2.44 eV (f = 1.10), respectively. In comparison with the first peak, this second one does not shift significantly in energy, and it grows dramatically with decreasing bond angle. This peak arises from HOMO → LUMO+1 and HOMO−1→ LUMO transitions, which are forbidden transitions for the linear wire that become allowed with the loss of linearity. A third peak at 2.97 eV (f = 0.43) can be observed for the system with Ag−Ag−Ag angles of 140°. Electron transitions for this peak are HOMO−1 →

LUMO+1, HOMO→ LUMO+2, and HOMO−2→ LUMO. Overall, the absorption spectra exhibit 2−3 strong peaks that are very sensitive (either in energy or in oscillator strength) to the changing of the bond angle.

Circular dichroism spectra have been calculated for all planar structures. As expected, the CD signals for the planar structures are zero.

Helix Structures

Dihedral Angle 10°. The first helical structures that we consider in this work are systems with a dihedral angle of 10° and different bond angles. Helical structures can be constructed with bond angles less than 140°, which is impossible with planar structures because a cyclic cluster is generated at 135°. Nonetheless, we still need to control the distance between loops (pitch), which cannot be less than the length of the bond between silver atoms in the chain (2.7 Å). In the system with a dihedral angle of 10°, the minimal possible bond angle is 130°. Therefore, we consider helices with a dihedral angle of 10° and bond angles of 170°, 160°, 150°, 140°, and 130°, denoted **170-10**, **160-10**, **150-10**, **140-10** and **130-10**, respectively (**Figure 4–5**).

Figure 4–5. Structures, absorption spectra, and CD spectra of helical Ag_8 with a dihedral angle of 10° and bond angles from 170° to 130°

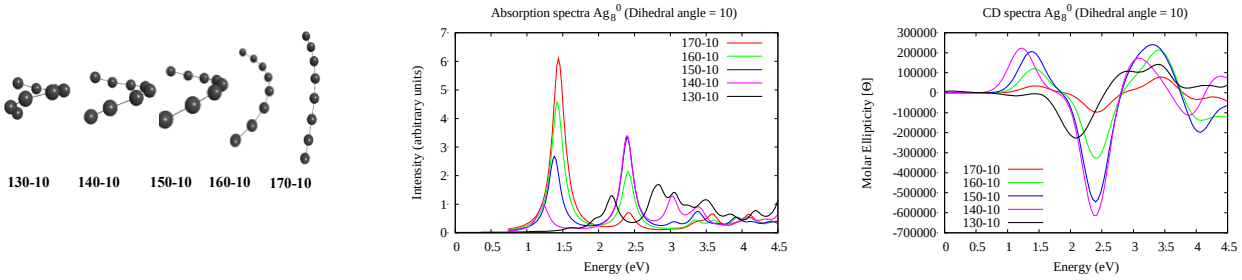

The calculated absorption spectra for **170-10**, **160-10**, **150-10,** and **140-10** look like absorption spectra for the planar analogs: structures with bond angles equivalent to 170°, 160°, and 150° show two peaks, and the system with angle 140° has three peaks. **Tables 4–1** and **Table 4–1** show the energies of these peaks, as well as absorption and circular dichroism spectral data including oscillator strength, molar ellipticity, and rotatory strength.

Table 4-1. Optical absorption and CD spectral data of Ag_8 nanowires: peak energy (E, eV), oscillator strength (*f*), molar ellipticity ($[\Theta]\cdot10^{-5}$, deg·cm^2·dmole^{-1}), and rotatory strength (R_m, 10^{-40} esu^2 ·cm^2)

	First peak				Second peak				Third peak			
	E, eV	*f*	$[\Theta]\cdot10^{-5}$	R_m	E, eV	*f*	$[\Theta]\cdot10^{-5}$	R_m	E, eV	*f*	$[\Theta]\cdot10^{-5}$	R_m
170-10	1.44	1.88	0.35	84.4	2.41	0.12	-0.97	-92.53	3.00	0.007	0.2	15.2
160-10	1.42	1.42	1.20	296.2	2.41	0.58	-3.28	-440.28	3.02	0.009	0.9	66.3
150-10	1.38	0.82	2.07	525.5	2.40	1.02	-5.46	-803.28	3.04	0.07	1.7	146.8
140-10	1.22	0.29	2.23	636.9	2.40	1.06	-6.14	-899.24	3.03	0.35	1.9	168.9

For structure **170-10**, the absorption spectrum exhibits the strong first peak at 1.44 eV and a very weak second peak at 2.41 eV with oscillator strengths of 1.88 and 0.12, respectively (**Table 4–1**). The first peak is predicted to arise primarily from transitions out of the HOMO into the LUMO (with a contribution to the transition dipole moment of 7.671). The second peak is composed of several transitions including HOMO → LUMO+1 and HOMO−1 → LUMO with contributions to the transition dipole moment of 1.000 and 0.657, respectively.

When the Ag−Ag−Ag angle is reduced to 160° (**160-10**), the intensity of the two first peaks changes with respect to those of **170-10**. We can observe a redshift of 0.02 eV for the first peak. The oscillator strength for the first peak decreased slightly, whereas the intensity of the second peak increased by ~4 times. Transitions that are responsible for these peaks are the same as in **170-10**, but contributions to the transition dipole moment changed. For the first peak, the contribution arising from HOMO → LUMO decreased and is now equal to 6.732. For the second peak, contributions of the HOMO → LUMO+1 and HOMO−1 → LUMO transitions increased and are equivalent to 2.263 and 1.436, respectively.

The optical absorption spectrum of structure **150-10** shows that the first peak is located at 1.38 eV and the second at 2.40 eV. The first peak has become smaller with respect to **160-10**, and the oscillator strength decreased by ~2 times (**Table 4–1**). The contribution to the transition dipole moment from the HOMO → LUMO transition for this peak is 5.2721. The second peak continues to become stronger and the oscillator strength increases by ~2 times with respect to **160-10** (**Figure 4–5**). The second peak is a composition of transitions HOMO → LUMO+1 and HOMO−1 → LUMO. Contributions to the transition dipole moment are 3.033 and 1.964, respectively.

For structure **140-10**, the first peak is very weak, with an oscillator strength of only 0.29, which is decreased by ~2 times with respect to **150-10**. This peak also redshifts by 0.16 eV with respect to **150-10**. The oscillator strength of the second peak has grown to 1.06, which is not greatly different than *f* for the **150-10** structure. The transitions that are responsible for these The transitions that are responsible for these peaks are the same as in the structure with a bond angle of 150°. The third peak at 3.00 eV, which was very weak in previous helical structures, becomes stronger (*f*=0.35) in **140-10** (**Table 4–1**). This peak arises from the HOMO → LUMO+2, HOMO-2→ LUMO, and HOMO-1 → LUMO+1 transitions.

Circular dichroism spectra were calculated for all **170-10**, **160-10**, **150-10,** and **140-10** structures by the TDDFT method (**Figure 4–5**). The CD signals arise from the same transitions as those seen in the UV−vis absorption spectrum. For the first peak, the results show that the intensities of the CD signals increased with decreasing Ag−Ag−Ag bond angle (**170-10** > **160-10** > **150-10 > 140-10**) (**Table 4–1**, **Figure 4–5**). In contrast, the optical absorption spectra exhibit the opposite tendency, and the intensity of the first peak decreases as the Ag−Ag−Ag bond angle decreases (**170-10** > **160-10** > **150-10 > 140-10**). The values of molar ellipticity [Θ] for the first peak are $0.35 \cdot 10^5$, $1.2 \cdot 10^5$, $2.1 \cdot 10^5$, and $2.2 \cdot 10^5$ deg·cm^2·dmol^{-1} for **170-10**, **160-10**, **150-10,** and **140-10**, respectively. Therefore, structure **170-10** shows the strongest first absorption peak and very weak response in the CD spectrum, whereas structure **140-10** has the smallest first absorption peak and the strongest peak in the CD spectrum. The first CD peak arises from the HOMO → LUMO transition and has a moderately positive rotatory strength, which increases with decreasing of the Ag− Ag−Ag angles from 170° to 140° (**Table 4–1**). The second CD peak has a negative rotatory strength for all structures. The intensities of this peak in the optical absorption and CD spectra increased with decreasing Ag−Ag−Ag bond angle (**170-10** < **160-10** < **150-10 < 140-10**). The molar ellipticities [Θ] of the second peak are $-0.9 \cdot 10^5$, $-3.3 \cdot 10^5$, $-5.5 \cdot 10^5$, and $-6.1 \cdot 10^5$ deg·cm^2·dmole^{-1} for **170-10**, **160-10**, **150-10,** and **140-10**, respectively. In addition, this peak is much stronger than the first (**Table 4–1**). The third peak, which is not noticeable in the absorption spectrum, appears with strong positive rotatory strength in the CD spectrum for structures **150-10** and **140-10**. The molar ellipticities [Θ] of this peak are $1.7 \cdot 10^5$ and $1.9 \cdot 10^5$ deg·cm^2·dmole^{-1} for **150-10** and **140-10.** The third peak appears

from the HOMO → LUMO+2, HOMO-2→ LUMO, and HOMO-1 → LUMO+1 transitions. Overall, the molar ellipticity and rotatory strength increase in the order 170°<160°<150°<140°.

Table 4-2. Spectral data of structure 130-10 peak energy (eV), oscillator strength (*f*), molar ellipticity ([Θ]·10^{-5}, deg·cm^2·dmole^{-1}), and rotatory strength (R$_m$, 10^{-40} esu^2 ·cm^2).

# Peak	E, eV	Absorption spectra		Circular Dichroism spectra	
		Intensity	*f*	[Θ]·10^{-5}	R$_m$
1	1.60	0.17	0.03	-0.2	-15.78
2	1.95	0.52	0.08	-2.1	-199.96
3	2.18	1.28	0.29	-2.1	-388.62
4	2.76	1.51	0.24	0.9	30.45
5	2.85	1.70	0.31	1.1	77.84
6	3.06	1.41	0.30	1.1	37.98

Figure 4–6. Absorption and CD spectra of helical Ag$_8$ (structure 130-10)

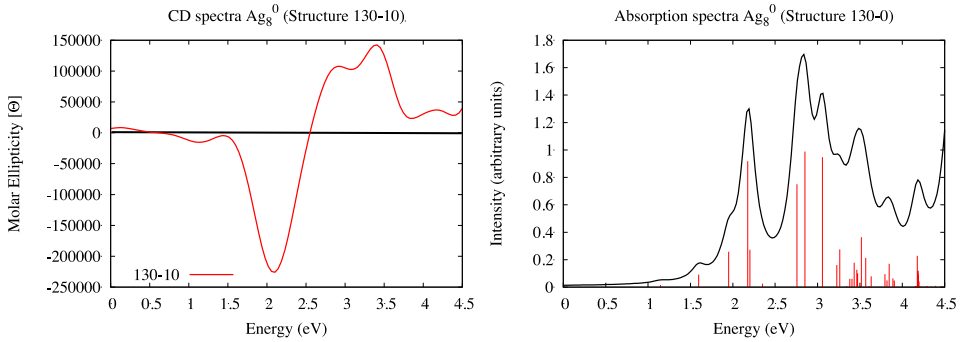

Figure 4–7. Kohn-Sham orbitals for helical structures 140-10 and 130-10

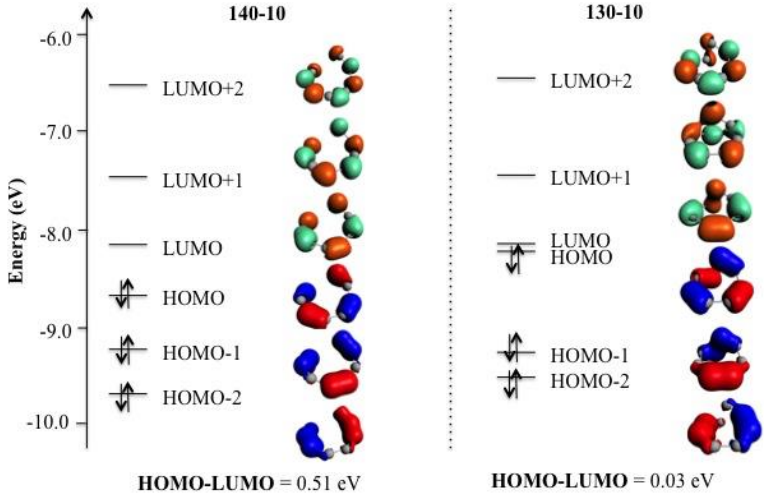

The **130-10** spectrum appears qualitatively different than the others (**Figure 4–6**). This spectrum is less intense and blueshifted, and a great number of transitions happen in the high-

energy region (>4.5 eV). The HOMO → LUMO transition, which was responsible for the first peak in structures **170-10**, **160-10**, **150-10,** and **140-10**, disappeared. Instead, the absorption spectrum and CD spectrum show a weak peak at 1.60 eV, which is composed primarily of HOMO−2 → LUMO and HOMO → LUMO+2 transitions. The next two peaks are located at 1.95 and 2.18 eV, and their oscillator strengths are 0.08 and 0.29, respectively (**Table 4–2**). These two peaks are responsible for the negative peak in the CD spectrum. These two peaks arise from the same transitions: HOMO−1 → LUMO, HOMO → LUMO+1, HOMO−2 → LUMO+1, and HOMO → LUMO +3. The next positive CD peak is a combination of three peaks at 2.76, 2.85, and 3.06 eV, which arise from HOMO−3 → LUMO+1, HOMO → LUMO+2, HOMO-1 → LUMO+1, and HOMO-2 → LUMO transitions. This dramatic difference in the optical properties of structure **130-10** and those of the corresponding structures with bond angles 140°, 150°, 160° and 170° can be attributed to a different electronic structure. A helix with dihedral and bond angles of 10° and 130° has a very compact structure: the pitch is almost equivalent to a metal bond length of 2.7 Å, which leads to the overlap of some of the silver orbitals (**Figure 4–7**). The HOMO-LUMO orbitals are very close to each other in the **130-10** structure; the HOMO-LUMO gap is equivalent to 0.03 eV.

Dihedral Angles 20°−70°. To understand how the value of the dihedral angle affects the optical properties of silver helices, we considered Ag8 nanowires with Ag−Ag−Ag−Ag dihedral angles from 20° to 70° and all possible Ag−Ag−Ag bond angles. The minimal bond angles which we considered are Ag− Ag−Ag = 130° for structures with a dihedral angle of 20°, Ag−Ag−Ag = 120° for structures with a dihedral angle of 30°, and Ag−Ag−Ag = 110° for systems with dihedral angles of 40°− 70°. The structures with smaller bond angles are very compact and have different electronic structures; the absorption and CD spectra of these systems are weak and look qualitatively different from the spectra with larger bond angles (see **Appendix B**).

The optical absorption spectra for the systems with dihedral angles of 20°−70° have a shape that is similar to that of the spectra of the systems with dihedral angles of 10° considered above. Our results show that the geometrical structure of the helix has the strongest effect on the location and intensity of the first peak in the spectrum. As shown in **Figure 4–8**, all considered structures with a bond angle of 170° exhibit a first peak with almost the same energy near 1.44−1.46 eV. The oscillator strengths of these structures increase as the dihedral angle

increases, and the difference between the excitation energy for structures **170-10** and **170-70** is 0.14 eV. Further decreasing of the bond angle in our systems shifts the first peak to the red region, and the oscillator strength decreases significantly. The dihedral angle of the helix structure also has an effect on the first absorption peak: the low-energy peak shifts to the blue and increases intensity as the dihedral angle becomes larger (**Figure 4–8**).

Figure 4–8. The effect of Ag-Ag-Ag bond angle on the peak location and oscillator strength of the first three peaks of the absorption spectra for silver helixes with dihedral angles 10° - 70°

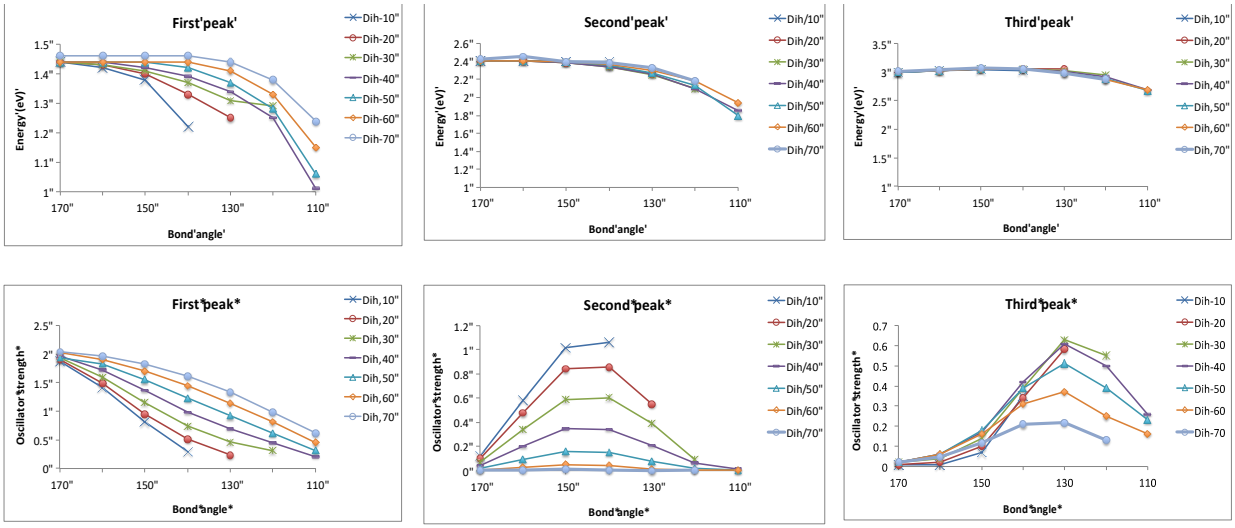

The energy of the second and third peaks is not significantly dependent on the dihedral angle of the silver helical structure, whereas the oscillator strength dramatically changes as this Ag− Ag−Ag−Ag angle increases. In contrast to the dihedral angle, the bond angle affects both location and intensity of these peaks. For structures with a bond angle of less than 150°, the second and third peaks shifted to the red for all dihedral angles.

The intensity of the second peak decreased as the dihedral angle became larger, and for the helix with a dihedral angle of 70°, the second peak disappeared. The oscillator strength for the second peak as a function of the bond angle has a maximum around 140°−150° for all dihedral angles; after 150°, the intensity of the peak decreases substantially. The systems with the strongest third peak are structures **130-20**, **130-30**, and **130-40** with a bond angle of 130° and dihedral angles of 20°− 40°, and the oscillator strength is 0.58−0.63 (see **Appendix B**). Further increasing of the dihedral angle and the increasing of the bond angle make the third peak less intense.

Thus, calculated absorption spectra for all considered structures (**Figure 4–8**) demonstrate interesting dependencies on the values of bond and dihedral angles. The first peak is the most sensitive to the changes of these parameters; the bond and dihedral angles strongly affect the peak location and intensity. Decreasing of the bond angle from 170° to 110° and dihedral angle from 70° to 10° gives us a shift of the first peak to the red region. The intensity of the first peak decreases with decreasing bond and dihedral angles. The second and third peak locations are not sensitive to the changes in the dihedral angle, whereas the decreasing of the bond angles from 170° to 110° redshifts them. The second peak intensity increased dramatically with decreasing dihedral angle from 70° to 10°, whereas decreasing the bond angle from 170° to 140° gives the maximum increase of the peak intensity, but further changes in this angle from 140° to 110° show a loss of the second peak strength. Oscillator strength values of the second peak for extreme cases with bond angles 170° and 110° are around zero. For all structures with dihedral angle 70°, the second peak is very weak and the oscillator strength does not exceed a value of 0.009; therefore, it is almost not noticeable in the absorption spectra. The third peak strength is almost the same for structures with dihedral angles 10°−40°; however, for systems with angles of 50°, 60°, and 70°, the intensity decreased (oscillator strength decreased as 10° ≈ 20° ≈ 30° ≈ 40° > 50° > 60° > 70°). The influence of bond angle on the intensity of the third peak is also shown in **Figure 4–8**. This peak becomes stronger with decreasing bond angles from 170° to 130°; after 130°, the absorption intensity decreased.

Figure 4–9. The effect of Ag-Ag-Ag bond angle on the first three peaks of the CD spectra for silver helixes with dihedral angles 10° - 70°

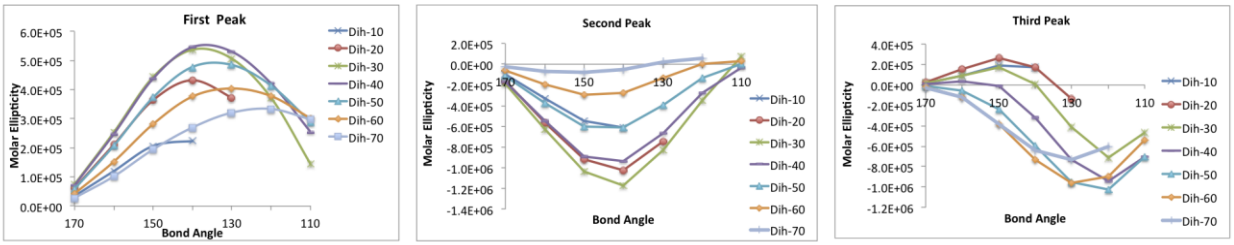

The dependence of the first three peaks of the CD spectra on the bond angle for helical structures with dihedral angles from 10° to 70° is presented in **Figure 4–9**. These results show that both the dihedral and bond angles affect the intensity of these peaks. The results for the first CD peak show that the molar ellipticity as a function of the bond angle reaches a maximum for which the location and intensity is different for each dihedral angle. For extreme cases such as structures with dihedral angles of 10° and 70°, the intensities of the first peak are similar to each

other and weaker with respect to systems with other dihedral angle values. The helical structures with dihedral angles of 10° and 70° exhibit a maximum of the first peak with bond angles of 140° and 120°, respectively. We observe the most intense signal for the first peak for the helix structures with dihedral angles of 30° and 40° with a bond angle of 140°; the molar ellipticity for these structures is equivalent to ~5.4 × 105 deg·cm2·dmol−1 (**Figure 4–9**). For all considered structures, this first peak arises from the HOMO → LUMO transition.

Unlike the absorption spectra, which indicate the absence of the second peak for structures with a dihedral angle of 70° (the oscillator strength of this peak is around zero, see **Appendix B** and **Figure 4–8**), the CD spectra detect the second peak for all calculated structures. The second CD peak has a negative rotatory strength for all calculated structures with dihedral angles of 10°−50°, whereas for systems with dihedral angles larger than 50° and bond angles less than 130°, this peak has a positive sign. The CD spectra achieve a maximum absolute value of molar ellipticity as a function of the bond angle at 140° (**Figure 4–9**); furthermore, the most intense second peak is obtained for structure **140-30**, and the molar ellipticity for it is equivalent to $11.7 \cdot 10^5$ deg·cm^2·dmole^{-1}. Electronic transitions for this peak are HOMO−1 → LUMO and HOMO → LUMO+1.

The third peak arises from HOMO → LUMO+2, HOMO− 2→ LUMO, and HOMO−1 → LUMO+1 transitions. This peak changes from a positive sign to a negative sign with the decreasing of the bond angle for structures with dihedral angles of 10°−40°; for systems with larger values of the dihedral angle, the third peak has only negative amplitude. The strongest positive third peak is observed for structure **150-20**, with the value of the molar ellipticity [Θ] for this structure corresponding to 2.6 deg·cm^2·dmole^{-1}. The most negative values of this peak were obtained for structures with a dihedral angle of 50° and a bond angle of 120°, and the molar ellipticity values for structure **120-50** are equal to $-10.2 \cdot 10^5$ deg·cm^2·dmole^{-1}, respectively.

Thus, the geometrical structure of the helix has the strongest effect on the location and intensity of the first peak. Decreasing the bond angle shifts the first peak to the red and the intensity of the absorption peak decreases. The energies of the second and third peaks are not significantly dependent on the dihedral angle of the silver helical structure, whereas the oscillator strength dramatically changes.

In addition, these results show that CD spectra are significantly dependent on the geometry of the cluster. The first peak has positive rotatory strength for all structures. The molar ellipticity as a function of the bond angle reaches a maximum for which the location and intensity is different for each dihedral angle. Extreme structures with dihedral angles of 10° and 70° have the weakest intensities with respect to systems with other dihedral angles, whereas the helices with Ag−Ag−Ag−Ag angles of 70° show the strongest first peak in the optical absorption spectra. The oscillator strength of the first peak decreased evenly with decreasing values of bond and dihedral angles and has a maximum of intensity for structure **170-70**, whereas the rotatory strength for this structure is the smallest; therefore, it has poor CD response. The second peak has a negative rotatory strength for all structures except clusters with dihedral angles of 60° and 70° (peak changes from negative sign to positive with decreasing bond angle). The magnitude of the third peak also changes sign from positive to negative with increasing bond angle for systems with dihedral angles less than 40°. Thus, experimentally measured CD spectra can provide information about the geometries of helical silver nanowires.

Helical silver chains Ag_n (n = 4, 6, 8, 10 and 12). The number of silver atoms in a helix chain can significantly affect the optical properties of these nanoparticles. In order to study the length dependence of the optical absorption and CD of these nanowires, TDDFT calculations have also been performed on Ag_n (n = 4, 6, 8, 10, 12) clusters with 170° and 160° Ag-Ag-Ag bond angles, 2.7 Å bond length, and a dihedral Ag-Ag-Ag-Ag angle of 10°. Furthermore, the results of calculations for nonplanar helical systems were compared with experimental data for DNA-stabilized silver clusters in the several atom size range.[91]

As shown in **Figure 4–10**, absorption spectra for helical systems Ag_4, Ag_6, and Ag_8 show only one strong peak at 2.19, 1.72, and 1.44 eV, respectively, whereas longer systems exhibit two strong peaks (1.24 and 2.12 eV in the case of Ag_{10} and 1.09 and 1.89 eV for Ag_{12}). As the number of silver atoms in the chain increases, the excitation spectrum redshifts.

Circular dichroism spectra (**Figure 4–10**) also become stronger and redshift as the particle size increases. The strongest spectrum is observed for Ag_{12}, and the weakest is observed for Ag_4. All systems exhibit a strong positive first peak. As described above, this peak arises from the HOMO−LUMO orbital transition. The HOMO−LUMO gap decreases in the order Ag_4 > Ag_6 > Ag_8 > Ag_{10} > Ag_{12} and is equivalent to 1.01, 0.70, 0.54, 0.43, and 0.37 eV, respectively. The second peak has a negative sign and appears with strong rotatory strength in

the CD spectrum for structures Ag_6, Ag_8, Ag_{10} and Ag_{12}. As discussed for Ag_8, this peak arises from the HOMO → LUMO +1 and HOMO−1 → LUMO transitions that are forbidden for perfectly linear wires. For the smallest system Ag_4, this peak is present in the absorption spectra at 3.59 eV; however, the calculated CD spectrum does not show anything in this area. The third CD peak is located in the higher-energy region, has a negative rotatory strength for helices Ag_4 and Ag_6, and arises from the same transitions as the second peak (HOMO → LUMO+1 and HOMO−1 → LUMO). At the same time, the largest nanowires (Ag_8, Ag_{10} and Ag_{12}) exhibit a third peak with positive sign. This peak arises from transitions HOMO → LUMO+2, HOMO−2 → LUMO, and HOMO−1 → LUMO +1 for all these structures. As the bond angle decreases to 160°, the first absorption peak for all considered structures loses intensity, whereas the second and the third peaks become stronger (**Figure 4–10**). The peaks of these structures arise from the same electronic transitions described for structures with bond angles of 170°. The CD spectra for structures with the bond angles of 160° have similar shape and peak locations as spectra for systems with bond angles of 170°, whereas the CD intensities of the peaks rise rapidly. This study of the length dependence of the optical absorption and CD spectra in the bare silver helical chains Agn (n = 4, 6, 8, 10 and 12) shows that as the number of silver atoms in the chain increases, the spectrum redshifts and peak intensities become stronger.

To investigate how our model can correctly reproduce chiroptical properties of real DNA-stabilized silver clusters, we performed a comparative analysis with experimental data. Swasey and co-workers investigated chiral electronic transitions in fluorescent silver clusters stabilized by DNA by absorption and CD spectroscopy.[91] They considered four different species (S1−S4) of pure AgN-DNA with between 4 and 12 neutral silver atoms in the system (**Table 4–3**, **Figure 4–11**).

The experimental results of samples that can contain 12 (S1), 6 (S2, S3) or 4 (S4) neutral silver atoms (**Table 4–3**) can be compared with TDDFT-calculated absorption and CD spectra for Ag_4, Ag_6 and Ag_{12} helical systems. For the system with 6 silver atoms, the theoretical and experimental CD spectra exhibit a similar spectral shape. With respect to both S2 and S3 experimental samples, the first positive calculated peak is red- shifted by about 0.3 eV, and the second negative theoretical peak is red-shifted by 0.36 or 0.15 eV. The third CD peak is blueshifted by 0.15 eV in comparison with the S2 sample and red-shifted by 0.08 eV with respect to the S3 sample. Overall, these values are within the range of typical TDDFT error. It

should also be emphasized that the theoretical calculations do not include effects such as the presence of DNA bases, so the overall agreement is quite good.

Table 4-3. Experimental energies of CD peaks and TDDFT data for related structures

	Experimental data[91]				TDDFT		
System	S1	S2	S3	S4	Ag_4	Ag_6	Ag_{12}
# Ag^0 atoms	12	6	6 or 7	4	4	6	12
1st peak	1.76 eV	2.09 eV	2.07 eV	2.54 eV	2.19 eV	1.72 eV	1.06 eV
2nd peak	3.16 eV	3.19 eV	2.98 eV	3.29 eV	–	2.83 eV	1.88 eV
3rd peak	3.42 eV	3.55 eV	3.32 eV	3.68 eV	3.77 eV	3.40 eV	2.49 eV

Figure 4–10. TDDFT optical absorption (upper pictures) and circular dichroism spectra (lower pictures) for Agn (n = 4, 6, 8, 10, 12) with 170° and 160° Ag-Ag-Ag bond angles and 10° Ag-Ag-Ag-Ag dihedral angles.

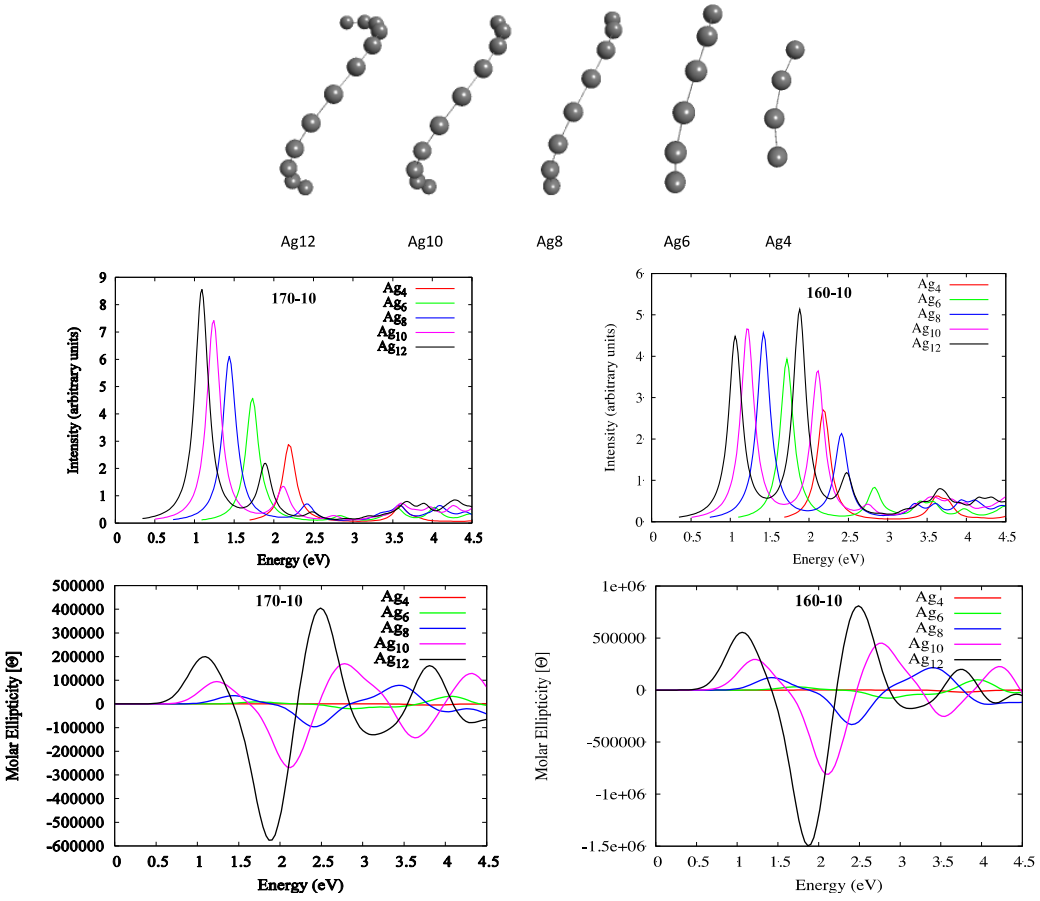

Figure 4–11. Experimental CD spectra of seven Gaussian peaks for A) S1, B) S2, C) S3 (aqueous solution) and D) S4 (50% MeOH) and calculated CD spectra for E) Ag_{12}, F) Ag_6 and G) Ag_4 helical clusters (Panels A–D: Reprinted from Reference 91.[86] Copyright 2014 American Chemical Society).

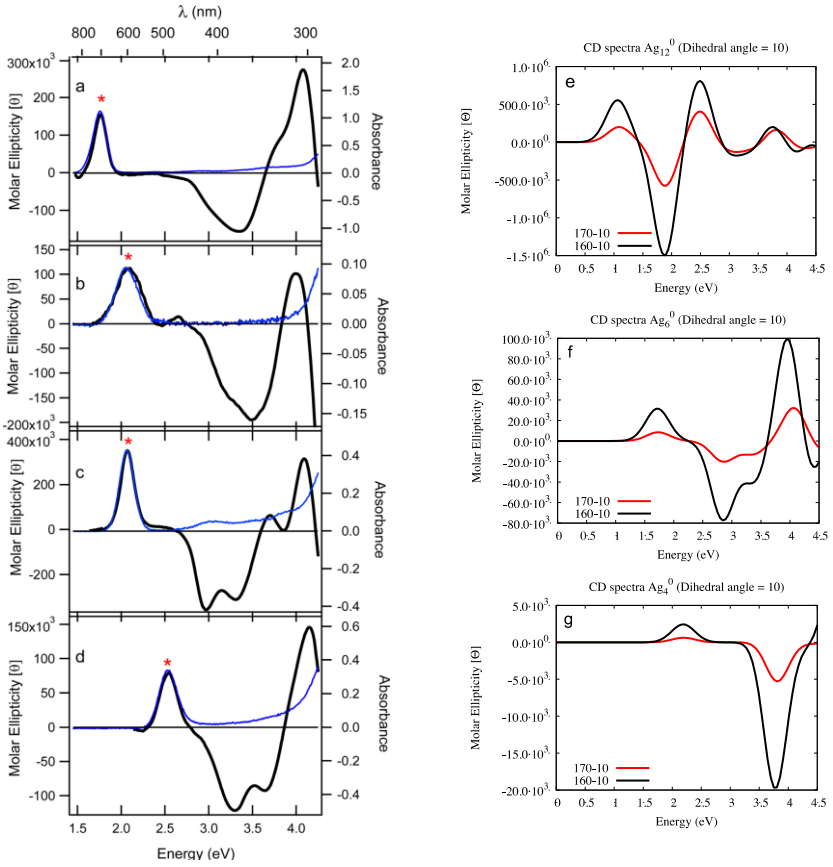

TDDFT calculations for the Ag_4 cluster show that the first peak is red-shifted by about 0.3 eV and the second one is absent in comparison to the S4 experimental system (**Table 4–3**). However, the third calculated negative CD peak of the Ag_4 structure is shifted to the red by only 0.11 eV with respect to the S4 sample.

The experimental data for Ag_{12} was decomposed to three CD peaks below 3.5 eV, with the second and third lowest-energy peaks only 0.26 eV apart.25 The second and third peaks fit within the same negative CD peak envelope. The calculated absorption and CD spectra of the Ag_{12} helical structure are very red-shifted with respect to experimental data for sample S1; for the first and second peaks this redshift is about 0.7 and 1.4 eV, respectively. A third peak with a negative rotatory strength is not present in the theoretical spectrum for this system; instead, the third theoretical peak has a positive sign. Thus, the theoretical and experimental results for the longest structure, Ag_{12}, show large differences in the peak locations. A higher level of theory

could be needed for this longer chain. Alternatively, the differences could be caused by effects such as the presence of DNA and cationic silver atoms in the experimental system; additional understanding of the interactions will be needed in order to yield close theory−experiment agreement for long silver chains. Nonetheless, calculations of the small bare clusters show reasonable agreement in spectral shapes and in peak locations (within typical TDDFT error) for theoretically predicted CD spectra of model systems with experimental data for silver−DNA clusters.[91] Overall, the results presented here show that the DNA-stabilized silver clusters can have a helical-chain shape.

Conclusions

TDDFT methods were employed for examination of the evolution of the absorption and circular dichroism spectra as a function of changing geometrical parameters such as bond and dihedral angles for silver nanowires of helical shape. Moreover, the effect of the length of the silver atom chain on the optical properties of neutral bare silver helical nanostructures was also investigated.

The influence of geometrical structures on the optical absorption and CD spectra were studied for planar and helical Ag_8 using the SAOP/TZP level of theory. Planar clusters show zero circular dichroism signals. Their absorption spectra exhibit three different intensity peaks, which are very sensitive to changing the bond angle. For all helical structures, the optical absorption spectra have a shape similar to that of the spectra of planar clusters. The first absorption peak arises from the HOMO-to-LUMO orbital transition for all considered structures. The second peak for structures Ag_6, Ag_8, Ag_{10} and Ag_{12} corresponds to the HOMO → LUMO+1 and HOMO−1 → LUMO transitions, which are forbidden for the linear structure and became allowed with the loss of linearity. For the Ag_4 cluster, this second peak, which is present in the absorption spectrum, is absent in the CD spectrum. The third CD peak has a negative rotatory strength for helices Ag_4 and Ag_6, and arises from the same transitions as the second peak. For Ag_n with $n > 6$, the circular dichroism spectrum exhibits a third peak that has a positive sign and arises from transitions HOMO → LUMO +2, HOMO−2 → LUMO, and HOMO−1 → LUMO+1.

The investigation of the geometrical structure of the helix shows that geometry has a strong effect on the location and intensity of the peaks in the spectrum. Furthermore, for these

helical structures we obtained strong circular dichroism spectra. The geometry of the helix has a great influence on the intensity and shape of the CD spectra. The sign of the first peak is always positive, whereas the second and third peak can change sign depending upon the dihedral and bond angles of the structure. Particular combinations of these angles can yield structures with more or less intense first, second, or third peaks, which can be very useful for constructing new materials with customized optical properties.

The effect of the number of silver atoms in a helix chain on the electronic properties has been investigated for Agn (n = 4, 6, 8, 10, 12) clusters. This study of the length dependence of the optical absorption and CD spectra in the bare silver helical chains shows that as the number of silver atoms in the chain increases, the spectrum redshifts and peak intensities become stronger. For small clusters, the calculated data are in reasonable agreement with experimental data for DNA- stabilized silver clusters.[91] For long silver chains, some differences in the theoretical and experimental results could be caused by effects such as the presence of DNA and cationic silver atoms in the experimental system, and additional understanding of these interactions will be needed in order to yield close theory−experiment agreement for these structures.

Acknowledgments

This material is based on work supported by the National Science Foundation under grant no. CHE-1213771. C.M.A. is also grateful to the Camille and Henry Dreyfus Foundation for a Camille Dreyfus Teacher-Scholar Award (2011-2016).

Chapter 5 - Time Dependent Density Functional Theory Study of Magnetic Circular Dichroism Spectra of Gold Clusters $Au_9(PH_3)_8^{3+}$ and $Au_9(PPh_3)_8^{3+}$

Natalia V. Karimova and Christine M. Aikens, *J. Phys. Chem. A* **2016**, 120, 9625–9635

Abstract

Magnetic circular dichroism (MCD) spectroscopy is a source of important data about the electronic structure and optical properties of different chemical systems. Theoretical simulation of the MCD spectra can be used to assist in the understanding of empirically measured MCD spectra. In the present paper, a theoretical investigation of electronic and optical properties of phosphine-protected gold clusters with a Au_9^{3+} core with D_{2h} symmetry was performed with time-dependent density functional theory. The influence of ligands on the optical properties of the golden core was investigated. Simulations of the optical absorption and MCD spectra were performed for the bare gold Au_9^{3+} cluster as well as for ligand–protected $Au_9(PH_3)_8^{3+}$ and $Au_9(PPh_3)_8^{3+}$ species. MCD spectra were calculated at a temperature of 298 K and a magnetic field of 7 T. A comparative analysis of theoretical and experimental data was also performed. The obtained results show that the theoretically simulated MCD spectrum for the $Au_9(PPh_3)_8^{3+}$ ion in gas phase exhibits a reasonable agreement with experimental results for the $[Au_9(PPh_3)_8](NO_3)_3$ system, although with a redshift of up to 0.5 μm^{-1}. Overall, MCD provides significant additional details about the electronic structure of the considered systems compared to the absorption spectra.

Introduction

Magnetic circular dichroism (MCD) spectroscopy is an important technique for investigation of the electronic structure and optical properties of different chemical systems. This type of spectroscopy yields more detailed information than a UV-Vis absorption spectrum, which is usually poorly resolved and often tends to appear very similar for different complexes.[94-96] It is well known that in the case of natural circular dichroism (CD) spectroscopy

the investigated species need to be optically active to obtain spectral signal and provide information about electronic structure, whereas the MCD signal does not depend on the optical activity of the sample and arises due to interaction of the electronic levels with the magnetic field. This fact makes MCD spectroscopy widely applicable. MCD spectroscopy has been applied to different groups of organic and inorganic molecules, metal complexes, and biological systems for characterization of metal sites in biological molecules.[26, 30, 31, 94-96, 101-103]

MCD spectroscopy is based on the measurement of the difference in absorption between left and right circularly polarized light, which is induced in the sample by a strong magnetic field oriented parallel to the direction of light propagation.[161, 162] The MCD signal can be either positive or negative. The obtained MCD spectrum can depend on the existence of degeneracy in the ground or excited states, as well as the symmetry and magnetic properties of the investigated molecule. There are three main sources of MCD intensity, which are referred to as the *A*, *B* and *C* terms.[162, 165, 166] Each of these terms corresponds to different spectral features (**Figure 5–1**). The nomenclature of *A*, *B* and *C* terms was introduced by Seber in 1932.[190] The *A* term arises when the molecule of interest contains degenerate excited states; this degeneracy is broken by the magnetic field, which leads to a derivative–shape of the signal in the MCD spectrum.[162] The *B* term arises because of the mixing of states caused by the applied magnetic field.[165] This term corresponds to the temperature–independent MCD intensity, and can be exhibited by all systems. The *C* term can be present in the MCD signal for systems with a degenerate ground state. This last term is temperature dependent and is observed only for paramagnetic systems.[166]

Figure 5–1.Origin of *A*, *B* and *C* terms in MCD spectra. Right circularly polarized (rcp) and left circularly polarized (lcp) light are shown with blue and green arrows, respectively.

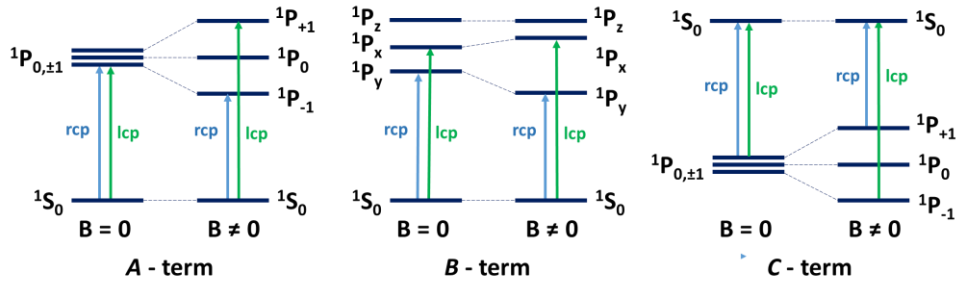

Unfortunately, the interpretation of experimental MCD spectra is a complicated process, especially for low–symmetry systems. Therefore, theoretical simulation of the MCD spectra can be used to assist in the understanding of empirically measured MCD spectra and can provide

useful information.

W. R. Mason and co–workers[96] applied MCD spectroscopy to investigate the electronic structure of different metal complexes with inorganic and organic ligands. For example, metal complexes with inorganic ligands that have been studied include square complexes (symmetry D_{4h}) PtX_4^{2-} and AuX_4^- (X = Cl, Br, I),[106, 107] $Pt(CN)_4^{2-}$,[108] $Pt(NH_3)_4^{2+}$,[109] linear complexes (symmetry $D_{\infty h}$) HgX_2 and AuX_2^- (X = Cl, Br, I),[110, 111] *etc*. Metal cluster complexes with organic ligands that have been studied include $Pt_3(CO)_3(P(t\text{–}Bu)_3)_3$, $Hg_3(dppm)_3^{4+}$, $Pt(AuPPh_3)_8^{2+}$, $Au_9(PPh_3)_8^{3+}$, $Au_8(PPh_3)_8^{2+}$, *etc*.[26, 30, 31, 94] For some of these complexes, a Hückel molecular orbital treatment was applied to aid in interpretation of MCD spectra.

Small phosphine–protected gold clusters are of interest due to their potential applications in catalysis, imaging, and as drug delivery agents.[26, 94, 191] Use of higher level theory such as time-dependent density functional theory (TDDFT) for simulation of MCD spectra will help to better understand the experimental spectra of these structures and will give detailed information about electronic structure and optical properties of the investigated structures. In this paper we investigate the electronic structure of the phosphine-protected centered gold cluster complex $Au_9(PPh_3)_8^{3+}$ with core symmetry D_{2h} using computational methods. Specifically, we probe the electronic structure through density functional theory and address the optical properties through TDDFT, through which we obtain the optical absorption and magnetic circular dichroism spectra for each system. We examine the bare Au_9^{3+} core, the phosphine-protected gold cluster complex $Au_9(PH_3)_8^{3+}$, and the triphenylphosphine-protected gold cluster system $Au_9(PPh_3)_8^{3+}$. Furthermore, we compare our theoretical results with experimental data for the complex $[Au_9(PPh_3)_8](NO_3)_3$ in acetonitrile solution at room temperature.[31]

Computational Method

All calculations in this work were performed with the Amsterdam Density Functional (ADF) program[158]. Scalar relativistic effects were included by utilizing the zero-order regular approximation (ZORA).[173] Geometry optimization was performed with the generalized gradient approximation Becke-Perdew exchange correlation functional[174, 175] and a triple-ζ Slater basis set (BP86/TZP). To trim down the computational time, we used a frozen core approximation for

heavy atoms, which reduces the size of the variational basis set (denoted TZP.4f for Au atoms, TZP.2p for P and TZP.1s for C). Optimized geometries were calculated only for naked and phosphine-protected gold clusters; large triphenylphosphine-protected systems were obtained by substituting hydrogen atoms in the optimized PH_3-protected gold clusters with PPh_3 ligands, without further geometry optimization.

Time-dependent density functional theory (TDDFT) was employed to calculate excited states to determine optical absorption and magnetic circular dichroism spectra. For these calculations the asymptotically correct Leeuwen-Baerends[176] (LB94) functional was used. This functional was combined with a double-ζ (DZ) Slater type basis set and frozen core approximation (denoted DZ.4f for Au atoms, DZ.2p for P and DZ.1s for C). The LB94 potential is an asymptotically correct type of exchange-correlation (XC) potential, which gives results superior to those obtained with LDA or GGA.[158] The XC potential should exhibit Coulombic ($-1/r$) decay as $r \rightarrow \infty$.[192] However, the XC potential of non–model functionals decay much faster than ($-1/r$) in the asymptotic region, which is a source of incorrect predictions for the highest occupied molecular orbital (HOMO) energies and excitation energies.[192] The LB94 functional has previously been employed successfully to examine the optical properties of ligand-protected gold nanoparticles such as $Au_{25}(SR)_{18}^-$ (R = H, CH_3, CH_2CH_3) and $Au_{36}(SPh)_{24}$.[193, 194] These previous results show that this functional often yields excitation energies that lie 0.15–0.20 eV below the experimental peaks.

In this article we focus on the excited states with wavenumbers lower than 3.0 μm^{-1}. The calculated absorption spectra are convoluted with a Lorentzian with a full width at half-maximum of 0.2 eV. The MCD spectra are calculated at a temperature of 298 K and a magnetic field of 7 T.

MCD Spectroscopy

Magnetic circular dichroism is the difference in absorption between left (lcp) and right (rcp) circularly polarized light, induced in the sample by a strong magnetic field oriented parallel to the direction of light propagation.[161, 162] The MCD sign is positive when absorption of the left circularly polarized light is greater than absorption of the right circularly polarized light.

$$\Delta A = A_- - A_+ = A_{lcp} - A_{rcp}$$

MCD data can be plotted in a few different ways: as the absorption difference (ΔA), as the absorption coefficient difference (Δk), as molar absorptivity ($\Delta\varepsilon_M$) and as molar ellipticity ($[\theta]_M$).[162-165] MCD intensity is often interpreted in terms of the equation:[162, 165]

$$\mathrm{MCD}(\hbar\omega) = \chi\hbar\omega \mathrm{B} \sum_J \left[A_J \left(-\frac{\partial f_J(\hbar\omega - \hbar\omega_J)}{\partial \hbar\omega} \right) + \left(B_J + \frac{C_J}{\kappa T} \right) f_J(\hbar\omega - \hbar\omega_J) \right]$$

where $\hbar\omega$ is the energy of incident light, $\hbar\omega_J$ is the excitation energy to state J, B is the amplitude of the applied magnetic field, T is the temperature, κ is Boltzmann's constant, χ is a collection of constants and experimental parameters that depend on what quantity is measured and units, f_J is a bandshape function and A_J, B_J and C_J are magnetic circular dichroism terms.[163]

In this project, the theoretical simulation of MCD spectra is based on the implementation in the Amsterdam Density Functional (ADF) program in which a magnetic perturbation of the TDDFT was applied for calculation of the MCD terms.[158] Using theoretically calculated A, B and C parameters and the MCD intensity equation, the MCD spectra can be simulated in terms of molar ellipticity $[\theta]_M$, which is independent of the major experimental parameters such as the concentration of absorption species, the path length and magnetic field:[162, 165]

$$[\theta]_M = \chi\hbar\omega \sum_J \left[A_J \left(-\frac{\partial f_J(\hbar\omega - \hbar\omega_J)}{\partial(\hbar\omega)} \right) + \left(B_J + \frac{C_J}{\kappa T} \right) f_J(\hbar\omega - \hbar\omega_J) \right]$$

where χ is the collection of constants which is approximately equal to 0.0014803.[165] To get molar ellipticity $[\theta]_M$ in the units (deg L m^{-1} mol^{-1} G^{-1}), the energy of incident light ($\hbar\omega$) and excitation energy to state J ($\hbar\omega_J$) should be in a.u.

The symmetry of the gold core of the $Au_9(PPh_3)_8^{3+}$ complex is D_{2h}. Therefore, we can expect the existence of only the B term for this type of system due to the absence of degenerate ground or excited states. In this case, the effect of the magnetic field on $\hbar\omega_J$ and the population of the ground state can be neglected and the equation for calculation of the molar ellipticity $[\theta]_M$ can be simplified:[165]

$$[\theta]_M = 0.0014803\omega \sum\nolimits_J B_J f_J(\hbar\omega - \hbar\omega_J)$$

The bandshape functions chosen are normalized Gaussian functions and their derivatives:[162]

$$f_J(\hbar\omega) = \frac{1}{\sqrt{\pi} W_J} e^{-((\hbar\omega_J - \hbar\omega)/W_J)^2}$$

$$\frac{\partial f_J(\hbar\omega)}{\partial(\hbar\omega)} = \frac{2(\hbar\omega_J - \hbar\omega)}{\sqrt{\pi}W_J^3} e^{-((\hbar\omega_J - \hbar\omega)/W_J)^2}$$

The bandwidth parameters W_J were chosen to reproduce the observed bandwidths:

$$W_J = Z\sqrt{\hbar\omega_J}$$

For the complexes discussed in this work, the parameter Z was chosen to be 0.010. The MCD spectra are calculated at a temperature of 298 K and a magnetic field of 7 T.

Results and Discussion

Geometries of $Au_9L_8^{3+}$ clusters (L = PH_3, PPh_3)

Figure 3–2 shows the geometries for Au_9^{3+} (1), $Au_9(PH_3)_8^{3+}$ (**2a** and **2b**), and $Au_9(PPh_3)_8^{3+}$ (**3**). The metal core of these systems has high symmetry D_{2h}. In these systems, one Au atom is located in the center of the cluster and is bound to eight peripheral gold atoms. For the bare gold cluster, the Au–Au bond lengths range from 2.71 – 2.89 Å, which are 0.00-0.16 Å longer than the same distances for the gold core in $Au_9(PPh_3)_8^{3+}$ determined by Briant and co–workers using x-ray crystallography (**Table C–1**).[61] The addition of phosphine–groups (i.e., PH_3) increased some of the gold – gold core bond distances up to 0.09 Å, whereas other metal bonds decreased by no more than 0.07 Å. In general, the gold-gold distances in $Au_9(PH_3)_8^{3+}$ are 0.04-0.08 Å longer than those in $Au_9(PPh_3)_8^{3+}$, which may be due to the use of the BP86 functional. In the $Au_9(PH_3)_8^{3+}$ (**2a**) and (**2b**) clusters, all PH_3 groups are coordinated to terminal gold atoms with Au-P distances ranging from 2.33 – 2.37 Å. More detailed information about bond distances, valence and torsion angles can be found in the **Appendix C** (**Table C–1** and **Figure C–1**).

From a geometrical structure search for PH_3–protected systems, we obtained various stable complexes of $Au_9(PH_3)_8^{3+}$ with different orientations of the hydrogen atoms in the phosphine groups, with energy differences less than 1 kcal/mol. Two of the most stable species are presented in **Figure 5–2**. These clusters contain the Au_9^{3+} core with D_{2h} symmetry. Due to the arrangement of the eight phosphine ligands bound to the gold atoms, complex $Au_9(PH_3)_8^{3+}$ (**2a**) has D_{2h} symmetry and $Au_9(PH_3)_8^{3+}$ (**2b**) has C_{2v} symmetry. Structure $Au_9(PH_3)_8^{3+}$ (**2a**) is the global minimum with an average stabilization energy per PH_3 ligand of 52.51 kcal/mol (**Table 5–1**). The energy of stabilization (E_{stab}), which shows how the addition of each phosphine ligand stabilize the gold core, is calculated as:

$$E_{stab} = \left(E_{complex} - E_{core} - 8 \cdot E_{ligand}\right) / 8$$

Figure 5–2. Structures of the gold clusters discussed in this work.

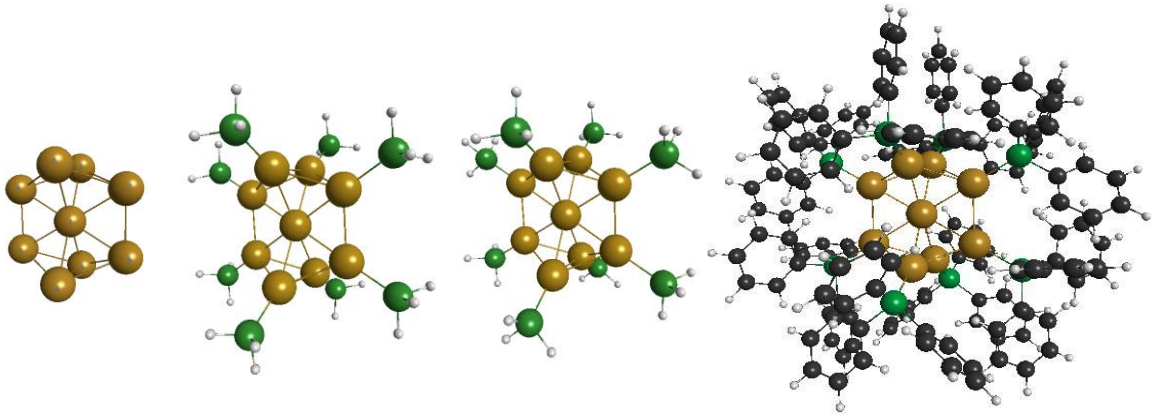

Au_9^{3+} (1) $Au_9(PH_3)_8^{3+}$ (2a) $Au_9(PH_3)_8^{3+}$ (2b) $Au_9(PPh_3)_8^{3+}$ (3)

Table 5-1. BP86/TZP energy of stabilization (E_{stab}, kcal/mol) of the Au_9^{3+} gold core per PH_3 ligand.

Structure	Core symmetry	Complex symmetry	E_{stab} (kcal/mol)
$Au_9(PH_3)_8^{3+}$ (2a)	D_{2h}	D_{2h}	52.51
$Au_9(PH_3)_8^{3+}$ (2b)	D_{2h}	C_{2v}	52.46

Figure 5–3. Absorption and MCD spectra for $Au_9(PH_3)_8^{3+}$ (2a) and $Au_9(PH_3)_8^{3+}$ (2b).

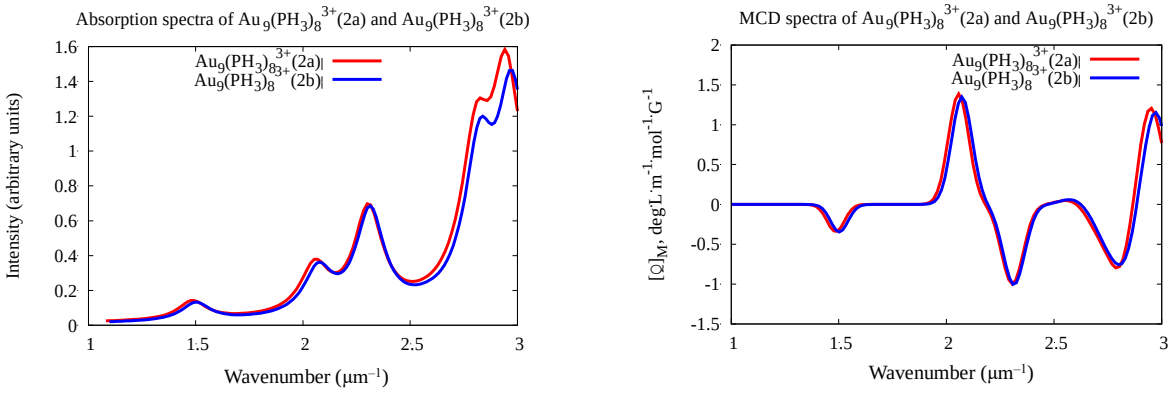

Absorption and MCD spectra were calculated for $Au_9(PH_3)_8^{3+}$ (**2a**) and $Au_9(PH_3)_8^{3+}$ (**2b**) structures. The results show that the spectral data are very similar for both complexes and do not depend on the hydrogen atom orientation in the wavenumber region up to 3.0 μm^{-1} (**Figure 5–3**).

As mentioned previously, coordinates for the largest cluster system studied, the triphenylphosphine−protected cluster, were obtained by replacement of hydrogen atoms in the optimized $Au_9(PH_3)_8^{3+}$ clusters with phenyl (Ph) groups (C_6H_5–) based on the optimized coordinates of the triphenylphosphine ligand, without further geometry optimization of the overall complex. It should be noted that substituting H−atoms with phenyl groups to yield $Au_9(PPh_3)_8^{3+}$ complexes can yield structures with overlapping phenyl rings. For example, the most stable complex $Au_9(PH_3)_8^{3+}$ (**2a**) cannot be used for creation of the $Au_9(PPh_3)_8^{3+}$ (**3**) structure due to overlapping C_6H_5–rings, whereas the next most stable structure $Au_9(PH_3)_8^{3+}$ (**2b**) (**2b**) works perfectly for this purpose. Therefore, cluster $Au_9(PH_3)_8^{3+}$ (**2b**) was chosen as the base for the triphenylphosphine ligand- protected cluster.

Optical Properties of Au_9^{3+}, $Au_9(PH_3)_8^{3+}$ and $Au_9(PPh_3)_8^{3+}$ Clusters

The bare Au_9^{3+} cluster. Our calculated data show that some orbitals of this cluster (**Figure 5–4**) can be considered as "superatom" orbitals, where the superatom orbitals arise primarily from valence electrons on the gold atoms.[195] The Au_9^{3+} cluster possesses 6 electrons so an occupation of $1S^2 1P^4 1D^0 2S^0$… is expected, where the S, P and D superatom orbitals can be formed from linear combinations of the valence s electrons on gold. The HOMO and LUMO orbitals in Au_9^{3+} are P superatom orbitals, so the HOMO → LUMO transition is forbidden. The HOMO–LUMO gap based on Kohn–Sham orbital energies for the naked Au_9^{3+} cluster is calculated to be 1.66 eV.

The optical absorption spectrum of the bare Au_9^{3+} cluster exhibits five strong peaks (**Figure 5–4**). Peaks in the optical absorption spectrum are labeled with Roman numerals whereas peaks in the MCD spectrum are labeled with Arabic numerals since the dominant peaks sometimes vary between the two types of spectra. The wavenumbers of the peaks and oscillator strengths for the five dominant transitions in the absorption spectra are shown in **Table 5–2**; additional information such as the transitions responsible for each excitation are presented in **Table C–2**. Although some weaker peaks are present, to simplify the analysis of the absorption spectra, only excited states with oscillator strengths higher than an average value of *f* for all excited states in the region below 3.0 μm^{-1} will be considered. For the absorption spectrum of the bare gold cluster Au_9^{3+}, the average value of the oscillator strength is 0.018 (**Table C–2**). Therefore, for this system only excitations with *f* stronger than 0.018 were taken into account.

Band I of the gas phase photoabsorption spectrum is centered at 1.77 μm^{-1} (f = 0.021) (**Figure 5–4**) and is predicted to arise primarily from transitions out of the HOMO into the LUMO+1 orbital (**Table C–2**). The second strong peak at 1.97 μm^{-1} is attributed to electronic transitions from HOMO → LUMO+2 and HOMO−1 → LUMO+1. The second peak is slightly more intense in comparison to the first peak (f = 0.027). Band III is located at 2.38 μm^{-1} (f = 0.049), and arises from the HOMO−1 → LUMO+1, HOMO → LUMO+2, and HOMO−7 → LUMO transitions.

Figure 5–4. Kohn-Sham orbitals, optical absorption and MCD spectra for the bare core Au_9^{3+} (D_{2h}).

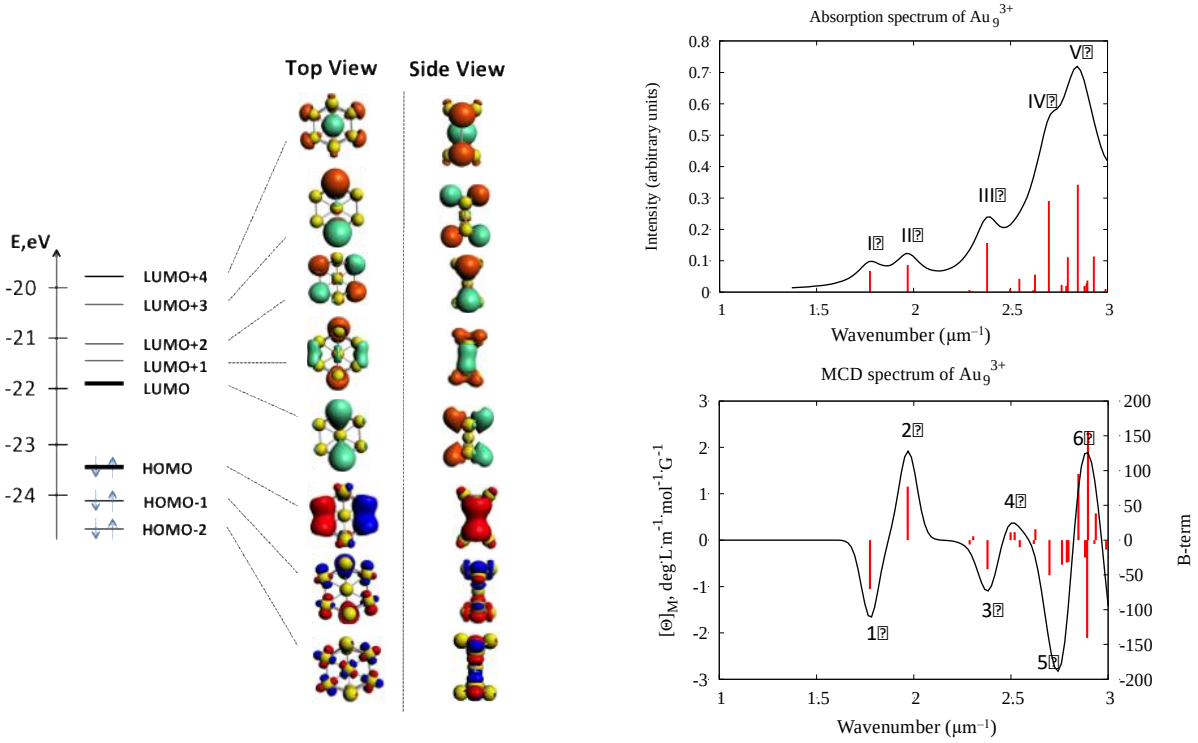

Table 5-2. Calculated absorption and MCD spectral data for bare gold core Au_9^{3+} (D_{2h}).

Absorption			MCD		
#	Wavenumber (μm^{-1})	Oscillator Strength	#	Wavenumber (μm^{-1})	$[\theta]_M$ deg L m^{-1} mol^{-1} G^{-1}
I	1.77	0.021	1	1.78	–1.65
II	1.97	0.027	2	1.97	+1.92
III	2.38	0.049	3	2.38	–1.09
IV	2.70	0.091	4	2.50	+0.37
			5	2.74	–2.83
V	2.85	0.108	6	2.89	+1.88

The high-energy (high–wavenumber) region of the absorption spectrum > 2.5 μm^{-1} consists of a series of closely spaced excited states. The overlap of these excited states when expected vibrational broadening is considered yields the broad fourth and fifth absorption peaks IV and V (**Figure 5–4**). The maxima of these broad peaks correspond to the wavenumbers of the strongest excitations that dominate in the spectrum. To analyze this part of the absorption spectrum, we will consider only excitations with oscillator strength (*f*) higher than 0.018. The calculations show that the fourth broad band IV is composed primarily of two important excitations at 2.63 (f = 0.018) and 2.70 (f = 0.091) μm^{-1}. The maximum of this peak is located at 2.70 μm^{-1} and coincides with the position of the strongest excitation (**Table 5–2** and **Table C–2**). This peak arises from HOMO → LUMO+2, HOMO−1 → LUMO+1, HOMO−7 → LUMO and HOMO−13 → LUMO transitions. Three relatively strong excitations at 2.80, 2.85, and 2.93 μm^{-1} contribute to form the fifth broad peak V, which has maximum absorption intensity at 2.85 μm^{-1}. This peak has contributions from multiple transitions: HOMO → LUMO+2, HOMO → LUMO+4, HOMO−1 → LUMO+1, HOMO−1 → LUMO+2, HOMO−1 → LUMO+4, HOMO−12 → LUMO+1, HOMO− 14 → LUMO+1, HOMO−13 → LUMO, and HOMO−18 → LUMO.

The magnetic circular dichroism spectrum of Au_9^{3+} provides more detailed information about the electronic structure of this system. The MCD and absorption spectra exhibit the same transitions. However, some of these excited states that were very weak and not noticeable in the absorption spectrum become more intense and observable with the application of a magnetic field and *vice versa*. The information about the wavenumber range of MCD peaks (μm^{-1}), wavenumber of the maximum magnitude (positive or negative) MCD peaks (μm^{-1}), and molar ellipticity $[\theta]_M$ (deg L m^{-1} mol^{-1} G^{-1}) for the Au_9^{3+} cluster can be found in **Table 5–2** and **Table C–3**. The MCD spectrum is more complicated for interpretation in comparison to the absorption spectrum. For example, some of the MCD peaks are formed by excitations with very small absolute values of *B*, whereas other peaks are combinations of very strong excited states. So, each MCD peak will be considered individually and the determination of the most important excited states will be performed for each specific peak. The primary excitations for each peak are presented in **Table C–3**.

The MCD spectrum of the naked golden core Au_9^{3+} exhibits six peaks (**Figure 5–4**, **Table 5–2** and **Table C–3**). The first peak 1 of the MCD spectrum is located at 1.78 μm^{-1} and is

negative; its molar ellipticity $[\theta]_M$ is –1.65 deg L m^{-1} mol^{-1} G^{-1}. The next MCD peak 2 at 1.97 μm^{-1} is positive ($[\theta]_M$ = +1.92 deg L m^{-1} mol^{-1} G^{-1}). The third peak 3 is located at 2.38 μm^{-1} and has the negative amplitude, with a molar ellipticity of –1.09 deg L m^{-1} mol^{-1} G^{-1}. These first three MCD peaks can be associated with the first three peaks from the UV-vis absorption spectrum (I-III): they arise from the same electronic transitions and are located at the same positions (**Table 5–2**). The next two MCD peaks (4 and 5) at 2.50 and 2.74 μm^{-1} are related to the fourth broad absorption peak IV centered at 2.70 μm^{-1}. The last MCD peak 6 considered at 2.89 μm^{-1} is positive and formed by relatively strong excitations at 2.85, 2.89, 2.90 and 2.94 μm^{-1}. This peak is related to the absorption peak V. These last three MCD peaks appear because of electronic transitions between HOMO–23 and LUMO+4 orbitals.

Complex $Au_9(PH_3)_8^{3+}$. The electronic structure and optical properties of the PH_3-ligand protected Au_9^{3+} complex were also investigated by TDDFT calculations (**Figure 5–5**, **Table 5–3** and **Table C–4**). As shown in **Figure 5–3**, the absorption and MCD spectra below 3.0 μm^{-1} are essentially independent of the H–atoms orientation in the PH_3 groups of structures $Au_9(PH_3)_8^{3+}$ (**2a**) and $Au_9(PH_3)_8^{3+}$(**2b**). Therefore, in this part we present data for the structure $Au_9(PH_3)_8^{3+}$ (**2b**), upon which the $Au_9(PPh_3)_8^{3+}$ system is based.

Figure 5–5. Kohn-Sham orbitals, optical absorption and MCD spectra for ligand protected cluster $Au_9(PH_3)_8^{3+}$ (2b).

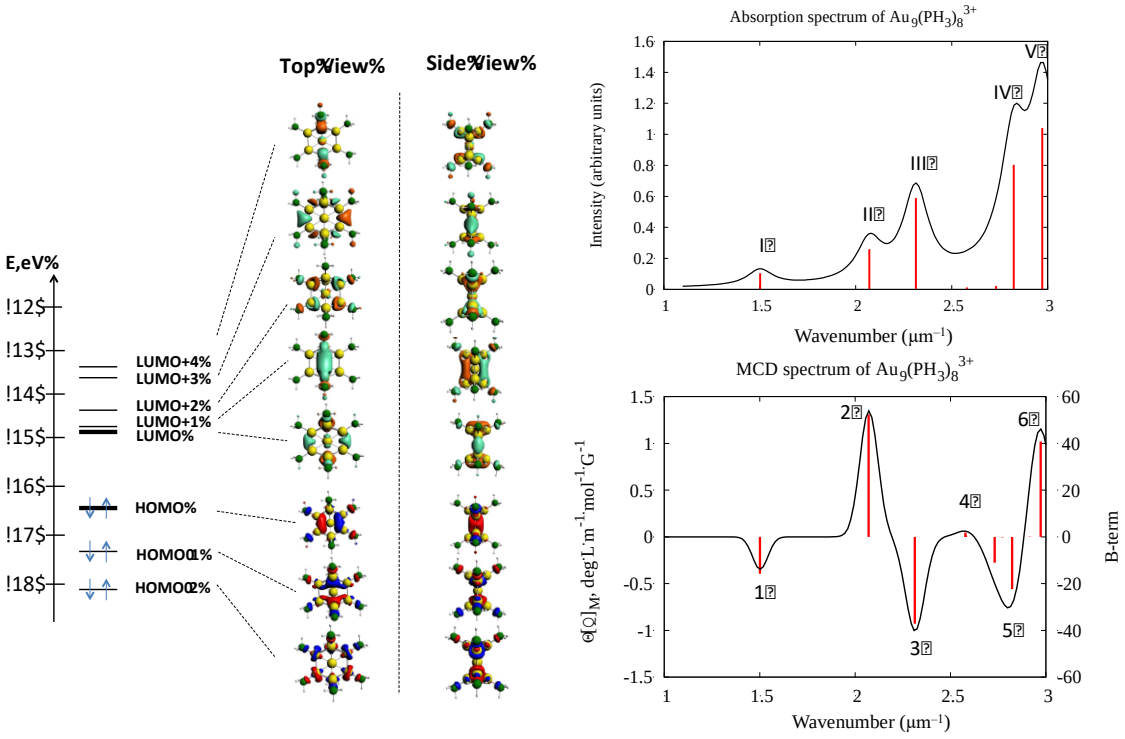

The optical absorption spectrum of the $Au_9(PH_3)_8^{3+}$ complex exhibits five strong peaks (I−V) in the region below 3.0 μm^{-1}. Each of these peaks is related to one strong excited state. These five sharp peaks are found at 1.50 (f = 0.033), 2.07 (f = 0.081), 2.31 (f = 0.185), 2.82 (f = 0.253) and 2.97 (f = 0.327) μm^{-1}. The transitions that are responsible for these peaks occur between HOMO-5 and LUMO+5. The first absorption band I arises from the HOMO → LUMO and HOMO → LUMO+5 electronic transitions. The symmetry of the HOMO orbital is P, the same as for the bare gold cluster, whereas the LUMO orbital now exhibits D character for the ligand-protected cluster $Au_9(PH_3)_8^{3+}$. This fact makes the HOMO → LUMO transitions possible, whereas this transition was forbidden for the bare Au_9^{3+} (**Figure 5–5**, **Table 5–3**).

Table 5-3. Calculated absorption and MCD spectral data for the $Au_9(PH_3)_8^{3+}$ (2b) complex.

Absorption			MCD		
#	Wavenumber (μm^{-1})	Oscillator strength	#	Wavenumber (μm^{-1})	$[\theta]_M$ deg L m^{-1} mol^{-1} G^{-1}
I	1.50	0.033	1	1.50	–0.34
II	2.07	0.081	2	2.07	+1.35
III	2.31	0.185	3	2.31	–1.00
–	–	–	4	2.58	+0.06
IV	2.82	0.253	5	2.80	–0.76
V	2.97	0.582	6	2.97	+1.15

Band II arises from the HOMO → LUMO+2 and HOMO-1 → LUMO transitions. Band III appears due to the same transitions as the second peak, although with the addition of a transition from the HOMO-2 → LUMO. Absorption band IV is a combination of electronic transitions including HOMO → LUMO+2, HOMO → LUMO+5, HOMO-1 → LUMO, and HOMO-2 → LUMO. The last absorption peak V appears because of transitions HOMO → LUMO+5, HOMO-1 → LUMO+2, and HOMO-2 → LUMO+2.

Comparison of the absorption data of $Au_9(PH_3)_8^{3+}$ and Au_9^{3+} shows that the spectra of the phosphine-ligand-protected gold cluster red-shift with respect to the bare system. The first peak of $Au_9(PH_3)_8^{3+}$ is shifted by 0.27 μm^{-1} into the lower-energy (i.e., lower-wavenumber) region of the spectrum with respect to the first peak of Au_9^{3+} cluster (**Figures 5–4** and **5–5**, **Tables 5–2** and **5–3**). The intensity of the absorption spectrum of the ligand- protected system is stronger in comparison to the bare gold core. Also, the addition of eight PH_3-ligands to the gold Au_9^{3+} core changed the symmetry of orbitals and made some electronic transitions that were forbidden in the bare cluster possible in $Au_9(PH_3)_8^{3+}$ (**Figures 5–4** and **5–5**, **Tables C–2 and C–**

4). An examination of the orbital energies for the PH_3-ligand- protected gold cluster $Au_9(PH_3)_8^{3+}$ shows that the band gap is 1.70 eV, which is slightly larger than the band gap for the pure gold core (1.66 eV).

The MCD spectra of the $Au_9(PH_3)_8^{3+}$ complex is presented in **Figure 5–5**. It exhibits six peaks (denoted 1−6). The primary excitations for each peak are presented in **Table C–5**. The peak positions in the MCD spectrum for this complex match the locations of the related peaks in the absorption spectrum (**Table 5–3**). Moreover, the MCD spectrum also reveals an additional peak 4 at 2.58 μm^{-1}. The excited states that contribute to this peak are barely noticeable in the absorption spectrum (**Figure 5–5**). Although it is also weak in the MCD spectrum, the change in sign compared to peaks 3 and 5 means that it is likely to be more observable. The electronic transitions that are responsible for these MCD peaks are similar to those for the absorption spectrum and the only differences occur because of the appearance of additional states in the MCD spectrum, such as the state at 2.73 μm^{-1} arising from the HOMO to the LUMO+6 which is present in the MCD spectrum but not noticeable in the absorption spectrum (**Tables C–4** and **C–5**).

The considered peaks from the MCD spectrum of the PH_3 ligand-protected species redshift from 0.06 to 0.28 μm^{-1} with respect to the corresponding MCD peaks of the pure gold core Au_9^{3+}. However, the shapes of these MCD curves are very close: all peaks in both MCD spectra have the same signs (**Figures 5–4** and **5–5**, **Tables 5–2** and **5–3**), which can mean that, in the considered region of the spectrum (with wavenumbers below 3.0 μm^{-1}), the PH_3 ligands produce a minimal effect on this part of the spectra, and the observed excited states essentially arise due to electronic transitions inside the Au_9^{3+} gold framework orbitals.

Complex $Au_9(PPh_3)_8^{3+}$. Analysis of the orbitals of the $Au_9(PPh_3)_8^{3+}$ (**3**) complex shows that the first three lowest unoccupied molecular orbitals LUMO, LUMO+1 and LUMO+2 exhibit similar significant superatom character as in the PH_3-stabilized complex: the LUMO and LUMO+2 orbitals have superatom D character, whereas the LUMO+1 is P. However, the LUMO+3 and LUMO+4 orbitals, which were considered to be superatom D orbitals in the small ligand-protected gold cluster $Au_9(PH_3)_8^{3+}$, are π^* orbitals on the PPh_3 ligands in the triphenylphosphine-protected gold complex (**Figure 5–6**). Also, in $Au_9(PPh_3)_8^{3+}$, the other lowest unoccupied molecular orbitals between LUMO+4 and LUMO+46 are essentially π^*

orbitals on the ligands. The HOMO orbitals in both $Au_9(PH_3)_8^{3+}$ and $Au_9(PPh_3)_8^{3+}$ clusters also exhibit similar superatom P character. The HOMO−1 and HOMO−2, which have superatom P and D character in $Au_9(PH_3)_8^{3+}$, can be considered to be a superatom P orbital and an orbital arising from π orbitals on the PPh_3 ligands, respectively, in the triphenylphosphine-protected gold cluster system. Also, for the $Au_9(PPh_3)_8^{3+}$ system, the three occupied orbitals below HOMO−2 with orbital energies from −15.380 to −15.744 eV arise primarily from π orbitals on the PPh_3 ligands, whereas the HOMO−6 orbital is a mixture of PPh_3 ligand π orbitals and gold *d* orbitals. Therefore, comparison of the orbitals of the phosphine-protected gold cluster complex and the triphenylphosphine–protected gold cluster system shows that, in the considered part of the spectra, the PPh_3 ligand has a larger effect on the electronic structure and optical properties of the gold core Au_9^{3+} than PH_3. In the $Au_9(PH_3)_8^{3+}$ cluster, the molecular orbitals (MOs) that participate in the most important electron transitions are primarily located on metal atoms of the gold core, whereas results for $Au_9(PPh_3)_8^{3+}$ show that electrons on the π orbitals on the PPh_3 ligands are also involved in transitions. The band gap for the $Au_9(PPh_3)_8^{3+}$ (**3**) structure is approximately equivalent to 1.53 eV; it should be noted that this is an approximation because a geometry optimization was not performed for this cluster.

Figure 5–6 gives the calculated optical absorption spectrum for the triphenylphosphine-protected gold complex $Au_9(PPh_3)_8^{3+}$. The spectrum of the $Au_9(PPh_3)_8^{3+}$ complex is more complicated with respect to the spectra of the Au_9^{3+} and $Au_9(PH_3)_8^{3+}$ systems. The absorption and MCD spectra for this structure consist of a number of weak and closely spaced excited states, particularly at higher energies. Therefore, we considered excitations with oscillator strengths > 0.010. The combination of small excitations from the calculations form seven strong broad peaks in the wavenumber region below 3.0 μm^{-1}. Electronic transitions that are responsible for these peaks occur between HOMO−17 and LUMO+46 (**Table C–6**). The first band is located at 1.33 μm^{-1} with oscillator strength of 0.035. Our obtained results show that this first absorption band of the $Au_9(PPh_3)_8^{3+}$ cluster red-shifts by 0.17 and 0.44 μm^{-1} with respect to band I for the $Au_9(PH_3)_8^{3+}$ and Au_9^{3+} systems, respectively (**Figure 5–7**). This peak arises from the HOMO → LUMO transition, similar to the PH_3 ligand-protected analog.

Figure 5–6. Kohn-Sham orbitals, optical absorption and MCD spectra for ligand protected cluster $Au_9(PPh_3)_8^{3+}$ (3) with golden core symmetry D_{2h}.

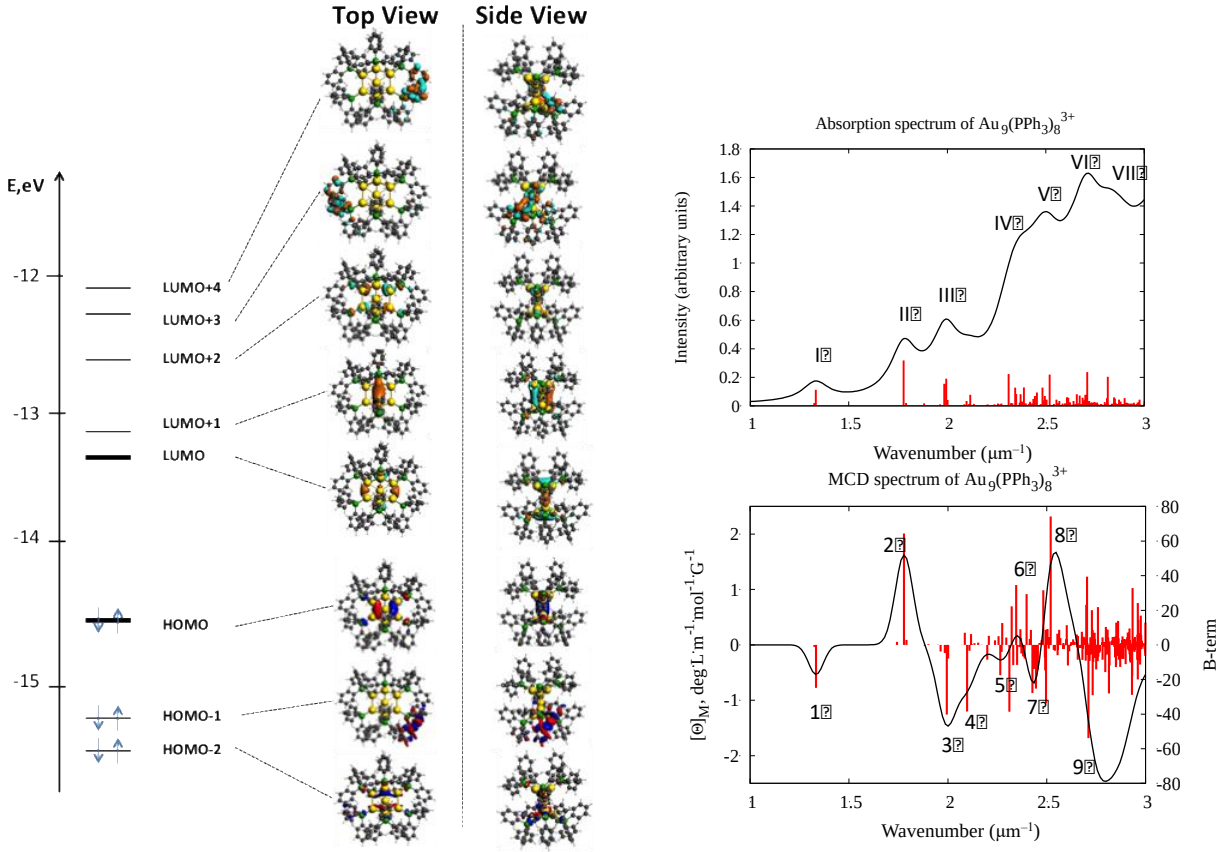

Figure 5–7. Theoretical absorption (left) and MCD (right) spectra of Au_9^{3+} (1), $Au_9(PH_3)_8^{3+}$ (2b) and $Au_9(PPh_3)_8^{3+}$ (3) clusters.

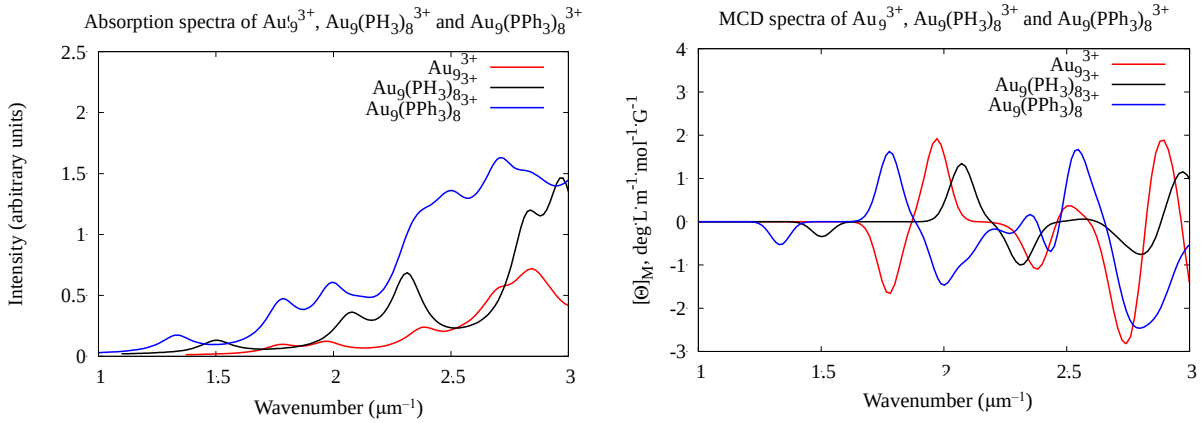

Table 5-4. Calculated absorption and MCD spectral data for $Au_9(PPh_3)_8^{3+}$ (3). Spectral data were considered for energies up to 3.0 μm^{-1}.

Theoretically calculated spectra				
Absorption		MCD		
#	Wavenumber (μm^{-1})	#	Wavenumber (μm^{-1})	$[\theta]_M$ deg L m^{-1} mol^{-1} G^{-1}
I	1.33	1	1.33	–0.53
II	1.78	2	1.78	+1.62
III	1.99	3	2.00	–1.47
		4	2.10	–0.84
IV	2.31	5	2.27	–0.27
		6	2.35	+0.17
V	2.52	7	2.44	–0.69
		8	2.55	+1.67
VI	2.71	9	2.80	–2.46
VII	2.81			

Band II of the absorption spectra at 1.78 μm^{-1} (f = 0.100) appears because of HOMO → LUMO+2 and HOMO−2 → LUMO transitions. The electron transition from the HOMO to the LUMO+2 orbital, which is a transition from a superatom P gold orbital to a D orbital, is also responsible for the appearance of band II in the absorption spectrum of the $Au_9(PH_3)_8^{3+}$ cluster. The transition out of the HOMO−2 to the LUMO is related to the transition between P and D superatom orbitals, as well. However, this type of transition is symmetry forbidden for the cluster with PH_3 ligands. Also, band II in the absorption spectrum of the triphenylphosphine-protected gold complex $Au_9(PPh_3)_8^{3+}$ is red-shifted by 0.29 μm^{-1} with respect to band II of $Au_9(PH_3)_8^{3+}$ (**Tables 5–3** and **5–4**).

The third peak (band III) is a combination of two excited states that are close in energy, where the strongest excitation is located at 1.99 (f = 0.060) μm^{-1} and arises due to the same transitions as the second peak, although with the addition of a transition from the HOMO to the LUMO+4. The fourth broad band is formed by five small excitations at 2.31, 2.34, 2.35, 2.37, and 2.39 μm^{-1}, where the first one dominates in this region of spectra (f = 0.070) and determines the maximum of the broad peak. This strongest excitation primarily arises from the HOMO−2 → LUMO+2 transition. Essential contributions to the fifth broad absorption peak (band V) are given by ten excitations in the wavenumber range of 2.44−2.57 μm^{-1}. The maximum of band V of the absorption spectrum is located at 2.52 μm^{-1}. This arises from the strongest excitation of

this series with an oscillator strength of 0.068; this excited state is due in part to transitions from the HOMO into the LUMO+25, LUMO+28, and LUMO+31 (which are transitions into the π* rings on the phenyl groups), from the HOMO−2 to the LUMO+2, and from the HOMO−6 to the LUMO+2. Next, the sixth peak (band VI) is constructed by eleven main excitations with energies from 2.61 to 2.72 μm^{-1}. The maximum of this peak is determined by the leading excitation at 2.71 μm−1 (f = 0.074), which arises primarily from HOMO−6 → LUMO+2 transitions. The last seventh broad band of the absorption spectra in the wavenumber region below 3.0 μm^{-1} is formed by eight narrowly spaced excitation states with a maximum at 2.81 μm^{-1} (f = 0.064), which arises from transitions HOMO → LUMO+4 and HOMO−2 → LUMO+12 (**Figure 5–6**, **Table 5–4**, and **Table C–6**). The last three peaks (V, VI, and VII) arise primarily from electron transitions from Au P orbitals → π* orbitals on the PPh_3 ligands (**Figure 5–6**). More detailed information about electronic transitions can be found in the **Appendix C**.

MCD spectral data for the $Au_9(PPh_3)_8^{3+}$ (**3**) complex is presented in **Figure 5–6**, **Table 5–4**, and **Table C–7**. The MCD spectrum is more complicated in comparison to the absorption spectrum for the same structure and exhibits more peaks (**Table 5–4**). The first two theoretical MCD peaks at 1.33 and 1.78 μm^{-1} have molar ellipticity values of −0.53 and +1.62 deg L m^{-1} mol^{-1} G^{-1}, respectively. These peaks correspond to the first two peaks from the absorption spectra and arise from the same transitions. For all three complexes (**1**, **2b**, and **3**) examined in detail in this work, the first MCD peak is negative and the second peak is positive. However, the peaks for the triphenylphosphine-stabilized cluster are predicted to lie at lower energy than those of the bare gold core or the simple phosphine-stabilized cluster (**Figure 5–7**). The MCD spectrum of $Au_9(PH_3)_8^{3+}$ is shifted to the red with respect to the MCD of the Au_9^{3+} cluster; additionally, a further red shift is observed when the hydrogen atoms in the $Au_9(PH_3)_8^{3+}$ complex were replaced with phenyl groups (C_6H_5−) yielding the triphenylphosphine ligand−protected clusters $Au_9(PPh_3)_8^{3+}$.

Table 5-5. Experimental electronic absorption and MCD spectral data for $[Au_9(PPh_3)_8](NO_3)_3$ in CH_3CN and PPM.

Experimental data in CH_3CN [31]				Experimental data in PMM thin films [94]							
295 K				295 K				10 K			
	Abs	MCD			Abs	MCD			Abs	MCD	
Band	Wave number (μm^{-1})	Wave number (μm^{-1})	Peak sign	Band	Wave number (μm^{-1})	Wave number (μm^{-1})	Peak sign	Band	Wave number (μm^{-1})	Wave number (μm^{-1})	Peak sign
	–	1.83	neg		–	1.87	neg	Ia	1.92	1.88	neg
	–	2.10	pos	I	2.06	2.08	pos	Ib	2.11	2.08	pos
I	2.26	2.21	pos	II	2.25	2.33	neg	II	2.25	2.22	pos
		2.37	neg								
II	2.64	2.60	neg	III	2.40	2.58	neg	III	2.41	2.34	neg
										2.61	neg
III	2.90	2.86	neg	IV	2.91	2.86	neg	IV	2.89	2.85	neg
VI	3.19	3.25	neg	V	3.18	3.21	neg	V	3.18	3.22	neg

Figure 5–8.Experimental electronic absorption (lower curve) and MCD (upper curve) spectra for $[Au_9(PPh_3)_8](NO_3)_3$ in a PMM thin film at 295 and 10 K. (Figure reproduced with permission from Reference [94]. Copyright 2000 American Chemical Society).

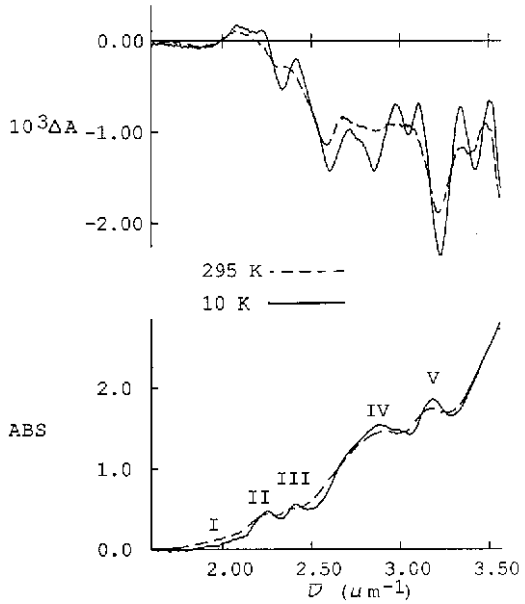

The next two MCD peaks 3 and 4 at 2.00 and 2.10 μm^{-1} are both negative and can be associated with the third absorption peak at 1.99 μm−1 where the 2.10 μm^{-1} peak may be observable as a shoulder in band III. The 2.10 peak μm^{-1} (peak 4 of the MCD spectrum) can be

attributed to additional transitions such as HOMO → LUMO+7 and HOMO → LUMO+8. These transitions into π* orbitals on the phenyl rings were not available for complexes **1** and **2b**, and this peak was not observed for these systems. The fifth and sixth MCD peaks are located at 2.27 and 2.35 μm^{-1} and are related to the fourth absorption peak (band IV), which is located at 2.31 μm^{-1}. Numerous excited states are responsible for these two MCD peaks, and **Table 5–4** reports the molar ellipticity values of the fitted curves. The strongest excited states in these two MCD peaks arise out of transitions from the HOMO−2 to the LUMO+2, and from the HOMO−6 to the LUMO. Whereas band IV in the absorption spectrum is broad and individual contributions to it are unlikely to be resolved, peaks 5 and 6 in the MCD spectrum have different signs and may be resolvable.

The next MCD peaks (7 and 8) at 2.44 and 2.55 μm^{-1} are related to the fifth absorption peak at 2.52 μm^{-1}. Again, numerous excited states make up these two MCD peaks, so we report the most negative and most positive molar ellipticity values. The strongest excited states that are responsible for these two MCD peaks arise from transitions out of the HOMO to the LUMO+25, LUMO+28, LUMO+29 and LUMO+31, and out of the HOMO−2 and HOMO−6 to the LUMO−2.

The last negative MCD peak 9 at 2.80 μm^{-1} is formed by the overlapping of multiple excited states and includes peaks that are responsible for the appearance of two last peaks on the absorption spectrum. To describe this MCD peak, we considered ten relatively strong excited states with wave- numbers 2.65−3.00 μm^{-1} that arise from electron transitions between HOMO−39 and LUMO−44. The obtained results show that the PPh_3 ligand greatly increases the number of electronic transitions and orbitals involved with respect to the $Au_9(PH_3)_8^{3+}$ cluster; the MO levels in the gold ligand-protected cluster become more dense when simple phosphines are substituted by PPh_3 ligands in the $Au_9(PH_3)_8^{3+}$ complex.

In order to see how our theoretical calculations compare to the experimental triphenylphosphine-protected gold cluster $Au_9(PPh_3)_8^{3+}$, we compared previously reported spectroscopic data to our results. The experimental measurement of optical absorption and MCD spectra in the vis–UV range 1.66 – 3.60 μm^{-1} for $[Au_9(PPh_3)_8](NO_3)_3$ was performed by Jaw and Mason in acetonitrile solution at room temperature[31] as well as in poly(methyl methacrylate) (PMM) thin films[94] at 295 and 10 K (**Table 5–5**, **Figure 5–8**). Since the theoretically calculated spectra are obtained only for wavenumbers up to 3.0 μm^{-1} and are

redshifted with respect to experimental data (**Tables 5–4** and **5–5**), in this article we will focus on empirically measured absorption and MCD spectra for the wavenumber region up to 3.25 μm^{-1}.

In these articles the authors proposed that the $Au_9(PPh_3)_8$ ion has D_{2h} skeletal symmetry. The absorption and MCD spectra in PMM are similar to the acetonitrile solution spectra (**Table 5–5**). The experimental absorption spectrum of $[Au_9(PPh_3)_8](NO_3)_3$ in CH_3CN at room temperature exhibits four main peaks (I, II, III, and IV) with wavenumbers up to 3.25 μm^{-1}. These peaks are located at 2.26, 2.64, 2.90, and 3.19 μm^{-1}. The absorption spectrum in PMM thin film at 295 K exhibits five bands: peak I is located in the low-energy region of the spectrum at 2.06 μm^{-1} and is unresolved in the acetonitrile solution, whereas peaks II−V are very close to bands I−IV of the spectrum in CH_3CN. The absorption spectrum in the PMM thin film at 10 K is better resolved and allows observation of the important transitions on the low-energy side (**Table 5–5**, **Figure 5–8**). At a temperature of 10 K, the optical spectrum of $[Au_9(PPh_3)_8](NO_3)_3$ in PMM has five main absorption bands. The first two peaks (Ia and Ib) are located in the low-energy region at 1.92 and 2.11 μm^{-1}. Bands II−V of the absorption spectrum at 10 K in PMM are the same as peaks I−IV and II−V of the absorption spectra in acetonitrile and PMM at room temperature, respectively.

The MCD spectra are very similar in terms of band position and relative band intensities (**Table 5–5**).[31, 94] All considered MCD spectra demonstrate the presence of excited states below 2.10 μm^{-1}. For MCD spectra in the CH_3CN solution and PMM thin film at room temperature, these states are lower in energy than the states associated with the first absorption peak (**Table 5–5**).

A comparative analysis of the theoretically simulated absorption and MCD spectra of the $Au_9(PPh_3)_8^{3+}$ (**3**) cluster in gas phase was performed with the experimental results for $[Au_9(PPh_3)_8](NO_3)_3$ in PMM thin film1 at 10 K because the best experimental spectral resolution was obtained for this system. Results showed that calculated absorption and MCD spectra redshift with respect to the experimental data. The calculated absorption spectrum has a reasonable agreement with experimental data (**Tables 5–4** and **5–5**). The first absorption peak I at 1.33 μm^{-1} in our calculated spectrum of the $Au_9(PPh_3)_8^{3+}$ (**3**) is located in the low-energy region and can be associated with band I in the experimental absorption spectrum, which is a combination of two peaks Ia and Ib at 1.92 and 2.11 μm^{-1} (**Figures 5–6, 5–7 and 5−8**, **Tables**

5–4 and **5–5**). The second TDDFT peak at 1.78 μm^{-1} can be related to peak II at 2.25 μm^{-1} in the experimental absorption curve. Therefore, the theoretical peak II is redshifted by 0.47 μm^{-1} with respect to the analogous peak in the empirical absorption spectrum. Peak III in the theoretical absorption spectrum, which is located at 1.99 μm^{-1}, is assigned to the empirical peak II at 2.41 μm^{-1}; the wavenumber difference between the calculated and experimental energies of these peaks is 0.42 μm^{-1}. The next two simulated absorption peaks IV and V at 2.31 and 2.52 μm^{-1} can be assigned with the empirical peak at 2.89 μm^{-1} and its shoulder (band number IV in **Figure 5–**8). The last measured absorption band V at 3.18 μm^{-1} can be associated with the two last theoretical peaks VI and VII at 2.71 and 2.81 μm^{-1}. In general, the theoretical spectra exhibit a red shift of approximately 0.4−0.5 μm^{-1} throughout the spectrum in comparison to the experimental data.

According to our comparative analysis of the theoretical and empirical absorption spectra for $Au_9(PPh_3)_8^{3+}$ and $[Au_9(PPh_3)_8](NO_3)_3$ in PMM, a relationship between calculated and experimental MCD data can be obtained. The first theoretically obtained MCD peak at 1.33 μm^{-1} is negative and can be associated with the first MCD peaks Ia and Ib in the experimental spectrum at 1.88 and 2.08 μm^{-1}. The positive peak II from the empirical MCD curve at 2.22 μm^{-1} can be assigned to the theoretical peak at 1.78 μm^{-1}, which also has a positive sign. The next band in the experimental MCD spectrum is the broad negative band III, which is a combination of two peaks at 2.34 and 2.61 μm^{-1}. This band can be related to two negative peaks at 2.00 and 2.10 μm^{-1} in the theoretical spectrum. The next experimental band (IV) of the MCD spectrum for $[Au_9(PPh_3)_8](NO_3)_3$ in PMM at 2.85 μm^{-1} can be associated with the set of theoretical peaks at 2.27, 2.35, 2.44, and 2.55 μm^{-1}. The experimental and theoretical spectra vary somewhat in this wavenumber range, which may be due in part to the complexity and number of excitations involved in this region of the spectrum. The last peak on the theoretical spectrum at 2.80 μm^{-1} is a strong negative peak, which can be assigned to the last peak at 3.22 μm^{-1} on the empirical curve. Comparison of the calculated MCD spectrum shows that the theoretical spectrum is red-shifted by up to 0.5 μm^{-1} with respect to the experimental one.

We can see from the data that the theoretical spectrum exhibits some low-energy peaks that are unresolved in experiment. However, the positions of the other simulated peaks are in good agreement with experimental data, given the wavenumber differences between related theoretical and experimental peaks of up to 0.5 μm^{-1}. Also, some of the theoretical peaks exhibit

different signs with respect to the peaks in the empirical spectrum. It is possible that differences could be caused by the presence of environmental (PMM thin film or solvent and NO^{3-} anions), configurational, and vibrational effects, as well as by limitations in the level of theory. However, overall the comparison of the theoretically simulated MCD spectrum for $Au_9(PPh_3)_8^{3+}$ in the gas phase with the experimental results for $[Au_9(PPh_3)_8](NO_3)_3$ in PMM showed that the calculated spectra are in reasonable agreement with experimental results.

Conclusions

In the present paper, the theoretical investigation of electronic and optical properties of phosphine-protected gold clusters were calculated with TDDFT. Simulations of the optical absorption and magnetic circular dichroism spectra were performed. The bare Au_9^{3+} core and ligand–protected $Au_9(PH_3)_8^{3+}$ and $Au_9(PPh_3)_8^{3+}$ clusters were chosen for investigation.

The geometry optimization procedure was performed only for bare and $Au_9(PH_3)_8^{3+}$ gold clusters, whereas large triphenylphosphine-protected gold systems were obtained by substituting hydrogen atoms in the optimized PH_3-protected gold clusters with PPh_3 ligands without further geometry optimization. The influence of different types of ligands on the optical and electronic properties of the gold core was investigated. Calculations showed that the nature of the ligand noticeably affects the electronic structure of the gold core: both optical absorption and MCD spectra redshift when ligands are added to the bare gold cluster. Furthermore, the triphenylphosphine-protected gold systems are more redshifted in comparison to the system with PH_3 ligands. However, the shapes of these MCD curves are very close, and the peaks in the MCD spectra have the same signs. For the phosphine-protected systems, the PH_3 ligands produce a minimal effect on this part of the spectra, and the observed excited states essentially arise due to electronic transitions inside the Au_9^{3+} gold framework orbitals.

The comparative analysis of theoretical and experimental data was also performed. Our results showed that the positions of the main peaks in the simulated spectra are in a good agreement with experimental data, given a wavenumber difference between related theoretical and experimental peaks of up to 0.5 μm^{-1}. The lowest energy peaks have the same signs in MCD for both the calculated and experimental spectra. In the more congested region of the spectrum, some of the theoretical peaks exhibit different signs with respect to the peaks in the empirical spectrum. It is possible that differences could be caused by the presence of the environmental,

configurational, and vibrational effects or by limitations in the level of theory. Nonetheless, the theoretically simulated MCD spectrum for $Au_9(PPh_3)_8^{3+}$ in the gas phase is in good agreement with the experimental results for $[Au_9(PPh_3)_8](NO_3)_3$.

Acknowledgement

This material is based on work supported by the National Science Foundation under Grant CHE-1507909. C.M.A. is grateful to the Camille and Henry Dreyfus Foundation for a Camille Dreyfus Teacher-Scholar Award (2011−2016). The computing for this project was performed on the Beocat Research Cluster at Kansas State University, which is funded in part by NSF grants CNS-1006860, EPS-1006860, and EPS-0919443.

Chapter 6 - Optical Properties of Small Gold Clusters $Au_8L_8^{2+}$ (L = PH_3, PPh_3): Magnetic Circular Dichroism Spectra

Natalia V. Karimova and Christine M. Aikens, *J. Phys. Chem. C* **2017**, 121 (35), 19478–19489

Abstract

A theoretical study of the optical and electronic properties of small phosphine–protected centered gold clusters with gold core symmetry C_{3v} was performed using density functional theory (DFT) and time–dependent density functional theory (TDDFT) methods. It is well known that magnetic circular dichroism (MCD) spectroscopy yields more detailed information about electronic structure and optical properties with respect to optical absorption spectroscopy. In this work, we combine electronic absorption and MCD spectroscopy for gold nanoclusters to gain a better understanding of their electronic states. These results can be used to help with interpretation of the experimentally measured MCD spectra, which is a very complicated process, especially for low–symmetry systems.

In the present paper, absorption and MCD spectra were calculated for ligand-protected gold clusters $Au_8(PPh_3)_8^{2+}$ and $Au_8(PH_3)_8^{2+}$, in addition to bare Au_8^{2+}. The influence of the nature of the ligands on the optical properties of gold cluster was investigated. Geometrical changes and changes in optical properties that occur in the Au_8 gold core during the ligation process were also determined. A comparative analysis of the obtained theoretical and experimental results was performed. The results show that the theoretically simulated optical absorption and MCD spectra for $Au_8(PPh_3)_8^{2+}$ exhibit a very good agreement with empirical spectra for $Au_8(PPh_3)_8(NO_3)_2$ in acetonitrile.

Introduction

Very small ligand–protected noble metal clusters (size < 2 nm) exhibit unique optical, electronic and catalytic properties that are different from the properties of the bulk; for instance, they demonstrate a non–zero HOMO–LUMO gap that can reach up to 3.0 eV.[4, 27, 29, 32, 170, 196]

These differences arise from size quantization effects in the metal core due to a small number of atoms. Small ligand-protected gold nanoclusters have attracted great interest for decades both in fundamental and applied research, especially in the fields of heterogeneous catalysis, nanoelectronics, drug delivery, bioanalysis, etc.[1-3] Two main families of organic ligands are usually used for stabilization of gold nanoclusters: phosphine and thiolate ligands. These ligands enable the creation of highly stable gold nanoparticles and nanoclusters.[4, 5] The structure of the thiolate–ligated gold clusters is more complicated compared to phosphine–ligated systems because the metal core is covered by multiple gold–thiolate motifs, whereas phosphine–protected gold nanoclusters have a simpler structure in which the metal core is surrounded by organic ligands attached in a radial fashion.[10, 27, 51, 194, 197] This simple structure of the phosphine–protected gold clusters makes them useful systems to investigate the nature of the inner metal core and organic ligand–metal interfaces.

Ultra-small phosphine–stabilized gold clusters have been extensively studied experimentally and theoretically including investigations into their geometry, bonding energy, optical properties and electronic structure. A large group of this class includes centered gold species such as $Au_8(PPh_3)_7^{2+}$,[23, 24] $Au_8(PPh_3)_8^{2+}$,[25-28] $Au_9(PPh_3)_8^{3+}$,[24, 28-32] $Au_{11}(PPh_3)_8X_2^+$ (X = Cl, SCN),[33, 34] $Au_{11}(PPh_3)_7Cl_3$,[34] $Au_{11}(L)_4X_2^+$ (L = BINAP and DIOP; X = Cl, Br, I),[40, 198] etc. In these centered clusters the structure of the metal core can be described as capped/bicapped centered hexagonal chairs.

It is well known that centered gold clusters with general formulas $(AuPPh_3)_n^{m+}$ and $Au(AuPPh_3)_n^{m+}$ are highly colored, and they have several absorption bands in the UV–vis region of their spectra.[26, 30, 31] Two the most famous representatives of this series are the $Au_8(PPh_3)_8^{2+}$ and $Au_9(PPh_3)_8^{3+}$ clusters. These clusters are widely applied in catalysis,[199-201] synthesis of intercluster compounds,[202, 203] nanophotonics and medical imaging.[28, 29] Gold clusters $Au_8(PPh_3)_8^{2+}$ and $Au_9(PPh_3)_8^{3+}$ help to prevent poisoning of electrodes by CO.[199, 200] These gold clusters can be nested onto supports such as titania and silica surfaces[52] and activated by subtraction of some or all ligands. Additionally, the ultra-small phosphine–protected clusters are used for creation of new types of compounds that exhibit unique electronic properties such as charge transfer and hopping processes between different kinds of clusters.[202, 203] For instance, clusters $Au_7(PPh_3)_7^+$ and $Au_8(PPh_3)_8^{2+}$ are used to form intercluster compounds from gold clusters and fullerides.[203] The obtained $Au_8(PPh_3)_8(C_{60})_2$ structure

exhibits a new arrangement of the fullerides, which has very important electron–transport properties. Another interesting intercluster compound contains the gold cluster $Au_9(PPh_3)_8^{3+}$ and polywolframat $PW_{12}O_{40}$.[63]

An additional important feature of these ultra-small gold clusters is their optical properties. Experimental investigation of the optical properties of these systems demonstrated the presence of luminescence with higher quantum yields than the larger clusters.[29] Also, small phosphine–protected gold clusters exhibit unique optical responses in their UV–vis spectra. When the particle sizes decrease from the nanometer to subnanometer range, the surface plasmon band disappears, and discrete peaks emerge in the UV–vis part of the spectrum.[26, 27, 29-31, 94]. Mason and co–workers extensively studied the optical properties of small phosphine–protected clusters with absorption and magnetic circular dichroism (MCD) spectra.[26, 30, 31] It is well known that the UV–vis absorption spectrum is usually poorly resolved and often tends to appear very similar even for different complexes, whereas MCD spectroscopy yields more detailed information.[94, 163, 170] Unfortunately, the interpretation of experimental MCD spectra is a complicated process, especially for low–symmetry systems. Therefore, the use of advanced analytical instruments together with high–level computation can aid in acquiring new important information about the optical and electronic properties of gold clusters. This obtained knowledge and a better understanding of gold cluster behavior may assist with the creation of novel cluster species with targeted properties. In our previous work, the density functional theory (DFT) and time–dependent density functional theory (TDDFT) levels of theory were applied to study optical properties and electronic structure for the $Au_9(PPh_3)_8^{3+}$ gold cluster.[170] The obtained optical absorption and MCD spectra are in reasonable agreement with experimental data and provide valuable information about the nature of each spectral peak and the effect of ligands (PH_3 and PPh_3) on the gold core behavior.

In this paper, we investigated the electronic structure of another triphenylphosphine-protected centered gold cluster $Au_8(PPh_3)_8^{2+}$ with core symmetry C_{3v} using computational methods. To study the electronic structure, DFT was utilized. Optical properties were examined using the TDDFT method to obtain optical absorption and MCD spectra for the system. In our previous study, the $Au_9(PPh_3)_8^{3+}$ cluster has a gold core with D_{2h} symmetry, which means that only B terms are present in the MCD spectrum. In contrast, in the current case of clusters with an octagold core with C_{3v} symmetry, the system will have degenerate states and *A*– and *B*–

terms are expected in the MCD spectrum. Additionally, the effects of different model functionals as well as Slater-type basis sets on the theoretical results (optical absorption and MCD spectra) were studied in this project. The obtained theoretical results were compared with experimental data[26] for the $[Au_8(PPh_3)_8](NO_3)_2$ complex in acetonitrile. The properties of the bare Au_8^{2+} core and the phosphine-protected gold cluster complex $Au_8(PH_3)_8^{2+}$ were also investigated.

Computational Method

All calculations in the present work were performed with the Amsterdam Density Functional (ADF) program.[158] Scalar relativistic effects were included by utilizing the zero-order regular approximation (ZORA).[173] Geometry optimization was performed with the generalized gradient approximation Becke-Perdew exchange-correlation functional[174, 175] and a triple-ζ Slater basis set (BP86/TZP). To trim down the computational time, we used a frozen core (fc) approximation for heavy atoms, which reduces the size of the variational basis set; a 4f frozen core was used for Au atoms, 2p for P, and 1s for C. Optimized geometries were calculated only for naked and simple phosphine–protected gold clusters. The geometry for the large triphenylphosphine–protected gold cluster $Au_8(PPh_3)_8^{2+}$ was taken from the Cambridge Crystallographic Data Centre (CCDC 907703). This crystal structure was obtained by Andersson and co–workers in 2013.[25] In this work, theoretical calculations of the optical absorption and MCD spectra for the $Au_8(PPh_3)_8^{2+}$ cluster were performed for this crystal structure without further optimization at the DFT level of theory. In order to understand the effects of ligands on the optical properties of the gold core, the optical absorption and MCD spectra of the bare and PH_3-protected Au_8^{2+} gold core were computed. Two types of $Au_8(PH_3)_8^{2+}$ clusters were considered: (i) clusters with fully optimized geometries; for example, structures $Au_8(PH_3)_8^{2+}$ (**2a** and **2b**) in **Figure 6–1**; and (ii) cluster $Au_8(PH_3)_8^{2+}$ (**3**) where the geometry of the Au_8^{2+} core was taken from the experimental structure and was constrained during the geometry optimization process (**Figure 6–1**).

To study the optical properties of ligand–protected clusters, time–dependent density functional theory was employed. It is well known that the type of functional plays an important role in the quality of theoretical results. For simulation of the optical absorption and magnetic circular dichroism spectra, five functionals were tested: LB94,[176] SAOP,[186] GRAC,[204] B3LYP[205]

and CAMY–B3LYP.[206] To study the optical properties of ligand–protected clusters, time–dependent density functional theory was employed. It is well known that the type of functional plays an important role in the quality of theoretical results. For simulation of the optical absorption and magnetic circular dichroism spectra, five functionals were tested: LB94,[176] SAOP,[186] GRAC,[204] B3LYP[205] and CAMY–B3LYP.[206] Two types of Slater-type basis sets were considered: a double–ζ (DZ) and triple–ζ (TZP) basis sets. Spectra obtained with DZ and TZP basis sets are similar: spectral shape is almost identical, but TZP results redshift with respect to DZ data (**Figure D–1**). Therefore, optical absorption and MCD spectra of system of interest are not basis sensitive, and a double–ζ (DZ) basis set will be use in this project. All functionals except for SAOP used a frozen core (fc) approximation (4f for Au atoms, 2p for P and 1s for C). In this article, we focus on the excited states with wavenumbers lower than 3.0 μm^{-1}. Implicit solvation effects on the spectra of the $Au_8(PH_3)_8^{2+}$ cluster were considered by employing the COSMO model[177] with parameters for acetonitrile using the LB94 functional.

The simulation of the MCD spectra is based on the relation:[162, 165]

$$\mathrm{MCD}(\hbar\omega) = \chi\hbar\omega \mathrm{B} \sum_J \left[A_J \left(-\frac{\partial f_J(\hbar\omega - \hbar\omega_J)}{\partial \hbar\omega} \right) + \left(B_J + \frac{C_J}{\kappa T} \right) f_J(\hbar\omega - \hbar\omega_J) \right] \qquad (6\text{–}1)$$

where $\hbar\omega$ is the energy of incident light, $\hbar\omega_J$ is the excitation energy to state J, B is the amplitude of the applied magnetic field, T is temperature, κ is Boltzmann's constant, χ is a collection of constants and experimental parameters that depend on what quantity is measured and the units, and f_J is a bandshape function. The A_J, B_J and C_J parameters describe magnetic circular dichroism terms that are important contributions to the observed MCD spectra.[163] Which term will be dominant depends on the type of investigated molecule: the A term is found only for molecules with degenerate excited states, and it has a derivative shape in the MCD spectrum; the B term arises in MCD spectra for systems with excited states close enough in energy to allow mixing; and the C term is present for paramagnetic molecules, which have a degenerate ground state, and this term is temperature dependent.[163]

Using our calculated A_J, B_J and C_J parameters and equation (6–**1**) we can calculate MCD spectra in terms of molar ellipticity $[\theta]_M$, which is independent of the major experimental parameters such as the concentration of absorption species (c), the path length (l) and magnetic field (B):[162, 165]

$$[\theta]_M = \chi\hbar\omega \sum_J \left[A_J \left(-\frac{\partial f_J(\hbar\omega - \hbar\omega_J)}{\partial \hbar\omega} \right) + \left(B_J + \frac{C_J}{\kappa T} \right) f_J(\hbar\omega - \hbar\omega_J) \right] \quad (6\text{–}2)$$

To get molar ellipticity $[\theta]_M$ in the units (deg L m^{-1} mol^{-1} G^{-1}), the energy of incident light (ω) and excitation energy to state J (ω_J) should be in a.u. and the collection of constants χ is approximately equivalent to 0.0014803.[165] The bandshape functions were chosen as normalized Gaussian functions and their derivatives:[162]

$$f_J(\omega) = \frac{1}{\sqrt{\pi} W_J} e^{-((\omega_J - \omega)/W_J)^2} \quad (6\text{–}3)$$

$$\frac{\partial f_J(\omega)}{\partial \omega} = \frac{2(\omega_J - \omega)}{\sqrt{\pi} W_J^3} e^{-((\omega_J - \omega)/W_J)^2} \quad (6\text{–}4)$$

The bandwidth parameters W_J were chosen to reproduce the observed bandwidths:

$$W_J = 0.0100\sqrt{\omega_J} \quad (6\text{–}5)$$

The MCD formalism is not gauge invariant. However, it was shown that MCD parameters depend very weakly on the choice of gauge.[162, 165] Coordinates of all simulated systems can be found in the **Appendix D**.

Results and Discussion

The geometrical structure of the $Au_8(PPh_3)_8^{3+}$ cluster stabilized by different types of counterions such as PF_6,[56] alizarinesulphonate ion,[51] and NO_3^-,[25] has been investigated experimentally using X–ray crystallography. The obtained structures of the $Au_8(PPh_3)_8^{3+}$ fragment are very similar for all considered studies. The results showed that the Au_8 gold core does not depart very much from C_{3v} symmetry: seven Au atoms form a centered chair structure and one gold atom is added above the ring. The measured Au–Au bond distances are typical for gold systems and are in the range of 2.582 to 2.892 Å (**Figure D–1**, **Table D–1**).[25, 51, 56] For this project, the geometry of the crystal structure of $Au_8(PPh_3)_8^{2+}$ reported by Andersson and co–workers in 2013[25] was used without further optimization at the DFT level of theory. This structure of the triphenylphosphine–protected gold cluster is presented in **Figure 6–1**.

The optical absorption spectra of $Au_8(PPh_3)_8^{2+}$ and $Au_8(PH_3)_8^{2+}$ were calculated using LB94, SAOP, GRAC, B3LYP, and CAMY–B3LYP functionals. Also, solvent effects on the optical absorption spectra were included using the COSMO model with acetonitrile solvent. The

results showed that the GRAC/DZ.fc method gives us a reasonable agreement with experiment for the absorption spectrum, so we will use it to calculate MCD spectra. The absorption spectrum in the acetonitrile slightly redshifts and exhibits a similar shape with respect to the spectrum in the gas phase. More detailed information can be found in the **Appendix D** (**Figure D–3**, **Figure D–4** and **Table D–2**).

Figure 6–1. A) Experimental electronic absorption (lower curve) and MCD (upper curve) spectra for $[Au_8(PPh_3)_8](NO_3)_2$ in acetonitrile at room temperature;[26] B) Crystal structure geometry of $Au_8(PPh_3)_8^{2+}$ (1);[25] and C) structures of two selected isomers of $Au_8(PH_3)_8^{2+}$ (2a) and (2b) with fully optimized geometries and cluster $Au_8(PH_3)_8^{2+}$ (3) with constrained experimental core.

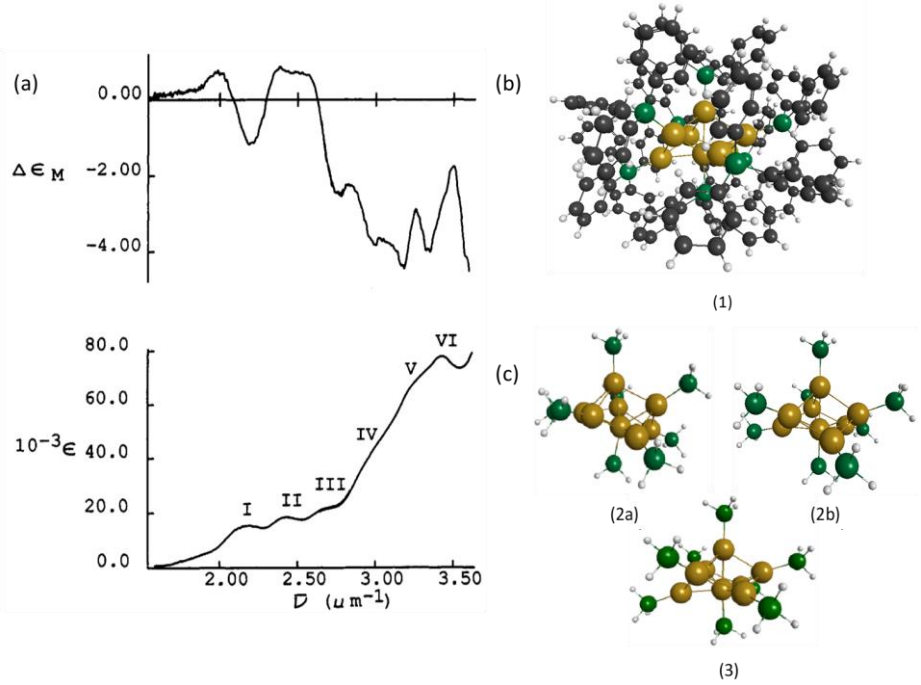

*Figure A reproduced with permission from Ref. [26]. (Copyright 1991 American Chemical Society)

Optical Properties of $Au_8(PPh_3)_8^{2+}$

Some orbitals of the $Au_8(PPh_3)_8^{2+}$ (**1**) cluster can be considered as "superatom" orbitals, where the superatom orbitals arise primarily from valence electrons on the gold atoms.[195] For the Au_8^{2+} gold core, we have 6 electrons with an expected occupation of $1S^2 1P^4 1D^0 2S^0$…, where S, P, and D are superatom orbitals that are formed from a linear combination of the valence 6s electrons of the gold atoms. The Kohn–Sham orbitals involved in low–energy

excitations of $Au_8(PPh_3)_8^{2+}$ are presented in Figure 2. The HOMO and HOMO–1 orbitals exhibit P character, whereas the first two LUMO are D superatom orbitals. The LUMO+2 is a mixture of atomic gold *s* and *p* orbitals, as well as π* orbitals on the triphenylphosphine–ligands. The other LUMO orbitals such as LUMO+3 and higher arise from the π* orbitals on the PPh_3 ligands (**Figure 6–2**). The HOMO–LUMO gap of $Au_8(PPh_3)_8^{2+}$ is 2.19 eV at the GRAC/DZ.fc level of theory.

Figure 6–2. Kohn–Sham orbitals and orbital energies of $Au_8(PPh_3)_8^{2+}$ at the GRAC/DZ.fc level of theory with IP = 0.325 a.u.

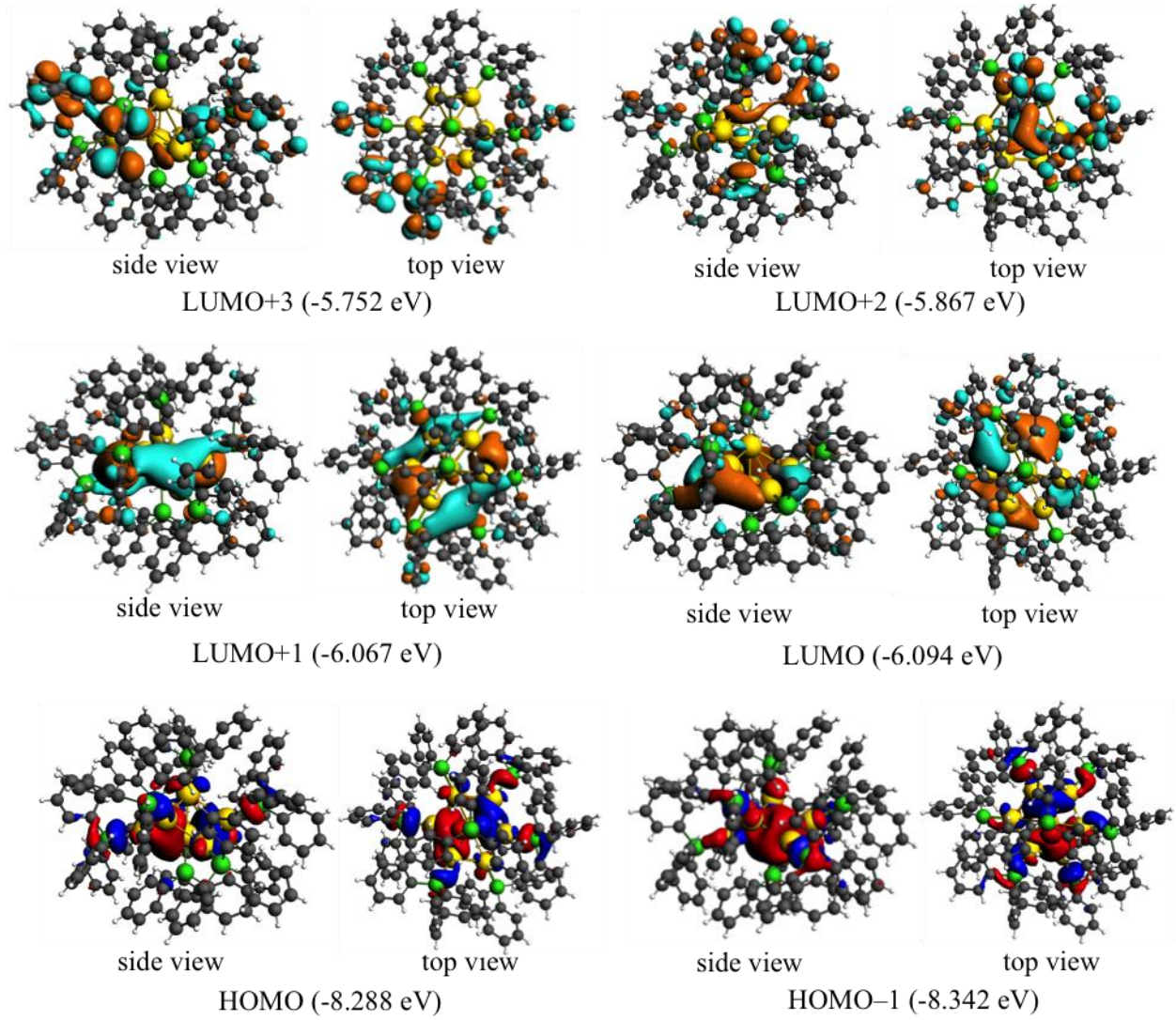

To study optical properties of the triphenylphosphine-protected small gold clusters, the optical absorption and MCD spectra were calculated using the GRAC/DZ.fc (IP = 0.325 a.u.) method. Calculation of the absorption spectrum for $Au_8(PPh_3)_8^{2+}$ (**1**) using the GRAC functional

allowed us to obtain a reasonable shape for the spectrum, which is in good agreement with experiment (**Figure 6–3**). The ionization potential for the $Au_8(PPh_3)_8^{2+}$ (1) cluster was calculated at the BP86/TZP.fc level of theory with the equation: IP = E[$Au_8(PPh_3)_8^{3+}$] – E[$Au_8(PPh_3)_8^{2+}$], which is the energy difference between the triphenylphosphine-protected Au_8 cluster with charges +3 and +2, without geometry optimization.

Figure 6–3. Calculated optical absorption and MCD spectra for $Au_8(PPh_3)_8^{2+}$ (1). Method GRAC/DZ.fc with IP = 0.325 a.u.

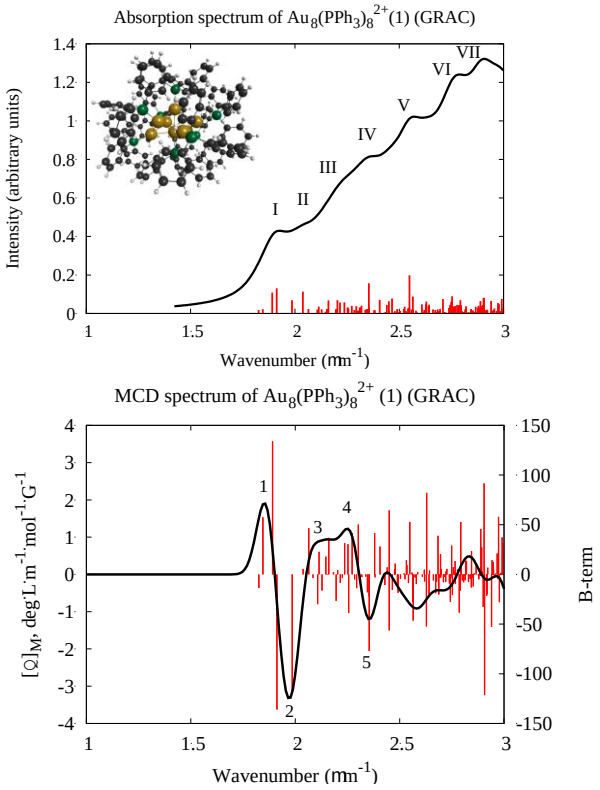

The results show that the theoretical absorption and MCD spectra of the $Au_8(PPh_3)_8^{2+}$ cluster are very complicated for interpretation due to the great number of excitations that occur in this system (**Figure 6–3**). Therefore, to simplify the spectral analysis of the absorption spectrum, only the excited states with oscillator strengths higher than $f \approx 0.01$, which is an average value for all excited states in the region below 3.0 μm^{-1}, will be considered. For the MCD spectrum, the determination of the most important excited states will be performed for each specific peak individually because of some of the peaks are formed by excitations with a very small absolute value of *B*, whereas other peaks are combinations of very strong excited states (**Tables D–3** and **D–4**). The obtained theoretical data will be compared with experimental absorption and MCD spectra for the $[Au_8(PPh_3)_8](NO_3)_2$ cluster in acetonitrile at room

temperature, measured by Jaw and Mason (**Figure D–5**).18 In this analysis, we will be focused only on excitations in the theoretical absorption and MCD spectra with wavenumbers below 2.45 μm^{-1}. In the region above 2.45 μm^{-1}, the theoretical results are expected to be especially sensitive to factors such as the type of model functional used, the presence of counterions, and slight differences in the geometry between the crystal structure of $Au_8(PPh_3)_8^{2+}$ and the structure of $[Au_8(PPh_3)_8](NO_3)_2$ in a solution of acetonitrile.

The absorption spectrum for $Au_8(PPh_3)_8^{2+}$ is presented in **Figure 6–3**. The shape of this simulated electronic spectrum is very close to the experimental spectrum (**Figure 6–1a**). The theoretical absorption spectrum exhibits seven bands with energy below 3.0 μm^{-1}: at 1.93, 2.04, 2.20, 2.35, 2.55, 2.79, and 2.91 μm^{-1}. This theoretical absorption spectrum of $Au_8(PPh_3)_8^{2+}$ is red-shifted with respect to the empirical spectrum[26] for $[Au_8(PPh_3)_8](NO_3)_2$ in acetonitrile (**Table 6–1**).

Table 6-1. Experimental[26] and theoretical electronic absorption and MCD spectral data for the $Au_8(PPh_3)_8^{2+}$ cluster.

Experiment					Theory				
	absorption	MCD			absorption		MCD		
	wavenumber (μm^{-1})	#	wavenumber (μm^{-1})	peak sign		wavenumber (μm^{-1})		wavenumber (μm^{-1})	$[\theta]_M$
		1	1.98	pos	I	1.93	1	1.86	+1.90
I	2.19	2	2.20	neg	II	2.04	2	1.97	–3.31
II	2.43	3	2.38	pos	III	2.20	3	2.15	+0.94
III	2.71	4	2.51	pos			4	2.25	+1.22
		5	2.76	neg	IV	2.35	5	2.35	–1.19

$[\theta]_M$ has units of deg L m^{-1} mol^{-1} G^{-1}

The calculated MCD spectrum for the $Au_8(PPh_3)_8^{2+}$ cluster is presented in **Figure 6–3**. According to the obtained results, we can conclude that the first five theoretical MCD peaks 1−5 are identical to the first five peaks from the experimentally measured MCD spectrum (**Figure 6–1a**). The first calculated MCD band 1 with a peak maximum at 1.86 μm^{-1} is a strong positive peak, which is a combination of four relatively strong excitations at 1.83, 1.85, 1.89, and 1.91 μm^{-1}. This theoretical peak is correlated with the first positive peak in the experimental MCD spectrum at 1.98 μm^{-1} (**Table 6–1**). This peak was not labeled in the experimental absorption spectrum; we denote it as band I in the theoretical absorption spectrum in **Figure 6–3**, and its maximum in absorption occurs at 1.93 μm^{-1}. It is common for MCD and absorption

spectra to differ slightly in the energy/wavenumber of the peak maxima due in part to the effect of the magnetic field on the excitation energies and because maxima in oscillator strength do not always correlate with maxima in the *A*, *B*, and *C* terms.

The next predicted MCD peak 2 considered at 1.97 μm^{-1} is negative and formed by two excitations at 1.99 and 2.06 μm^{-1}. This peak is red-shifted by 0.23 μm^{-1} with respect to experimental peak 2 (**Table 6–1**). This peak corresponds to band II in the theoretical absorption spectrum at 2.04 μm^{-1} (band I in the experimental spectrum at 2.19 μm^{-1}). The next two theoretical MCD bands 3 and 4 are positive with maxima at 2.15 and 2.25 μm^{-1}. These two peaks are formed by excitations with wavenumbers from 2.11 to 2.27 μm^{-1}. The calculated MCD peaks 3 and 4 are related to positive third and fourth bands in the experimental MCD spectrum and red-shifted by 0.23 and 0.26 $\mu m^{-1}$with respect to the empirical peaks, respectively. The theoretical peak 5 has a minimum at 2.35 μm^{-1}. This peak is a combination of excitations from 2.30 to 2.45 μm^{-1}. The theoretical MCD peak 5 can be correlated to the negative MCD peak 5 at 2.76 $\mu m^{-1}$from the experimental spectrum (**Figure 6–3** and **Table 6–1**).

In order to see similarities and differences in the absorption and MCD bands below 2.45 μm^{-1}, an analysis of the electronic transitions of the calculated absorption and MCD spectra was also performed. These results showed that band I in the absorption spectrum is related to peak 1 in the MCD: they arise from similar electronic transitions such as HOMO → LUMO, HOMO → LUMO+1, HOMO−1 → LUMO, and HOMO−1 → LUMO+1 (Tables S3 and S4). This first peak in the absorption and MCD spectra can be assigned to the intramolecular transitions inside the gold cluster framework because these transitions occur from “superatom” orbitals of P character to D “superatom” orbitals within the gold core. Band II in the absorption spectrum arises from electronic transitions out of HOMO and HOMO−1 to LUMO+2, whereas the negative peak 2 in the MCD spectrum appears because of transitions from HOMO to the LUMO+2 and LUMO+3. However, despite some differences in the set of electronic transitions that form band II in the absorption and peak 2 in the MCD spectra, for both types of spectroscopy this band arises due to electronic transitions out of P “superatom” orbitals of the gold core to the π* orbitals on the PPh_3 ligands. Bands III and IV from the absorption and peaks 3−5 from the MCD spectra appear due to transitions between HOMO−1 and LUMO+19 orbitals. These bands are again observed because of excitations between “superatom” P orbitals of gold atoms and π* orbitals of the triphenylphosphine ligands.

The next part of the spectrum with wavenumbers above 2.45 μm^{-1} exhibits a shape similar to the experimental spectrum in the range 2.80−3.5 μm^{-1}, but the intensity of this part of the theoretical spectrum is much weaker than in the experiment (**Figure 6–3**). The analysis of the excitations with wavenumbers > 2.45 μm^{-1} showed that this part of the spectrum arises due to transitions from the occupied orbitals that are mixture of the d orbitals on the gold core and π orbitals on the triphenylphosphine ligands to the unoccupied π* orbitals of the PPh_3 ligands (**Tables D–3** and **D–4**). Analysis of the *B* term values for every excited state in the wavenumber region 2.45−3.0 μm^{-1} showed that many pairs of excitations are located near to each other in energy and have very similar high absolute values of the *B* parameter although with opposite signs, which makes their strengths cancel out (**Figure 6–3**). Differences in the theoretical and the experimental MCD signal intensities in the high-energy region (above 2.45 μm^{-1}) could arise as an effect of solvent molecules and/or counterions, which are not included in these calculations. Also, the structure crystal structure of $Au_8(PPh_3)_8^{2+}$, with respect to the structure of $[Au_8(PPh_3)_8](NO_3)_2$ in a solution of acetonitrile, could be more symmetrical, and extra symmetry elements that exist in the crystal structure could make some types of transitions not allowed (or much weaker). Additionally, the type of model functional could not be sufficient to appropriately simulate the excitations in the organic part of the system (the electron transitions from the occupied π orbitals to the unoccupied π* orbitals of organic ligands, which are responsible for this part of spectrum). Overall, multiple factors could be responsible for the discrepancy between the experimental and theoretical peak intensities above 2.45 μm^{-1}.

Ligand Effect (PPh_3 vs. PH_3).

To understand the effect of the ligand nature on the optical properties of the gold core, the optical absorption and MCD spectra for the Au_8^{2+} cluster protected by PH_3 were calculated and compared with the results for the $Au_8(PPh_3)_8^{2+}$ cluster. Two types of $Au_8(PH_3)_8^{2+}$ clusters were considered: (i) cluster $Au_8(PH_3)_8^{2+}$ (**2**) with fully optimized geometry; and (ii) cluster $Au_8(PH_3)_8^{2+}$ (**3**) where the geometry of the Au_8^{2+} core was taken from the experimental crystal structure and was constrained during the geometry optimization process (**Figure 6–1c**).

Fully optimized $Au_8(PH_3)_8^{2+}$ structure. During the full geometry optimization process of $Au_8(PH_3)_8^{2+}$, eight isomers were found with energy differences up to 1.2 kcal/mol. Geometries and relative energies of all $Au_8(PH_3)_8^{2+}$ isomers (**2a**−**2i**) are shown in the **Appendix D** (**Table**

D–1 and **Figure D–6**). The most energetically preferable structure with no imaginary frequencies is $Au_8(PH_3)_8^{2+}$ (**2a**). The geometries of the Au_8 core in the seven most stable isomers of $Au_8(PH_3)_8^{2+}$ (**2a**, **2c**−**2i**) are slightly different in comparison to the structure of the gold core surrounded by triphenylphos- phine ligands in $Au_8(PPh_3)_8^{2+}$ (**1**): the central six Au atoms exhibit a "half-chair cyclohexane" structure instead of the expected "chair cyclohexane" structure (**Figure D–6**). However, the least stable of these isomers, $Au_8(PH_3)_8^{2+}$ (**2b**), has a structure of the Au_8 core that is very similar to the gold core in the experimental $Au_8(PPh_3)_8^{2+}$ (**1**) cluster:[25] seven Au atoms form a centered "chair" structure, and one gold atom is added above the ring. The results showed that Au−Au bonds and Au−P distances in the theoretical $Au_8(PH_3)_8^{2+}$ (**2b**) cluster are longer than in the crystal structure of $Au_8(PPh_3)_8^{2+}$ (**1**) by up to 0.23 and 0.04 Å, respectively. This difference can be explained by the different size of the PH_3 and PPh_3 ligands as well as application of the GGA exchange correlation functional BP86 for geometry optimization, which usually predicts elongated bond lengths.

Figure 6–4. Optical absorption and MCD spectra for A) $Au_8(PH_3)_8^{2+}$ (2b) and B) $Au_8(PH_3)_8^{2+}$ (3). Method GRAC/DZ.fc (IP = 0.40 a.u.).

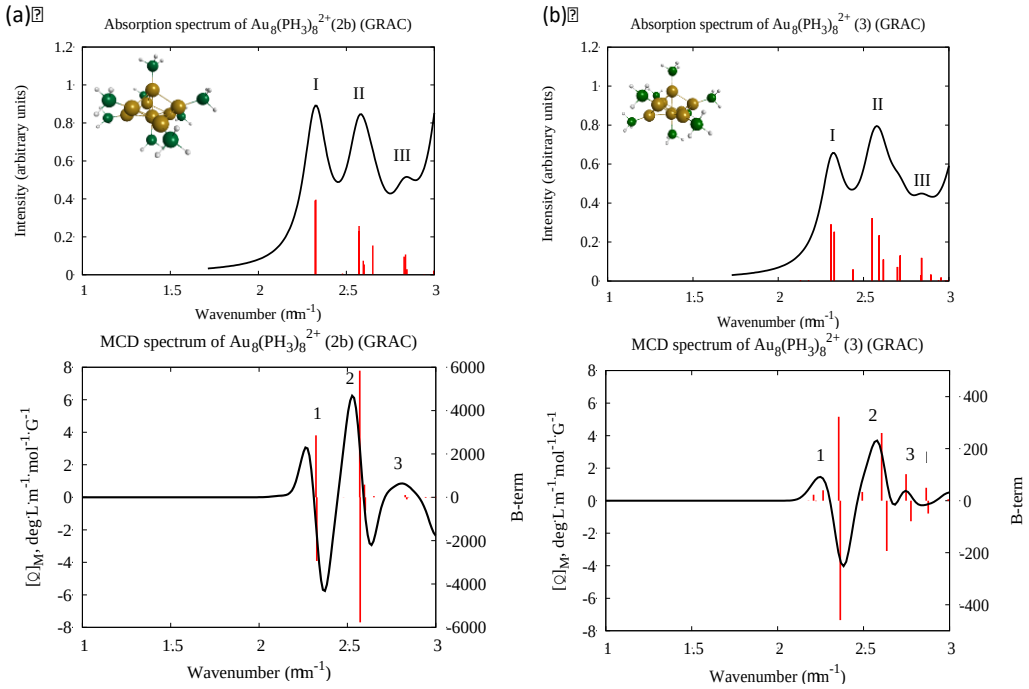

Because the $Au_8(PH_3)_8^{2+}$ (**2b**) cluster has a Au8 gold core shape very similar to that observed for the empirical $Au_8(PPh_3)_8^{2+}$ (**1**) structure, the optical absorption and MCD spectra will be theoretically simulated for this isomer using GRAC/DZ.fc (IP = 0.40 au) (**Figure 6–4**).

Figure 6–5. Kohn–Sham orbitals of $Au_8(PH_3)_8^{2+}$ (2b). Method GRAC/DZ.fc (IP = 0.40 a.u.).

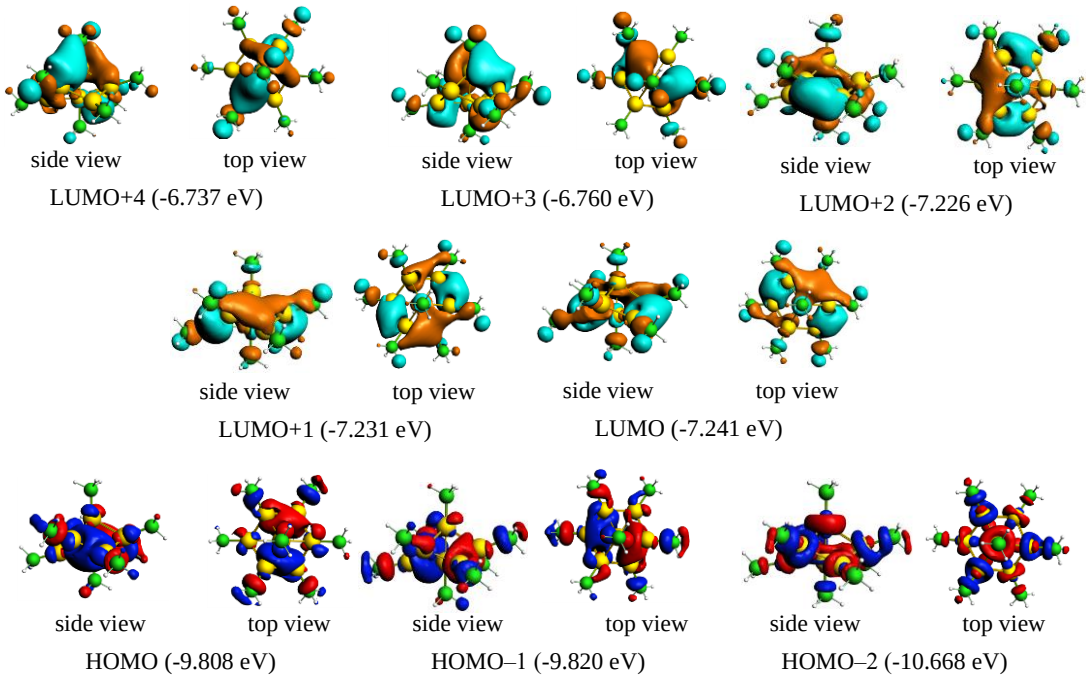

Table 6-2. Calculated absorption and MCD spectral data for $Au_8(PH_3)_8^{2+}$ (**2b**) and $Au_8(PH_3)_8^{2+}$ (**3**) structures. Method GRAC/DZ.fc (IP = 0.40 a.u.).

Spectral data for $Au_8(PH_3)_8^{2+}$ (**2b**)					Spectral data for $Au_8(PH_3)_8^{2+}$ (**3**)				
no	absorption		MCD		no.	absorption		MCD	
	wavenumber (μm^{-1})	no.	wavenumber (μm^{-1})	$[\theta]_M$		wavenumber (μm^{-1})	no.	wavenumber (μm^{-1})	$[\theta]_M$
I	2.35	1	2.27	+3.01	I	2.32	1	2.25	+1.47
			2.37	–2.76				2.39	–4.03
II	2.56	2	2.53	+6.25	II	2.58	2	2.58	+3.69
			2.64	–2.71		2.74[s]		2.70	–0.48
III	2.84	3	2.81	+0.85	III	2.83	3	2.74	+0.60
								2.83	–0.28

[s] – shoulder peak
$[\theta]_M$ has units of deg L m^{-1} mol^{-1} G^{-1}

Analysis of the orbitals for $Au_8(PH_3)_8^{2+}$ (2b) shows that the orbitals between HOMO–2 and LUMO+4 are primarily located on the gold core (**Figure 6–5**), whereas for the triphenylphosphine–protected gold cluster, the π and π* orbitals of the ligands are also involved in the formation of orbitals that are located above the LUMO+1 and below the HOMO–1 orbitals (**Figure 6–2**). Despite this, there are some similarities in orbital character for the PH_3

and PPh_3 stabilized Au_8^{2+} cores: in both systems the HOMO and HOMO–1 orbitals are P "superatom" orbitals, and LUMO and LUMO+1 exhibit D character (**Figure 6–5**). The HOMO–LUMO gap for the simple phosphine–protected gold cluster $Au_8(PH_3)_8^{2+}$ (**2b**) is equivalent to 2.58 eV using GRAC/DZ.fc (IP = 0.40 a.u.).

In the $Au_8(PH_3)_8^{2+}$ (**2b**) cluster, the gold core is highly symmetric with essentially C_{3v} symmetry. Systems with C_{3v} symmetry have degenerate states, which means that *A*– and *B*– terms would be expected in the MCD spectrum. However, addition of the PH_3 ligands lowers the symmetry of the system and the degenerate states split slightly, although they remain nearly degenerate. In this case, the MCD spectrum of the $Au_8(PH_3)_8^{2+}$ (**2b**) cluster will display only *B* terms because there are no degenerate excited states, which are necessary for observing *A* terms. The states, which are no longer degenerate due to ligation of the core, are still very close in energy and have approximately equal absolute values of *B*, but with opposite sign. In the absorption spectrum, the nearly degenerate states are also close in energy and exhibit very similar oscillator strength values (**Figure 6–4**).

The calculated absorption and MCD spectra of the $Au_8(PH_3)_8^{2+}$ (**2b**) cluster have three related bands I, II, and III (labeled 1, 2, and 3 in the MCD spectrum) under 3.0 μm^{-1} (**Figure 6–4**, **Table 6–2**). Both of these spectra arise out of the same electron transitions. Absorption band I is located at 2.35 μm^{-1}; it is formed by two strong near–degenerate excitations at 2.32 (f = 0.123) and 2.33 (f = 0.123) μm^{-1} (Table 2). This absorption band is related to the first band of the MCD spectrum, which contains positive and negative peaks at 2.27 and 2.37 μm^{-1}. The calculated MCD band 1 arises from the same excitations as absorption band I. The absolute values of the *B* terms for these excited states are very close, but they have the opposite sign: B = 2858.1 and –2935.9, respectively (**Table D–5** and **Table D–6**). The shape of the convoluted MCD signal for these nearly degenerate excitations has a shape similar to the derivative–like shape, which is generally supposed to be observed only in the case of degenerate states (when the *A*–term appears) (Figure 4). It is satisfying to note that these nearly degenerate states yield the same overall character, even though the state is not perfectly degenerate. Band I in the absorption spectrum and band 1 in the MCD spectrum arise from electronic transitions HOMO→ LUMO+2, HOMO–1 → LUMO and HOMO–1 → LUMO+1, which correspond to electronic transitions from occupied P to unoccupied D "superatom" orbitals of the gold core

(**Table D–5** and **Table D–6**), which is similar to the first band in the triphenylphosphine-stabilized system.

The next absorption band is band II with a maximum at 2.56 μm^{-1}. This band is a combination of the five excitations at 2.57 (f = 0.071), 2.57 (f = 0.081), 2.60 (f = 0.023), 2.60 (f = 0.017) and 2.65 (f = 0.048) μm^{-1}. These excitations form band 2 in the theoretical MCD spectrum. The calculated MCD band 2 also includes two peaks: a positive peak at 2.53 μm^{-1} and a negative one at 2.64 μm^{-1}. Band II in the absorption and band 2 in the MCD spectra arise from transitions out of HOMO and HOMO–1 to the LUMO+3, LUMO+4, and LUMO+5, which correspond to electron transitions inside the gold core framework (**Figure 6–5**, **Table D–5** and **Table D–6**), which do not have a direct analog in the triphenylphosphine-stabilized system. The last band in the theoretical absorption and MCD spectra under 3.0 μm^{-1} is band III (band 3). It is relatively weak in both types of spectra. This band is located at 2.84 μm^{-1} in the absorption spectrum. In the MCD spectrum, band 3 is a small, positive peak at 2.81 μm^{-1}. The excitations involved in the formation of this band are located at 2.83, 2.84 and 2.84 μm^{-1}. This peak arises due to electron transitions from the *d* orbitals of gold atoms (HOMO–2) to orbitals with D "superatom" character such as LUMO, LUMO+1, and LUMO+2.

Comparison of the theoretical spectra for the PH_3 ligand-protected gold core with theoretical data for the PPh_3–stabilized system shows that the calculated absorption and MCD spectra for the $Au_8(PH_3)_8^{2+}$ cluster are blueshifted with respect to $Au_8(PPh_3)_8^{2+}$ by ~0.5 μm^{-1}.

Cluster $Au_8(PH_3)_8^{2+}$ with experimental gold core. Cluster $Au_8(PH_3)_8^{2+}$ (**3**) was obtained by substitution of the PPh_3 ligands by simple PH_3 in the crystal structure of $Au_8(PPh_3)_8^{2+}$ (**1**). Geometry optimization was performed only for the ligand shell, whereas the gold core was constrained and kept at the experimental crystal structure geometry during the optimization process. The results showed that the positions of the PH_3 ligands in $Au_8(PH_3)_8^{2+}$ (**3**) and the fully optimized $Au_8(PH_3)_8^{2+}$ (**2b**) are very similar: the maximum difference in Au-P distances is 0.008 Å.

Calculated optical absorption and MCD spectra for $Au_8(PH_3)_8^{2+}$ (**3**) exhibit very similar spectral shapes and peaks position to those observed for the $Au_8(PH_3)_8^{2+}$ (**2b**) cluster (**Figure 6–4** and **Table 6–2**). However, the intensity of the absorption and MCD signals is ~2 times weaker for the cluster with experimental core $Au_8(PH_3)_8^{2+}$ (**3**). This can be explained by the slightly different geometry of the gold core: the experimental gold core is less symmetric than the Au8

core in the theoretical $Au_8(PH_3)_8^{2+}$ (**2b**) cluster. This can be a cause of the more significant splitting of the degenerate excited states in $Au_8(PH_3)_8^{2+}$ (**3**) with the less symmetrical core than in the $Au_8(PH_3)_8^{2+}$ (**2b**) structure. These results show that for gold clusters protected by simple ligands, the difference in the geometry of the gold core in $Au_8(PH_3)_8^{2+}$ (**2b**) and $Au_8(PH_3)_8^{2+}$ (**3**) affects only the intensity of the spectra and has no major effect on the shape and peak position. The HOMO−LUMO gap (2.58 eV) of $Au_8(PH_3)_8^{2+}$ (**3**) is similar to the gap of the fully optimized structure $Au_8(PH_3)_8^{2+}$ (**2b**). Therefore, the band gap increases by 0.37 eV when PPh3 ligands are substituted by the simple phosphine ligands PH_3.

Absorption and MCD spectra for both $Au_8(PH_3)_8^{2+}$ structures are less complicated with respect to the triphenylphosphine–protected gold core: they exhibit just a few relatively strong excitations, which form three bands in the region up to 3.0 μm^{-1} (**Figures 6–3** and **6–4**). All of these excited states occur due to electron transitions within the Au_8^{2+} gold core framework only. The simulated spectra for $Au_8(PPh_3)_8^{2+}$ exhibit a great number of excitations in the energy region up to 3.0 μm^{-1}, which are possible due to electron transitions between orbitals of the gold core, between the gold core and ligands, and within the ligands. So, PPh_3 ligands have a stronger effect on the optical properties of Au_8^{2+} in comparison to the PH_3 ligands in the spectral region under 3.0 μm^{-1}.

Optimized bare gold core (Au_8^{2+}). In order to understand what changes happen to the bare gold core during the ligation process, the simulation of its geometrical structure and optical properties were also performed. The optimized geometry of the bare Au_8^{2+} cluster exhibits a structure similar to the Au_8 fragment in $Au_8(PH_3)_8^{2+}$ and $Au_8(PPh_3)_8^{2+}$, where the seven Au–atoms form a centered "chair–cyclohexane" structure with one gold atom added above the ring (**Table D–1**). The symmetry of the bare gold structure is idealized C_{3v}. A comparison of the Au–Au bonds between the central gold atom and the other seven peripheral atoms in the bare Au_8^{2+} gold cluster and in the fully optimized $Au_8(PH_3)_8^{2+}$ (**2b**) showed that metal bonds become shorter by up to 0.10 Å during ligation by PH_3 (**Table D–1**).

The HOMO–LUMO gap of bare Au_8^{2+} is 1.39 eV, which is 1.20 eV less than the obtained bandgap for PH_3-stabilized complexes at the GRAC/DZ.fc level of theory. The HOMO, LUMO, LUMO+1 and LUMO+2 Kohn–Sham orbitals for Au_8^{2+} are presented in **Figure 6–6**. These orbitals are superatom orbitals. The doubly degenerate HOMO and singly degenerate LUMO orbitals have P superatom character, whereas the doubly degenerate

LUMO+1 and singly degenerate LUMO+2 are D orbitals. For all considered systems (Au_8^{2+}, $Au_8(PH_3)_8^{2+}$ and $Au_8(PPh_3)_8^{2+}$), the HOMO is a P superatom orbital. However, the LUMO orbital is sensitive to the presence of the ligand shell: for the bare gold cluster the LUMO has P character, whereas when PH_3 or PPh_3 ligands are present in the system, the LUMO is D. For Au_8^{2+} and $Au_8(PH_3)_8^{2+}$ clusters, the LUMO+1 and LUMO+2 are D superatom orbitals. However, for the $Au_8(PPh_3)_8^{2+}$ cluster the LUMO+1 is D, but LUMO+2 and higher orbitals are primarily π* orbitals of the triphenylphosphine ligands.

Figure 6–6. Kohn–Sham orbitals of Au_8^{2+}. Method GRAC/DZ.fc (IP = 0.60 a.u.).

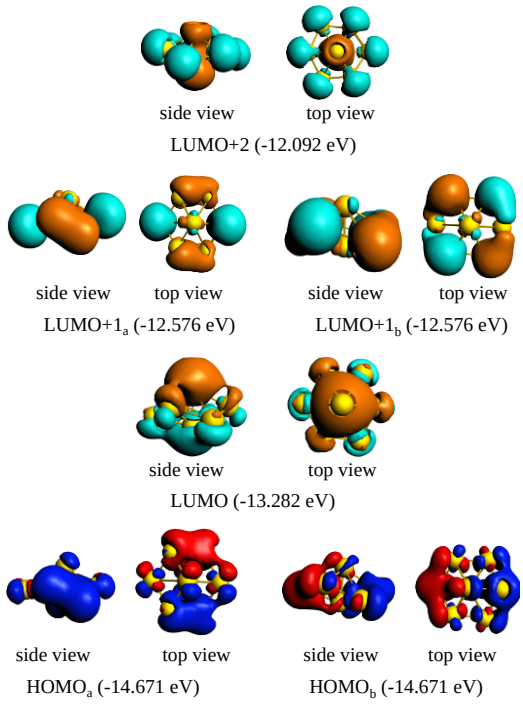

The absorption and MCD spectra were calculated for the Au_8^{2+} cluster using GRAC/DZ.fc with IP = 0.60 a.u. These spectra are presented in **Figure 6–7**. The first peaks in both spectra redshift by 0.15 μm^{-1} and 0.57 μm^{-1} with respect to $Au_8(PPh_3)_8^{2+}$ and $Au_8(PH_3)_8^{2+}$, respectively. The calculated absorption spectrum for the gold core exhibits four bands in energy below 3.0 μm^{-1}: 1.78, 1.98, 2.40 and 2.79 μm^{-1} (**Figure 6–7**, **Table D–7**). Because both the HOMO and LUMO have P character, a transition between these orbitals is forbidden. Absorption band I arises from HOMO → LUMO+1 transitions. The second and third bands are located at 1.98 and 2.40 μm^{-1}. The second band appears due to HOMO → LUMO+1 and HOMO → LUMO+2 electron transitions, whereas the third peak arises from the same HOMO to LUMO+1 and LUMO+2 transitions, as well as an additional electronic transition between

HOMO–6 → LUMO. The high–energy band IV at 2.79 μm^{-1} arises because of electron transitions between HOMO–11 and LUMO+2 orbitals. The HOMO–6 (singly degenerate) and HOMO–11 (doubly degenerate) orbitals both are a mixture of atomic gold *d* orbitals. The obtained results showed some similarities as well as differences from orbitals involved in the absorption spectra of the bare Au_8^{2+}, $Au_8(PH_3)_8^{2+}$, and $Au_8(PPh_3)_8^{2+}$ clusters.

Figure 6–7. Optical absorption and MCD spectra for optimized bare the Au_8^{2+} (C_{3v}) gold core. Method GRAC/DZ.fc (IP = 0.60 a.u.).

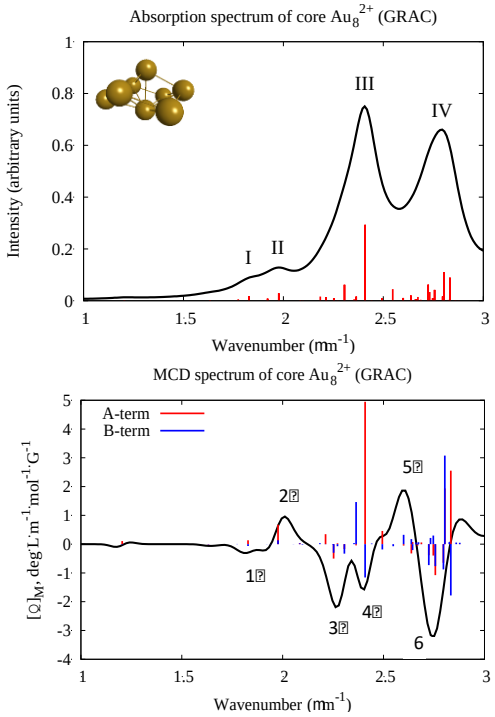

Table 6-3. Calculated absorption and MCD spectral data for bare Au_8^{2+} using GRAC/DZ.fc (IP = 0.60 a.u.).

absorption		MCD		
band no.	wavenumber (μm^{-1})	band no.	wavenumber (μm^{-1})	$[\theta]_M$, deg L m^{-1} mol^{-1} G^{-1}
I	1.78	1	1.80	–0.31
			1.90	–0.22
II	1.98	2	2.01	+0.96
III	2.40	3	2.26	–2.19
		4	2.40	–1.57
IV	2.79	5	2.59	+1.86
		6	2.76	–3.23

The results showed that for the Au_8^{2+} and $Au_8(PH_3)_8^{2+}$ clusters similar orbitals are involved in the considered part of the absorption spectra. The first two peaks arise due to the

gold cluster framework only: from superatom P to superatom D orbitals. The remaining part of the absorption spectra (up to 3.0 μm^{-1}) for Au_8^{2+} and $Au_8(PH_3)_8^{2+}$ clusters appears essentially due to electron transitions from the d orbitals on the gold core to the superatom P and D orbitals. In the case of the $Au_8(PPh_3)_8^{2+}$ system, the first absorption peak arises because of electron transitions between P → D, which is similar to the bare and PH_3 ligand-protected systems. However, the electronic transitions involved in the formation of the rest of the absorption spectra are different from the transitions observed for Au_8^{2+} and $Au_8(PH_3)_8^{2+}$ clusters: absorption bands between 2.0 and 2.45 μm^{-1}appear because of the electronic transitions from the gold core superatom orbital P to the π* orbitals on the PPh_3 ligands. Excitations with wavenumbers 2.45−2.86 μm^{-1} are assigned to electron transitions from occupied orbitals that are mixtures of the d orbitals on the gold core and π orbitals on the triphenyl- phosphine ligands to the unoccupied π* orbitals of the PPh_3 ligands. So, in the case of triphenylphosphine-protected gold cluster, the π and π* orbitals of the PPh_3 ligands are actively involved.

The theoretical MCD spectrum of the bare gold core (**Figure 6–7**) exhibits five bands and is not as clean as the simple phosphine-stabilized system. For this core with symmetry C_{3v}, the MCD spectrum contains both *A*– and *B*–terms (**Figure 6–7**), which indicates the presence of degenerate excited states. Band 1 is negative and contains two peaks at 1.80 and 1.90 μm^{-1}. The second MCD band has positive magnitude and is located at 2.01 μm^{-1}. These first two MCD bands correlate with absorptions bands I and II at 1.78 and 1.98 μm^{-1}. Peaks 3 and 4 arise from two negative bands at 2.26 and 2.40 μm^{-1}, which are assigned to absorption band III (**Table 6–3**).

Conclusions

The theoretical calculation of the optical absorption and magnetic circular dichroism spectra were performed for $Au_8(PPh_3)_8^{2+}$, $Au_8(PH_3)_8^{2+}$ and Au_8^{2+} clusters using TDDFT. Geometry optimization was performed only for $Au_8(PH_3)_8^{2+}$ and Au_8^{2+} structures, whereas the geometry of $Au_8(PPh_3)_8^{2+}$ was obtained from the experimental crystal structure. Different model functionals and basis sets were tested for calculation of optical absorption and MCD spectra.

The obtained results show that the theoretical absorption and MCD spectra of $Au_8(PPh_3)_8^{2+}$ calculated with the GRAC functional are in good agreement with experimental data. The first five theoretical MCD bands (1−5) have the same shape as the first five peaks in the experimental MCD spectrum for $[Au_8(PPh_3)_8](NO_3)_2$. The theoretical MCD band 1 arises

due to transitions of the gold cluster framework only, whereas peaks 2−5 appear because of the electronic transitions from the gold core orbitals to the π* orbitals on the PPh_3 ligands. The high- energy part of the theoretical MCD spectrum (wavenumber range > 2.45 μm^{-1}) is poorly simulated, with peak intensity much weaker than experiment. The bands in this part of the spectrum occur due to electron transitions primarily from the occupied π to the unoccupied π* orbitals of the ligands.

Comparison of the theoretical spectra for the PH_3 ligand–protected gold core with theoretical data for the PPh_3–stabilized system showed that triphenylphosphine ligands have a stronger effect on the optical properties of the Au_8^{2+} gold core in comparison to the PH_3 ligands. Moreover, the absorption and MCD spectra for $Au_8(PH_3)_8^{2+}$ are less complicated with respect to the triphenylphosphine-protected gold core. In this system, all excited states with wavenumbers up to 3.0 μm^{-1} occur due to electronic transitions within the Au_8^{2+} gold core framework only. The calculated optical spectrum for $Au_8(PH_3)_8^{2+}$ is blueshifted with respect to $Au_8(PPh_3)_8^{2+}$ by ~0.5 μm^{-1}. Optical absorption and MCD spectral data showed that for gold clusters protected by simple PH_3 ligands, the differences in the geometry of the gold core in the fully optimized cluster $Au_8(PH_3)_8^{2+}$ (**2b**) and in the cluster with crystal structure core $Au_8(PH_3)_8^{2+}$ (**3**) primarily affect the intensity of the spectra, and have no major effect on the shape and peak positions.

Geometrical parameters and optical properties of the bare Au_8^{2+} cluster were compared with ligand-stabilized species. This allows for an understanding of the effects of the gold core deformation and changes in optical properties after ligation. The calculations also showed that ligands have an effect on the electronic structure of the gold core. Both optical absorption and MCD spectra of the bare gold cluster are red-shifted with respect to $Au_8(PPh_3)_8^{2+}$ and $Au_8(PH_3)_8^{2+}$. The HOMO−LUMO gaps are 1.39, 2.58, 2.58, and 2.19 eV for Au_8^{2+}, $Au_8(PH_3)_8^{2+}$ (**2b**), $Au_8(PH_3)_8^{2+}$ (**3**) and $Au_8(PPh_3)_8^{2+}$ (**1**), respectively.

Overall, the obtained theoretical MCD spectrum for the triphenylphosphine-stabilized Au8 system is in very good agreement with the experimental curve. The theoretical analysis provides significant additional information about the electronic structure for this system.

Acknowledgement

This material is based on work supported by the National Science Foundation under Grant CHE-1507909. The computing for this project was performed on the Beocat Research

Cluster at Kansas State University, which is funded in part by NSF grants CNS-1006860, EPS-1006860, and EPS-0919443.

Chapter 7 - Theoretical Study of the Plasmon Resonance in AgNPs: MCD Spectroscopy

Natalia V. Karimova, Christine Aikens

Abstract

Localized surface plasmon resonance (LSPR) is an optical phenomenon generated from collective oscillation of the surface electrons in a conduction band by direct illumination. Plasmonic behavior of neutral and charged silver nanoparticles (AgNPs) of different sizes and shapes was investigated using TDDFT methods. Optical absorption and MCD spectra were simulated for octahedral (Ag_{19}^{-1}, Ag_{19}^{+1}, Ag_{38}^{+4}, Ag_{44}^{-2}), tetrahedral (Ag_{10}^{+2}, Ag_{20}^{0}, Ag_{35}^{+1}, Ag_{35}^{-5}) and icosahedral (Ag_{13}^{-5}, Ag_{13}^{+5}, Ag_{43}^{+3}) silver nanoparticles. Moreover, in order to be able to calculate spectra for negatively charged systems, an augmented triple-ζ basis set with frozen core (ATZP.fc) for silver atoms was developed for the Amsterdam Density Functional (ADF) program. For the considered structures, *A* and *B* terms are expected in the MCD spectrum. The degeneracy of the plasmonic excited state is broken by the magnetic field, which leads to a derivative shape of the signal in the MCD spectrum. These theoretical results show that clusters Ag_{10}^{+2}, Ag_{20}^{0}, Ag_{19}^{-1}, Ag_{19}^{+1}, Ag_{38}^{+4}, Ag_{13}^{-5}, Ag_{13}^{+5}, and Ag_{43}^{+3} can be considered as plasmonic NPs: the optical absorption spectra of all these structures have a strong sharp peak and this peak is correlated with a strong derivative-shaped band in the MCD spectra.

Introduction

The localized surface plasmon resonance (LSPR) is an optical phenomenon that arises from the interaction between an electromagnetic wave and the conduction electrons in materials. Direct illumination drives the conduction electrons in a nanoparticle to collectively oscillate.[207, 208] Resonance behavior can be observed when two conditions are satisfied: the dielectric constant of the particle is negative and the particle is much smaller than the wavelength of light in the surrounding medium.[208, 209] These two conditions are realized in metallic nanoparticles such as Au, Ag, Al and Cu.[113, 210-229] Silver and gold nanoparticles are particularly interesting

systems due to their capability to produce high quality localized surface plasmon resonances in the visible region of the electromagnetic spectrum (**Figure 7–1**). These metals have a high density of conduction electrons and relatively low degree of losses. In fact, silver nanoparticles have the strongest plasmon resonances of all known materials.[207] A resonant frequency strongly depends on the composition, size, geometry, dielectric environment and separation of NPs.[189, 208, 220-222, 230-236]

Figure 7–1. Optical spectroscopy measurements of individual silver NPs

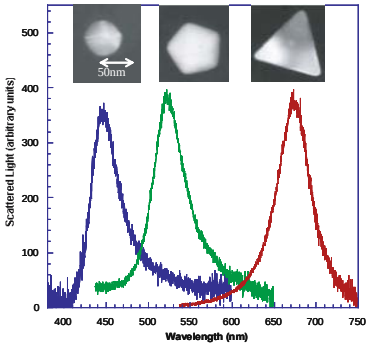

*Reprinted with permission from Ref.[235] (Copyright 2002 American Institute of Physics).

Plasmonic nanoparticles have received great attention from scientists across the world because of their potential applications in different areas of science and technology such as catalysis, biosensing,[209] particle growth process,[227] near-field microscopy, photolithography, surface enhanced Raman scattering, data storage, medical therapeutics and diagnostic technologies,[237-239] *etc*.

The optical properties of plasmonic NPs can be tuned by changing their shape, size, composition, structure (e.g. solid or hollow) and dielectric environment.[189, 213, 220-222, 240, 241] Metallic nanoparticles can exhibit various sizes and shapes such as spheres, triangles, cubes, prisms, bipyramids, octahedrons, nanorods, nanoshells, and nanostars. Theoretical and experimental research showed that an increase in edges or sharpness of a NP results in a red shift of the extinction spectra due to an increase in charge separation, while increased symmetry results in increases in the LSPR intensity.[235, 242] These nanoparticles have localized surface plasmon resonance peaks that vary from the visible to infrared regions.

The number of resonance absorption peaks is dependent on the number of modes in which the nanoparticle can be polarized. Thereby, non-spherical NPs show multiple plasmonic peaks, which are red-shifted in comparison to spherical systems.[220, 240] The size of the NPs

strongly affects the plasmonic behavior of the system. Many theories and experiments have studied the influence of size on the plasmonic peak position. In fact, experimental results and many theoretical calculations evidenced a blue shift of the plasmonic band with decreasing size of NPs.[243]

MCD spectroscopy is a very useful technique for determination of the plasmon band for colloidal gold and silver NPs.[112, 113] Considerable magneto–optical activity has been observed in aqueous solutions of colloidal noble metal nanoparticles with diameters up to 50 nm when a magnetic field was applied.[113] The absorption and MCD spectra of gold and silver NPs both exhibit localized surface plasmon resonances. MCD spectra show pronounced Zeeman splitting in the plasmon absorption bands, and the MCD spectral shape is derivative–like.

It is well known that the interpretation of experimental MCD spectra is a complicated process, especially for low–symmetry systems. Therefore, theoretical simulation of the MCD spectra can be used to assist in the understanding of empirically measured MCD spectra and can provide useful information.

In this paper, the plasmonic behavior of neutral and charged silver nanoparticles (AgNPs) of different sizes and shapes was investigated using TDDFT methods. The considered silver clusters have a closed shell structure so that they are "magic number" clusters. The most stable species is associated with total shell–closing electron count of 2, 8, 18, 20, 34, 58, 92, 138, *etc*., for spherical and approximately spherical systems.[6] The frontier orbitals of these nanoparticles are commonly named "superatom orbitals". These orbitals look like the *s*, *p*, *d* orbitals of the hydrogen atom but are delocalized over the metallic core. They are labeled S, P, D, F, G, H, *etc*. The optical absorption and MCD spectra were simulated for octahedral (Ag_{19}^{-1}, Ag_{19}^{+1}, Ag_{38}^{+4}, Ag_{44}^{-2}), tetrahedral (Ag_{10}^{+2}, Ag_{20}^{0}, Ag_{35}^{+1}, Ag_{35}^{-5}) and icosahedral (Ag_{13}^{-5}, Ag_{13}^{+5}, Ag_{43}^{+3}) silver nanoparticles (**Figure 7–2**). Clusters Ag_{38}^{+4} and Ag_{43}^{+3} represent truncated octahedral and truncated icosahedral clusters. Furthermore, in order to be able to simulate spectra for negatively charged systems, an augmented triple-ζ basis set with frozen core (ATZP.fc) for silver atoms was developed for the Amsterdam Density Functional (ADF) program.

Figure 7–2. Considered AgNPs: Tetrahedral, Octahedral and Icosahedral shapes.

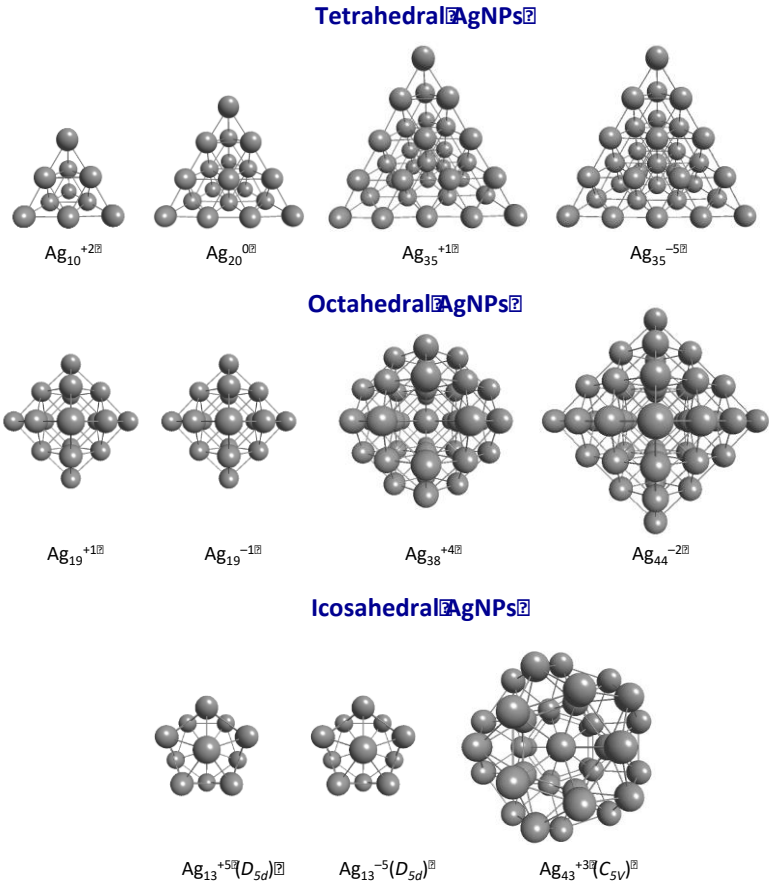

Computational Method

The Amsterdam Density Functional (ADF) program was employed for performing DFT and TDDFT calculations.[158] Scalar relativistic effects were included by utilizing the zero–order regular approximation (ZORA).[173] The geometries used to perform the TDDFT calculations were obtained with Becke-Perdew (BP86) functional,[174, 175] which was combined with a double-ζ (DZ) Slater type basis set. TDDFT was employed to calculate excited states to determine optical absorption and magnetic circular dichroism spectra. For these calculations the asymptotically correct LB94[186] and SAOP[186] functionals were used (the latter functional was only used for clusters of size up to 19 atoms). The LB94 functional was combined with a new Slater-type frozen core augmented triple-ζ (ATZP.fc) basis set for silver atoms. This basis set is not a standard basis set of ADF and was developed for this project because of the negatively charged silver clusters of interest in this work. To test the proposed ATZP.fc basis set, optical

absorption and MCD spectra were additionally calculated for selected clusters with sizes up to 20 atoms with standard all-electron triple-ζ (TZP) and quadruple-ζ (QZ4P) basis sets. Tests were performed for small clusters of different charge: Ag_{10}^{+2} (T_d), Ag_{20}^{0} (T_d), and Ag_{13}^{-5} (I_h). These results can be found in **Appendix E**.

All calculations (geometry optimizations and excitation calculations) have been performed employing the O_h and T_d point group symmetry for octahedral and tetrahedral clusters, respectively. For icosahedral clusters, D_{5d} or C_{5v} point group symmetry has been used due to the issue that the complete I_h group is not supported by ADF.

Equations used for calculation of the MCD spectra have been already discussed and can be found in **Chapter 2** (equations 2.44 – 2.49). MCD spectra were calculated at a temperature of 5.5 K and a magnetic field of 7 T. Parameter Z was chosen to be 0.0182.

It should be noted that calculation of the MCD spectrum is very time consuming process especially for large clusters (size > 20 atoms). Therefore, MCD spectra up to 5 eV were calculated only for small clusters. For simulation of the MCD spectra of larger nanoparticles, only excited states with the strongest oscillator strengths were considered.

Augmented Basis Set for Silver Atom

Application of the standard TZP basis set for calculation of the optical absorption and MCD spectra of systems of interest does not give reliable results for large negatively charged clusters such as Ag_{35}^{-5} (T_d), Ag_{44}^{-2} (O_h) and Ag_{43}^{-1} (I_h). Employment of the all-electron quadruple-ζ polarized (QZ4P) basis set for calculation of MCD spectra is not computationally possible due to the size of the considered silver clusters. Therefore, to be able to perform a study of optical properties for silver clusters with nuclearity up to 44 atoms, addition of diffuse functions to the standard TZP basis set is necessary. Unfortunately, the ADF program does not contain a basis set for silver atoms with diffuse functions, which are necessary for calculation of negatively charged systems. Furthermore, ADF uses Slater–type orbitals in the basis sets and there are no libraries with different available basis sets, unlike the case of basis sets composed of Gaussian type orbitals. In this project, a frozen core augmented TZP basis set for silver atom is suggested. This new ATZP.fc basis set for silver atom was generated by adding field–induced polarization (FIP) functions to the standard TZP basis set. These FIP functions are much more diffuse than usual polarization functions and can help to improve the description of anions.

Chong and co–workers[244-246] designed an efficient procedure for augmenting basis sets. They proposed and tested the procedure for generating FIP functions to be added to standard Slater–type orbital basis sets for the elements H to Kr. Their results showed that the new augmenting functions improved the performance of standard basis sets significantly. Their new ATZP.fc basis sets for elements 1–36 are about the same size as the standard TZ2P set and are significantly smaller than the large QZ4P set.[244]

The first step of this procedure involves finding values of exponents ζ_1 and ζ_2 for unperturbed functions 1s and 2p, respectively. For this purpose, the energy of the highest occupied atomic orbitals (HOAO) can be used. For example, exponent ζ_1 for the unperturbed 1s orbital can be calculated using equations (7–1)–(7–3):[244-246]

$$\zeta_1 = \frac{3\zeta_0}{(2\tilde{n} + 1)} \tag{7–1}$$

$$\zeta_0 = \sqrt{-2\varepsilon_{HOAO}} \tag{7–2}$$

$$\tilde{n} = \sqrt{-\frac{Ry}{\varepsilon_{HOAO}}} \tag{7–3}$$

where ñ is an effective (noninteger) principal quantum number, *Ry* is the Rydberg constant in a.u., ε_{HOAO} is the energy of the asymptotic highest occupied orbital in a.u. (Clementi and Roetti data)[247] and ζ_0 is the asymptotic orbital exponent.

Then, the obtained results can be used to derive the FIP functions via a perturbative solution of one–electron one–center equations for the orbitals in a uniform electric field.[244] For example, for s–elements the first–order perturbed orbital can be approximated by a single 2p with a ζ_3 exponent. The best value for the ζ_3 exponent giving the highest overlap with the perturbed orbital is given by equation (7–4):[244, 245]

$$\zeta_3 = 0.8117 \cdot \zeta_1 \tag{7–4}$$

Moreover, these authors estimated a convenient formula for changing the principal quantum number *n* of the STO. This equation (7–5) can be used for the calculation of exponents for diffuse functions of interest:[244, 245]

$$(2n_{target} + 1)\zeta_{source} = (2n_{source} + 1)\zeta_{target} \tag{7–5}$$

In our current research, a similar approach for calculation of exponents of diffuse functions for a silver atom basis set was used. The ATZP.fc basis set was obtained by addition

of three diffuse functions (2p, 4d and 5s) to the standard TZP basis set from the ADF program. The exponents for the considered diffuse functions are ζ_{2p}, ζ_{4d} and ζ_{5s}, respectively. Silver is an s–element, with its last electron in a 5s orbital. Therefore, the ζ_1 exponent for the unperturbed 1s orbital can be calculated using equations (7–1)–(7–3). According to Clementi and Roetti data, the value of ε_{HOAO} for the silver atom is –0.2551 a.u. (**Table 7–1**).[247]

The exponent for the 2p diffuse function (ζ_{2p}) is similar to the ζ_3 exponent from Chong work[244, 245] and can be found using equation (7–4).

The exponent for the 4d diffuse function (ζ_{4d}) was not evaluated in previous papers.[244, 245] However, data for STO expansions of first– and second–order perturbed hydrogenic radial functions $R_{l|m|}{}^{k}$ for the 1s, 2s and $2p_m$ states from reference[246] allowed us to derive a formula for exponent ζ_{4d}. The best value for ζ_{4d} giving the best overlap with the perturbed orbital is given by equation (7-6):

$$\zeta_{4d} = 0.9486 \cdot \zeta_1 \qquad (7–6)$$

The exponent for the 5s diffuse function (ζ_{5s}) is less straightforward. For calculation of this exponent, two–step calculations were applied. First, an s–type FIP function such as ζ_{2s} can be calculated from ζ_1 with Chong's equation (7–7).[244, 245] Then, equation (7–8) was used to change the principal quantum number of the s–orbital from 2 to 5:[244, 245]

$$\zeta_{2s} = 0.7363 \cdot \zeta_1 \qquad (7–7)$$

$$\zeta_{5s} = \frac{11 \cdot \zeta_{2s}}{5} \qquad (7–8)$$

Therefore, three diffuse functions (2p, 4d and 5s) with exponents ζ_{2p}, ζ_{4d} and ζ_{5s} were added to the standard TZP basis set from the ADF program. It should be mentioned that the ZORA/QZ4P auxiliary fit set was used for our ATZP basis set. Also, for accurate description of Hartree-Fock exchange, the ADF program needs more diffuse fit functions in the fit procedure. This can be achieved by including the "AddDiffuseFit" keyword in the Create run section. This should increase the accuracy of the total energy and improve convergence.[158] The obtained values of the exponents can be found in **Table 7–1**.

All presented results in this work were obtained using the LB94/ATZP.fc level of theory. To test the quality of the obtained basis set, optical absorption spectra were recalculated for small selected clusters with LB94 and SAOP methods and different basis sets such as ATZP

(all electrons), TZP and QZ4P. Tests were performed for small clusters of different charge: Ag_{10}^{+2} (T_d), Ag_{13}^{-5} (I_h), Ag_{19}^{+1} (O_h), and Ag_{19}^{-1} (O_h). These results can be found in **Appendix E**. These obtained results showed that for the considered structures, the shapes of the calculated optical absorption spectra are very similar for all considered functionals and basis sets except for negatively charged Ag_{13}^{-5} (I_h), which is very sensitive to the type of basis set **(Appendix E)**.

Table 7-1. Energy of asymptotic 5s orbital of silver (ε_{HOAO}), effective principal quantum number for silver (ñ), and calculated orbital exponents for silver atoms (ζ_0, ζ_1, ζ_{2p}, ζ_{4d} and ζ_{5s}).

Parameter	Value
ε_{HOAO} (a.u.)[247]	– 0.2551
ñ	1.3996
ζ_0	0.7143
ζ_1	0.5641
ζ_{2p}	0.4579
ζ_{4d}	0.5351
ζ_{5s}	0.9138

Results and Discussion

In this research, all considered structures are magic number clusters. Magic numbers corresponding to the closure of electronic shells are known to be 2, 8, 18, 20, 34, 40, 58, 92, 138, *etc*., for spherical (and often for approximately spherical) systems. The total number of electrons and the HOMO-LUMO gaps are summarized in **Table 7–2** for all considered clusters.

These systems have degenerate excited states. Therefore, both *A*– and *B*– terms are expected in the MCD spectrum. This excited state degeneracy is broken by the magnetic field, which leads to a derivative–shape of the signal in the MCD spectrum.

Table 7-2. Number of electrons and HOMO-LUMO gaps (ΔHL) of AgNPs (LB94/ATZP.fc)

AgNP	Total number of electrons	ΔHL gap (eV)
Tetrahedral		
Ag_{10}^{+2}	8	2.91
Ag_{20}^{0}	20	1.94
Ag_{35}^{+1}	34	0.02
Ag_{35}^{-5}	40	0.94
Octahedral		
Ag_{19}^{+1}	18	0.23
Ag_{19}^{-1}	20	0.54
Ag_{38}^{+4}	34	0.51
Ag_{44}^{-2}	46	0.46
Icosahedral		
Ag_{13}^{+5}	8	2.73
Ag_{13}^{-5}	18	0.42
Ag_{43}^{+3}	40	0.47

Tetrahedral AgNPs.

First, optical absorption and MCD spectra were calculated for silver nanoparticles of tetrahedral structure: Ag_{10}^{+2}, Ag_{20}^{0}, Ag_{35}^{+1} and Ag_{35}^{-5} (**Figure 7–2**, **Figure 7–4**). According to the obtained results at the LB94/ATZP.fc level of theory (**Figure 7–4**), the optical spectra of all considered tetrahedral structures have a strong sharp peak below 5 eV. However, only the Ag_{10}^{+2} and Ag_{20}^{0} clusters have a single sharp peak in the optical absorption spectrum, whereas the larger clusters Ag_{35}^{+1} and Ag_{35}^{-5} have a peak composed of multiple electronic states. Also, the MCD spectra of the Ag_{10}^{+2} and Ag_{20}^{0} clusters have a derivative-shaped band that correlates with the single peak in the absorption spectra. The positions of the plasmonic peaks in the optical absorption and MCD spectra are summarized in **Table 7–3**.

The main peak of the optical absorption spectrum of the Ag_{10}^{+2} cluster is formed by one excited state at 4.22 eV with oscillator strength f = 1.012. The theoretical MCD spectrum of this structure has a strong derivative shape band, which is related to the peak in the absorption spectrum and arises from the same transitions. This plasmonic band can be assigned to a linear combination of electronic transitions from P to D superatomic orbitals, and from Ag *d* orbitals to superatomic P.

Table 7-3. Theoretical optical absorption (ABS) and MCD spectral data of the single sharp peak in plasmonic tetrahedral AgNPs: peak position (eV), oscillator strength (*f*), *A*- and *B*-terms (atomic units = a.u.), and transition dipole (*D*). (LB94/ATZP.fc)

AgNPs	State symmetry	ABS		MCD			
		Peak, eV	*f*	Peak, eV	*A*-term, a.u.	*B*-term, a.u.	*D*
Ag_{10}^{+2}	T_2	4.22	1.012	4.22	10.78	-66.95	9.78
Ag_{20}^{0}	T_2	3.90	2.432	3.90	23.56	-122.05	25.44

Figure 7–3. Theoretical optical absorption and MCD spectra of tetrahedral AgNPs (LB94/ATZP.fc).

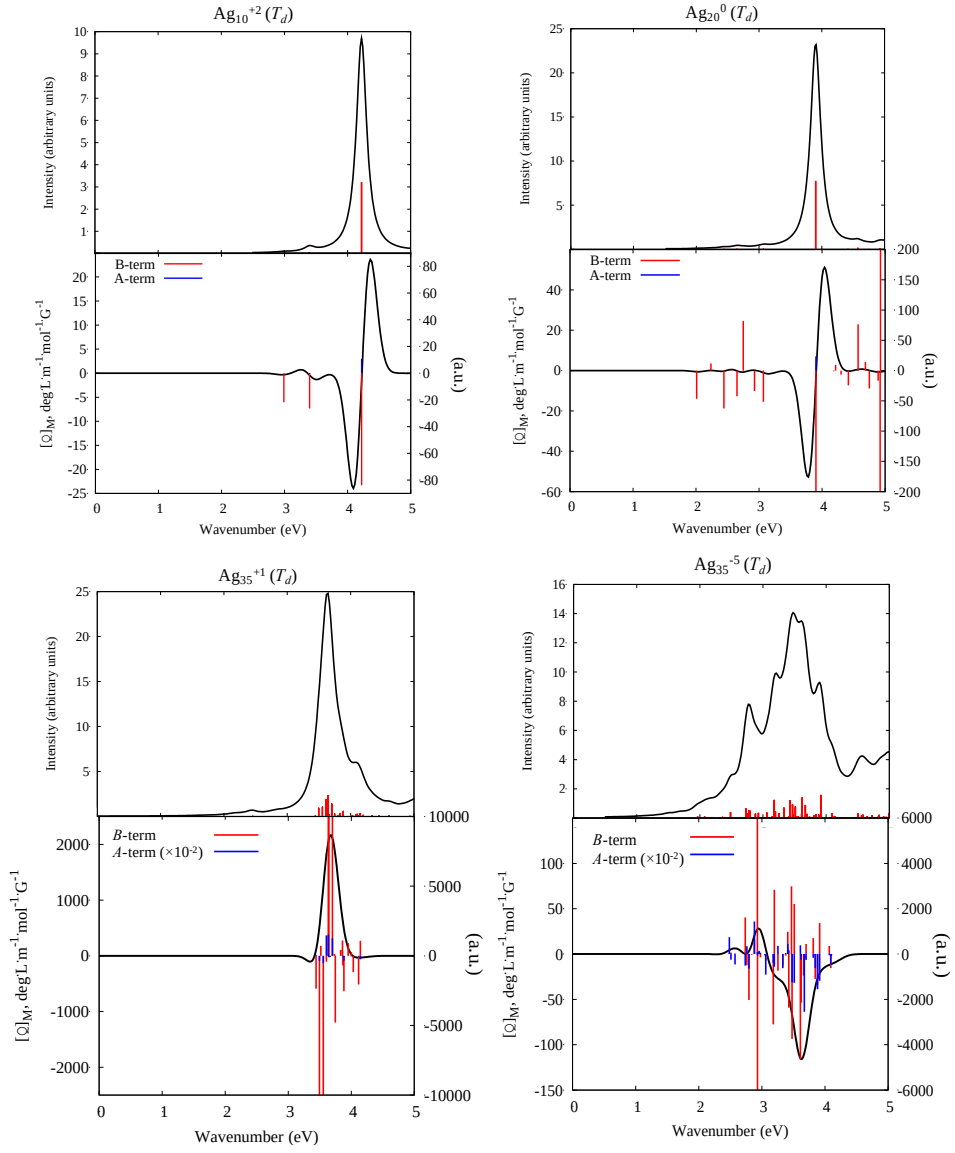

Optical absorption and MCD spectra of the neutral silver cluster Ag_{20}^{0} evidence that this particle is also plasmonic: the absorption spectra has a strong, sharp peak and the MCD

spectrum contains a derivative-shaped band (**Figure 7–4**, **Table 7–3**). The optical absorption and MCD peaks arise from the same excited state at 3.90 eV. This excitation occurs due to primary electronic transitions D → G, and from Ag *d* orbitals to superatomic F and G orbitals. The selection rules are somewhat relaxed from those of the higher symmetry spherical case (ΔL = ±1).

The larger clusters Ag_{35}^{+1} and Ag_{35}^{-5} have one strong band in the optical absorption spectra with maxima at 3.64 and 3.62 eV. These bands are wide and formed by numerous weak excited states with oscillator strengths no higher than 0.497. Calculated MCD spectra of these AgNPs do not have any derivative-shaped peaks correlated with the absorption band in the considered part of spectrum (**Figure 7–4**). Therefore, these particles most likely are not plasmonic.

Octahedral AgNPs.

The next considered silver structures are silver nanoparticles with octahedral shape: Ag_{19}^{+1}, Ag_{19}^{-1}, Ag_{38}^{+4}, and Ag_{44}^{-2}. The obtained results showed that only the largest Ag_{44}^{-2} cluster should not exhibit plasmonic behavior (**Figure 7–5**).

The positively charged Ag_{19} cluster has one strong absorption peak at 4.34 eV (**Figure 7–5, Table 7–4**). Two excited states form this peak: they are located at 4.34 and 4.38 eV. This strong absorption band can be assigned with the MCD derivative-shaped band at 4.34 eV. This peak can be considered as plasmonic. This plasmonic band arises from a mixture of transitions D → F, D → P, P → S, and from Ag *d* orbitals to superatomic S unoccupied orbital. All these transitions correspond to the expected spherical selection rule of ΔL = ±1.

Table 7-4. Theoretical optical absorption (ABS) and MCD spectral data of the plasmonic band of octahedral AgNPs: peak position (eV), oscillator strength (*f*), *A*- and *B*- terms (atomic units = a.u.), and transition dipole (*D*). (LB94/ATZP.fc)

AgNPs	State symmetry	ABS		MCD			
		Peak, eV	*f*	Peak, eV	*A*-term, a.u.	*B*-term, a.u.	*D*
Ag_{19}^{+1}	T_{1u}	4.34	1.192	4.34	9.58	-3186.2	11.21
	T_{1u}	4.38	0.289	4.38	0.66	3234.1	2.69
Ag_{19}^{-1}	T_{1u}	4.08	1.530	4.08	19.58	-495.68	15.31
Ag_{38}^{+4}	T_{1u}	4.27	2.807	4.27	42.98	-955.74	26.85
Ag_{44}^{-2}	T_{1u}	4.04	2.700	4.04	26.79	–4061.8	27.28

The three strong peaks in the absorption spectrum of Ag_{19}^{-1} lie at 4.08, 4.43 and 4.82 eV. The peak at 4.08 eV is the strongest one and arises from only one excited state. Calculation of the MCD spectrum for the Ag_{19}^{-1} cluster shows that only this first strongest absorption peak correlates with the derivative–like MCD peak at 4.08 eV (**Figure 7–5, Table 7–3**). The primary transitions responsible for the formation of this band are P → S and *d* → F.

Figure 7–4. Theoretical optical absorption and MCD spectra of octahedral AgNPs (LB94/ATZP.fc).

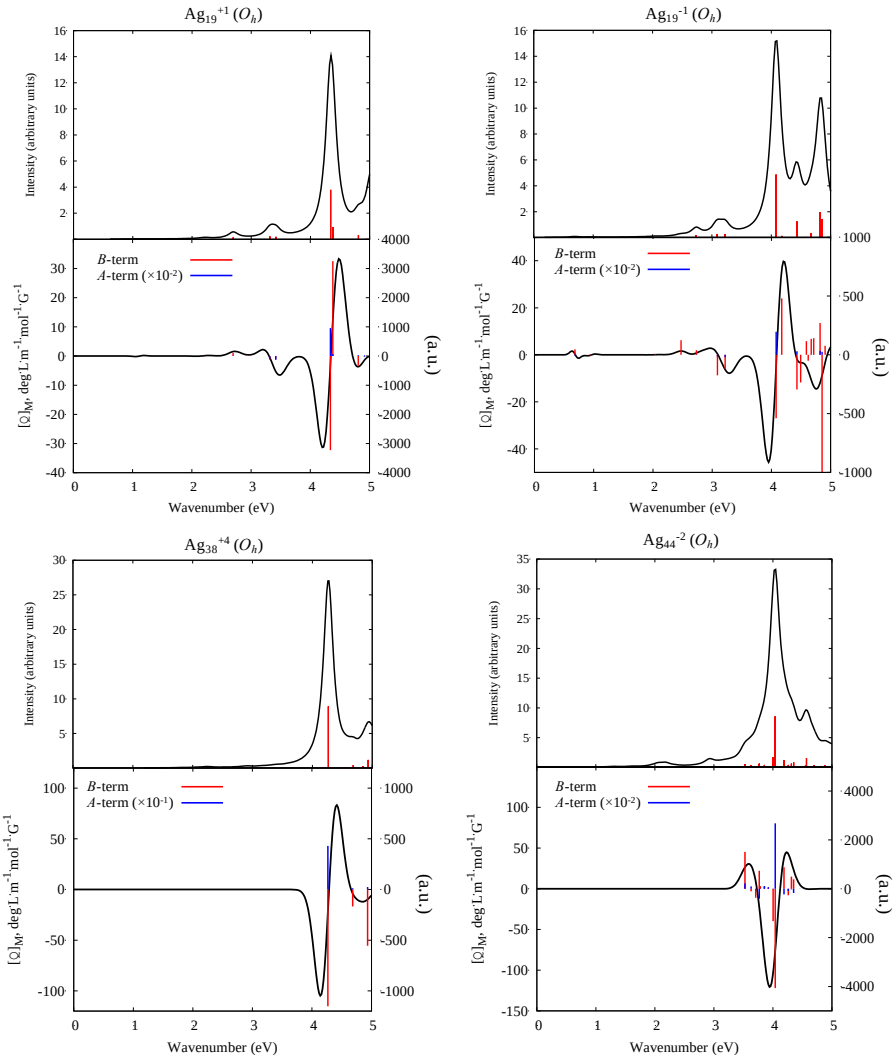

The next larger octahedral cluster is Ag_{38}^{+4}. The optical spectrum of this cluster exhibits a sharp peak at 4.27 eV (**Figure 7–5, Table 7–3**). This absorption band can be assigned to the MCD band with a derivative shape at 4.27 eV. The optical absorption and MCD plasmonic bands arise from the same excited state, which occurs from mixed transitions F → G, *d* → P and *d* → G.

The neutral Ag_{44} (O_h) cluster has four electrons in a triply degenerate HOMO. Adding two electrons yields the Ag_{44}^{-2} cluster with a completely filled shell. Previous theoretical research of Bae and Aikens showed that the Ag_{44}^{-2} cluster could be plasmonic.[213] Its optical absorption spectrum exhibits a sharp peak at 4.46 eV. Using the LB94/ATZP.fc level of theory, the optical properties of the Ag_{44}^{-2} cluster were also investigated (**Figure 7–5**). The optical absorption spectrum of this structure has a sharp peak at 4.04 eV. This peak is formed by numerous excited states with energies from 3.29 and 4.6 eV. Three of the strongest excited states from this region occur at 4.00 eV (f = 0.542), 4.04 eV (f = 2.700) and 4.19 eV (f = 0.392). According to the calculated MCD data for the Ag_{44}^{-2} cluster, it can be seen that the strongest excited state, responsible for the formation of the optical absorption peak at 4.04 eV, exhibits the strongest *A*– and *B*–terms in the MCD spectrum. However, the shape of the MCD spectral line does not have shape of a derivative.

Icosahedral AgNPs.

The first two considered icosahedral clusters, Ag_{13}^{+5} and Ag_{13}^{-5}, were calculated using D_{5d} symmetry because the complete I_h group is not supported by ADF (**Figure 7–6, Table 7–5**). Dipole-allowed irreducible representations of D_{5d} symmetry are A_2 and E. Thus, every excited state for an I_h symmetry structure will be split due to using lower D_{5d} symmetry. In the case of the MCD spectra, for each peak we observe two excited states with the same wavenumbers but different sign for the *B*–term. *A*–terms for states with A_2 symmetry will be equivalent to zero. For the Ag_{13}^{+5} cluster (I_h*/represented with* D_{5d}), the optical absorption exhibits two main peaks: a weak peak is located at 3.65 eV and a strong peak appears at 4.33 eV. Calculation of the MCD spectrum for the Ag_{13}^{+5} (I_h/D_{5d}) cluster shows that this structure exhibits two plasmonic peaks in the region of the spectrum below 5 eV. The MCD spectrum has two bands, which are correlated with the two optical absorption bands (at 3.65 and 4.33 eV). Both MCD bands have the shape of a derivative. The first band (3.65 eV) is a weak plasmonic peak, whereas the second peak (4.33 eV) is strong. These two plasmonic peaks arise from the mixed transitions P $\rightarrow$ S and P $\rightarrow$ D.

Optical absorption and MCD spectra of the negatively charged Ag_{13}^{-5} cluster appear more complex. In the energy region below 5 eV, six strong peaks were obtained in the optical absorption spectrum: 0.96, 1.65, 2.22, 2.44, 2.86 and 4.14 eV. The MCD spectrum of this cluster also exhibits six peaks. The intensities of the MCD signals decrease with increasing

energies of the excited states (**Figure 7–6**). The first MCD peak at 0.96 eV arises due to D → P electronic transitions. The next three peaks at 1.65, 2.22 and 2.44 eV appear because of mixed transitions D → P and D → F. The primary transitions responsible for the last two peaks at 2.86 and 4.14 eV are P → S and D → F. It should be noted that optical absorption and MCD spectra of the Ag_{13}^{-5} cluster are very sensitive to the type of basis set used for calculation (**Appendix E)**. This can be related to a very large negative charge of this system.

In this project, using a basis set with diffuse functions is very important not only for negatively charged clusters, but for large positively charged systems as well. For example, the results obtained for Ag_{43}^{+3} (I_h) nanoparticle with regular TZP basis set showed that this cluster is not plasmonic: the optical absorption spectrum exhibits multiple peaks and the MCD spectrum shape is far away from derivative (**Figure 7–3**). However, application of our ATZP.fc basis set with diffuse functions changes the spectra: the absorption spectrum exhibits one strong sharp peak, which is related to a derivative–shaped band in the MCD spectrum.

Figure 7–5. Optical absorption and MCD spectra of Ag_{43}^{+3} (I_h) cluster calculated using TZP and ATZP.fc basis set.

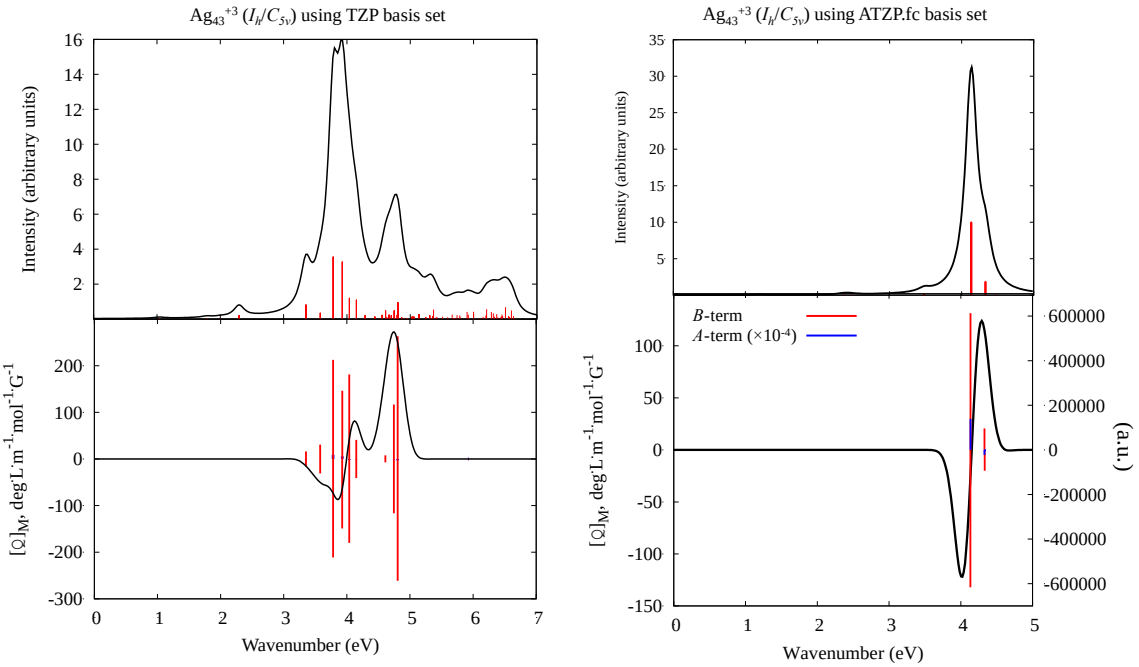

The results obtained at the LB94/ATZP.fc level of theory showed that this magic number cluster with 40 electrons has one strong peak in the optical absorption spectrum at 4.13 eV (**Figure 7–3**, **Table 7–5**). This sharp peak of the Ag_{43}^{+3} cluster appears from two excited states (A_1 and E_1) in the absorption and MCD spectra due to the splitting of peaks because C_{5v}

has lower symmetry than I_h. The MCD spectrum of this cluster has one strong peak with the shape of a derivative. This plasmonic peak arises due to electronic transitions P → S, P → D, and F → G.

Figure 7–6. Theoretical optical absorption and MCD spectra of icosahedral AgNPs (LB94/ATZP.fc).

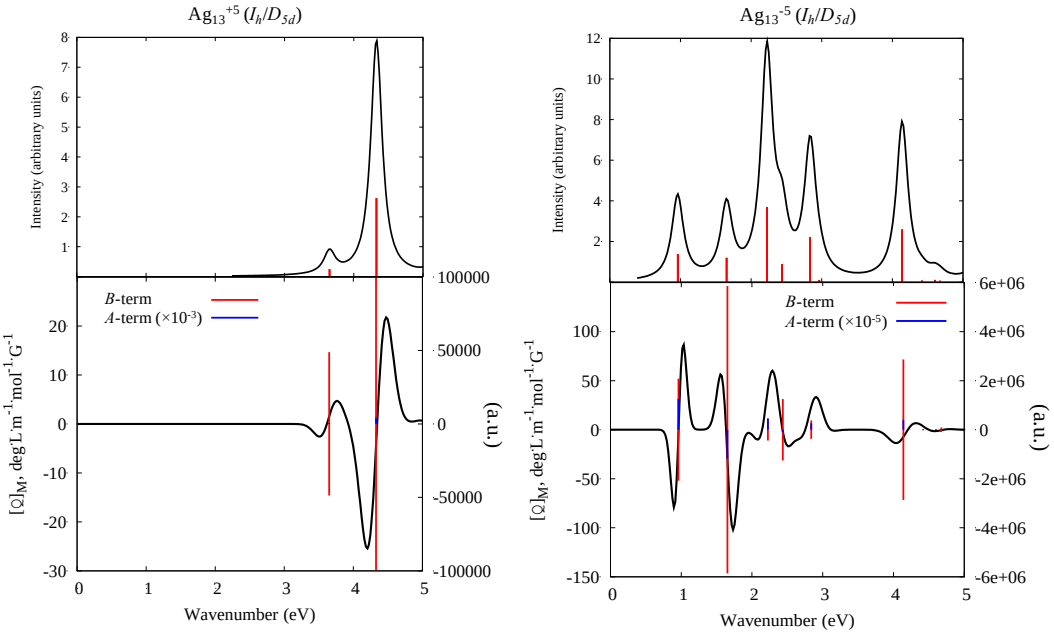

Table 7-5. Theoretical optical absorption (ABS) and MCD spectral data of plasmonic band of icosahedral AgNPs: peak position (eV), oscillator strength (*f*), *A*- and *B*- terms (atomic units = a.u.), and transition dipole (*D*). (LB94/ATZP.fc)

AgNPs	Peak #	State Symmetry	ABS		MCD			
			Peak, eV	*f*	Peak, eV	*A*-term, a.u.	*B*-term, a.u.	*D*
Ag_{13}^{+5} (I_h/D_{5d})	1	*E*	3.65	0.078	3.65	0.65	–48746.0	0.58
		A_2	3.65	0.079	3.65	0.00	48839.0	0.29
	2	*E*	4.33	0.824	4.33	4.33	0.63E+06	5.18
		A_2	4.33	0.825	4.33	0.00	–0.63E+06	2.59
Ag_{13}^{-5} (I_h/D_{5d})	1	*E*	0.96	0.435	0.96	12.62	–0.21E+07	12.33
		A_2	0.96	0.434	0.96	0.00	0.21E+07	6.15
	2	*E*	1.65	0.376	1.65	–11.81	0.59E+07	6.19
		A_2	1.65	0.376	1.65	0.00	–0.59E+07	3.10
	3	*E*	2.22	1.156	2.22	4.66	–0.44E+07	14.14
		A_2	2.22	1.156	2.22	0.00	0.44E+07	7.07
	4	*E*	2.44	0.274	2.44	–1.08	–0.13E+07	3.06
		A_2	2.44	0.273	2.44	0.00	0.13E+07	1.53
	5	*E*	2.84	0.692	2.84	2.58	–0.37E+07	6.63

		A_2	2.84	0.692	2.84	0.00	0.37E+07	3.32
	6	E	4.14	0.813	4.14	3.99	–0.29E+07	5.34
		A_2	4.14	0.813	4.14	0.00	0.29E+07	2.67
Ag_{43}^{+3} (I_h/C_{5v})	1	E_1	4.13	3.137	4.13	13.93	0.61E+06	20.65
		A_1	4.13	3.170	4.13	0.00	-0.62E+06	10.43

Conclusions

In this project, the plasmonic behavior of neutral and charged silver nanoparticles of different sizes and shapes was investigated using TDDFT at the LB94/ATZP.fc level of theory. Optical absorption and MCD spectra were simulated for octahedral (Ag_{19}^{-1}, Ag_{19}^{+1}, Ag_{38}^{+4}, Ag_{44}^{-2}), tetrahedral (Ag_{10}^{+2}, Ag_{20}^{0}, Ag_{35}^{+1}, Ag_{35}^{-5}) and icosahedral (Ag_{13}^{-5}, Ag_{13}^{+5}, Ag_{43}^{+3}) silver nanoparticles.

A frozen core augmented triple-ζ basis set (ATZP.fc) for silver atoms was developed for the Amsterdam Density Functional program. This basis set was combined with the LB94 functional. The optical absorption spectra of Ag_{10}^{+2} (T_d), Ag_{13}^{-5} (I_h), Ag_{19}^{+1} (O_h), Ag_{19}^{-1} (O_h) clusters were also calculated using the SAOP functional combined with different types of basis sets such as all-electron ATZP, TZP and QZ4P. Comparison of the obtained results showed that LB94/ATZP.fc works well: the shape of the optical absorption spectra is identical in all used methods for all considered systems except Ag_{13}^{-5} (I_h). The optical absorption spectrum of the Ag_{13}^{-5} cluster is very sensitive to the type of basis set used for calculation (this can be related to the large negative charge of the particle).

Additionally, the quality of the ATZP.fc basis set was tested for large clusters such as Ag_{43}^{+3} (I_h). For this system, optical absorption and MCD spectra were also simulated using the regular TZP basis set. The results showed that diffuse functions in the basis set are very important not only for negatively charged clusters but for large positive structures as well. Optical absorption and MCD spectra of Ag_{43}^{+3} (I_h) calculated using the TZP basis set suggested that this cluster is not plasmonic. The MCD spectrum does not exhibit a derivative shape. Application of the ATZP.fc basis set changed this situation: the absorption spectrum now exhibits one strong sharp peak, which is related to the derivative–shaped band in the MCD spectrum.

The obtained theoretical data evidenced that clusters Ag_{10}^{+2}, Ag_{20}^{0}, Ag_{19}^{-1}, Ag_{19}^{+1}, Ag_{38}^{+4}, Ag_{13}^{-5}, Ag_{13}^{+5}, and Ag_{43}^{+3} can be considered as plasmonic NPs: the optical absorption

spectra of all these structures have a strong sharp peak and this peak is correlated with the strong derivative-shaped MCD band.

Acknowledgement

This material is based on work supported by the Air Force Office of Scientific Research, Grant Number FA9550-15-1-0114. The computing for this project was performed on the Beocat Research Cluster at Kansas State University, which is funded in part by NSF grants CNS-1006860, EPS-1006860, and EPS-0919443.

Chapter 8 - Conclusions

Small silver and gold nanoclusters protected by various types of ligands have held great attention for the few last decades, especially in the fields of medicine, luminescence, catalysis, nanoelectronics, drug delivery, bioanalysis, *etc*. Understanding of the optical properties and electronic structures of already known structures will help to develop novel silver and gold nanostructures with improved characteristics or new properties. Computational chemistry is a very powerful tool to help scientists obtain additional important knowledge about systems of interest.

Theoretical investigation of the optical properties and electronic structures of silver and gold nanoparticles was a main goal of this work. DFT and TDDFT levels of theory were employed for these purposes. To get more detailed information about optical properties and electronic structures of systems of interest, examination of theoretical optical absorption spectra was combined with theoretical CD and MCD spectra.

CD spectroscopy was applied to study chiral systems such as (i) gold clusters protected by bidentate phosphine ligands and (ii) Ag:DNA nanoparticles. The main purpose and findings of these studies were as follows:

i. To contribute to an understanding of the origin of chirality and the differences in chiroptical activity of gold clusters stabilized by different phosphine ligands, the optical properties of $[Au_{11}X_4Cl_2]^+$ and $[Au_8X_3(PPh_3)_2]^{2+}$ (X = DIOP, BINAP) clusters were examined. It was shown that the gold core geometry deformation due to ligation and the nature of the ligand play the most important roles in the chiroptical activity of the gold clusters considered in this work.

ii. The empirical structure of the Ag:DNA clusters is unknown and is under debate. In this project, optical absorption and CD spectra were used to check a hypothesis about the rod shape of the metal core of these AgNPs. Helical silver nanowires Ag_n (n = 4, 6, 8, 10, 12) were suggested as model systems to simulate CD spectra of real Ag:DNA nanoparticles. The effects of the helical chain length and geometrical parameters such as bond and dihedral angles on the electronic properties were examined. This study of the length dependence of the optical absorption and CD spectra in the bare silver helical chains shows that as the number of silver atoms in the chain increases, the spectrum

redshifts and peak intensities become stronger. Overall, the investigation of the geometrical structure of the helix shows that geometry has a strong effect on the location and intensity of the peaks in the spectrum.

MCD spectroscopy was used for (iii) studying the optical properties of small centered phosphine–protected gold nanoclusters, and (iv) studying of the plasmon behavior of bare silver nanoparticles:

iii. Simulations of the optical absorption and magnetic circular dichroism spectra of $Au_9(PPh_3)_8^{3+}$ (D_{2h}) and $Au_8(PPh_3)_8^{2+}$ (C_{3v}) were performed. The obtained theoretical MCD spectra for these triphenylphosphine-stabilized gold systems are in very good agreement with the experimental curve. It was shown that the low–energy part of the spectra (below ~1.9 μm^{-1}) arises due to transitions within the gold cluster framework only, whereas the spectral peaks in the region between ~1.9 and 2.5 μm^{-1} appear because of the electronic transitions from the gold core orbitals to the π* orbitals on the PPh_3 ligands. The high–energy bands (above 2.5 μm^{-1}) occur due to electron transitions primarily from the occupied π to the unoccupied π* orbitals of the ligands.

iv. Plasmonic behavior of neutral and charged silver nanoparticles of different sizes and shapes was investigated. A frozen core augmented triple-ζ basis set (ATZP.fc) for silver atom was developed for the Amsterdam Density Functional program. It was shown that the diffuse functions in the basis set are very important not only for negatively charged clusters but for large positive structures also. The obtained theoretical data evidenced that clusters Ag_{10}^{+2}, Ag_{20}^{0}, Ag_{19}^{-1}, Ag_{19}^{+1}, Ag_{38}^{+4}, Ag_{13}^{-5}, Ag_{13}^{+5}, and Ag_{43}^{+3} can be considered as plasmonic NPs: optical absorption spectra of all these structures have a strong sharp peak and this peak is correlated with the strong derivative shape MCD band.

Overall, CD and MCD spectroscopy yield more detailed information about optical properties and electronic structure of the different chemical systems, and combination of these techniques with optical absorption spectra can be used to assist in gaining a deeper understanding of nanoparticle properties.

References

(1) Ramírez, J.; Sanaú, M.; Fernández, E. Gold(0) Nanoparticles for Selective Catalytic Diboration. *Angew. Chem. Int. Ed.* **2008,** *47* (28), 5194-5197.

(2) William, L. B.; Alain, D.; Thomas, W. E. Surface Plasmon Subwavelength Optics. *Nature* **2003,** *424* (6950), 824-830.

(3) Shibu, E. S.; Muhammed, M. A. H.; Tsukuda, T.; Pradeep, T. Ligand Exchange of $Au_{25}SG_{18}$ Leading to Functionalized Gold Clusters: Spectroscopy, Kinetics, and Luminescence. *J. Phys. Chem. C* **2008,** *112* (32), 12168-12176.

(4) Fernando, A.; Weerawardene, K. L. D. M.; Karimova, N. V.; Aikens, C. M. Quantum Mechanical Studies of Large Metal, Metal Oxide, and Metal Chalcogenide Nanoparticles and Clusters. *Chem. Rev.* **2015,** *115* (12), 6112-6216.

(5) Mingos, D. M. P. *Gold Clusters, Colloids and Nanoparticles I*. Springer: 2014; Vol. 161, p 282.

(6) Walter, M.; Akola, J.; Lopez-Acevedo, O.; Jadzinsky, P. D.; Calero, G.; Ackerson, C. J.; Whetten, R. L.; Grönbeck, H.; Häkkinen, H. A unified view of ligand-protected gold clusters as superatom complexes. *Proc. Natl. Acad. Sci. U.S.A.* **2008,** *105* (27), 9157-9162.

(7) Jiang, D.; Overbury, S. H.; Dai, S. Structure of $Au_{15}(SR)_{13}$ and Its Implication for the Origin of the Nucleus in Thiolated Gold Nanoclusters. *J. Am. Chem. Soc.* **2013,** *135* (24), 8786-8789.

(8) Das, A.; Liu, C.; Byun, H. Y.; Nobusada, K.; Zhao, S.; Rosi, N.; Jin, R. Structure Determination of $[Au_{18}(SR)_{14}]$. *Angew. Chem. Int. Ed.* **2015,** *54* (10), 3140-3144.

(9) Tofanelli, M. A.; Salorinne, K.; Ni, T. W.; Malola, S.; Newell, B.; Phillips, B.; Hakkinen, H.; Ackerson, C. J. Jahn-Teller effects in $Au_{25}(SR)_{18}$. *Chem. Sci* **2016,** *7* (3), 1882-1890.

(10) Heaven, M. W.; Dass, A.; White, P. S.; Holt, K. M.; Murray, R. W. Crystal Structure of the Gold Nanoparticle $N(C_8H_{17})_4Au_{25}(SCH_2CH_2Ph)_{18}$. *J. Am. Chem. Soc.* **2008,** *130* (12), 3754-3755.

(11) Zhu, M.; Aikens, C. M.; Hollander, F. J.; Schatz, G. C.; Jin, R. Correlating the Crystal Structure of A Thiol-Protected Au_{25} Cluster and Optical Properties. *J. Am. Chem. Soc.* **2008,** *130* (18), 5883-5885.

(12) Zhu, M.; Eckenhoff, W. T.; Pintauer, T.; Jin, R. Conversion of Anionic $[Au_{25}(SCH_2CH_2Ph)_{18}]^-$ Cluster to Charge Neutral Cluster via Air Oxidation. *J. Phys. Chem. C* **2008,** *112* (37), 14221-14224.

(13) Zeng, C.; Li, T.; Das, A.; Rosi, N. L.; Jin, R. Chiral Structure of Thiolate-Protected 28-Gold-Atom Nanocluster Determined by X-ray Crystallography. *J. Am. Chem. Soc.* **2013,** *135* (27), 10011-10013.

(14) Crasto, D.; Malola, S.; Brosofsky, G.; Dass, A.; Häkkinen, H. Single Crystal XRD Structure and Theoretical Analysis of the Chiral $Au_{30}S(S\text{-}t\text{-}Bu)_{18}$ Cluster. *J. Am. Chem. Soc.* **2014,** *136* (13), 5000-5005.

(15) Zeng, C.; Qian, H.; Li, T.; Li, G.; Rosi, N. L.; Yoon, B.; Barnett, R. N.; Whetten, R. L.; Landman, U.; Jin, R. Total Structure and Electronic Properties of the Gold Nanocrystal $Au_{36}(SR)_{24}$. *Angew. Chem. Int. Ed.* **2012,** *51* (52), 13114-13118.

(16) Qian, H.; Eckenhoff, W. T.; Zhu, Y.; Pintauer, T.; Jin, R. Total Structure Determination of Thiolate-Protected Au_{38} Nanoparticles. *J. Am. Chem. Soc.* **2010,** *132* (24), 8280-8281.

(17) Liu, C.; Li, T.; Li, G.; Nobusada, K.; Zeng, C.; Pang, G.; Rosi, N. L.; Jin, R. Observation of Body-Centered Cubic Gold Nanocluster. *Angew. Chem. Int. Ed.* **2015,** *54* (34), 9826-9829.

(18) Malola, S.; Lehtovaara, L.; Knoppe, S.; Hu, K.-J.; Palmer, R. E.; Bürgi, T.; Häkkinen, H. $Au_{40}(SR)_{24}$ Cluster as a Chiral Dimer of 8-Electron Superatoms: Structure and Optical Properties. *J. Am. Chem. Soc.* **2012,** *134* (48), 19560-19563.

(19) Dharmaratne, A. C.; Krick, T.; Dass, A. Nanocluster Size Evolution Studied by Mass Spectrometry in Room Temperature $Au_{25}(SR)_{18}$ Synthesis. *J. Am. Chem. Soc.* **2009,** *131* (38), 13604-13605.

(20) Jadzinsky, P. D.; Calero, G.; Ackerson, C. J.; Bushnell, D. A.; Kornberg, R. D. Structure of a Thiol Monolayer-Protected Gold Nanoparticle at 1.1 Å Resolution. *Science* **2007,** *318* (5849), 430-433.

(21) Negishi, Y.; Nakazaki, T.; Malola, S.; Takano, S.; Niihori, Y.; Kurashige, W.; Yamazoe, S.; Tsukuda, T.; Häkkinen, H. A Critical Size for Emergence of Nonbulk Electronic and Geometric Structures in Dodecanethiolate-Protected Au Clusters. *J. Am. Chem. Soc.* **2015,** *137* (3), 1206-1212.

(22) Protected Metal Clusters: From Fundamentals to Applications. Tsukuda, T.; Häkkinen, H., Eds. Elsevier Science: 2015; Vol. 9, p 372.

(23) Van der Velden, J. W. A.; Bour, J. J.; Bosman, W. P.; Noordik, J. H. Synthesis and X-ray Crystal Structure Determination of the Cationic Gold Cluster Compound $[Au_8(PPh_3)_7](NO_3)_2$. *J. Chem. Soc., Chem. Commun.* **1981,** (23), 1218-1219.

(24) Bos, W.; Bour, J. J.; Van Der Velden, J. W. A.; Steggerda, J. J.; Casalnuovo, A. L.; Pignolet, L. H. Gold Clusters. Reactivity of $[Au_9(PPh_3)_8]^{3+}$ and $[Au_8(PPh_3)_7]^{2+}$ Towards Isopropyl Isocyanide. *J. Org. Chem.* **1983,** *253* (3), C64-C66.

(25) Anderson, D. P.; Alvino, J. F.; Gentleman, A.; Qahtani, H. A.; Thomsen, L.; Polson, M. I. J.; Metha, G. F.; Golovko, V. B.; Andersson, G. G. Chemically-Synthesised, Atomically-Precise Gold Clusters Deposited and Activated on Titania. *Phys. Chem. Chem. Phys.* **2013,** *15* (11), 3917-3929.

(26) Jaw, H. R. C.; Mason, W. R. Electronic Absorption and MCD Spectra for the $Au_8(PPh_3)_8^{2+}$ Ion. *Inorg. Chem.* **1991,** *30* (18), 3552-3555.

(27) Gutrath, B. S.; Schiefer, F.; Homberger, M.; Englert, U.; Şerb, M. D.; Bettray, W.; Beljakov, I.; Meded, V.; Wenzel, W.; Simon, U. Molecular and Electronic Structure of the Cluster $[Au_8(PPh_3)_8](NO_3)_2$. *Eur. J. Inorg. Chem.* **2016,** *2016* (7), 975-981.

(28) Mollenhauer, D.; Gaston, N. Phosphine Passivated Gold Clusters: How Charge Transfer Affects Electronic Structure and Stability. *Phys. Chem. Chem. Phys.* **2016,** *18* (43), 29686-29697.

(29) Wen, F.; Englert, U.; Gutrath, B.; Simon, U. Crystal Structure, Electrochemical and Optical Properties of $[Au_9(PPh_3)_8](NO_3)_3$. *Eur. J. Inorg. Chem.* **2008,** *2008* (1), 106-111.

(30) Adrowski, M. J.; Mason, W. R. Electronic Absorption and MCD Spectra for $Pd(AuPPh_3)_8^{2+}$, $Pt(AuPPh_3)_8^{2+}$, and Related Platinum-Centered Gold Cluster Complexes. *Inorg. Chem.* **1997,** *36* (7), 1443-1453.

(31) Jaw, H. R. C.; Mason, W. R. Magnetic Circular Dichroism Spectra for the $Au_9(PPh_3)_8^{3+}$ Ion. *Inorg. Chem.* **1991,** *30* (2), 275-278.

(32) Wen, F.; Englert, U.; Homberger, M.; Simon, U. Single-crystal X-ray Analysis of $[Au_9(PPh_3)_8](NO_3)_3$. *Z. Anorg. Allg. Chem.* **2006,** *632* (12-13), 2159-2159.

(33) Vollenbroek, F. A.; Bour, J. J.; Van Der Veden, J. W. A. Gold- phosphine cluster compounds : The reactions of $[Au_9L_8]^{3+}$ (L = PPh_3) with L, SCN^- and Cl^- to $[Au_8L_8]^{2+}$ $(Au_{11}L_8(SCN)_2]^+$ and $[Au_{11}L_8Cl_2]^+$. *Recl. Trav. Chim. Pays-Bas* **1980,** *99* (4), 137-141.

(34) McKenzie, L. C.; Zaikova, T. O.; Hutchison, J. E. Structurally Similar Triphenylphosphine-Stabilized Undecagolds, $Au_{11}(PPh_3)_7Cl_3$ and $Au_{11}(PPh_3)_8Cl_2Cl$, Exhibit Distinct Ligand Exchange Pathways with Glutathione. *J. Am. Chem. Soc.* **2014,** *136* (38), 13426-13435.

(35) Mingos, D. M. P. Structural and Bonding Patterns in Gold Clusters. *Dalton Trans.* **2015,** *44* (15), 6680-6695.

(36) Fang, J.; Zhang, B.; Yao, Q.; Yang, Y.; Xie, J.; Yan, N. Recent Advances in the Synthesis and Catalytic Applications of Ligand-protected, Atomically Precise Metal Nanoclusters. *Coord. Chem. Rev.* **2016,** *322*, 1-29.

(37) Gutrath, B. S.; Englert, U.; Wang, Y.; Simon, U. A Missing Link in Undecagold Cluster Chemistry: Single- Crystal X- ray Analysis of $[Au_{11}(PPh_3)_7Cl_3]$. *Eur. J. Inorg. Chem.* **2013,** *2013* (12), 2002-2006.

(38) Gutrath, B. S.; Merkens, C.; Schiefer, F.; Englert, U.; Schmid, G.; Simon, U. Isolation, Optical Properties and Core Structure of a Water-soluble, Phosphine-stabilized $[Au_9]^{3+}$ Cluster. *Z. Naturforsch. B Chem. Sci.* **2013,** *68* (5/6), 569-574.

(39) Yao, H.; Iwatsu, M. Water-Soluble Phosphine-Protected Au_{11} Clusters: Synthesis, Electronic Structure, and Chiral Phase Transfer in a Synergistic Fashion. *Langmuir* **2016,** *32* (13), 3284-3293.

(40) Takano, S.; Tsukuda, T. Amplification of the Optical Activity of Gold Clusters by the Proximity of BINAP. *J. Phys. Chem. Lett.* **2016,** *7* (22), 4509-4513. Direct link: <http://pubs.acs.org/doi/abs/10.1021%2Facs.jpclett.6b02294>

(41) Yanagimoto, Y.; Negishi, Y.; Fujihara, H.; Tsukuda, T. Chiroptical Activity of BINAP-Stabilized Undecagold Clusters. *J. Phys. Chem. B* **2006,** *110* (24), 11611-11614.

(42) Tamura, M.; Fujihara, H. Chiral Bisphosphine BINAP-Stabilized Gold and Palladium Nanoparticles with Small Size and Their Palladium Nanoparticle-Catalyzed Asymmetric Reaction. *J. Am. Chem. Soc.* **2003,** *125* (51), 15742-15743.

(43) Yao, L.-Y.; Yam, V. W.-W. Diphosphine-Stabilized Small Gold Nanoclusters: From Crystal Structure Determination to Ligation-Driven Symmetry Breaking and Anion Exchange Properties. *J. Am. Chem. Soc.* **2016,** *138* (48), 15736-15742.

(44) Robinson, P. S. D.; Nguyen, T.-L.; Lioe, H.; O'Hair, R. A. J.; Khairallah, G. N. Synthesis and Gas-phase Uni- and Bi-molecular Ractivity of Bisphosphine Ligated Gold Clusters, $[Au_xL_y]^{n+}$. *Int. J. Mass Spectrom.* **2012,** *330-332*, 109-117.

(45) Provorse, M. R.; Aikens, C. M. Origin of Intense Chiroptical Effects in Undecagold Subnanometer Particles. *J. Am. Chem. Soc.* **2010,** *132* (4), 1302-1310.

(46) Shichibu, Y.; Kamei, Y.; Konishi, K. Unique [Core+Two] Structure and Optical Property of a Dodeca-Ligated Undecagold Cluster: Critical Contribution of the Exo Gold Atoms to the Electronic Structure. *Chem. Commun.* **2012,** *48* (61), 7559-7561.

(47) Knoppe, S.; Lehtovaara, L.; Häkkinen, H. Electronic Structure and Optical Properties of the Intrinsically Chiral 16-Electron Superatom Complex $[Au_{20}(PP_3)_4]^{4+}$. *J. Phys. Chem. A* **2014,** *118* (23), 4214-4221.

(48) Knoppe, S.; Zhang, Q.-F.; Wan, X.-K.; Wang, Q.-M.; Wang, L.-S.; Verbiest, T. Second-Order Nonlinear Optical Scattering Properties of Phosphine-Protected Au_{20} Clusters. *Ind. Eng. Chem. Res* **2016,** *55* (39), 10500-10506.

(49) Konishi, K. Phosphine-coordinated pure-gold clusters: Diverse geometrical structures and unique optical properties/responses. *Struct. Bonding* **2014,** *161*, 49-86.

(50) Boca, R. Tetrahedral Gold-Phosphine Clusters: a Relativistic Molecular Orbital Study. *J. Chem. Soc., Dalton Trans.* **1994,** (14), 2061-2064.

(51) Manassero, M.; Naldini, L.; Sansoni, M. A New Class of Gold Cluster Compounds. Synthesis and X-ray Structure of the Octakis(triphenylphosphinegold) dializarinsulphonate, $[Au_8(PPh_3)_8](aliz)_2$. *J. Chem. Soc., Chem. Commun.* **1979,** (9), 385-386.

(52) Alvino, J. F.; Bennett, T.; Anderson, D.; Donoeva, B.; Ovoshchnikov, D.; Adnan, R. H.; Appadoo, D.; Golovko, V.; Andersson, G.; Metha, G. F. Far-infrared Absorption Spectra of Synthetically-prepared, Ligated Metal Clusters with Au_6, Au_8, Au_9 and Au_6Pd Metal Cores. *RSC Advances* **2013,** *3* (44), 22140-22149.

(53) Van der Velden, J. W. A.; Bour, J. J.; Bosman, W. P.; Noordik, J. H. Reactions of Cationic Gold Glusters with Lewis Bases. Preparation and X-ray Structure Investigation of $[Au_8(PPh_3)_7](NO_3)_2.2CH_2Cl_2$ and $Au_6(PPh_3)_4[Co(CO)_4]_2$. *Inorg. Chem.* **1983,** *22* (13), 1913-1918.

(54) Yang, Y.; Sharp, P. R. New Gold Clusters $[Au_8L_6](BF_4)_2$ and $[(AuL)_4](BF_4)_2$ (L = P(mesityl)$_3$). *J. Am. Chem. Soc.* **1994,** *116* (15), 6983-6984.

(55) Kamei, Y.; Shichibu, Y.; Konishi, K. Generation of Small Gold Clusters with Unique Geometries through Cluster-to-Cluster Transformations: Octanuclear Clusters with Edge-sharing Gold Tetrahedron Motifs. *Angew. Chem. Int. Ed.* **2011,** *50* (32), 7442-7445.

(56) Vollenbroek, F. A.; Bosman, W. P.; Bour, J. J.; Noordik, J. H.; Beurskens, P. T. Reactions of Gold-Phosphine Cluster Compounds. Preparation and X-ray Structure Determination of Octakis(triphenylphosphine)octa-gold bis(hexafluorophosphate). *J. Chem. Soc., Chem. Commun.* **1979,** (9), 387-388.

(57) Schulz-Dobrick, M.; Jansen, M. Synthesis and Characterization of Intercluster Compounds Consisting of Various Gold Clusters and Differently Charged Keggin Anions. *Z. Anorg. Allg. Chem.* **2008,** *634* (15), 2880-2884.

(58) Van der Velden, J. W. A.; Bour, J. J.; Steggerda, J. J.; Beurskens, P. T.; Roseboom, M.; Noordik, J. H. Gold clusters. Tetrakis[1,3-bis(diphenylphosphino)propane]hexagold dinitrate: preparation, x-ray analysis, and gold-197 Moessbauer and phosphorus-31{proton} NMR spectra. *Inorg. Chem.* **1982,** *21* (12), 4321-4324.

(59) Kobayashi, N.; Kamei, Y.; Shichibu, Y.; Konishi, K. Protonation-Induced Chromism of Pyridylethynyl-Appended [Core+Exo]-Type Au_8 Clusters. Resonance-Coupled Electronic Perturbation through pi-Conjugated Group. *J. Am. Chem. Soc.* **2013,** *135* (43), 16078-16081.

(60) Schulz-Dobrick, M.; Jansen, M. Supramolecular Intercluster Compounds Consisting of Gold Clusters and Keggin Anions. *Eur. J. Inorg. Chem.* **2006,** *2006* (22), 4498-4502.

(61) Briant, C. E.; Hall, K. P.; Mingos, D. M. P. Structural Characterisation of Two Crystalline Modifications of $[Au_9\{P(C_6H_4OMe\text{-}p)_3\}_8](NO_3)_3$: the First Example of Skeletal Isomerism in Metal Cluster Chemistry. *J. Chem. Soc., Chem. Commun.* **1984,** (5), 290-291.

(62) Hall, K. P.; Theoblad, B. R. C.; Gilmour, D. I.; Mingos, D. M. P.; Welch, A. J. Synthesis and Structural Characterization of $[Au_9\{P(p\text{-}C_6H_4OMe)_3\}_8](BF_4)_3$; a Cluster with a Centred Crown of Gold Atoms. *J. Chem. Soc., Chem. Commun.* **1982,** (10), 528-530.

(63) Schulz-Dobrick, M.; Jansen, M. Characterization of Gold Clusters by Crystallization with Polyoxometalates: the Intercluster Compounds $[Au_9(dpph)_4][Mo_8O_{26}]$, $[Au_9(dpph)_4][PW_{12}O_{40}]$ and $[Au_{11}(PPh_3)_8Cl_2]_2[W_6O_{19}]$. *Z. Anorg. Allg. Chem.* **2007,** *633* (13-14), 2326-2331.

(64) Van der Velden, J. W. A.; Bour, J. J.; Bosman, W. P.; Noordik, J. H.; Beurskens, P. T. The Electrochemical Preparation of $[Au_9(PPh_3)_8]^+$. A Comparative Study of the Structures and Properties of $[Au_9(PPh_3)_8]^+$ and $[Au_9(PPh_3)_8]^{3+}$. *Recl. Trav. Chim. Pays-Bas* **1984,** *103* (1), 13-16.

(65) Albano, V. G.; Bellon, P. L.; Manassero, M.; Sansoni, M. Intermetallic Pattern in Metal-atom Clusters. Structural Studies on $Au_{11}X_3(PR_3)_7$ Species. *J. Chem. Soc. D* **1970,** (18), 1210-1211.

(66) Nunokawa, K.; Onaka, S.; Yamaguchi, T.; Ito, T.; Watase, S.; Nakamoto, M. Synthesis and Characterization of the Au_{11} Cluster with Sterically Demanding Phosphine Ligands by Single Crystal X-ray Diffraction and XPS Spectroscopy. *Bull. Chem. Soc. Jpn.* **2003,** *76* (8), 1601-1602.

(67) Nunokawa, K.; Onaka, S.; Ito, M.; Horibe, M.; Yonezawa, T.; Nishihara, H.; Ozeki, T.; Chiba, H.; Watase, S.; Nakamoto, M. Synthesis, Single Crystal X-ray Analysis, and TEM for a Single-sized Au_{11} Cluster Stabilized by SR Ligands: The Interface between Molecules and Particles. *J. Org. Chem.* **2006,** *691* (4), 638-642.

(68) Copley, R. C. B.; Mingos, D. M. P. The Novel Structure of the $[Au_{11}(PMePh_2)_{10}]^{3+}$ Cation: Crystal Structures of $[Au_{11}(PMePh_2)_{10}][C_2B_9H_{12}]_3.4THF$ and $[Au_{11}(PMePh_2)_{10}][C_2B_9H_{12}]_3$(THF = Tetrahydrofuran). *J. Chem. Soc., Dalton Trans.* **1996,** (4), 479-489.

(69) Smits, J.; Bour, J.; Vollenbroek, F.; Beurskens, P. Preparation and X-ray Structure Determination of [Pentakis{1,3-bis(diphenylphosphino)propane}] undecagoldtris(thiocyanate), $[Au_{11}\{PPh_2C_3H_6PPh_2\}_5](SCN)_3$. *J. Crystallogr. Spectrosc. Res.* **1983,** *13* (5), 355-363.

(70) Sharma, J.; Chhabra, R.; Cheng, A.; Brownell, J.; Liu, Y.; Yan, H. Control of Self-Assembly of DNA Tubules Through Integration of Gold Nanoparticles. *Science* **2009,** *323*, 112-116.

(71) Liu, H.; Shen, X.; Wang, Z.-G.; Kuzyk, A.; Ding, B. Helical Nanostructures Based on DNA Self-Assembly. *Nanoscale* **2014,** *6*, 9331-9338.

(72) Fan, Z.; Govorov, A. O. Helical Metal Nanoparticle Assemblies with Defects: Plasmonic Chirality and Circular Dichroism. *J. Phys. Chem. C* **2011,** *115* (27), 13254-13261.

(73) Song, C.; Blaber, M. G.; Zhao, G.; Zhang, P.; Fry, H. C.; Schatz, G. C.; Rosi, N. L. Tailorable Plasmonic Circular Dichroism Properties of Helical Nanoparticle Superstructures. *Nano Lett.* **2013,** *13* (7), 3256-3261.

(74) Schreiber, R.; Ngoc, L.; Zhiyuan, F.; Anton, K.; Philipp, N.; Tao, Z.; David, S.; Bernard, Y.; Wan, K.; Alexander, G., et al. Chiral Plasmonic DNA Nanostructures with Switchable Circular Dichroism. *Nat. Commun.* **2013,** *4*, 2948:1-2948:6.

(75) Kuzyk, A.; Schreiber, R.; Fan, Z.; Pardatscher, G.; Roller, E.-M.; Hogele, A.; Simmel, F. C.; Govorov, A. O.; Liedl, T. DNA-Based Self-Assembly of Chiral Plasmonic Nanostructures with Tailored Optical Response. *Nature* **2012,** *483* (7389), 311-314.

(76) Oemrawsingh, S. S. R.; Markesevic, N.; Gwinn, E. G.; Eliel, E. R.; Bouwmeester, D. Spectral Properties of Individual DNA-Hosted Silver Nanoclusters at Low Temperatures. *J. Phys. Chem. C* **2012,** *116* (48), 25568-25575.

(77) Petty, J. T.; Zheng, J.; Hud, N. V.; Dickson, R. M. DNA-Templated Ag Nanocluster Formation. *J. Am. Chem. Soc.* **2004,** *126* (16), 5207-5212.

(78) Ritchie, C. M.; Johnsen, K. R.; Kiser, J. R.; Antoku, Y.; Dickson, R. M.; Petty, J. T. Ag Nanocluster Formation Using a Cytosine Oligonucleotide Template. *J. Phys. Chem. C* **2007,** *111* (1), 175-181.

(79) Petty, J. T.; Fan, C.; Story, S. P.; Sengupta, B.; St. John Iyer, A.; Prudowsky, Z.; Dickson, R. M. DNA Encapsulation of 10 Silver Atoms Producing a Bright, Modulatable, Near-Infrared-Emitting Cluster. *J. Phys. Chem. Lett.* **2010,** *1* (17), 2524-2529.

(80) Yeh, H.-C.; Sharma, J.; Han, J. J.; Martinez, J. S.; Werner, J. H. A DNA‚àíSilver Nanocluster Probe That Fluoresces upon Hybridization. *Nano Lett.* **2010,** *10* (8), 3106-3110.

(81) Schultz, D.; Gardner, K.; Oemrawsingh, S. S. R.; Markešević, N.; Olsson, K.; Debord, M.; Bouwmeester, D.; Gwinn, E. Evidence for Rod-Shaped DNA-Stabilized Silver Nanocluster Emitters. *Adv. Mater.* **2013,** *25* (20), 2797-2803.

(82) Sharma, J.; Rocha, R. C.; Phipps, M. L.; Yeh, H.-C.; Balatsky, K. A.; Vu, D. M.; Shreve, A. P.; Werner, J. H.; Martinez, J. S. A DNA-Templated Fluorescent Silver Nanocluster with Enhanced Stability. *Nanoscale* **2012,** *4* (14), 4107-4110.

(83) Gwinn, E. G.; O'Neill, P.; Guerrero, A. J.; Bouwmeester, D.; Fygenson, D. K. Sequence-Dependent Fluorescence of DNA-Hosted Silver Nanoclusters. *Adv. Mater.* **2008,** *20* (2), 279-283.

(84) Richards, C. I.; Choi, S.; Hsiang, J.-C.; Antoku, Y.; Vosch, T.; Bongiorno, A.; Tzeng, Y.-L.; Dickson, R. M. Oligonucleotide-Stabilized Ag Nanocluster Fluorophores. *J. Am. Chem. Soc.* **2008,** *130* (15), 5038-5039.

(85) Schultz, D.; Gwinn, E. G. Silver Atom and Strand Numbers in Fluorescent and Dark Ag:DNAs. *Chem. Commun.* **2012,** *48* (46), 5748-5750.

(86) Copp, S. M.; Schultz, D.; Swasey, S.; Pavlovich, J.; Debord, M.; Chiu, A.; Olsson, K.; Gwinn, E. Magic Numbers in DNA-Stabilized Fluorescent Silver Clusters Lead to Magic Colors. *J. Phys. Chem. Lett.* **2014,** *5* (6), 959-963.

(87) O'Neill, P. R.; Gwinn, E. G.; Fygenson, D. K. UV Excitation of DNA Stabilized Ag Cluster Fluorescence via the DNA Bases. *J. Phys. Chem. C* **2011,** *115* (49), 24061-24066.

(88) Driehorst, T.; O'Neill, P.; Goodwin, P. M.; Pennathur, S.; Fygenson, D. K. Distinct Conformations of DNA-Stabilized Fluorescent Silver Nanoclusters Revealed by Electrophoretic Mobility and Diffusivity Measurements. *Langmuir* **2011,** *27* (14), 8923-8933.

(89) Soto-Verdugo, V.; Metiu, H.; Gwinn, E. The Properties of Small Ag Clusters Bound to DNA Bases. *J. Chem. Phys* **2010,** *132* (19), 195102:1 - 195102:10.

(90) Dale, B. B.; Senanayake, R. D.; Aikens, C. M. Research Update: Density Functional Theory Investigation of the Interactions of Silver Nanoclusters with Guanine. *APL Materials* **2017,** *5* (5), 053102:1-053102:9.

(91) Swasey, S. M.; Karimova, N.; Aikens, C. M.; Schultz, D. E.; Simon, A. J.; Gwinn, E. G. Chiral Electronic Transitions in Fluorescent Silver Clusters Stabilized by DNA. *ACS Nano* **2014,** *8* (7), 6883–6892.

(92) Gwinn, E.; Schultz, D.; Copp, S.; Swasey, S. DNA-Protected Silver Clusters for Nanophotonics. *Nanomaterials* **2015,** *5* (1), 180.

(93) Berdakin, M.; Taccone, M. I.; Pino, G. A.; Sanchez, C. G. DNA-protected silver emitters: charge dependent switching of fluorescence. *Phys. Chem. Chem. Phys.* **2017,** *19* (8), 5721-5726.

(94) Mason, W. R. Electronic Absorption and MCD Spectra for $Pt(AuPPh_3)_8^{2+}$ and $Au(AuPPh_3)_8^{3+}$ Cluster Complexes in Poly(methyl methacrylate) Thin Films at 295 and 10 K. *Inorg. Chem.* **2000,** *39* (2), 370-374.

(95) Yao, H.; Saeki, M.; Sasaki, A. Boronic Acid-Protected Gold Clusters Capable of Asymmetric Induction: Spectral Deconvolution Analysis of Their Electronic Absorption and Magnetic Circular Dichroism. *Langmuir* **2012,** *28* (8), 3995-4002.

(96) Mason, W. R. *Comprehensive Coordination Chemistry II*. Elsevier Science: 2003; Vol. 2, p 327-337.

(97) Peralta, G. A.; Seth, M.; Ziegler, T. Magnetic Circular Dichroism of Porphyrins Containing M = Ca, Ni, and Zn. A Computational Study Based on Time-Dependent Density Functional Theory. *Inorg. Chem.* **2007,** *46* (22), 9111-9125.

(98) Peralta, G. A.; Seth, M.; Zhekova, H.; Ziegler, T. Magnetic Circular Dichroism of Phthalocyanine (M = Mg, Zn) and Tetraazaporphyrin (M = Mg, Zn, Ni) Metal Complexes. A Computational Study Based on Time-Dependent Density Functional Theory. *Inorg. Chem.* **2008,** *47* (10), 4185-4198.

(99) Rhoda, H. M.; Crandall, L. A.; Geier, G. R.; Ziegler, C. J.; Nemykin, V. N. Combined MCD/DFT/TDDFT Study of the Electronic Structure of Axially Pyridine Coordinated Metallocorroles. *Inorg. Chem.* **2015,** *54* (10), 4652-4662.

(100) Mack, J.; Morita, Y.; Higashibayashi, S.; Sakurai, H.; Kobayashi, N. Magnetic Circular Dichroism Spectroscopy and Electronic Structures of C_3 Symmetry Buckybowls. *Chem. Phys. Lett.* **2013,** *556*, 188-194.

(101) Kirk, M. L.; Peariso, K. Recent Applications of MCD Spectroscopy to Metalloenzymes. *Curr. Opin. Struct. Biol.* **2003,** *7* (2), 220-227.

(102) Zaitoun, M. A.; Mason, W. R.; Lin, C. T. Magnetic Circular Dichroism Spectra for Colloidal Gold Nanoparticles in Xerogels at 5.5 K. *J. Phys. Chem. B* **2001,** *105* (29), 6780-6784.

(103) Jaw, H. R. C.; Savas, M. M.; Mason, W. R. Electronic Absorption and MCD Spectra for the Binuclear Three-Coordinate Gold(I) Complex $Au_2(dmpm)_3^{2+}$ (dmpm = bis(dimethylphosphino)methane). *Inorg. Chem.* **1989,** *28* (24), 4366-4369.

(104) Bradley, J. M.; Silkstone, G.; Wilson, M. T.; Cheesman, M. R.; Butt, J. N. Probing a Complex of Cytochrome c and Cardiolipin by Magnetic Circular Dichroism Spectroscopy: Implications for the Initial Events in Apoptosis. *J. Am. Chem. Soc.* **2011,** *133* (49), 19676-19679.

(105) Kadish, K. M. *Handbook of porphyrin science : with applications to chemistry, physics, materials science, engineering, biology and medicine*. Singapore : World Scientific: Singapore, 2010.

(106) Isci, H.; Mason, W. R. Ligand-to-Metal Charge-Transfer Spectra of Tetrahaloaurate(III) and Trans-Dicyanodihaloaurate(III) Ions. *Inorg. Chem.* **1983,** *22* (16), 2266-2272.

(107) Isci, H.; Mason, W. R. Magnetic Circular Dichroism Spectra for the Intense UV Bands of the Tetrachloro- and Tetrabromoplatinate(II) Ions. *Inorg. Chem.* **1984,** *23* (11), 1565-1569.

(108) Isci, H.; Mason, W. R. Electronic Structure and Spectra of Square-Planar Alkyl Isocyanide Complexes. *Inorg. Chem.* **1975,** *14* (4), 913-918.

(109) Mason, W. R. Magnetic Circular Dichroism Spectra for the TetraAmmineplatinum(II) and Bis(ethylenediamine)platinum(II) Cations. *Inorg. Chem.* **1986,** *25* (17), 2925-2929.

(110) Savas, M. M.; Mason, W. R. Electronic and MCD Spectra of Linear Two-Coordinate Dihalo-, Halo(trialkylphosphine)-, and Bis(triethylphosphine)gold(I) Complexes. *Inorg. Chem.* **1987,** *26* (2), 301-307.

(111) Savas, M. M.; Mason, W. R. Vapor-Phase Electronic Absorption Spectra and Solution Magnetic Circular Dichroism and Absorption Spectra for Dihalo- and Halomethylmercury(II). *Inorg. Chem.* **1988,** *27* (4), 658-665.

(112) Zaitoun, M. A.; Mason, W. R.; Lin, C. T. Magnetic Circular Dichroism Spectra for Colloidal Gold Nanoparticles in Xerogels at 5.5 K. *J. Phys. Chem. B* **2001,** *105* (29), 6780-6784.

(113) Artemyev, M.; Krutokhvostov, R.; Melnikau, D.; Oleinikov, V.; Sukhunova, A.; Nabiev, I. Low-Field Magnetic Circular Dichroism in Silver and Gold Colloidal Nanoparticles of Different Sizes, Shapes, and Aggregation State. *Plasmonics* **2012,** *8457*, 845729/1-10.

(114) Schaaff, G. T.; Whetten, R. L. Giant Gold-Glutathione Cluster Compounds: Intense Optical Activity in Metal-Based Transitions. *J. Phys. Chem. B* **2000,** *104* (12), 2630-2641.

(115) Li, Y.; Li, W.; Zhang, J. Frontispiece: Gold-Catalyzed Enantioselective Annulations. *Chemistry – A European Journal* **2017,** *23* (3), 467-512.

(116) Jadzinsky, P. D.; Calero, G.; Ackerson, C. J.; Bushnell, D. A.; Kornberg, R. D. Structure of a Thiol Monolayer-Protected Gold Nanoparticle at 1.1 Angstrom Resolution. *Science* **2007,** *318* (5849), 430-433.

(117) Lorenzo, M. O.; Baddeley, C. J.; Muryn, C.; Raval, R. Extended Surface Chirality from Supramolecular Assemblies of Adsorbed Chiral Molecules. *Nature* **2000,** *404* (6776), 376.

(118) Jay, A. S.; Hiten, M. K.; Philippe, P.; Shuji, N.; Eric, W. B. Enantiospecific Electrodeposition of a Chiral Catalyst. *Nature* **2003,** *425* (6957), 490.

(119) Zeng, C.; Chen, Y.; Kirschbaum, K.; Appavoo, K.; Sfeir, M. Y.; Jin, R. Structural Patterns at All Scales in a Nonmetallic Chiral $Au_{133}(SR)_{52}$ Nanoparticle. *Sci. Adv.* **2015,** *1* (2), 1-6.

(120) Yao, H.; Miki, K.; Nishida, N.; Sasaki, A.; Kimura, K. Large Optical Activity of Gold Nanocluster Enantiomers Induced by a Pair of Optically Active Pencilamines. *J. Am. Chem. Soc.* **2005,** *127* (44), 15536-15543.

(121) Jaganathan, H.; Kinsella, J. M.; Ivanisevic, A. Circular Dichroism Study of the Mechanism of Formation of DNA Templated Nanowires. *ChemPhysChem* **2008,** *9* (15), 2203-2206.

(122) Yan, J.; Su, H.; Yang, H.; Hu, C.; Malola, S.; Lin, S.; Teo, B. K.; Häkkinen, H.; Zheng, N. Asymmetric Synthesis of Chiral Bimetallic $[Ag_{28}Cu_{12}(SR)_{24}]^{4-}$ Nanoclusters via Ion Pairing. *J. Am. Chem. Soc.* **2016,** *138* (39), 12751-12754.

(123) Dolamic, I.; Knoppe, S.; Dass, A.; Bürgi, T. First Enantioseparation and Circular Dichroism Spectra of Au_{38} Clusters Protected by Achiral Ligands. *Nat. Commun.* **2012,** *3*, 798-802.

(124) Knoppe, S.; Malola, S.; Lehtovaara, L.; Bürgi, T.; Häkkinen, H. Electronic Structure and Optical Properties of the Thiolate-Protected $Au_{28}(SMe)_{20}$ Cluster. *J. Phys. Chem. A* **2013,** *117* (40), 10526-10533.

(125) Varnholt, B.; Dolamic, I.; Knoppe, S.; Burgi, T. On the Flexibility of the Gold-thiolate Interface: Racemization of the $Au_{40}(SR)_{24}$ Cluster. *Nanoscale* **2013,** *5* (20), 9568-9571.

(126) Knoppe, S.; Dolamic, I.; Dass, A.; Bürgi, T. Separation of Enantiomers and CD Spectra of $Au_{40}(SCH_2CH_2Ph)_{24}$: Spectroscopic Evidence for Intrinsic Chirality. *Angew. Chem. Int. Ed.* **2012,** *51* (30), 7589-7591.

(127) Knoppe, S.; Bürgi, T. Chirality in Thiolate-Protected Gold Clusters. *Acc. Chem. Res* **2014,** *47* (4), 1318–1326.

(128) Knoppe, S.; Dass, A.; Burgi, T. Strong Non-Linear Effects in the Chiroptical Properties of the Ligand-Exchanged Au_{38} and Au_{40} Clusters. *Nanoscale* **2012,** *4* (14), 4211-4216.

(129) Si, S.; Gautier, C.; Boudon, J.; Taras, R.; Gladiali, S.; Bürgi, T. Ligand Exchange on Au_{25} Cluster with Chiral Thiols. *J. Phys. Chem. C* **2009,** *113* (30), 12966-12969.

(130) Kumar, S.; Jin, R. Water-Soluble $Au_{25}(Capt)_{18}$ Nanoclusters: Synthesis, Thermal Stability, and Optical Properties. *Nanoscale* **2012,** *4* (14), 4222-4227.

(131) Pei, Y.; Gao, Y.; Zeng, X. C. Structural Prediction of Thiolate-Protected Au_{38}: A Face-Fused Bi-icosahedral Au Core. *J. Am. Chem. Soc.* **2008,** *130* (25), 7830-7832.

(132) Lopez-Acevedo, O.; Tsunoyama, H.; Tsukuda, T.; Häkkinen, H.; Aikens, C. M. Chirality and Electronic Structure of the Thiolate-Protected Au_{38} Nanocluster. *J. Am. Chem. Soc.* **2010,** *132* (23), 8210-8218.

(133) Jiang, D. TheExpanding Universe of Thiolated Gold Nanoclusters and Beyond. *Nanoscale* **2013,** *5* (16), 7149-7160.

(134) Van der Velden, J. W. A.; Bour, J. J.; Pet, R.; Bosman, W. P.; Noordik, J. H. Preparation and X-ray Structure Determination of Tris[bis(diphenylphosphino)methane]diiodotetragold. *Inorg. Chem.* **1983,** *22* (21), 3112-3115.

(135) Mingos, D. Gold - A Flexible Friend in Cluster Chemistry. *J. Chem. Soc., Dalton Trans.* **1996,** (5), 561-566.

(136) Knoppe, S.; Lehtovaara, L.; Hakkinen, H. Electronic Structure and Optical Properties of the Intrinsically Chiral 16-Electron Superatom Complex $[Au_{20}(PP_3)_4]^{4+}$. *J. Phys. Chem. A* **2014,** *118* (23), 4214-4221.

(137) Chen, J.; Zhang, Q.-F.; Bonaccorso, T. A.; Williard, P. G.; Wang, L.-S. Controlling Gold Nanoclusters by Diphospine Ligands. *J. Am. Chem. Soc.* **2014,** *136* (1), 92-95.

(138) Garzón, I. L.; Beltrán, M. R.; González, G.; Gutıerrez-González, I.; Michaelian, K.; Reyes-Nava, J. A.; Rodrıguez-Hernández, J. I. Chirality, Defects, and Disorder Ingold Clusters. *EPJ D* **2003,** *24* (1), 105-109.

(139) Noguez, C.; Garzón, I. L. Optically Active Metal Nanoparticles. *Chem. Soc. Rev.* **2009,** *38* (3), 757-771.

(140) Garzón, I. L.; Reyes-Nava, J. A.; Rodríguez-Hernández, J. I.; Sigal, I.; Beltrán, M. R.; Michaelian, K. Chirality in Bare and Passivated Gold Nanoclusters. *Phys. Rev. B* **2002,** *66* (7), 073403:1-073403:4.

(141) Häkkinen, H.; Moseler, M.; Landman, U. Bonding in Cu, Ag, and Au Clusters: Relativistic Effects, Trends, and Surprises. *Phys. Rev. Lett.* **2002,** *89* (3), 033401.

(142) Häkkinen, H.; Moseler, M.; Kostko, O.; Morgner, N.; Hoffmann, M. A.; v. Issendorff, B. Symmetry and Electronic Structure of Noble-Metal Nanoparticles and the Role of Relativity. *Phys. Rev. Lett.* **2004,** *93* (9), 093401.

(143) Goldsmith, M.-r.; George, C. B.; Zuber, G.; Naaman, R.; Waldeck, D. H.; Wipf, P.; Beratan, D. N. The Chiroptical Signature of Achiral Metal Clusters Induced by Dissymmetric Adsorbates. *Phys. Chem. Chem. Phys.* **2006,** *8* (1), 63-67.

(144) Gautier, C.; Bürgi, T. Chiral N-Isobutyryl-cysteine Protected Gold Nanoparticles: Preparation, Size Selection, and Optical Activity in the UV−vis and Infrared. *J. Am. Chem. Soc.* **2006,** *128* (34), 11079-11087.

(145) Humblot, V.; Haq, S.; Muryn, C.; Hofer, W. A.; Raval, R. From Local Adsorption Stresses to Chiral Surfaces: (R,R)-Tartaric Acid on Ni(110). *J. Am. Chem. Soc.* **2002,** *124* (3), 503.

(146) Gautier, C.; Bürgi, T. Chiral Inversion of Gold Nanoparticles. *J. Am. Chem. Soc.* **2008,** *130* (22), 7077-7084.

(147) Sharpless, K. B. Searching for New Reactivity (Nobel Lecture). *Angew. Chem. Int. Ed.* **2002,** *41* (12), 2024-2032.

(148) Noyori, R. Asymmetric Catalysis: Science and Opportunities (Nobel Lecture). *Angew. Chem. Int. Ed.* **2002,** *41* (12), 2008-2022.

(149) Sánchez-Castillo, A.; Noguez, C.; Garzón, I. L. On the Origin of the Optical Activity Displayed by Chiral-Ligand-Protected Metallic Nanoclusters. *J. Am. Chem. Soc.* **2010,** *132* (5), 1504-1505.

(150) Wan, X.-K.; Yuan, S.-F.; Lin, Z.-W.; Wang, Q.-M. A Chiral Gold Nanocluster Au20 Protected by Tetradentate Phosphine Ligands. *Angew. Chem. Int. Ed.* **2014,** *53* (11), 2923-2926.

(151) Levine, I. N. *Quantum Chemistry*. 6 ed.; Pearson Education, Inc.: 2009; p 751.

(152) Lewars, E. G. *Computational Chemistry. Introduction to the Theory and Applications of Molecular and Quantum Mechanics* Kluwer Academic Publishers, 2004; p 471.

(153) Jensen, F. *Introduction to Computational Chemistry*. Chichester, New York : Wiley: 1999; p 599.

(154) Cramer, C. J. *Essentials of Computational Chemistry: Theories and Models*. Hoboken, NJ: Wiley: 2006; p 596.

(155) Li, W.-K.; Blinder, S. M. Introducing Relativity into Quantum Chemistry. *J. Chem. Educ.* **2011,** *88* (1), 71-73.

(156) Lenthe, v. E.; Ehlers, A. W.; Baerends, E. J. Geometry Optimizations in the Zero Order Regular Approximation for Relativistic Effects. *J. Chem. Phys.* **1999,** *110* (18), 8943-8953.

(157) Dreuw, A.; Head-Gordon, M. Single-Reference ab Initio Methods for the Calculation of Excited States of Large Molecules. *Chem. Rev.* **2005,** *105* (11), 4009-4037.

(158) te Velde, G.; Bickelhaupt, F. M.; Baerends, E. J.; Fonseca Guerra, C.; van Gisbergen, S. J. A.; Snijders, J. G.; Ziegler, T. Chemistry with ADF. *J. Comput. Chem.* **2001,** *22* (9), 931-967.

(159) Autschbach, J.; Ziegler, T.; van Gisbergen, S. J. A.; Baerends, E. J. Chiroptical Properties from Time-Dependent Density Functional Theory. I. Circular Dichroism Spectra of Organic Molecules. *J. Chem. Phys* **2002,** *116* (16), 6930-6940.

(160) Crawford, T. D. Ab initio Calculation of Molecular Chiroptical Properties. *Theor. Chem. Acc.* **2006,** *115* (4), 227-245.

(161) Piepho, S. B.; Schatz, P. N. *Group Theory in Spectroscopy: With Applications to Magnetic Circular Dichroism*. New York : Wiley: New York, 1983.

(162) Seth, M.; Krykunov, M.; Ziegler, T.; Autschbach, J. Application of Magnetically Perturbed Time-Dependent Density Functional Theory to Magnetic Circular Dichroism. II. Calculation of A Terms. *J. Chem. Phys* **2008,** *128* (23), 234102/1-13.

(163) Mason, W. R. *A Practical Guide to Magnetic Circular Dichroism Spectroscopy*. John Wiley & Sons, Inc., Hoboken, New Jersey: 2007; p 240.

(164) Kobayashi, N.; Muranaka, A. *Circular Dichroism and Magnetic Circular Dichroism Spectroscopy for Organic Chemists*. The Royal Society of Chemistry: 2012; p 216.

(165) Seth, M.; Krykunov, M.; Ziegler, T.; Autschbach, J.; Banerjee, A. Application of Magnetically Perturbed Time-Dependent Density Functional Theory to Magnetic Circular Dichroism: Calculation of B Terms. *J. Chem. Phys* **2008,** *128* (14), 144105/1-17.

(166) Seth, M.; Ziegler, T.; Autschbach, J. Application of Magnetically Perturbed Time-Dependent Density Functional Theory to Magnetic Circular Dichroism. III. Temperature-Dependent Magnetic Circular Dichroism Induced by Spin-Orbit Coupling. *J. Chem. Phys* **2008,** *129* (10), 104105/1-12.

(167) Kang, X.; Wang, S.; Song, Y.; Jin, S.; Sun, G.; Yu, H.; Zhu, M. Bimetallic Au_2Cu_6 Nanoclusters: Strong Luminescence Induced by the Aggregation of Copper(I) Complexes with Gold(0) Species. *Angew. Chem. Int. Ed.* **2016,** *55* (11), 3611-3614.

(168) Wang, Y.; Wan, X.-K.; Ren, L.; Su, H.; Li, G.; Malola, S.; Lin, S.; Tang, Z.; Häkkinen, H.; Teo, B. K., et al. Atomically Precise Alkynyl-Protected Metal Nanoclusters as a Model Catalyst: Observation of Promoting Effect of Surface Ligands on Catalysis by Metal Nanoparticles. *J. Am. Chem. Soc.* **2016,** *138* (10), 3278.

(169) Liu, J.; Krishna, K. S.; Losovyj, Y. B.; Chattopadhyay, S.; Lozova, N.; Miller, J. T.; Spivey, J. J.; Kumar, C. S. S. R. Ligand-Stabilized and Atomically Precise Gold Nanocluster Catalysis: A Case Study for Correlating Fundamental Electronic Properties with Catalysis. *Chem. Eur. J* **2013,** *19* (31), 10201.

(170) Karimova, N. V.; Aikens, C. M. Time Dependent Density Functional Theory Study of Magnetic Circular Dichroism Spectra of Gold Clusters $Au_9(PH_3)_8^{3+}$ and $Au_9(PPh_3)_8^{3+}$. *J. Phys. Chem. A* **2016,** *120*, 9626-9635.

(171) Gutrath, B. S.; Englert, U.; Wang, Y.; Simon, U. A Missing Link in Undecagold Cluster Chemistry: Single-Crystal X-ray Analysis of $[Au_{11}(PPh_3)_7Cl_3]$. *Eur. J. Inorg. Chem.* **2013,** *2013* (12), 2002-2006.

(172) Sugiuchi, M.; Shichibu, Y.; Nakanishi, T.; Hasegawa, Y.; Konishi, K. Cluster Electronic Interaction in a Superatomic Au_{13} Cluster Bearing -Bonded Acetylide Ligands. *Chem. Commun.* **2015,** *51* (70), 13519-13522.

(173) van Lenthe, E.; van Leeuwen, R.; Baerends, E. J.; Snijders, J. G. Relativistic Regular Two-Component Hamiltonians. *Int. J. Quantum Chem.* **1996,** *57* (3), 281-293.

(174) Becke, A. D. Density-Functional Exchange-Energy Approximation with Correct Asymptotic Behavior. *Phys. Rev. A* **1988,** *38* (6), 3098-3100.

(175) Perdew, J. P. Density-Functional Approximation for the Correlation Energy of the Inhomogeneous Electron Gas. *Phys. Rev. B* **1986,** *33* (12), 8822-8824.

(176) van Leeuwen, R.; Baerends, E. J. Exchange-Correlation Potential with Correct Asymptotic Behavior. *Phys. Rev. A* **1994,** *49* (4), 2421-2431.

(177) Klamt, A. Conductor-like Screening Model for Real Solvents: A New Approach to the Quantitative Calculation of Solvation Phenomena. *J. Phys. Chem.* **1995,** *99* (7), 2224-2235.

(178) Fan, Z.; Govorov, A. O. Plasmonic Circular Dichroism of Chiral Metal Nanoparticle Assemblies. *Nano Lett.* **2010,** *10* (7), 2580-2587.

(179) Zhang, Z.-Y.; Zhao, Y.-P. The visible extinction peaks of Ag nanohelixes: A periodic effective dipole model. *Appl. Phys. Lett.* **2011,** *98* (8), 083102.

(180) Zhang, Z.-Y.; Zhao, Y.-P. Optical properties of helical Ag nanostructures calculated by discrete dipole approximation method. *Appl. Phys. Lett.* **2007,** *90* (22), 221501.

(181) Zhang, Z.-Y.; Zhao, Y.-P. Optical properties of helical and multiring Ag nanostructures: The effect of pitch height. *J. Appl. Phys.* **2008,** *104* (1), 013517.

(182) Elizondo, S. L. First-principles Study of Helical Silver Single-Wall Nanotubes and Nanowires Materials Research Society Symposium Proceedings. *Mater. Res. Soc. Symp. Proc.* **2005,** *900*, 409-414.

(183) Elizondo, S. L.; Mintmire, J. W. Ab initio study of helical silver single-wall nanotubes and nanowires. *Phys. Rev. B* **2006,** *73* (4), 045431.

(184) Elizondo, S. L.; Mintmire, J. W. Simulations of metal nanowires. *Int. J. Quantum Chem.* **2005,** *105* (6), 772-780.

(185) O'Neill, B. *Elementary differential geometry*. New York, Academic Press: 1966; p 411.

(186) Schipper, P. R. T.; Gritsenko, O. V.; van Gisbergen, S. J. A.; Baerends, E. J. Molecular Calculations of Excitation Energies and (Hyper)Polarizabilities with a Statistical Average of Orbital Model Exchange-Correlation Potentials. *J. Chem. Phys* **2000,** *112* (3), 1344-1352.

(187) Kelley, A. M. *Condensed-phase molecular spectroscopy and photophysics*. John Wiley & Sons, Inc.: 2013; p 344.

(188) Woody, R. W., Circular dichroism, Methods in Enzymology. Academic Press: 1995; Vol. Volume 246, pp 34-71.

(189) Guidez, E. B.; Aikens, C. M. Theoretical analysis of the optical excitation spectra of silver and gold nanowires. *Nanoscale* **2012,** *4* (14), 4190-4198.

(190) Serber, R. The Theory of the Faraday Effect in Molecules. *Phy. Rev.* **1932,** *41* (4), 489-506.

(191) Hashimoto, A.; Yoshinari, N.; Konno, T. Structural Conversion of a Triphenylphosphine Gold Cluster by Octahedral Metal Complexes with 2-aminoethanethiolate. *Chem. Lett.* **2015,** *44* (6), 749-751.

(192) Tsai, C.-W.; Su, Y.-C.; Li, G.-D.; Chai, J.-D. Assessment of Density Functional Methods with Correct Asymptotic Behavior. *Phys. Chem. Chem. Phys.* **2013,** *15* (21), 8352-8361.

(193) Aikens, C. M. Effects of Core Distances, Solvent, Ligand, and Level of Theory on the TDDFT Optical Absorption Spectrum of the Thiolate-Protected Au_{25} Nanoparticle. *J. Phys. Chem. A* **2009,** *113* (40), 10811-10817.

(194) Nimmala, P. R.; Knoppe, S.; Jupally, V. R.; Delcamp, J. H.; Aikens, C. M.; Dass, A. $Au_{36}(SPh)_{24}$ Nanomolecules: X-ray Crystal Structure, Optical Spectroscopy, Electrochemistry, and Theoretical Analysis. *J. Phys. Chem. B* **2014,** *118* (49), 14157-14167.

(195) Walter, M.; Akola, J.; Lopez-Acevedo, O.; Jadzinsky, P. D.; Calero, G.; Ackerson, C. J.; Whetten, R. L.; Granbeck, H.; Hakkinen, H. A Unified View of Ligand-Protected Gold Clusters as Superatom Complexes. *Proc. Natl. Acad. Sci. U.S.A.* **2008,** *105* (27), 9157-9162.

(196) Jain, P. A DFT-Based Study of the Low-Energy Electronic Structures and Properties of Small Gold Clusters. *Struct. Chem.* **2005,** *16* (4), 421-426.

(197) Qian, H.; Zhu, Y.; Jin, R.; Eckenhoff, W. T.; Pintauer, T. Total Structure Determination of Thiolate-Protected Au_{38} Nanoparticles. *J. Am. Chem. Soc.* **2010,** *132* (24), 8280-8281.

(198) Yanagimoto, Y.; Negishi, Y.; Fujihara, H.; Tsukuda, T. Chiroptical Activity of BINAP-Stabilized Undecagold Clusters. *J. Phys. Chem. B* **2006,** *110* (24), 11611-11614.

(199) Yoon, B.; Hakkinen, H.; Landman, U.; Worz, A. S.; Antonietti, J.-M.; Abbet, S.; Judai, K.; Heiz, U. Charging Effects on Bonding and Catalyzed Oxidation of CO on $[Au_8]$ Clusters on MgO. *Science* **2005,** *307*, 403.

(200) Andersson, G. G.; Golovko, V. B.; Alvino, J. F.; Bennett, T.; Wrede, O.; Mejia, S. M.; Al Qahtani, H. S.; Adnan, R.; Gunby, N.; Anderson, D. P., et al. Phosphine-Stabilised Au_9 Clusters Interacting with Titania and Silica Surfaces: The First Evidence for the Density of States Signature of the Support-Immobilised Cluster. *J. Chem. Phys* **2014,** *141* (1), 014702.

(201) Kilmartin, J.; Sarip, R.; Grau-Crespo, R.; Di Tommaso, D.; Hogarth, G.; Prestipino, C.; Sankar, G. Following the Creation of Active Gold Nanocatalysts from Phosphine-Stabilized Molecular Clusters. *ACS Catalysis* **2012,** *2* (6), 957-963.

(202) Schulz-Dobrick, M.; Jansen, M. Intermolecular Forces in Intercluster Compounds Consisting of Gold Clusters and Fullerides and in a Series of Model Compounds $C_{60}{\cdot}2(PR_3)AuCl$. *CrystEngComm* **2008,** *10* (6), 661-664.

(203) Schulz-Dobrick, M.; Jansen, M. Intercluster Compounds Consisting of Gold Clusters and Fullerides: $Au_7(PPh_3)_7C_{60}$ x THF and $Au_8(PPh_3)_8(C_{60})_2$. *Angew. Chem. Int. Ed. (English)* **2008,** *47* (12), 2256-2259.

(204) Grüning, M.; Gritsenko, O. V.; van Gisbergen, S. J. A.; Baerends, E. J. Shape Corrections to Exchange-Correlation Potentials by Gradient-Regulated Seamless Connection of Model Potentials for Inner and Outer Region. *J. Chem. Phys* **2001,** *114* (2), 652-660.

(205) Stephens, P. J.; Devlin, F. J.; Chabalowski, C. F.; Frisch, M. J. Ab Initio Calculation of Vibrational Absorption and Circular Dichroism Spectra Using Density Functional Force Fields. *J. Phys. Chem.* **1994,** *98* (45), 11623-11627.

(206) Seth, M.; Ziegler, T. Range-Separated Exchange Functionals with Slater-Type Functions. *J. Chem. Theory Comput.* **2012,** *8* (3), 901-907.

(207) Kumbhar, A. S.; Kinnan, M. K.; Chumanov, G. Multipole Plasmon Resonances of Submicron Silver Particles. *J. Am. Chem. Soc.* **2005,** *127*, 12444-12445.

(208) Maier, S. A. *Plasmonics : fundamentals and applications*. 1st edition.. ed.; New York : Springer: New York, 2007; p 224.

(209) Mayergoyz, I. D. *Plasmon Resonances in Nanoparticles*. Singapore : World Scientific Publishing Company: Singapore, 2012; p 325.

(210) Daeha Seo, J. C. P.; Hyunjoon, S. Polyhedral Gold Nanocrystals with Oh Symmetry-,Äâ From Octahedra to Cubes. *J. Am. Chem. Soc.* **2006,** *128*, 14863-14870.

(211) Payne, E. K.; Shuford, K. L.; Park, S.; Schatz, G. C.; Mirkin, C. A. Multipole Plasmon Resonances in Gold Nanorods. *J. Phys. Chem.* **2006,** *110*, 2150-2154.

(212) Kim, F.; Connor, S.; Song, H.; Kuykendall, T.; Yang, P. Platonic gold nanocrystals. *Angew. Chem.* **2004,** *116*, 3759-3763.

(213) Bae, G.-T.; Aikens, C. M. Time-Dependent Density Functional Theory Studies of Optical Properties of Ag Nanoparticles: Octahedra, Truncated Octahedra, and Icosahedra. *J. Phys. Chem. C* **2012,** *116*, 10356-10367.

(214) Johnson, H. E.; Aikens, C. M. Electronic Structure and TDDFT Optical Absorption Spectra of Silver Nanorods. *J. Phys. Chem. A* **2009,** *113*, 4445-4450.

(215) Harb, M.; Rabilloud, F.; Simon, D. Structural, Electronic, Magnetic and Optical Properties of Icosahedral Silver-Nickel Nanoclusters. *Phis. Chem. Chem. Phys* **2010,** *12*, 4246-4254.

(216) Sekhon, J. S.; Verma, S. S. Tunable Plasmonic Properties of Silver Nanorods for Nanosensing Applications. *J. Mater. Sci* **2012,** *47*, 1930-1937.

(217) Millstone, J. E.; Park, S.; Shuford, K. L.; Qin, L.; Schatz, G. C.; Chad, A. M. Observation of a Quadrupole Plasmon Mode for a Colloidal Solution of Gold Nanoprisms. *J. Am. Chem. Soc.* **2005,** *127*, 5312-5313.

(218) Fan, J. A.; Wu , C.; Bao, K.; Bao, J.; Bardhan, R.; Halas, N. J.; Manoharan, V. N.; Nordlander, P.; Shvets, G.; Capasso, F. Self-Assembled Plasmonic Nanoparticle Clusters. *Science* **2010,** *328*, 1135-1138.

(219) Yin, J.; Yashu, Z.; Yue, C.; Wu, Z.; Wu, S.; Li, J.; Zhihao, W. Ag Nanoparticle/ZnO Hollow Nanosphere Arrays: Large Scale Synthesis and Surface Plasmon Resonance Effect Induced Raman Scattering Enhancement. *J. Mater. Chem.* **2012,** *22*, 7902-7909.

(220) Kelly, K. L.; Coronado, E.; Zhao, L. L.; Schatz, G. C. The Optical Properties of Metal Nanoparticles: The Influence of Size, Shape, and Dielectric Environment. *J. Phys. Chem. B* **2003,** *107*, 668-677.

(221) Lee, K.-S.; El-Sayed, M. A. Gold and Silver Nanoparticles in Sensing and Imaging: Sensitivity of Plasmon Response to Size, Shape, and Metal Composition. *J. Phys. Chem.* **2006,** *110*, 19220-19225.

(222) Mahmoud, M. A.; El-Sayed, M. A. Different Plasmon Sensing Behavior of Silver and Gold Nanorods. *J. Phys. Chem. Lett.* **2013,** *4*, 1541-1545.

(223) Matthew Pelton, G. B. *Introduction to metal-nanoparticle plasmonics*. Wiley: United States of America, 2013; p 275.

(224) Najiminaini, M.; Vasefi, F.; Kaminska, B.; Carson, J. J. L. Effect of surface plasmon energy matching on the sensing capability of metallic nano-hole arrays. *Appl. Phys. Lett.* **2012,** *100*, 063110-1-063110-4.

(225) Bark, O. M.; Amendola, V.; Aikens, C. M.; Wenseleers, W.; Li, R.; Negro, L. D.; Schatz, G. C.; Stellacci, F. Silver Nanoparticles with Broad Multiband Linear Optical Absorption. *Angew.Chem.Int.Ed.* **2009,** *48*, 5921-5926.

(226) Jain, P. K.; El-Sayed, M. A. Plasmonic coupling in noble metal nanostructures. *Chem. Phys. Lett.* **2010,** *487*, 153-164.

(227) Jin, R.; Cao, Y. C.; Hao, E.; Metraux, G. S.; Schatz, G. C.; Mirkin, C. A. Controlling Anisotropic Nanoparticle Growth Through Plasmon Excitation. *Nature* **2003,** *425*, 487-490.

(228) Jin, R.; Cao, Y. W.; Mirkin, C. A.; Kelly, K. L.; Schatz, G. C.; Zheng, J. G. Photoinduced Conversion of Silver Nanospheres to Nanoprisms. *Science* **2001,** *294*, 1901-1903.

(229) Fong, W.-K.; Hanley, T. L.; Thierry, B.; Kirby, N.; Boyd, B. J. Plasmonic Nanorods Provide Reversible Control over Nanostructure of Self-Assembled Drug Delivery Materials. *Langmuir* **2010,** *26* (9), 6136-6139.

(230) Petryayeva, E.; Krull, U. J. Localized Surface Plasmon Resonance: Nanostructures, Bioassays and Biosensing - A Review. *Anal. Chim. Acta* **2011,** *706* (1), 8-24.

(231) Noguez, C. Surface plasmons on metal nanoparticles: The influence of shape and physical environment. *J. Phys. Chem. C* **2007,** *111* (10), 3606-3619.

(232) Juluri, B. K.; Zheng, Y. B.; Ahmed, D.; Huang, T. J.; Jensen, L. Effects of geometry and composition on charge-induced plasmonic shifts in gold nanoparticles. *J. Phys. Chem. C* **2008,** *112* (19), 7309-7317.

(233) Kun, Q.; Sweeny, B. C.; Johnston-Peck, A. C.; Wenxin, N.; Graham, J. O.; DuChene, J. S.; Jingjing, Q.; Yi-Chung, W.; Engelhard, M. H.; Dong, S., et al. Surface plasmon-driven water reduction: gold nanoparticle size matters.(Report). *J. Am. Chem. Soc.* **2014,** *136* (28), 9842-9845.

(234) Vodnik, V. V.; Bozanic, D. K.; Bibic, N.; Saponjic, Z. V.; Nedeljkovic , J. M. Optical properties of shaped silver nanoparticles. *J. Nanosci. Nanotechnol.* **2008,** *8* (7), 3511-3515.

(235) Mock, J. J.; Barbic, M.; Smith, D. R.; Schultz, D. A.; Schultz, S. Shape effects in plasmon resonance of individual colloidal silver nanoparticles. *J. Chem. Phys* **2002,** *116* (15), 6755-6759.

(236) Kuwata, H.; Tamaru, H.; Esumi, K.; Miyano, K. Resonant Light Scattering from Metal Nanoparticles: Practical Analysis Beyond Rayleigh Approximation. *Appl. Phys. Lett.* **2003,** *83* (22), 4625-4627.

(237) Hirsch, L., Diagnostic and Therapeutic Applications of Metal Nanoshells. West, J., Ed. ProQuest Dissertations Publishing: 2004; p 112.

(238) Pissuwan, D.; Valenzuela, S.; Killingsworth, M.; Xu, X.; Cortie, M. Targeted destruction of murine macrophage cells with bioconjugated gold nanorods. *J. Nanopart. Res* **2007,** *9* (6), 1109-1124.

(239) Hirsch, L. R.; Stafford, R. J.; Banksont, J. A.; Sershen, S. R.; Rivera, B.; Price, R. E.; Hazle, J. D.; Halas, N. J.; West, J. L. Nanoshell-mediated Near-infrared Thermal Therapy of Tumors Under Magnetic Resonance Guidance. *Proc. Natl. Acad. Sci. U.S.A.* **2003,** *100* (23), 13549.

(240) Noguez, C., Surface Plasmons on Metal Nanoparticles: The Influence of Shape and Physical Environment. In *J. Phys. Chem. C*, 2007; Vol. 111, pp 3806-3819.

(241) Aikens, C. M.; Li, S.; Schatz, G. C. From Discrete Electronic States to Plasmons: TDDFT Optical Absorption Properties of Ag_n (n = 10, 20, 35, 56, 84, 120) Tetrahedral Clusters. *J. Phys. Chem. C* **2008,** *112* (30), 11272-11279.

(242) Lu, X.; Rycenga, M.; Skrabalak, S.; Wiley, B.; Xia, Y., Chemical Synthesis of Novel Plasmonic Nanoparticles. In *Annu. Rev. Phys. Chem.*, 2009; Vol. 60, pp 167-192.

(243) Tiggesbaumker, J.; Koller, L.; Lutz, H.; Meiwesbroer, K. Giant-resonances in Silver Cluster Photofragmentation *Chem. Phys. Lett.* **1992,** *190* (1-2), 42-47.

(244) Chong, D. P. Augmenting Basis Set for Time-Dependent Density Functional Theory Calculation of Excitation Energies: Slater-Type Orbitals for Hydrogen to Krypton. *Mol. Phys.* **2005,** *103* (6-8), 749-761.

(245) Chong, D. P.; Grüning, M.; Baerends, E. J. STO and GTO Field-induced Polarization Functions for H to Kr. *J. Comput. Chem.* **2003,** *24* (13), 1582-1591.

(246) Zeiss, G. D.; Scott, W. R.; Suzuki, N.; Chong, D. P.; Langhoff, S. R. Finite-Field Calculations of Molecular Polarizabilities Using Field-Induced Polarization Functions: Second- and Third-Order Perturbation Correlation Corrections to the Coupled Hartree-Fock Polarizability of H_2O. *Mol. Phys.* **1979,** *37* (5), 1543-1572.

(247) Clementi, E.; Roetti, C. Roothaan-Hartree-Fock Atomic Wavefunctions: Basis Functions and Their Coefficients for Ground and Certain Excited States of Neutral and Ionized Atoms, $Z \leq 54$. *At. Data Nucl. Data Tables* **1974,** *14* (3–4), 177-478.

Appendix A - Supporting information for "Chiroptical Activity in BINAP– and DIOP– stabilized Octa– and Undecagold Clusters"

Figure A-1. The most stable isomers of the $Au_{11}(L1)_4Cl_2^+$ cluster at the BP86/DZ.fc level of theory in the gas phase. Hydrogen atoms were eliminated.

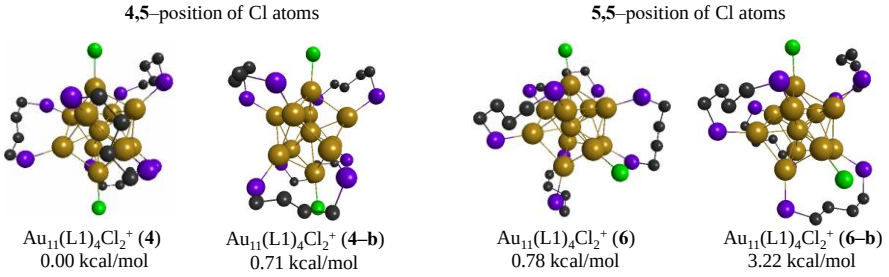

Figure A-2. The most stable isomers of the $Au_{11}(L2)_4Cl_2^+$ cluster at the BP86/DZ.fc level of theory in the gas phase. Hydrogen atoms were eliminated.

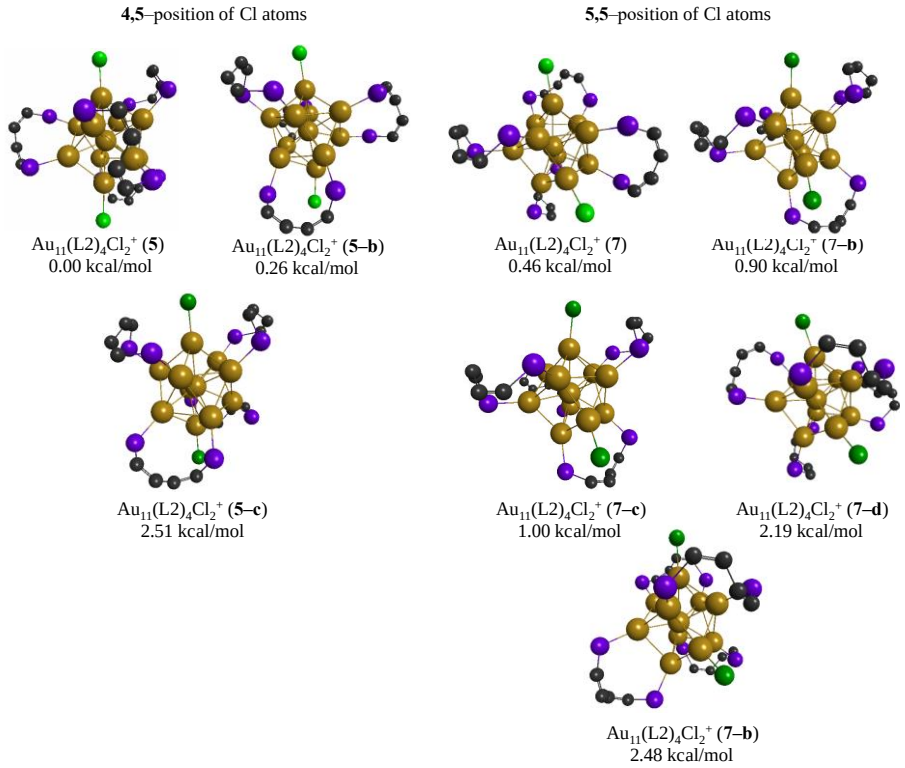

Figure A-3. Gold atom positions in the isolated Au_{11}^{3+} gold core.

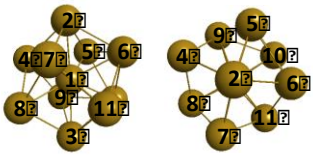

Table A-1. Geometrical parameters for experimental crystal structures $Au_{11}(DIOP)_4Cl_2^+$ and $Au_{11}(PPh_3)_8Cl_2^+$ and theoretical structures $Au_{11}X_4Cl_2^+$ where X = L1, L2.

Parameter	Experiment[34, 40]		Theory (BP86/DZ.fc)							
			Gas				COSMO			
	$Au_{11}(DIOP)_4Cl_2^+$	$Au_{11}(PPh_3)_8Cl_2^+$	Complex (4)	Complex (6)	Complex (5)	Complex (7)	Complex (4)	Complex (6)	Complex (5)	Complex (7)
Au1Au2	2.689	2.713	2.782	2.791	2.763	2.802	2.724	2.768	2.729	2.772
Au1Au3	2.689	2.689	2.773	2.688	2.765	2.682	2.767	2.696	2.740	2.693
Au1Au4	2.641	2.639	2.694	2.701	2.696	2.712	2.732	2.693	2.713	2.703
Au1Au5	2.695	2.695	2.727	2.73	2.732	2.734	2.736	2.743	2.742	2.743
Au1Au6	2.685	2.701	2.728	2.752	2.735	2.746	2.732	2.742	2.745	2.748
Au1Au7	2.657	2.728	2.676	2.694	2.682	2.695	2.680	2.700	2.691	2.705
Au1Au8	2.657	2.677	2.675	2.663	2.679	2.667	2.705	2.679	2.695	2.688
Au1Au9	2.685	2.644	2.731	2.709	2.738	2.701	2.732	2.731	2.750	2.717
Au1Au10	2.695	2.688	2.725	2.73	2.731	2.733	2.732	2.734	2.743	2.746
Au1Au11	2.642	2.700	2.699	2.789	2.702	2.776	2.697	2.772	2.709	2.754
Au2Cl	2.378	2.355	2.454	2.450	2.451	2.458	2.504	2.505	2.496	2.500
Au3Cl	2.378	–	2.454	–	2.452	–	2.505	–	2.498	–
Au11Cl	–	2.356	–	2.452	–	2.449	–	2.509	–	2.501
Au…P	~2.282	~2.28	~2.443	~2.440	~2.449	~2.447	~2.443	~2.441	~2.449	~2.445

Figure A-4. Gold atom positions in $Au_8(PH_3)_2$ fragment.

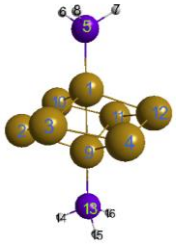

Table A-2. Geometrical parameters for experimental crystal structures $[Au_8(BINAP)_3(PPh_3)_2]^{2+}$ theoretical structures $Au_8X_3(PH_3)_2^{2+}$ where X = L1, L2.

	Experiment[40]	Theory (BP86/DZ.fc) gas phase	
	$[Au_8(BINAP)_3(PPh_3)_2]^{2+}$	(**8**)	(**9**)
Au (1)–Au(9)	2.523	2.593	2.593
Au (1)–Au(2)	3.103	3.182	3.182
Au (1)–Au(3)	2.803	2.867	2.867
Au (1)–Au(4)	3.022	3.124	3.124
Au (1)–Au(10)	2.856	2.846	2.846
Au (1)–Au(11)	3.109	3.127	3.127
Au (1)–Au(12)	2.825	2.863	2.863
Au (9)–Au(2)	2.786	2.846	2.846
Au (9)–Au(3)	3.109	3.127	3.127
Au (9)–Au(4)	2.856	2.863	2.863
Au (9)–Au(10)	3.022	3.182	3.182
Au (9)–Au(11)	2.803	2.867	2.867
Au (9)–Au(12)	3.103	3.124	3.124
Au(1)–P(5)	2.303	2.430	2.433
Au(9)–P(13)	2.303	2.430	2.433
~<Au–(P^P)>	2.305	2.498	2.487

Figure A-5. UV–vis and CD spectra of A) $[Au_{11}(L1)_4Cl_2]^+$ (4); B) $[Au_{11}(L1)_4Cl_2]^+$ (6); C) $[Au_{11}(L2)_4Cl_2]^+$ (5); D) $[Au_{11}(L2)_4Cl_2]^+$ (7); E) $[Au_8(L1)_3(PH_3)_2]^{2+}$ (8) and F) $[Au_8(L2)_3(PH_3)_2]^{2+}$ (9) structures. Method: LB94/DZ.fc (gas phase).

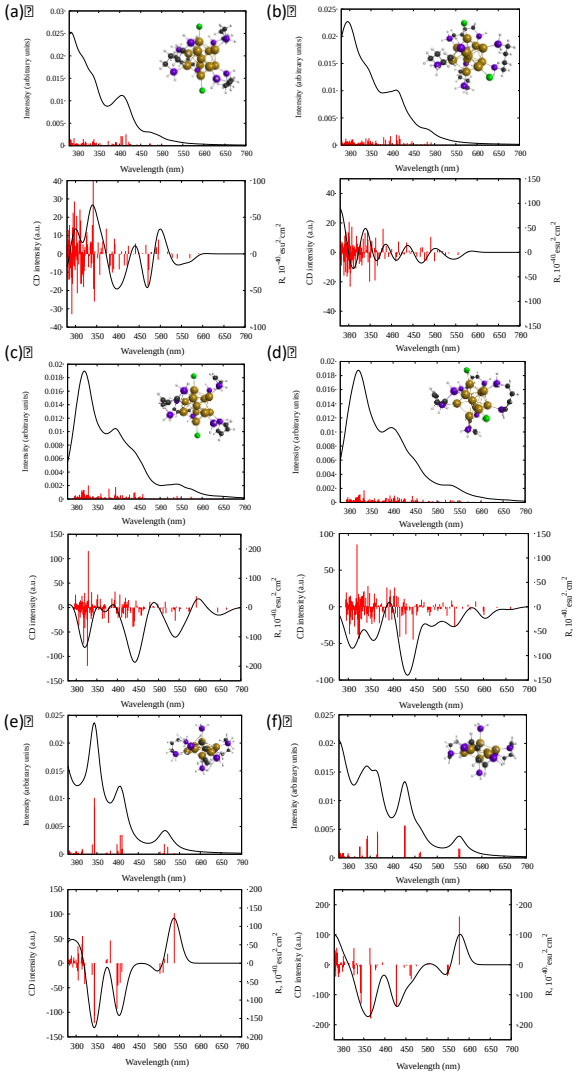

Table A-3. Optical absorption and CD data for $[Au_{11}(L1)_4Cl_2]^+$ (4): peak positions, excited state wavelength, oscillator strengths (*f*), rotatory strengths (*R*, 10^{-40} esu^{2}cm^2), and orbitals involved in electronic transitions. Method LB94/DZ.fc (in chloroform).

ABS		CD		Excited state			f	R	Electron transitions		Weight	Transition dipole moment			Orbitals involved	
#	Peak, nm	#	Peak, nm	no.	E/eV	E/nm			From	To		x	y	z	from	to
–	–	1	533	1	2.301	539	0.0005	-1.07	187a	188a	0.9653	0.5731	0.3044	0.2101	HOMO	LUMO
				2	2.409	515	0.0006	-0.66	187a	189a	0.3932	0.0657	-1.947	0.5001	HOMO	LUMO+1
									186a	188a	0.3611	0.7227	1.0109	-1.5059	HOMO–1	LUMO
									185a	188a	0.1633	-1.273	0.4826	0.0162	HOMO–2	LUMO
				3	2.481	500	0.0056	0.39	186a	189a	0.5707	0.2371	0.6848	0.854	HOMO–1	LUMO+1

									185a	189a	0.1813	0.0564	-0.2694	-1.1543	HOMO–2	LUMO+1
									186a	188a	0.0941	-0.3635	-0.5084	0.7574	HOMO–1	LUMO
									185a	188a	0.0884	-0.9228	0.3499	0.0117	HOMO–2	LUMO
I	459	2	481	4	2.512	494	0.0257	1.70	186a	190a	0.3188	-0.7829	1.1654	0.3271	HOMO–1	LUMO+2
									187a	189a	0.2365	0.0499	-1.4786	0.3798	HOMO	LUMO+1
									185a	188a	0.213	1.4238	-0.5398	-0.0181	HOMO–2	LUMO
									185a	189a	0.1298	0.0475	-0.2265	-0.9707	HOMO–2	LUMO+1
				5	2.541	488	0.0128	-6.21	185a	190a	0.2663	-0.2109	-0.5677	0.3158	HOMO–2	LUMO+2
									186a	189a	0.2435	0.153	0.4421	0.5513	HOMO–1	LUMO+1
									187a	190a	0.1472	-0.6416	-0.4559	-1.0521	HOMO	LUMO+2
									186a	188a	0.1342	0.4291	0.6002	-0.894	HOMO–1	LUMO
									185a	188a	0.1025	0.9822	-0.3724	-0.0125	HOMO–2	LUMO
				7	2.628	472	0.0732	-42.48	187a	191a	0.2385	0.2319	-0.1938	-0.03	HOMO	LUMO+3
									185a	188a	0.1922	1.3224	-0.5014	-0.0168	HOMO–2	LUMO
									186a	191a	0.1785	-1.2756	0.2765	-0.2712	HOMO–1	LUMO+3
									187a	190a	0.1659	0.6698	0.4759	1.0984	HOMO	LUMO+2
				9	2.650	468	0.0726	35.30	185a	190a	0.4586	-0.2711	-0.7295	0.4057	HOMO–2	LUMO+2
									186a	188a	0.1747	-0.4793	-0.6704	0.9987	HOMO–1	LUMO
									185a	191a	0.1274	0.3079	0.6769	-0.7293	HOMO–2	LUMO+3
		3	453	10	2.703	459	0.1498	26.89	185a	189a	0.2579	-0.0645	0.3079	1.3192	HOMO–2	LUMO+1
									186a	190a	0.1702	-0.5515	0.821	0.2305	HOMO–1	LUMO+2
									187a	190a	0.154	0.6363	0.4521	1.0435	HOMO	LUMO+2
									187a	192a	0.0965	0.8352	-0.0967	-0.4695	HOMO	LUMO+4
II	412	4	423	13	2.943	421	0.6122	-47.74	185a	191a	0.4381	0.5419	1.1913	-1.2834	HOMO–2	LUMO+3
									186a	191a	0.2153	-1.324	0.2869	-0.2814	HOMO–1	LUMO+3
				14	3.006	412	0.6170	-5.33	187a	192a	0.27	1.3245	-0.1534	-0.7446	HOMO	LUMO+4
									186a	192a	0.2207	-0.2078	-0.8424	-0.4863	HOMO–1	LUMO+4
									186a	191a	0.0959	0.8745	-0.1895	0.1859	HOMO–1	LUMO+3
		5	385	15	3.064	405	0.6598	23.95	185a	192a	0.3222	0.6879	0.9196	0.4351	HOMO–2	LUMO+4
									186a	191a	0.1329	1.0195	-0.2209	0.2167	HOMO–1	LUMO+3
									187a	192a	0.122	0.8819	-0.1021	-0.4957	HOMO	LUMO+4
III	351s	6	349	25	3.536	351	0.1609	7.94	181a	189a	0.2849	0.3746	-0.486	0.4641	HOMO–6	LUMO+1
									181a	188a	0.2152	-0.7274	0.0008	0.4457	HOMO–6	LUMO
				26	3.557	349	0.0674	0.81	187a	193a	0.5044	-0.0338	0.4077	-0.1122	HOMO	LUMO+5
									181a	189a	0.1405	0.2623	-0.3403	0.325	HOMO–6	LUMO+1
									181a	188a	0.1082	0.5142	-0.0005	-0.3151	HOMO–6	LUMO
				28	3.576	347	0.0708	5.46	181a	189a	0.3867	-0.4339	0.563	-0.5377	HOMO–6	LUMO+1

Table A-4. Optical absorption and CD data for $[Au_{11}(L1)_4Cl_2]^+$ (6): peak positions, excited state wavelength, oscillator strengths (*f*), rotatory strengths (*R*, 10^{-40} esu^{2}cm^2), and orbitals involved in electronic transitions. Method LB94/DZ.fc (in chloroform).

ABS		CD		Excited state			f	R	Electron transitions		Weight	Transition dipole moment			Orbitals involved	
#	Peak, nm	#	Peak, nm	no.	E/eV	E/nm			From	To		x	y	z	from	to
I	480s	1	493	4	2.52	492	0.027	-29.92	187a	189a	0.3079	-0.335	0.293	-1.713	HOMO	LUMO+1
									187a	190a	0.284	0.642	1.538	0.334	HOMO	LUMO+2
									185a	188a	0.1504	-1.163	-0.495	0.556	HOMO–2	LUMO
				6	2.58	480	0.048	-4.00	187a	191a	0.2343	0.612	-0.065	-0.245	HOMO	LUMO+3
									187a	189a	0.2029	0.269	-0.235	1.374	HOMO	LUMO+1
									187a	190a	0.1884	0.517	1.238	0.269	HOMO	LUMO+2
									186a	191a	0.1263	-0.896	-0.632	-0.203	HOMO–1	LUMO+3
				7	2.63	471	0.029	-28.41	185a	190a	0.2383	-0.130	0.685	0.449	HOMO–2	LUMO+2
									185a	188a	0.2146	1.361	0.579	-0.651	HOMO–2	LUMO
									186a	191a	0.1566	-0.988	-0.697	-0.224	HOMO–1	LUMO+3
									186a	190a	0.0997	0.828	-0.379	0.061	HOMO–1	LUMO+2
									187a	192a	0.0776	-0.652	0.230	0.233	HOMO	LUMO+4
		2	460	9	2.66	465	0.039	38.17	186a	190a	0.2405	-1.278	0.585	-0.094	HOMO–1	LUMO+2
									187a	191a	0.1867	0.538	-0.057	-0.215	HOMO	LUMO+3
									185a	190a	0.1404	0.099	-0.523	-0.343	HOMO–2	LUMO+2
									185a	188a	0.1192	1.008	0.429	-0.482	HOMO–2	LUMO
									186a	188a	0.1136	-0.228	0.503	-0.592	HOMO–1	LUMO
				10	2.70	460	0.012	29.51	187a	192a	0.4882	-1.617	0.570	0.578	HOMO	LUMO+4
									185a	190a	0.19	0.115	-0.605	-0.396	HOMO–2	LUMO+2
									186a	191a	0.1402	0.924	0.651	0.209	HOMO–1	LUMO+3
									185a	189a	0.0593	0.078	-0.601	-0.186	HOMO–2	LUMO+1
									186a	190a	0.0376	0.502	-0.230	0.037	HOMO–1	LUMO+2
				11	2.73	454	0.036	29.75	186a	192a	0.517	-0.189	0.142	1.620	HOMO–1	LUMO+4
									185a	191a	0.2284	-0.282	0.332	-1.055	HOMO–2	LUMO+3
									187a	192a	0.0831	0.663	-0.234	-0.237	HOMO	LUMO+4
									185a	192a	0.0309	-0.252	0.202	-0.219	HOMO–2	LUMO+4
II	418	3	430	12	2.78	446	0.070	-4.28	185a	192a	0.4517	0.955	-0.768	0.829	HOMO–2	LUMO+4
									185a	191a	0.327	-0.335	0.394	-1.251	HOMO–2	LUMO+3
				13	2.91	426	0.669	-160.91	186a	191a	0.2888	1.276	0.900	0.289	HOMO–1	LUMO+3
									187a	190a	0.1868	0.485	1.161	0.252	HOMO	LUMO+2
									185a	189a	0.1436	-0.117	0.900	0.278	HOMO–2	LUMO+1
				14	2.96	420	0.685	33.05	187a	192a	0.2078	-1.008	0.355	0.360	HOMO	LUMO+4
		4	400						185a	188a	0.1816	-1.181	-0.503	0.565	HOMO–2	LUMO
				15	3.01	412	0.684	76.13	185a	192a	0.3992	0.863	-0.694	0.750	HOMO–2	LUMO+4
									185a	191a	0.2019	0.253	-0.297	0.945	HOMO–2	LUMO+3

									186a	190a	0.0687	0.643	-0.294	0.047	HOMO–1	LUMO+2
III	348s	5	345	21	3.45	359	0.024	26.57	183a	189a	0.4815	0.207	0.353	0.216	HOMO–4	LUMO+1
									183a	188a	0.2878	0.585	0.106	-0.054	HOMO–4	LUMO
				27	3.55	349	0.024	-19.24	182a	190a	0.5123	0.092	0.202	0.292	HOMO–5	LUMO+2
									183a	190a	0.1496	-0.013	0.280	0.065	HOMO–4	LUMO+2
									181a	190a	0.1262	0.032	0.055	-0.075	HOMO–6	LUMO+2
									180a	188a	0.0589	-0.402	-0.181	0.176	HOMO–7	LUMO
				28	3.56	348	0.151	10.28	180a	188a	0.4297	-1.084	-0.487	0.476	HOMO–7	LUMO
				31	3.62	343	0.029	11.53	187a	193a	0.5987	0.112	0.029	-0.236	HOMO	LUMO+5
									186a	193a	0.207	0.292	0.212	0.105	HOMO–1	LUMO+5
				33	3.63	341	0.028	3.12	186a	193a	0.3973	-0.404	-0.294	-0.145	HOMO–1	LUMO+5
									180a	190a	0.1597	0.325	-0.580	0.264	HOMO–7	LUMO+2
				35	3.65	340	0.075	7.53	180a	190a	0.5406	-0.597	1.064	-0.485	HOMO–7	LUMO+2
		6	316	42	3.72	333	0.070	-31.19	187a	194a	0.4787	-0.690	0.750	0.543	HOMO	LUMO+6
				44	3.75	331	0.100	-42.60	186a	194a	0.3245	-0.622	0.315	-0.158	HOMO–1	LUMO+6
				50	3.82	325	0.070	-25.40	178a	188a	0.6079	0.399	0.047	-0.213	HOMO–9	LUMO
									186a	195a	0.1529	0.318	0.275	0.143	HOMO–1	LUMO+7
				66	4.02	309	0.069	-7.88	186a	197a	0.5099	0.942	0.343	0.689	HOMO–1	LUMO+9
				53	3.86	321	0.088	77.11	178a	189a	0.3334	0.143	-0.784	-0.117	HOMO–9	LUMO+1
				61	3.96	313	0.113	-2.03	176a	189a	0.2017	0.338	-0.060	-0.021	HOMO–11	LUMO+1
									187a	196a	0.1258	0.170	-0.183	0.003	HOMO	LUMO+8

Table A-5. Optical absorption and CD data for $[Au_{11}(L2)_4Cl_2]^+$ (5): peak positions, excited state wavelength, oscillator strengths (f), rotatory strengths (R, 10^{-40} esu^{2}cm^2), and orbitals involved in electronic transitions. Method: LB94/DZ.fc (solvent = chloroform).

				Excited state			f	R				Transition dipole moment				
ABS		CD							Electron transitions		Weight				Orbitals involved	
#	Peak, nm	#	Peak, nm	no.	E/eV	E/nm			From	To		x	y	z	from	to
I	552s	1	568	1	2.186	567	0.013	-20.63	178a	180a	0.5159	0.4155	-0.4116	-1.1643	HOMO-1	LUMO
		2	533						179a	180a	0.4601	-0.8227	-0.733	1.2035	HOMO	LUMO
				2	2.245	552	0.032	6.59	179a	180a	0.4266	0.7818	0.6965	-1.1437	HOMO	LUMO
									178a	180a	0.4132	0.3669	-0.3636	-1.0283	HOMO-1	LUMO
				3	2.318	535	0.013	-16.86	179a	181a	0.6331	-0.8906	2.2768	-0.2345	HOMO	LUMO+1
									179a	182a	0.2558	-0.2228	-0.9775	-0.0752	HOMO	LUMO+2
II	497s	3	495	4	2.339	530	0.009	-4.59	178a	181a	0.415	1.5902	0.3693	1.356	HOMO-1	LUMO+1
									178a	182a	0.2765	-0.1607	-1.3458	-0.6466	HOMO-1	LUMO+2
									179a	182a	0.1246	0.1548	0.6791	0.0522	HOMO	LUMO+2
									177a	180a	0.1046	-0.7499	0.3606	-0.6776	HOMO-2	LUMO

				5	2.396	518	0.058	124.78	179a	182a	0.3532	0.2574	1.1297	0.0869	HOMO	LUMO+2
									178a	181a	0.3033	-1.3433	-0.312	-1.1454	HOMO-1	LUMO+1
									179a	181a	0.1217	-0.3841	0.9819	-0.1011	HOMO	LUMO+1
				7	2.468	502	0.081	-124.55	177a	181a	0.3106	0.1551	0.9654	0.3121	HOMO-2	LUMO+1
									178a	182a	0.2932	-0.1611	-1.3492	-0.6482	HOMO-1	LUMO+2
				8	2.486	499	0.065	-168.33	178a	183a	0.7842	1.5418	0.7959	-1.2145	HOMO-1	LUMO+3
				9	2.494	497	0.139	-121.40	177a	180a	0.6235	1.7733	-0.8526	1.6024	HOMO-2	LUMO
				10	2.549	486	0.030	-53.09	177a	181a	0.4048	-0.1742	-1.0846	-0.3506	HOMO-2	LUMO+1
									178a	184a	0.2712	-0.1923	0.8188	-0.1469	HOMO-1	LUMO+4
									179a	184a	0.213	0.5442	0.0637	0.6283	HOMO	LUMO+4
				11	2.566	483	0.128	-106.24	177a	183a	0.2681	0.237	1.1663	0.3719	HOMO-2	LUMO+3
									179a	184a	0.2079	-0.5358	-0.0627	-0.6186	HOMO	LUMO+4
III	452	4	440	12	2.583	480	0.017	34.76	178a	184a	0.3822	0.2268	-0.9657	0.1732	HOMO-1	LUMO+4
									177a	182a	0.2906	0.4858	0.358	-1.4033	HOMO-2	LUMO+2
				13	2.669	465	0.076	-27.95	179a	185a	0.7844	1.4191	-0.5082	-0.5923	HOMO	LUMO+5
				14	2.695	460	0.213	36.16	177a	182a	0.377	-0.5418	-0.3993	1.5649	HOMO-2	LUMO+2
				15	2.704	459	0.093	80.38	178a	185a	0.6273	-0.7704	-0.3341	0.0538	HOMO-1	LUMO+5
				16	2.718	456	0.184	71.64	177a	183a	0.3562	0.2654	1.3064	0.4166	HOMO-2	LUMO+3
				17	2.747	451	0.235	-133.59	177a	183a	0.1435	-0.1676	-0.8248	-0.263	HOMO-2	LUMO+3
				18	2.786	445	0.067	24.19	177a	184a	0.2182	-0.9692	-0.0226	0.5943	HOMO-2	LUMO+4
				19	2.799	443	0.225	-166.90	177a	184a	0.4363	1.3672	0.0319	-0.8384	HOMO-2	LUMO+4
IV	420	5	405	22	2.951	420	0.251	-40.99	179a	187a	0.2689	-1.2228	0.1701	-0.0136	HOMO	LUMO+7
									178a	187a	0.2322	-0.7453	0.1719	-0.0068	HOMO-1	LUMO+7
				24	3.061	405	0.098	-8.93	179a	188a	0.7017	-0.4014	0.8452	0.3779	HOMO	LUMO+8
				28	3.107	399	0.182	13.50	178a	188a	0.4003	-0.8855	-0.4052	0.0144	HOMO-1	LUMO+8
V	378s	6	373	30	3.182	390	0.041	-38.95	178a	189a	0.6961	-0.1459	-0.6816	0.5387	HOMO-1	LUMO+9
				40	3.282	378	0.164	165.92	172a	180a	0.5029	0.4653	0.2384	-0.8624	HOMO-7	LUMO
				45	3.326	373	0.015	37.39	179a	192a	0.6214	-0.1173	-0.1772	-0.1999	HOMO	LUMO+12
				50	3.371	368	0.056	-17.29	178a	192a	0.2484	0.0089	0.3399	-0.4129	HOMO-1	LUMO+12
									173a	182a	0.2251	-0.4112	0.1304	-0.0881	HOMO-6	LUMO+2
				51	3.376	367	0.125	-76.41	173a	182a	0.3369	0.5027	-0.1594	0.1077	HOMO-6	LUMO+2
				52	3.386	366	0.075	2.60	178a	192a	0.4036	0.0113	0.4324	-0.5251	HOMO-1	LUMO+12
				56	3.434	361	0.110	-43.62	177a	190a	0.3662	0.104	-0.0464	-0.4279	HOMO-2	LUMO+10
									172a	182a	0.3489	-0.8065	0.3006	-0.62	HOMO-7	LUMO+2
				59	3.450	359	0.089	106.08	177a	190a	0.4159	-0.1106	0.0493	0.455	HOMO-2	LUMO+10
									172a	182a	0.2289	-0.6517	0.2429	-0.5011	HOMO-7	LUMO+2
				60	3.472	357	0.036	30.59	172a	183a	0.8449	0.0095	0.6093	0.1498	HOMO-7	LUMO+3
				61	3.477	357	0.028	43.29	171a	181a	0.9144	-0.1753	0.1734	-0.589	HOMO-8	LUMO+1

				62	3.485	356	0.007	-42.34	170a	180a	0.9256	0.0221	0.0662	-0.1597	HOMO-9	LUMO

Table A-6. Optical absorption and CD data for $[Au_{11}(L2)_4Cl_2]^+$ (7): peak positions, excited state wavelength, oscillator strengths (*f*), rotatory strengths (*R*, 10^{-40} esu^{2}cm^2), and orbitals involved in electronic transitions. Method LB94/DZ.fc (in chloroform).

				Excited state			f	R	Electron transitions		Weight	Transition dipole moment			Orbitals involved	
ABS		CD														
#	nm	#	nm	no.	E/eV	E/nm			From	To		x	y	z	from	to
I	558s	1	540	1	2.22	558	0.026	1.80	179a	180a	0.738	-2.244	-0.168	-0.852	HOMO	LUMO
									179a	181a	0.1387	0.474	-0.561	-0.200	HOMO	LUMO+1
				3	2.29	540	0.019	-15.20	179a	181a	0.6626	1.021	-1.206	-0.431	HOMO	LUMO+1
									179a	180a	0.0916	0.778	0.058	0.296	HOMO	LUMO
				4	2.35	527	0.021	-0.27	179a	182a	0.5617	0.630	0.614	1.331	HOMO	LUMO+2
									178a	182a	0.1535	0.170	-0.462	-0.908	HOMO–1	LUMO+2
									177a	181a	0.0937	-0.200	-0.395	-0.262	HOMO–2	LUMO+1
									179a	180a	0.0757	0.698	0.052	0.265	HOMO	LUMO
									177a	180a	0.0263	-0.066	-0.092	0.573	HOMO–2	LUMO
II	499s	2	490	8	2.48	499	0.132	-84.57	177a	180a	0.2601	0.200	0.280	-1.753	HOMO–2	LUMO
									179a	184a	0.2358	0.275	-0.308	0.560	HOMO	LUMO+4
									178a	181a	0.1705	0.265	1.469	-0.548	HOMO–1	LUMO+1
				9	2.52	491	0.057	-13.74	179a	184a	0.4798	0.389	-0.435	0.792	HOMO	LUMO+4
									178a	181a	0.1254	-0.225	-1.250	0.466	HOMO–1	LUMO+1
									177a	182a	0.0988	-0.747	0.516	-0.211	HOMO–2	LUMO+2
				10	2.54	488	0.101	-65.23	178a	184a	0.2412	-0.024	-0.613	-0.718	HOMO–1	LUMO+4
									178a	182a	0.2013	-0.187	0.509	1.001	HOMO–1	LUMO+2
									177a	181a	0.1326	0.229	0.452	0.300	HOMO–2	LUMO+1
									177a	180a	0.0997	-0.123	-0.172	1.073	HOMO–2	LUMO
				11	2.56	485	0.050	-53.59	178a	183a	0.5632	2.138	-0.056	0.211	HOMO–1	LUMO+3
									177a	182a	0.2985	-1.291	0.891	-0.365	HOMO–2	LUMO+2
				12	2.60	477	0.043	-48.50	178a	184a	0.4578	0.032	0.836	0.979	HOMO–1	LUMO+4
									177a	183a	0.3678	0.171	-0.984	-0.312	HOMO–2	LUMO+3
III	457	3	450	13	2.63	472	0.081	41.85	179a	185a	0.367	-1.143	-0.285	0.917	HOMO	LUMO+5
									177a	184a	0.217	0.963	0.556	0.146	HOMO–2	LUMO+4
									177a	183a	0.1456	0.107	-0.615	-0.195	HOMO–2	LUMO+3
									177a	182a	0.0957	-0.721	0.498	-0.204	HOMO–2	LUMO+2
									178a	183a	0.0688	-0.737	0.019	-0.073	HOMO–1	LUMO+3
				14	2.67	464	0.143	44.87	177a	183a	0.2147	-0.129	0.741	0.235	HOMO–2	LUMO+3
									179a	185a	0.1244	-0.660	-0.164	0.530	HOMO	LUMO+5

				15	2.69	460	0.410	-147.54	177a	182a	0.2482	-1.147	0.792	-0.324	HOMO–2	LUMO+2
									179a	185a	0.1426	0.704	0.175	-0.565	HOMO	LUMO+5
									178a	183a	0.0916	-0.840	0.022	-0.083	HOMO–1	LUMO+3
									179a	184a	0.0841	-0.158	0.176	-0.321	HOMO	LUMO+4
									178a	181a	0.0703	0.163	0.906	-0.338	HOMO–1	LUMO+1
				16	2.73	455	0.053	29.64	178a	185a	0.5871	-0.311	0.019	0.152	HOMO–1	LUMO+5
									179a	186a	0.1537	0.358	-0.144	-0.457	HOMO	LUMO+6
									178a	184a	0.0522	0.011	0.276	0.323	HOMO–1	LUMO+4
									178a	183a	0.0324	-0.497	0.013	-0.049	HOMO–1	LUMO+3
									179a	185a	0.0282	-0.311	-0.077	0.250	HOMO	LUMO+5
				17	2.75	452	0.278	-69.75	177a	184a	0.5297	1.472	0.850	0.223	HOMO–2	LUMO+4
				18	2.79	444	0.103	-96.33	179a	186a	0.5521	0.670	-0.270	-0.856	HOMO	LUMO+6
									177a	185a	0.1408	-0.246	-0.099	0.251	HOMO–2	LUMO+5
									179a	185a	0.0712	0.488	0.122	-0.392	HOMO	LUMO+5
				19	2.82	439	0.066	-46.84	177a	185a	0.603	0.506	0.204	-0.517	HOMO–2	LUMO+5
									179a	187a	0.1044	-0.196	-0.319	-0.055	HOMO	LUMO+7
				20	2.87	432	0.176	-6.97	179a	187a	0.6168	0.472	0.767	0.133	HOMO	LUMO+7
IV	413s	4	408	21	2.88	430	0.064	-19.01	178a	186a	0.774	-0.170	-0.295	0.419	HOMO–1	LUMO+6
				22	2.94	422	0.116	28.76	178a	187a	0.64	0.827	0.133	-0.576	HOMO–1	LUMO+7
				24	3.01	413	0.125	6.10	179a	188a	0.4313	-1.117	0.391	0.279	HOMO	LUMO+8
				26	3.06	405	0.061	-16.54	179a	189a	0.5151	0.109	0.587	0.062	HOMO	LUMO+9
									178a	188a	0.2613	-0.404	0.106	-0.146	HOMO–1	LUMO+8
									179a	188a	0.0404	-0.339	0.118	0.085	HOMO	LUMO+8
				27	3.08	403	0.118	28.69	178a	188a	0.3895	-0.492	0.129	-0.178	HOMO–1	LUMO+8
									179a	189a	0.3788	-0.093	-0.502	-0.053	HOMO	LUMO+9
									179a	188a	0.032	-0.301	0.105	0.075	HOMO	LUMO+8
				29	3.13	396	0.072	-5.50	177a	188a	0.7184	0.021	-0.441	-0.797	HOMO–2	LUMO+8
									178a	189a	0.1116	-0.193	0.188	-0.162	HOMO–1	LUMO+9
									175a	180a	0.0239	-0.036	-0.012	-0.037	HOMO–4	LUMO
V	369s	5	369	40	3.26	380	0.054	13.43	177a	189a	0.5833	0.095	-0.879	-0.101	HOMO–2	LUMO+9
				42	3.29	377	0.057	-30.96	175a	182a	0.532	-0.451	0.031	-0.104	HOMO–4	LUMO+2
									172a	180a	0.164	-0.535	0.263	-0.168	HOMO–7	LUMO
				44	3.31	374	0.063	22.17	174a	182a	0.7734	-0.192	-0.587	0.382	HOMO–5	LUMO+2
									172a	180a	0.0429	0.273	-0.134	0.086	HOMO–7	LUMO
				49	3.36	369	0.082	39.46	179a	192a	0.5011	0.568	0.381	-0.246	HOMO	LUMO+12
				56	3.42	362	0.052	-63.64	171a	180a	0.495	0.311	0.052	-0.225	HOMO–8	LUMO
									177a	190a	0.1335	0.048	-0.095	0.291	HOMO–2	LUMO+10

									172a	182a	0.1223	0.272	0.029	-0.590	HOMO–7	LUMO+2
				57	3.43	361	0.055	9.13	177a	190a	0.3231	0.075	-0.148	0.453	HOMO–2	LUMO+10
									178a	192a	0.2266	-0.040	0.213	-0.240	HOMO–1	LUMO+12
									172a	182a	0.1207	-0.269	-0.029	0.585	HOMO–7	LUMO+2
				59	3.45	360	0.059	-4.65	175a	184a	0.4575	-0.230	0.181	0.231	HOMO–4	LUMO+4
									178a	192a	0.1695	0.034	-0.184	0.207	HOMO–1	LUMO+12
									177a	190a	0.1176	0.045	-0.089	0.272	HOMO–2	LUMO+10
									172a	182a	0.0621	-0.193	-0.021	0.418	HOMO–7	LUMO+2
				64	3.50	355	0.074	87.85	171a	181a	0.3819	0.506	0.306	-0.329	HOMO–8	LUMO+1
									172a	183a	0.1505	0.049	0.127	0.050	HOMO–7	LUMO+3
									170a	180a	0.1423	0.127	-0.308	0.324	HOMO–9	LUMO
				67	3.54	351	0.088	49.23	170a	180a	0.3136	-0.188	0.454	-0.478	HOMO–9	LUMO
									177a	192a	0.0942	0.023	0.161	0.005	HOMO–2	LUMO+12
									172a	184a	0.0527	-0.152	0.052	0.028	HOMO–7	LUMO+4
Vi	330s	6	333													
				69	3.56	348	0.094	-172.14	169a	180a	0.575	0.206	0.004	-0.461	HOMO–10	LUMO
									170a	180a	0.0955	-0.103	0.250	-0.263	HOMO–9	LUMO
				75	3.63	342	0.051	51.12	169a	181a	0.6681	-0.733	-0.570	0.264	HOMO–10	LUMO+1
				76	3.64	341	0.009	-7.78	168a	180a	0.7958	-0.205	0.057	-0.143	HOMO–11	LUMO
									169a	181a	0.0543	0.209	0.162	-0.075	HOMO–10	LUMO+1
				80	3.68	337	0.037	6.47	172a	185a	0.5891	0.162	-0.313	0.328	HOMO–7	LUMO+5
									170a	182a	0.1637	0.089	-0.344	0.127	HOMO–9	LUMO+2
				81	3.69	336	0.047	54.55	169a	182a	0.7974	-0.672	0.339	-0.469	HOMO–10	LUMO+2
				83	3.72	334	0.049	-17.41	171a	184a	0.4048	0.168	0.470	0.322	HOMO–8	LUMO+4
									167a	180a	0.21	0.133	0.271	0.447	HOMO–12	LUMO
				85	3.73	333	0.064	-66.01	168a	181a	0.3774	0.415	-0.471	0.197	HOMO–11	LUMO+1
									176a	187a	0.1951	0.170	-0.085	0.012	HOMO–3	LUMO+7
									167a	180a	0.1755	0.121	0.247	0.408	HOMO–12	LUMO
				89	3.76	330	0.166	55.86	179a	193a	0.6479	-1.089	0.019	0.685	HOMO	LUMO+13
				93	3.79	327	0.047	-5.28	168a	182a	0.5068	0.101	-0.054	-0.671	HOMO–11	LUMO+2
									174a	187a	0.2187	0.196	-0.039	-0.058	HOMO–5	LUMO+7
				97	3.83	324	0.050	-4.39	170a	184a	0.4232	-0.452	-0.453	-0.099	HOMO–9	LUMO+4
									169a	183a	0.3176	-0.396	0.445	0.082	HOMO–10	LUMO+3
									178a	193a	0.0743	-0.031	0.329	0.050	HOMO–1	LUMO+13
				101	3.86	322	0.094	-4.04	171a	185a	0.2443	0.177	0.276	0.289	HOMO–8	LUMO+5
									169a	184a	0.2338	-0.250	-0.210	0.008	HOMO–10	LUMO+4
									172a	186a	0.1232	0.096	0.123	0.293	HOMO–7	LUMO+6
				102	3.86	321	0.061	125.60	168a	183a	0.2997	-0.104	0.333	-0.073	HOMO–11	LUMO+3
									167a	182a	0.2249	0.017	0.278	0.284	HOMO–12	LUMO+2

									178a	193a	0.1048	-0.036	0.390	0.059	HOMO–1	LUMO+13
				103	3.87	320	0.060	-49.91	169a	184a	0.4856	0.359	0.302	-0.012	HOMO–10	LUMO+4
									170a	184a	0.1377	0.257	0.257	0.056	HOMO–9	LUMO+4
									168a	183a	0.1193	0.065	-0.210	0.046	HOMO–11	LUMO+3
				105	3.89	319	0.079	11.42	172a	187a	0.5797	0.712	-0.374	0.115	HOMO–7	LUMO+7
				112	3.95	314	0.084	-36.56	170a	185a	0.3151	-0.127	-0.382	-0.254	HOMO–9	LUMO+5
									167a	183a	0.1489	-0.191	0.037	-0.133	HOMO–12	LUMO+3
									168a	184a	0.1073	-0.104	0.162	-0.245	HOMO–11	LUMO+4
									177a	193a	0.0858	-0.128	0.035	-0.165	HOMO–2	LUMO+13
				113	3.96	314	0.110	-50.47	179a	195a	0.4252	0.754	-0.112	-0.356	HOMO	LUMO+15
				114	3.96	313	0.081	20.98	168a	184a	0.4451	-0.211	0.330	-0.499	HOMO–11	LUMO+4
									179a	195a	0.1343	0.424	-0.063	-0.200	HOMO	LUMO+15

Table A-7. Optical absorption and CD data for $[Au_8(L1)_3(PH_3)]^{2+}$ (8): peak positions, excited state wavelength, oscillator strengths (*f*), rotatory strengths (*R*, 10^{-40} esu^2cm^2), and orbitals involved in electronic transitions. Method LB94/DZ.fc (in chloroform).

ABS		CD		Excited state			f	R	Electron transitions		Weight	Transition dipole moment			Orbitals involved	
#	Peak nm	#	Peak nm	no.	E/eV	E/nm			From	To		x	y	z	from	to
I	530	1	548	2B	2.26	548	0.030	157.52	71a	70b	0.621	-2.034	-1.763	0.000	HOMO–1	LUMO+1
									69b	72a	0.240	-1.544	-0.528	0.000	HOMO	LUMO
									69b	73a	0.107	1.120	0.673	0.000	HOMO	LUMO+3
				3B	2.32	534	0.272	15.91	71a	71b	0.980	0.360	0.177	0.000	HOMO–1	LUMO+2
									71a	70b	0.008	0.217	0.188	0.000	HOMO–1	LUMO+1
									69b	73a	0.005	-0.231	-0.139	0.000	HOMO	LUMO+3
				4A	2.34	529	0.330	-13.05	71a	73a	0.815	0.000	0.000	-3.114	HOMO–1	LUMO+3
									68b	70b	0.066	0.000	0.000	0.733	HOMO–2	LUMO+1
									71a	72a	0.043	0.000	0.000	-0.639	HOMO–1	LUMO
									69b	70b	0.040	0.000	0.000	-0.601	HOMO	LUMO+1
		2	495	5A	2.49	498	0.002	-8.88	69b	72b	0.749	0.000	0.000	-0.376	HOMO	LUMO+4
				6B	2.51	494	0.012	-21.06	71a	72b	0.502	0.262	-0.993	0.000	HOMO–1	LUMO+4
									69b	74a	0.465	0.976	-0.555	0.000	HOMO	LUMO+5
II	425	3	420	7B	2.91	426	0.633	-104.34	69b	75a	0.950	1.015	0.691	0.000	HOMO	LUMO+6
				8A	2.92	424	0.634	-110.88	68b	70b	0.851	0.000	0.000	-2.406	HOMO–2	LUMO+1
				9A	3.04	408	0.020	-16.61	68b	71b	0.974	0.000	0.000	0.177	HOMO–2	LUMO+2
				10A	3.09	401	0.014	-41.84	70a	72a	0.900	0.000	0.000	-0.494	HOMO–3	LUMO
				11B	3.10	400	0.083	-106.80	66b	72a	0.886	-0.362	-0.087	0.000	HOMO–6	LUMO
				12B	3.21	386	0.092	84.66	67b	72a	0.399	-0.048	0.219	0.000	HOMO–5	LUMO

									71a	73b	0.206	0.228	0.146	0.000	HOMO–1	LUMO+7
III	353	4	352	13B	3.30	376	0.041	14.75	69b	76a	0.832	0.022	0.174	0.000	HOMO	LUMO+8
				14A	3.32	374	0.040	10.80	71a	76a	0.345	0.000	0.000	-0.327	HOMO–1	LUMO+8
				15B	3.51	353	0.873	-110.00	69b	77a	0.975	0.719	0.354	0.000	HOMO	LUMO+10
				16A	3.51	353	0.889	-133.54	69b	73b	0.516	0.000	0.000	-0.244	HOMO	LUMO+7
				17A	3.73	332	0.008	-1.55	71a	77a	0.698	0.000	0.000	0.464	HOMO–1	LUMO+10
				18A	3.82	325	0.022	5.89	69b	75b	0.746	0.000	0.000	-0.266	HOMO	LUMO+11
				19B	3.82	324	0.022	4.30	71a	75b	0.840	-0.243	-0.104	0.000	HOMO–1	LUMO+11

Table A-8. Optical absorption and CD data for $[Au_8(L2)_3(PH_3)]^{2+}$ (9): peak positions, excited state wavelength, oscillator strengths (*f*), rotatory strengths (*R*, 10^{-40} esu^2cm^2), and orbitals involved in electronic transitions. Method LB94/DZ.fc (in chloroform).

ABS		CD		Excited state			f	R	Electron transitions		Weight	Transition dipole moment			Orbitals involved	
#	Peak, nm	#	Peak, nm	no.	E/eV	E/nm			From	To		x	y	z	from	to
I	565	1	587	2B	2.12	585	0.0214	202.58	68a	67b	0.625	2.126	1.740	0.000	HOMO–1	LUMO+1
									66b	69a	0.239	1.550	0.562	0.000	HOMO	LUMO
									66b	70a	0.108	-1.105	-0.637	0.000	HOMO	LUMO+2
				3B	2.19	566	0.2496	-33.577	68a	68b	0.958	0.366	0.300	0.000	HOMO–1	LUMO+3
									66b	70a	0.022	-0.467	-0.269	0.000	HOMO	LUMO+2
		2	553	4A	2.20	564	0.2860	-54.298	68a	70a	0.729	0.000	0.000	3.001	HOMO–1	LUMO+2
II	474	3	470	7B	2.58	480	0.4588	-139.86	68a	70b	0.705	0.591	0.911	0.000	HOMO–1	LUMO+5
									66b	71a	0.141	0.460	0.023	0.000	HOMO	LUMO+6
									66b	70a	0.035	0.559	0.322	0.000	HOMO	LUMO+2
				8A	2.60	477	0.3607	-85.414	68a	71a	0.031	0.000	0.000	0.176	HOMO–1	LUMO+6
									66b	67b	0.003	0.000	0.000	0.147	HOMO	LUMO+1
				9A	2.67	465	0.2117	-117.98	68a	72a	0.945	0.000	0.000	-0.172	HOMO–1	LUMO+8
									68a	73a	0.020	0.000	0.000	-0.083	HOMO–1	LUMO+9
									66b	70b	0.012	0.000	0.000	0.106	HOMO	LUMO+5
				10B	2.68	462	0.1132	-68.715	66b	73a	0.849	-0.485	-0.346	0.000	HOMO	LUMO+9
									65b	69a	0.064	0.595	0.335	0.000	HOMO–2	LUMO
III	450	3		11A	2.77	448	0.0974	-18.493	68a	71a	0.001	0.000	0.000	0.032	HOMO–1	LUMO+6
									66b	72b	0.799	0.000	0.000	-0.022	HOMO	LUMO+10
									68a	74a	0.192	0.000	0.000	0.024	HOMO–1	LUMO+11
									68a	73a	0.002	0.000	0.000	-0.028	HOMO–1	LUMO+9
									66b	70b	0.001	0.000	0.000	-0.027	HOMO	LUMO+5

				12B	2.78	447	0.0384	-24.879	65b	69a	0.851	2.118	1.193	0.000	HOMO–2	LUMO
				13B	2.80	443	0.2537	-75.669	68a	72b	0.567	-0.487	0.873	0.000	HOMO–1	LUMO+10
									66b	74a	0.392	-0.507	0.679	0.000	HOMO	LUMO+11
									67a	68b	0.010	0.175	-0.310	0.000	HOMO–3	LUMO+3
				14A	2.81	442	0.1905	-39.906	68a	75a	0.805	0.000	0.000	1.503	HOMO–1	LUMO+12
				17B	3.01	412	0.0000	-3.5551	65b	70a	0.874	0.151	-0.246	0.000	HOMO–2	LUMO+2
IV	371	4	372	22B	3.26	380	0.0016	-11.025	66a	68b	0.877	-0.498	-0.045	0.000	HOMO–4	LUMO+3
									65b	72a	0.086	0.270	0.147	0.000	HOMO–2	LUMO+8
				23A	3.27	379	0.0050	-24.407	67a	70a	0.829	0.000	0.000	-0.097	HOMO–3	LUMO+2
									64b	68b	0.055	0.000	0.000	-0.070	HOMO–5	LUMO+3
									66b	74b	0.024	0.000	0.000	0.094	HOMO	LUMO+15
									65b	71b	0.009	0.000	0.000	0.105	HOMO–2	LUMO+7
									65a	70a	0.004	0.000	0.000	-0.001	HOMO–7	LUMO+2
				24B	3.32	373	0.4640	-227.2	66b	76a	0.923	-0.156	-0.243	0.000	HOMO	LUMO+14
				25A	3.33	373	0.4743	-195.6	64b	68b	0.693	0.000	0.000	-0.248	HOMO–5	LUMO+3
									66a	70a	0.189	0.000	0.000	0.668	HOMO–4	LUMO+2
V	346	4		26B	3.36	369	0.0741	104.65	67a	69b	0.489	0.459	-0.836	0.000	HOMO–3	LUMO+4
									67a	68b	0.431	-1.034	1.838	0.000	HOMO–3	LUMO+3
				27B	3.57	348	0.3472	-90.145	68a	74b	0.327	0.110	-0.011	0.000	HOMO–1	LUMO+15
									68a	73b	0.274	-0.405	-0.297	0.000	HOMO–1	LUMO+13
									65b	72a	0.247	0.454	0.247	0.000	HOMO–2	LUMO+8
				28A	3.58	346	0.2715	-53.001	66b	74b	0.449	0.000	0.000	0.403	HOMO	LUMO+15
									68a	77a	0.380	0.000	0.000	-0.131	HOMO–1	LUMO+16
									68a	76a	0.105	0.000	0.000	-0.204	HOMO–1	LUMO+14
				29A	3.65	340	0.1603	-10.178	66b	73b	0.599	0.000	0.000	0.474	HOMO	LUMO+13
									66a	70a	0.104	0.000	0.000	0.490	HOMO–4	LUMO+2
									65a	69a	0.046	0.000	0.000	0.298	HOMO–7	LUMO
				30B	3.65	339	0.1404	0.21868	68a	73b	0.466	-0.524	-0.384	0.000	HOMO–1	LUMO+13
				31B	3.69	336	0.0006	-30.346	66a	69b	0.767	-0.502	-0.196	0.000	HOMO–4	LUMO+4
				33B	3.71	334	0.0065	72.485	62b	69a	0.439	0.306	0.226	0.000	HOMO–9	LUMO
									64a	67b	0.382	-0.312	-0.146	0.000	HOMO–8	LUMO+1
				35B	3.74	332	0.0116	-14.233	66b	78a	0.804	0.168	-0.004	0.000	HOMO	LUMO+17

Appendix B - Supporting information for "Time–Dependent Density Functional Theory Investigation of the Electronic Structure and Chiroptical Properties of Curved and Helical Silver Nanowires"

Note: For absorption and CD spectra the first three main peaks are considered. The first two peaks have the same location in the absorption and CD spectra. The third strong absorption peak corresponds to the third excitation state on the CD spectra, which sometimes is not a minimum/maximum of the third CD peak, because the large third peak of CD spectra can arise from the overlap between the third and fourth strong excited states.

Figure B-1. Structures, optical absorption spectra, and circular dichroism spectra of helical Ag_8. Structures with dihedral angle 10° – 30°.

STRUCTURE	ABSORPTION SPECTRA	CD SPECTRA
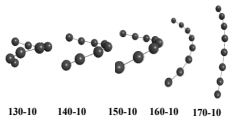	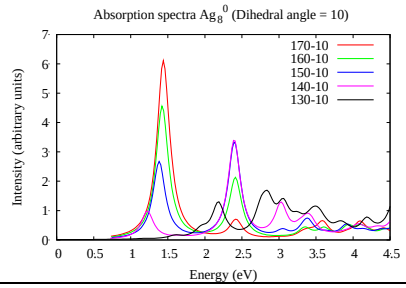	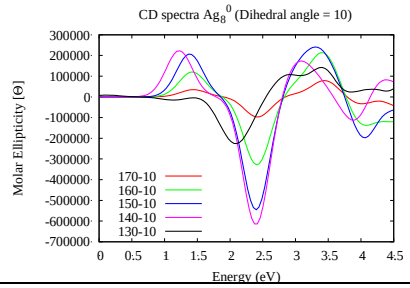
2a	2b	2c
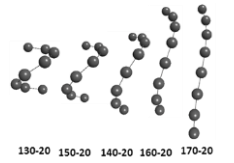	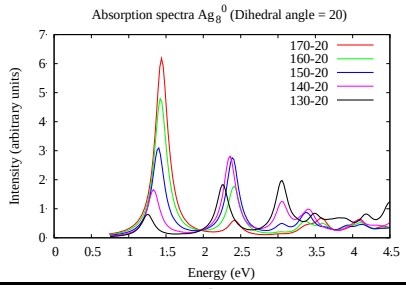	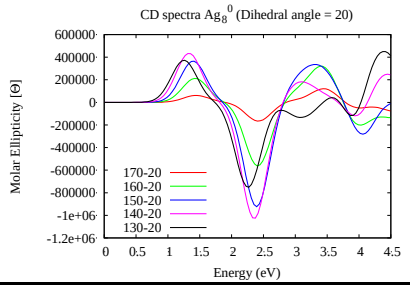
3a	3b	3c
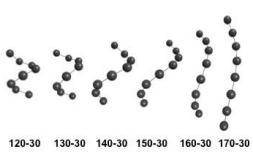	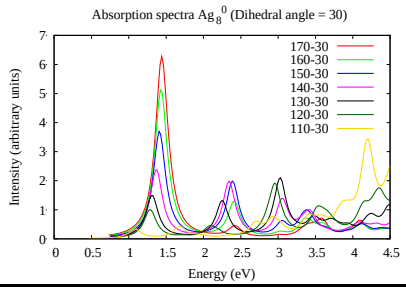	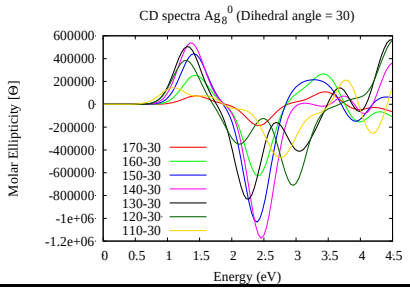
4a	4b	4c

Figure B–1. Structures, optical absorption spectra, and circular dichroism spectra of helical Ag_8. Structures with dihedral angle 40° – 70°.

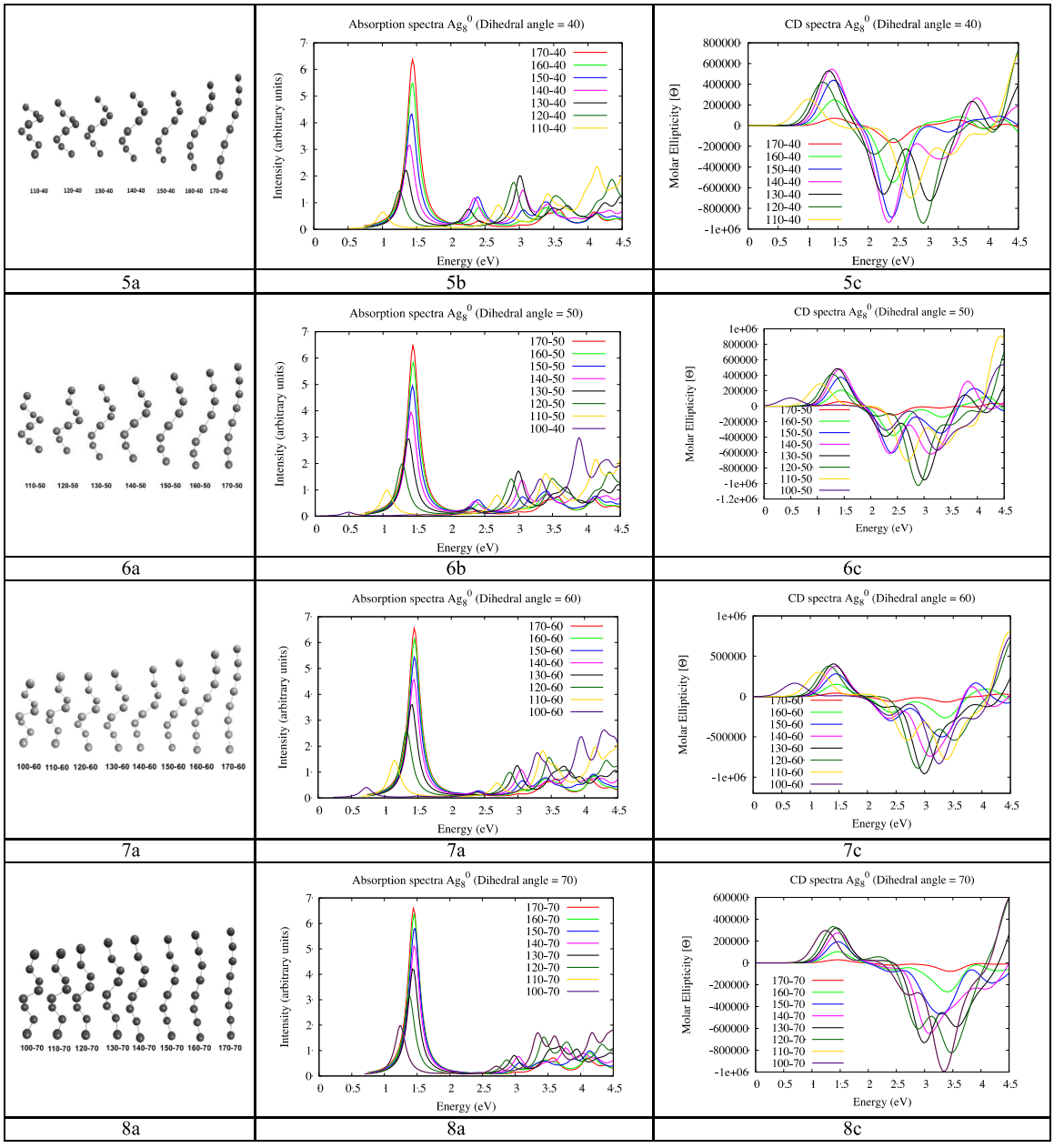

Figure B–2. Absorption and CD spectra for systems Ag_8 with small bond angles

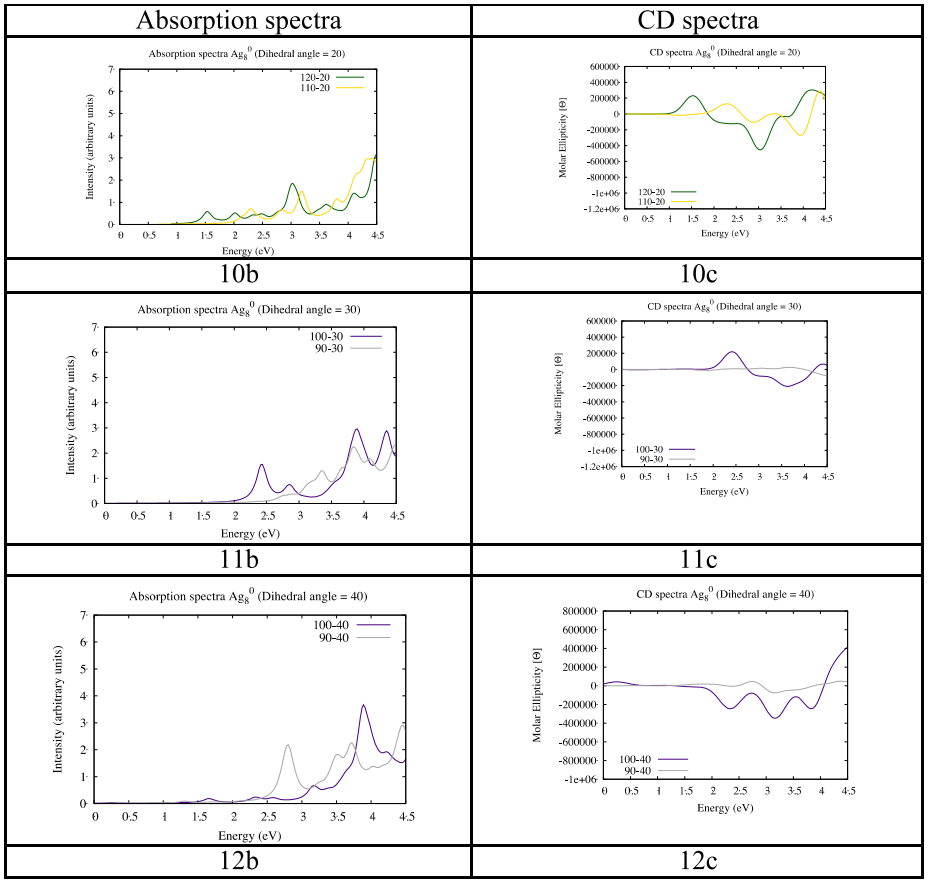

1. Dihedral angle = 10

Table B-1. First Peak: energy (eV), oscillator strength (*f*), molar ellipticity ($[\Theta]\cdot10^{-5}$, $deg\cdot cm^2\cdot dmole^{-1}$) and rotatory strength (R_m, 10^{-40} $esu^2\cdot cm^2$)

Structure	E, eV	*f*	$[\Theta]\cdot10^{-5}$	R_m
170-10	1.44	1.88	0.35	84.4
160-10	1.42	1.42	1.20	296.2
150-10	1.38	0.82	2.07	525.5
140-10	1.22	0.29	2.23	636.9

Table B-2. Second Peak: energy (eV), oscillator strength (*f*), molar ellipticity ($[\Theta]\cdot10^{-5}$, $deg\cdot cm^2\cdot dmole^{-1}$) and rotatory strength (R_m, 10^{-40} $esu^2\cdot cm^2$)

# Peak	E, eV	*f*	$[\Theta]\cdot10^{-5}$	R_m
170-10	2.41	0.12	-0.97	-92.53
160-10	2.41	0.58	-3.28	-440.28
150-10	2.40	1.02	-5.46	-803.28
140-10	2.40	1.06	-6.14	-899.24

Table B-3. Third Peak: energy (eV), oscillator strength (*f*), molar ellipticity ([Θ]·10^{-5}, deg·cm^2·dmole^{-1}) and rotatory strength(R_m, 10^{-40} esu^2 ·cm^2)

# Peak	E, eV	*f*	[Θ]·10^{-5}	R_m
170-10	3.00	0.007	0.2	15.2
160-10	3.02	0.009	0.9	66.3
150-10	3.04	0.07	1.7	146.8
140-10	3.03	0.35	1.9	168.9

Table B-4. Spectral data of structure 130-10. energy (eV), oscillator strength (*f*), molar ellipticity ([Θ]·10^{-5}, deg·cm^2·dmole^{-1}) and rotatory strength(R_m, 10^{-40} esu^2 ·cm^2)

		Absorption spectra	Circular dichroism spectra	
# Peak	E, eV	*f*	[Θ]·10^{-5}	R_m
1	1.60	0.03	-20185.0	15.78
2	1.95	0.08	-206401.4	-199.96
3	2.18	0.29	-211480.6	-388.62
4	2.76	0.24	93240.1	30.45
5	2.85	0.31	107488.3	77.84
6	3.06	0.30	105179.6	37.98

2. Dihedral angle = 20

Table B-5. First Peak: energy (eV), oscillator strength (*f*), molar ellipticity ([Θ]·10^{-5}, deg·cm^2·dmole^{-1}) and rotatory strength (R_m, 10^{-40} esu^2 ·cm^2)

Structure	E, eV	*f*	[Θ]·10^{-5}	R_m
170-20	1.44	1.90	0.6	147.7
160-20	1.43	1.49	2.1	516.7
150-20	1.40	0.96	3.6	918.1
140-20	1.33	0.51	4.3	1139.4
130-20	1.25	0.24	3.7	1033.0

Table B-6. Second Peak: energy (eV), oscillator strength (*f*), molar ellipticity ([Θ]·10^{-5}, deg·cm^2·dmole^{-1}) and rotatory strength (R_m, 10^{-40} esu^2 ·cm^2)

Structure	E, eV	*f*	[Θ]·10^{-5}	R_m
170-20	2.41	0.10	-1.6	-156.3
160-20	2.41	0.48	-5.6	-742.3
150-20	2.39	0.84	-9.2	-1360.5
140-20	2.35	0.86	-10.2	-1530.3
130-20	2.26	0.55	-7.5	-1162.5

Table B-7. Third Peak: energy (eV), oscillator strength (*f*), molar ellipticity ([Θ]·10^{-5}, deg·cm^2·dmole^{-1}) and rotatory strength (R_m, 10^{-40} esu^2 ·cm^2)

Structure	E, eV	*f*	[Θ]·10^{-5}	R_m
170-20	3.00	0.01	0.3	23.7
160-20	3.02	0.02	1.8	98.3
150-20	3.05	0.10	2.6	208.9
140-20	3.05	0.34	1.7	172.1
130-20	3.05	0.58	-1.3	-136.1

3. Dihedral angle = 30

Table B-8. First Peak: energy (eV), oscillator strength (*f*), molar ellipticity ([Θ]·10^{-5}, deg·cm^2·dmole^{-1}) and rotatory strength (R$_m$, 10^{-40} esu^2 ·cm^2)

Structure	E, eV	*f*	[Θ]·10^{-5}	R$_m$
170-30	1.44	1.93	0.7	176.2
160-30	1.43	1.60	2.5	625.9
150-30	1.41	1.15	4.4	1103.8
140-30	1.37	0.74	5.4	1382.2
130-30	1.31	0.46	5.1	1341.2
120-30	1.29	0.31	3.7	1063.3

Table B-9. Second Peak: energy (eV), oscillator strength (*f*), molar ellipticity ([Θ]·10^{-5}, deg·cm^2·dmole^{-1}) and rotatory strength (R$_m$, 10^{-40} esu^2 ·cm^2)

Structure	E, eV	*f*	[Θ]·10^{-5}	R$_m$
170-30	2.41	0.07	-1.9	-172.9
160-30	2.41	0.34	6.3	-841.6
150-30	2.39	0.59	-10.3	-1522.0
140-30	2.34	0.60	-11.7	-1691.3
130-30	2.25	0.39	-8.3	-1280.9
120-30	2.10	0.09	-3.5	-401.9

Table B-10. Third Peak: energy (eV), oscillator strength (*f*), molar ellipticity ([Θ]·10^{-5}, deg·cm^2·dmole^{-1}) and rotatory strength (R$_m$, 10^{-40} esu^2 ·cm^2)

Structure	E, eV	*f*	[Θ]·10^{-5}	R$_m$
170-30	3.00	0.02	0.2	20.9
160-30	3.03	0.04	0.9	86.5
150-30	3.05	0.14	1.7	152.7
140-30	3.05	0.39	0.08	11.6
130-30	3.03	0.63	-4.11	-441.3
120-30	2.95	0.55	-7.1	-746.4

4. Dihedral angle = 40

Table B-11. First Peak: energy (eV), oscillator strength (*f*), molar ellipticity ([Θ]·10^{-5}, deg·cm^2·dmole^{-1}) and rotatory strength (R$_m$, 10^{-40} esu^2 ·cm^2)

Structure	E, eV	*f*	[Θ]·10^{-5}	R$_m$
170-40	1.44	1.97	0.7	171.3
160-40	1.44	1.72	2.5	604.6
150-40	1.42	1.36	4.4	1081.4
140-40	1.39	0.99	5.5	1374.9
130-40	1.34	0.69	5.3	1380.9
120-40	1.25	0.45	4.2	1180.9
110-40	1.01	0.20	2.5	889.1

Table B-12. Second Peak: energy (eV), oscillator strength (*f*), molar ellipticity ([Θ]·10^{-5}, deg·cm^2·dmole^{-1}) and rotatory strength (R$_m$, 10^{-40} esu^2 ·cm^2)

Structure	E, eV	*f*	[Θ]·10^{-5}	R$_m$
170-40	2.41	0.039	-1.6	-148.6
160-40	2.41	0.20	-5.5	-724.8
150-40	2.39	0.35	-8.9	-1306.1
140-40	2.34	0.34	-9.4	-1422.3
130-40	2.26	0.21	-6.6	-1034.1
120-40	2.10	0.06	-2.8	-413.3
110-40	1.85	0.01	-0.3	-6.9

Table B-13. Third Peak: energy (eV), oscillator strength (*f*), molar ellipticity ([Θ]·10^{-5}, deg·cm^2·dmole^{-1}) and rotatory strength (R$_m$, 10^{-40} esu^2 ·cm^2)

Structure	E, eV	*f*	[Θ]·10^{-5}	R$_m$
170-40	3.00	0.02	0.07	10.6
160-40	3.03	0.06	0.4	33.9
150-40	3.05	0.17	-0.1	-0.3
140-40	3.05	0.42	-3.2	-294.2
130-40	3.01	0.61	-7.7	-818.4
120-40	2.92	0.50	-9.4	-1040.3
110-40	2.69	0.26	-7.0	-847.9

5. Dihedral angle = 50

Table B-14. First Peak: energy (eV), oscillator strength (*f*), molar ellipticity ([Θ]·10^{-5}, deg·cm^2·dmole^{-1}) and rotatory strength (R$_m$, 10^{-40} esu^2 ·cm^2)

Structure	E, eV	*f*	[Θ]·10^{-5}	R$_m$
170-50	1.44	1.94	0.6	140.5
160-50	1.44	1.82	2.1	500.3
150-50	1.44	1.55	3.7	906.9
140-50	1.42	1.23	4.8	1178.2
130-50	1.37	0.92	4.9	1245.1
120-50	1.28	0.62	4.1	1130.8
110-50	1.06	0.31	2.9	957.5

Table B-15. Second Peak: energy (eV), oscillator strength (*f*), molar ellipticity ([Θ]·10^{-5}, deg·cm^2·dmole^{-1}) and rotatory strength (R$_m$, 10^{-40} esu^2 ·cm^2)

Structure	E, eV	*f*	[Θ]·10^{-5}	R$_m$
170-50	2.41	0.02	-1.1	-96.1
160-50	2.41	0.09	-3.8	-479.3
150-50	2.40	0.16	-6.1	-862.2
140-50	2.36	0.15	-6.1	-901.9
130-50	2.27	0.08	-3.9	-620.7
120-50	2.13	0.02	-1.3	-212.7
110-50	1.80	0.005	-0.003	-1.44

Table B-16. Third Peak: energy (eV), oscillator strength (*f*), molar ellipticity ([Θ]·10^{-5}, deg·cm^2·dmole^{-1}) and rotatory strength (R$_m$, 10^{-40} esu^2 ·cm^2)

Structure	E, eV	*f*	[Θ]·10^{-5}	R$_m$
170-50	3.00	0.02	-0.1	-2.8
160-50	3.03	0.06	-0.5	-30.2
150-50	3.05	0.18	-2.4	-177.7
140-50	3.05	0.39	-5.9	-598.2
130-50	2.99	0.51	-9.5	-1114.1
120-50	2.89	0.39	-10.2	-1139.1
110-50	2.68	0.23	-7.1	-883.8

6. Dihedral angle = 60

Table B-17. First Peak: energy (eV), oscillator strength (*f*), molar ellipticity ([Θ]·10^{-5}, deg·cm^2·dmole^{-1}) and rotatory strength (R$_m$, 10^{-40} esu^2 ·cm^2)

Structure	E, eV	*f*	[Θ]·10^{-5}	R$_m$
170-60	1.44	2.02	0.4	101.4
160-60	1.44	1.91	1.5	365.4
150-60	1.44	1.71	2.8	675.3
140-60	1.44	1.44	3.8	909.0
130-60	1.41	1.14	4.1	1012.8
120-60	1.33	0.81	3.8	991.8
110-60	1.15	0.45	3.0	931.4

Table B-18. Second Peak: energy (eV), oscillator strength (*f*), molar ellipticity ([Θ]·10^{-5}, deg·cm^2·dmole^{-1}) and rotatory strength (R$_m$, 10^{-40} esu^2 ·cm^2)

Structure	E, eV	*f*	[Θ]·10^{-5}	R$_m$
170-60	2.41	0.005	-0.6	-44.4
160-60	2.41	0.03	-1.9	-232.6
150-60	2.40	0.05	-3.0	-414.7
140-60	2.37	0.04	-2.7	-397.5
130-60	2.30	0.01	-1.3	-218.6
120-60	2.18	0.002	-0.01	-35.1
110-60	1.94	0.005	0.3	54.9

Table B-19. Third Peak: energy (eV), oscillator strength (*f*), molar ellipticity ([Θ]·10^{-5}, deg·cm^2·dmole^{-1}) and rotatory strength (R$_m$, 10^{-40} esu^2 ·cm^2)

Structure	E, eV	*f*	[Θ]·10^{-5}	R$_m$
170-60	3.01	0.02	-0.2	-12.7
160-60	3.03	0.06	-1.2	-77.3
150-60	3.06	0.16	-3.9	-297.9
140-60	3.05	0.31	-7.3	-752.9
130-60	2.99	0.37	-9.6	-1135.5
120-60	2.88	0.25	-8.9	-973.1
110-60	2.69	0.16	-5.4	-713.3

7. Dihedral angle = 70

Table B-20. First Peak: energy (eV), oscillator strength (*f*), molar ellipticity ([Θ]·10^{-5}, deg·cm^2·dmole^{-1}) and rotatory strength (R$_m$, 10^{-40} esu^2 ·cm^2)

Structure	E, eV	*f*	[Θ]·10^{-5}	R$_m$
170-70	1.46	2.04	0.3	65.1
160-70	1.46	1.97	1.0	239.8
150-70	1.46	1.83	1.9	462.8
140-70	1.46	1.61	2.7	654.9
130-70	1.44	1.33	3.2	779.1
120-70	1.38	0.99	3.3	835.7
110-70	1.24	0.62	3.0	835.6

Table B-21. Second Peak: energy (eV), oscillator strength (*f*), molar ellipticity ([Θ]·10^{-5}, deg·cm^2·dmole^{-1}) and rotatory strength (R$_m$, 10^{-40} esu^2 ·cm^2)

Structure	E, eV	*f*	[Θ]·10^{-5}	R$_m$
170-70	2.43	0.003	-0.2	-21.8
160-70	2.45	0.008	-0.6	-57.4
150-70	2.40	0.009	-0.8	-102.0
140-70	2.39	0.002	-0.5	-67.1
130-70	2.33	0.000	1.9	16.4
120-70	2.18	0.007	0.6	53.4

Table B-22. Third Peak: energy (eV), oscillator strength (*f*), molar ellipticity ([Θ]·10^{-5}, deg·cm^2·dmole^{-1}) and rotatory strength (R$_m$, 10^{-40} esu^2 ·cm^2)

Structure	E, eV	*f*	[Θ]·10^{-5}	R$_m$
170-70	3.00	0.002	-0.3	-15.4
160-70	3.03	0.047	-1.2	-88.2
150-70	3.06	0.12	-3.8	-308.2
140-70	3.04	0.21	-6.4	-687.9
130-70	2.98	0.23	-7.3	-872.6
120-70	2.88	0.13	-6.0	-603.9

Figure B-4. TDDFT A) optical absorption and B) circular dichroism spectra for Ag$_n$ (*n* = 4, 6, 8, 10, 12) with 170° Ag-Ag-Ag bond angles and 10° Ag-Ag-Ag-Ag torsional angles.

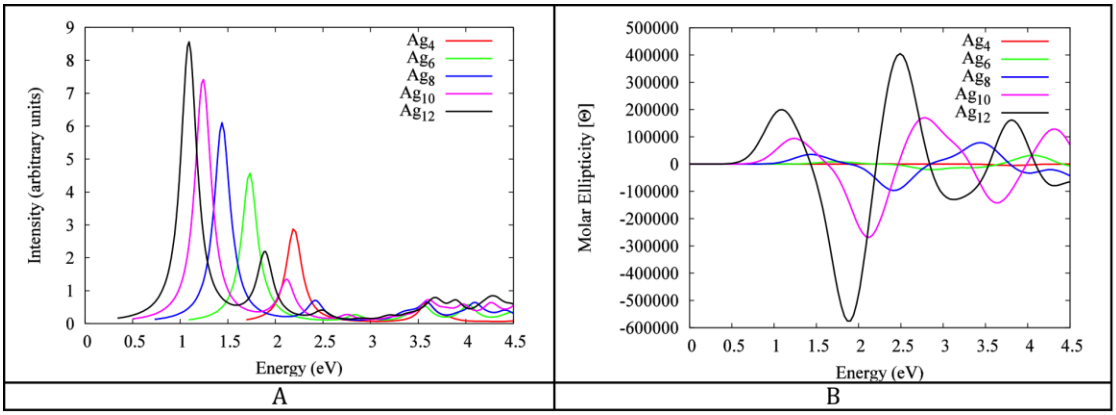

Table B-23. Calculated excitation energies, oscillator strengths, and molar ellipticities for silver wires Ag_n (n = 4, 6, 8, 10, 12) with 170° bond angles and 10° dihedral angles.

			ABS	CD
	# Peak	E, eV	Osc.str.	Molar Ellipt.[Θ]
Ag_4	1	2.19	0.91	617.6
	2	-	-	-
	3	3.77	0.03	-5289.6
Ag_6	1	1.73	1.43	8501.7
	2	2.84	0.06	-20245.6
	3	3.39	0.04	-12766.8
Ag_{10}	1	1.24	2.23	94106.8
	2	2.12	0.39	-268957.5
	3	2.80	0.06	170088.7
Ag_{12}	1	1.08	2.39	199489.7
	2	1.88	0.64	-575845.2
	3	2.49	0.09	404790.9

Figure B–3. TDDFT A) optical absorption and B) circular dichroism spectra for Ag_n (n = 4, 6, 8, 10, 12) with 160° Ag-Ag-Ag bond angles and 10° Ag-Ag-Ag-Ag torsional angles.

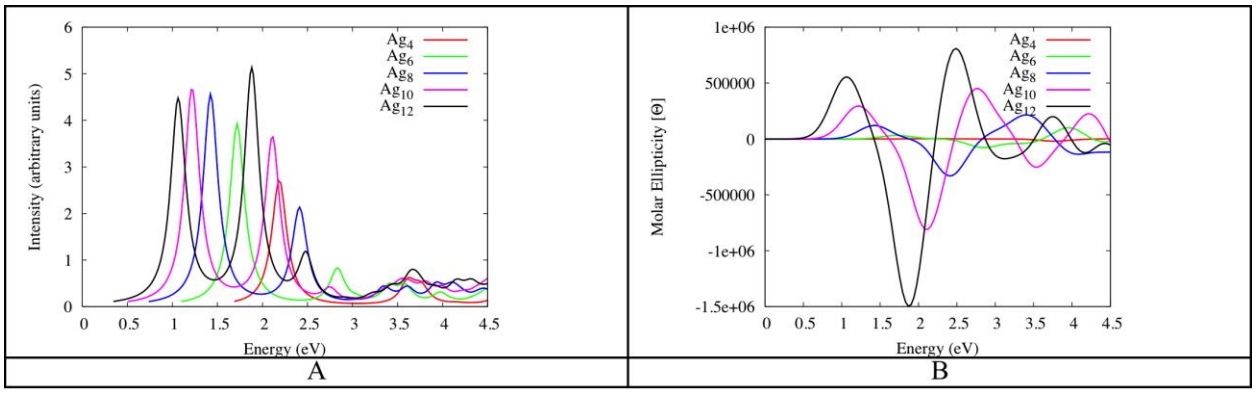

Table B-24. Calculated excitation energies, oscillator strengths, and molar ellipticities for silver wires Ag_n (n = 4, 6, 8, 10, 12) with 160° bond angles and 10° dihedral angles.

			ABS	CD
	# Peak	E, eV	Osc.str.	Molar Ellipt.[Θ]
Ag_4	1	2.19	0.853	2425.17
	2	-	-	-
	3	3.77	0.07	-19691.9
Ag_6	1	1.72	1.224	31402.1
	2	2.83	0.239	-77414.3
	3	3.40	0.108	-39591.7
Ag_{10}	1	1.22	1.44	293031.9
	2	2.11	1.12	-802668.0
	3	2.85	0.09	409539.7
Ag_{12}	1	1.06	1.35	555612.39

	2	1.88	1.58	-1496963.5
	3	2.48	0.32	809781.9

Appendix C - Supporting information for "Time Dependent Density Functional Theory Study of Magnetic Circular Dichroism Spectra of Gold Clusters $Au_9(PH_3)_8^{3+}$ and $Au_9(PPh_3)_8^{3+}$"

Figure C–1. Structure of the bare core Au_9^{3+} and ligand protected clusters $Au_9(PH_3)_8^{3+}$ and $Au_9(PPh_3)_8^{3+}$. The symmetry of the gold core for all of these structures is D_{2h}.

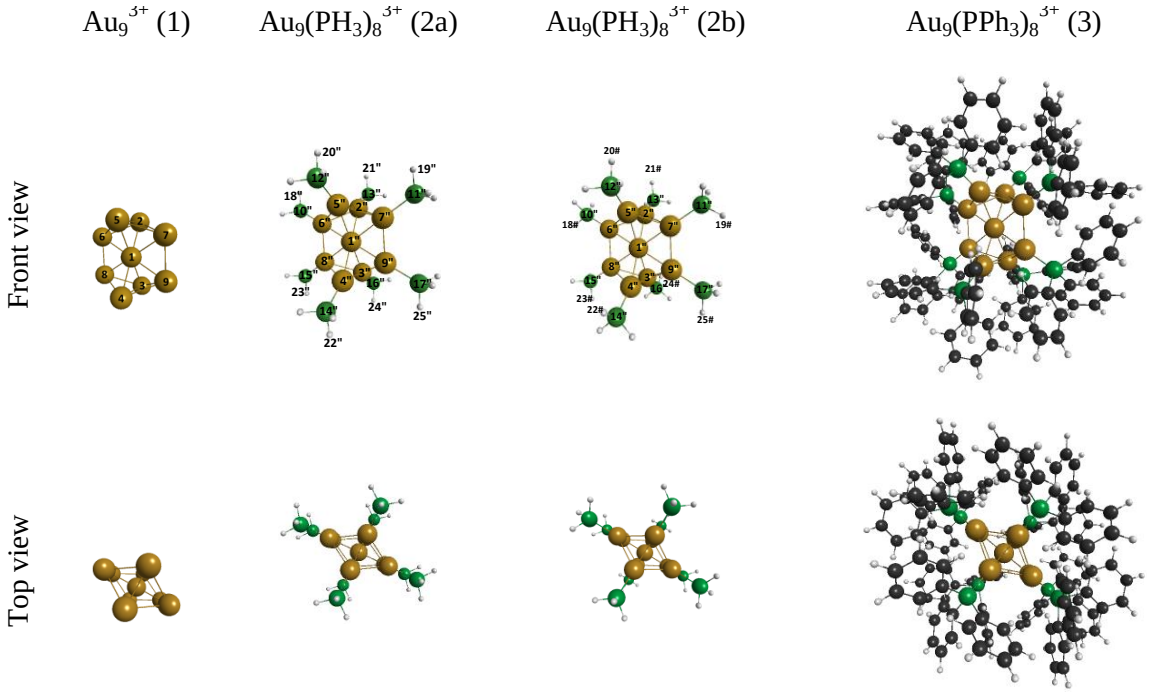

Figure C–2. The most stable structures of $Au_9(PH_3)_8^{3+}$.

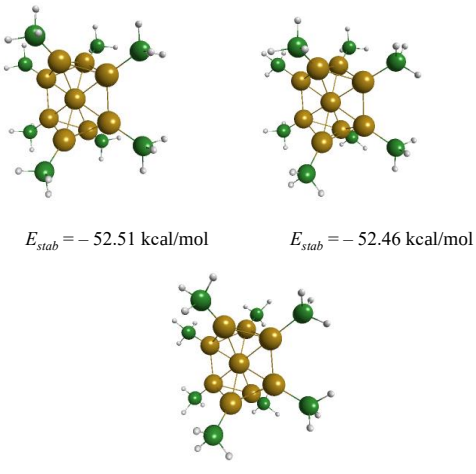

E_{stab} = – 52.51 kcal/mol E_{stab} = – 52.46 kcal/mol

E_{stab} = – 52.40 kcal/mol

Table C–1. Calculated geometrical parameters for Au_9^{3+} and ligand protected clusters $Au_9(PH_3)_8^{3+}$ (2a) and $Au_9(PH_3)_8^{3+}$ (2b) and experimental geometrical parameters for $Au_9(PPh_3)_8^{3+}$. Essential bond distances (Å) and dihedral angles (degrees).

Bonds	**Au_9^{3+}**	**$Au_9(PH_3)_8^{3+}$ (2a)**	**$Au_9(PH_3)_8^{3+}$ (2b)**	**Experiment[61]**
Au_1-Au_2	2.84 Å	2.78 Å	2.77 Å	2.689
Au_1-Au_3	2.84 Å	2.78 Å	2.77 Å	
Au_1-Au_4	2.84 Å	2.78 Å	2.77 Å	
Au_1-Au_5	2.84 Å	2.78 Å	2.77 Å	
Au_1-Au_6	2.73 Å	2.80 Å	2.79 Å	2.735
Au_1-Au_7	2.73 Å	2.80 Å	2.79 Å	
Au_1-Au_8	2.73 Å	2.80 Å	2.79 Å	
Au_1-Au_9	2.73 Å	2.80 Å	2.79 Å	
Au_2-Au_5	2.71 Å	2.80 Å	2.79 Å	2.751
Au_3-Au_4	2.71 Å	2.80 Å	2.79 Å	
Au_6-Au_8	2.87 Å	2.86 Å	2.86 Å	2.783
Au_7-Au_9	2.87 Å	2.86 Å	2.86 Å	
Au_2-Au_6	2.89 Å	2.94 Å	2.94 Å	2.866
Au_2-Au_7	2.89 Å	2.94 Å	2.94 Å	
Au_3-Au_8	2.89 Å	2.94 Å	2.94 Å	
Au_4-Au_8	2.89 Å	2.94 Å	2.94 Å	
Au_4-Au_9	2.89 Å	2.94 Å	2.94 Å	
Au_5-Au_6	2.89 Å	2.94 Å	2.94 Å	
Au_5-Au_7	2.89 Å	2.94 Å	2.94 Å	2.899
Au_6-P_{10}	–	2.37 Å	2.37 Å	
Au_7-P_{11}	–	2.37 Å	2.37 Å	
Au_8-P_{15}	–	2.37 Å	2.36 Å	
Au_9-P_{17}	–	2.37 Å	2.36 Å	
Au_5-P_{12}	–	2.33 Å	2.32 Å	
Au_2-P_{13}	–	2.33 Å	2.32 Å	
Au_3-P_{16}	–	2.33 Å	2.33 Å	
Au_4-P_{14}	–	2.33 Å	2.33 Å	
Angles	**Au_9^{3+}**	**$Au_9(PH_3)_8^{3+}$ (2a)**	**$Au_9(PH_3)_8^{3+}$ (2b)**	
$\angle H_{18}$-P_{10}-Au_6-Au_8	–	180°	0°	
$\angle H_{19}$-P_{11}-Au_7-Au_9	–	180°	0°	
$\angle H_{20}$-P_{12}-Au_5-Au_4	–	180°	180°	
$\angle H_{21}$-P_{13}-Au_2-Au_3	–	180°	180°	
$\angle H_{22}$-P_{14}-Au_4-Au_5	–	180°	0°	
$\angle H_{23}$-P_{15}-Au_8-Au_6	–	180°	180°	
$\angle H_{24}$-P_{16}-Au_3-Au_2	–	180°	0°	
$\angle H_{25}$-P_{17}-Au_9-Au_7	–	180°	180°	

Table C–2. Absorption spectrum data for the bare golden core Au_9^{3+}: peak energies (μm^{-1}), oscillator strengths (*f*) and transitions responsible for these peaks. Golden core symmetry D_{2h}.

Peak #	Peak Max (μm^{-1})	Excitation state (μm^{-1})	f	Weight	Contributions to transition dipole moment			Transition	
					x	y	z	Occ.	Unocc.
1	1.77	1.77	0.021	0.9098	2.6287	0	0	HOMO	LUMO+1
2	1.97	1.97	0.027	0.7275	0	0	-2.8192	HOMO	LUMO+2
				0.2214	0	0	1.5261	HOMO-1	LUMO+1
3	2.38	2.38	0.049	0.414	0	0	-0.7688	HOMO-7	LUMO
				0.399	0	0	1.8641	HOMO-1	LUMO+1
				0.0629	0	0	0.7544	HOMO	LUMO+2
4	2.70	2.63	0.018	0.5962	0	0	-0.4162	HOMO-13	LUMO
				0.2194	0	0	0.5327	HOMO-7	LUMO
				0.0562	0	0	0.666	HOMO-1	LUMO+1
				0.0152	0	0	0.3532	HOMO	LUMO+2
		2.70	0.091	0.191	0	0	-0.4904	HOMO-7	LUMO
				0.1541	0	0	-1.088	HOMO-1	LUMO+1
				0.0806	0	0	-0.802	HOMO	LUMO+2
5	2.85	2.80	0.035	0.7465	0	0	0.3266	HOMO-12	LUMO+1
				0.0552	0	0	0.1227	HOMO-13	LUMO
				0.0384	0	0	0.2161	HOMO-7	LUMO
				0.0359	0	0	-0.1963	HOMO-14	LUMO+1
				0.0328	0	0	0.5022	HOMO	LUMO+2
				0.0326	0	0	0.4918	HOMO-1	LUMO+1
				0.0162	0	0	-0.2383	HOMO-1	LUMO+4
		2.85	0.108	0.2998	1.7619	0	0	HOMO	LUMO+4
				0.1347	0.8256	0	0	HOMO-1	LUMO+2
		2.93	0.036	0.5481	0	0	-0.327	HOMO-18	LUMO
				0.2073	0	0	-0.4606	HOMO-14	LUMO+1
				0.0225	0	0	0.2746	HOMO-1	LUMO+4
				0.0182	0	0	-0.3591	HOMO-1	LUMO+1
				0.012	0	0	-0.297	HOMO	LUMO+2

*The excited states with oscillator strength *f* stronger than 0.018 are considered ($f \sim 0.018$ is the average value of the oscillator strengths of all excited states in the region below 3.0 μm^{-1}).

Table C–3. MCD spectral data for the bare golden core Au_9^{3+} with symmetry D_{2h}. Peak energies (μm^{-1}), value of *B*–term (B), dipole momentum (D) and transitions responsible for MCD peaks.

Peak	Peak Max/Min (μm^{-1})	Excitation state (μm^{-1})	State	B	D	Contributions to transition dipole moment				Transitions	
						Weight	x	y	z	Occ.	Unocc.
1	1.78	1.77	$1B_{3u}$	-70.45	0.131	0.9098	2.6287	0	0	HOMO	LUMO+1

2	1.97	1.97	$1B_{1u}$	76.68	0.151	0.7275	0	0	-2.8192	HOMO	LUMO+2
						0.2214	0	0	1.5261	HOMO-1	LUMO+1
3	2.38	2.38	$3B_{1u}$	-41.70	0.228	0.414	0	0	-0.7688	HOMO-7	LUMO
						0.399	0	0	1.8641	HOMO-1	LUMO+1
						0.0629	0	0	0.7544	HOMO	LUMO+2
4	2.50	2.50	$2B_{3u}$	11.32	0.015	0.7687	1.0956	0	0	HOMO-9	LUMO
						0.1879	-1.0407	0	0	HOMO-1	LUMO+2
		2.52	$3B_{3u}$	11.51	0.001	0.5453	1.7656	0	0	HOMO-1	LUMO+2
						0.3554	-2.0392	0	0	HOMO	LUMO+4
		2.54	$2B_{2u}$	-10.08	0.058	0.5476	0	-1.291	0	HOMO-1	LUMO+3
5	2.74	2.63	$4B_{1u}$	15.80	0.074	0.5962	0	0	-0.4162	HOMO-13	LUMO
						0.2194	0	0	0.5327	HOMO-7	LUMO
						0.0562	0	0	0.666	HOMO-1	LUMO+1
						0.0152	0	0	0.3532	HOMO	LUMO+2
		2.70	$5B_{1u}$	-50.50	0.371	0.2469	0	0	-0.2642	HOMO-13	LUMO
						0.2194	0	0	0.1802	HOMO-12	LUMO+1
						0.191	0	0	-0.4904	HOMO-7	LUMO
						0.1541	0	0	-1.088	HOMO-1	LUMO+1
		2.76	$4B_{2u}$	-35.32	0.029	0.8436	0	0.9869	0	HOMO-16	LUMO
		2.79	$4B_{3u}$	-32.11	0.025	0.8019	-0.3679	0	0	HOMO-17	LUMO
						0.0831	-0.2122	0	0	HOMO-8	LUMO+3
						0.0424	0.6694	0	0	HOMO	LUMO+4
		2.80	$6B_{1u}$	-31.44	0.137	0.7465	0	0	0.3266	HOMO-12	LUMO+1
						0.0552	0	0	0.1227	HOMO-13	LUMO
						0.0384	0	0	0.2161	HOMO-7	LUMO
						0.0359	0	0	-0.1963	HOMO-14	LUMO+1
						0.0328	0	0	0.5022	HOMO	LUMO+2
						0.0326	0	0	0.4918	HOMO-1	LUMO+1
						0.0162	0	0	-0.2383	HOMO-1	LUMO+4
						0.3561	0	0	-0.7089	HOMO-23	LUMO+1
6	2.89	2.85	$5B_{3u}$	95.15	0.414	0.2998	1.7619	0	0	HOMO	LUMO+4
						0.1347	0.8256	0	0	HOMO-1	LUMO+2
		2.89	$6B_{3u}$	-140.39	0.033	0.8226	0.1676	0	0	HOMO-15	LUMO+1
						0.0633	0.2008	0	0	HOMO-12	LUMO+2
						0.0584	-0.1746	0	0	HOMO-8	LUMO+3
		2.90	$7B_{1u}$	156.82	0.044	0.5685	0	0	-0.7671	HOMO-14	LUMO+1
						0.3468	0	0	0.2616	HOMO-18	LUMO
		2.94	$7B_{3u}$	38.47	0.001	0.848	0.1628	0	0	HOMO-20	LUMO
						0.0918	-0.2399	0	0	HOMO-12	LUMO+2

*Each MCD peak was considered independently.

Table C–4. Absorption spectrum data for the complex $Au_9(PH_3)_8^{3+}$ (2b): peak energies (μm^{-1}), oscillator strengths (*f*) and transitions responsible for these peaks. Golden core symmetry D_{2h}.

Peak	Peak Max (μm^{-1})	Excitation state (μm^{-1})	f	Weight	Contributions to transition dipole moment			Transition	
					x	y	z	Occ.	Unocc.
1	1.5	1.5	0.033	0.9763	0	2.3486	0	HOMO	LUMO
				0.0106	0	-0.6113	0	HOMO	LUMO+5
2	2.07	2.07	0.081	0.7798	0	0	3.2285	HOMO	LUMO+2
				0.194	0	0	-1.264	HOMO-1	LUMO
3	2.31	2.31	0.185	0.721	0	0	2.3057	HOMO-1	LUMO
				0.1444	0	0	1.3149	HOMO	LUMO+2
				0.1078	0	0	-0.9371	HOMO-2	LUMO
4	2.82	2.82	0.253	0.8202	0	0	-2.3395	HOMO-2	LUMO
				0.0465	0	0	-0.5298	HOMO-1	LUMO
				0.0457	0	0	0.3231	HOMO-5	LUMO+1
				0.0322	0	0	-0.5618	HOMO	LUMO+2
5	2.97	2.97	0.327	0.4341	0	-2.7741	0	HOMO	LUMO+5
				0.3374	0	1.3023	0	HOMO-2	LUMO+2
				0.1817	0	-1.4297	0	HOMO-1	LUMO+2

*The excited states with oscillator strength *f* stronger than 0.030 are considered (f ~ 0.030 is the average value of the oscillator strengths of all excited states in the region below 3.0 μm^{-1}).

Table C–5. MCD spectral data for the complex $Au_9(PH_3)_8^{3+}$ (2b): peak energies (μm^{-1}), value of *B*–term (B), dipole momentum (D) and transitions responsible for MCD peaks. Golden core symmetry D_{2h}.

Peak	Peak Max/Min (μm^{-1})	Excitation state (μm^{-1})	State	B	D	Contributions to transition dipole moment				Transitions	
						Weight	x	y	z	Occ.	Unocc.
1	1.50	1.50	$1B_2$	-15.81	0.238	0.9763	0	2.3486	0	HOMO	LUMO
						0.0106	0	-0.6113	0	HOMO	LUMO+5
2	2.07	2.07	$1A_1$	52.47	0.431	0.7798	0	0	3.2285	HOMO	LUMO+2
						0.194	0	0	-1.264	HOMO-1	LUMO
3	2.31	2.31	$2A_1$	-37.12	0.879	0.721	0	0	2.3057	HOMO-1	LUMO
						0.1444	0	0	1.3149	HOMO	LUMO+2
						0.1078	0	0	-0.9371	HOMO-2	LUMO
4	2.58	2.58	$2B_2$	1.80	0.016	0.6802	0	-2.9698	0	HOMO-1	LUMO+2
						0.3167	0	2.5438	0	HOMO	LUMO+5
5	2.80	2.73	$2B_1$	-11.07	0.027	0.9749	1.2006	0	0	HOMO	LUMO+6
		2.82	$4A_1$	-22.38	0.981	0.8202	0	0	-2.3395	HOMO-2	LUMO
						0.0465	0	0	-0.5298	HOMO-1	LUMO

						0.0457	0	0	0.3231	HOMO-5	LUMO+1
						0.8202	0	0	-2.3395	HOMO-2	LUMO
6	2.97	2.97	$5B_2$	40.88	1.207	0.4341	0	-2.7741	0	HOMO	LUMO+5
						0.3374	0	1.3023	0	HOMO-2	LUMO+2
						0.1817	0	-1.4297	0	HOMO-1	LUMO+2

*Each MCD peak was considered independently.

Table C–6. Absorption spectrum data for the complex $Au_9(PPh_3)_8^{3+}$ (3): peak energies (μm^{-1}), oscillator strengths (*f*) and transitions responsible for these peaks. Golden core symmetry D_{2h}.

Peak	Peak Max (μm^{-1})	Excitation state (μm^{-1})	f		Contributions to transition dipole moment			Transition	
				Weight	x	y	z	Occ.	Unocc.
1	1.33	1.33	0.035	0.8037	2.2063	0.0477	-0.0115	HOMO	LUMO
2	1.78	1.78	0.100	0.7798	0.1141	-0.0642	-3.2411	HOMO	LUMO+2
				0.0904	-0.0026	0.001	0.7516	HOMO-2	LUMO
3	1.99	1.98	0.049	0.5465	0.1211	-0.0979	-0.0358	HOMO	LUMO+4
		1.99	0.060	0.3148	-0.0046	0.0018	1.3241	HOMO-2	LUMO
				0.0339	-0.0225	0.0126	0.6383	HOMO	LUMO+2
4	2.31	2.31	0.070	0.393	2.0124	-0.0779	0.0228	HOMO-2	LUMO+2
				0.1041	0.478	0.0717	0.0161	HOMO	LUMO+13
		2.34	0.040	0.3653	-0.2851	-0.0988	0.0236	HOMO	LUMO+19
				0.2933	0.0123	-0.0599	1.2401	HOMO-6	LUMO
		2.35	0.026	0.1234	0.0079	-0.0388	0.8036	HOMO-6	LUMO
		2.37	0.026	0.6301	0.1888	-0.0218	-0.197	HOMO-8	LUMO
				0.2836	-0.1076	-0.154	0.3916	HOMO	LUMO+20
		2.39	0.040	0.5626	0.0538	0.1932	-0.3064	HOMO-6	LUMO+1
				0.067	-0.0058	0.0284	-0.5873	HOMO-6	LUMO
5	2.52	2.44	0.015	0.4705	-1.1813	-0.0545	0.0015	HOMO	LUMO+25
				0.2459	0.9827	-0.0948	0.036	HOMO	LUMO+28
		2.45	0.022	0.6579	-0.0619	-0.0475	0.5331	HOMO	LUMO+26
				0.2117	0.3957	-0.1757	-0.1565	HOMO	LUMO+27
				0.0336	-0.3625	0.0349	-0.0133	HOMO	LUMO+28
				0.0141	0.2045	0.0094	-0.0003	HOMO	LUMO+25
		2.46	0.029	0.6554	0.6948	-0.3086	-0.2748	HOMO	LUMO+27
				0.1913	0.0333	0.0256	-0.2869	HOMO	LUMO+26
				0.0808	-0.5614	0.0541	-0.0205	HOMO	LUMO+28
		2.48	0.040	0.5585	0.3041	0.128	-0.2039	HOMO	LUMO+29
				0.2248	-0.9307	0.0897	-0.0341	HOMO	LUMO+28
				0.0449	-0.3615	-0.0167	0.0005	HOMO	LUMO+25

		2.49	0.012	0.0486	0.4321	-0.0417	0.0158	HOMO	LUMO+28
		2.50	0.011	0.0903	-0.215	-0.0354	0.0368	HOMO	LUMO+31
				0.0791	0.1141	0.0481	-0.0765	HOMO	LUMO+29
				0.0351	0.367	-0.0354	0.0134	HOMO	LUMO+28
		2.50	0.013	0.7859	0.0054	-0.1151	-0.1118	HOMO	LUMO+30
				0.1515	-0.278	-0.0458	0.0475	HOMO	LUMO+31
				0.0155	-0.2436	0.0235	-0.0089	HOMO	LUMO+28
				0.0067	-0.1394	-0.0064	0.0002	HOMO	LUMO+25
		2.50	0.021	0.0894	-0.5855	0.0565	-0.0214	HOMO	LUMO+28
				0.1748	0.2991	0.0493	-0.0511	HOMO	LUMO+31
				0.0238	-0.2624	-0.0121	0.0003	HOMO	LUMO+25
				0.0067	-0.2532	0.0098	-0.0029	HOMO-2	LUMO+2
		2.52	0.068	0.4455	-0.4752	-0.0783	0.0813	HOMO	LUMO+31
				0.1119	-0.652	0.0629	-0.0239	HOMO	LUMO+28
				0.0407	-0.3415	-0.0158	0.0004	HOMO	LUMO+25
				0.0155	0.3308	0.0035	-0.0055	HOMO-6	LUMO+2
				0.0146	-0.3714	0.0144	-0.0042	HOMO-2	LUMO+2
		2.57	0.011	0.922	0.5146	0.0469	0.0441	HOMO	LUMO+33
6	2.71	2.61	0.019	0.8163	-0.0343	-0.1539	-0.1782	HOMO-1	LUMO+8
				0.0101	-0.0082	-0.1712	0.0549	HOMO-13	LUMO+1
		2.61	0.018	0.5851	-0.0814	0.3408	0.2005	HOMO-15	LUMO
				0.1643	0.0332	0.6915	-0.2219	HOMO-13	LUMO+1
	87	2.64	0.010	0.6834	-0.0541	-0.5656	-0.0474	HOMO-19	LUMO
				0.1514	0.035	-0.2213	-0.0176	HOMO-18	LUMO
				0.0526	-0.0219	0.2313	0.0845	HOMO-20	LUMO
		2.66	0.025	0.5009	-0.1334	-0.636	-0.9173	HOMO-15	LUMO+1
		2.67	0.023	0.3233	0.0047	0.1532	0.2508	HOMO-17	LUMO+1
				0.2583	0.0967	-0.3068	-0.1645	HOMO-2	LUMO+6
				0.116	0.064	0.3052	0.4403	HOMO-15	LUMO+1
		2.69	0.018	0.4194	-0.1228	0.3898	0.2091	HOMO-2	LUMO+6
				0.2475	-0.254	-0.2733	-0.0396	HOMO-2	LUMO+7
		2.70	0.024	0.4432	-0.0234	0.0677	-0.232	HOMO-2	LUMO+8
				0.1764	-0.2139	-0.2301	-0.0333	HOMO-2	LUMO+7
				0.0503	0.0424	-0.1347	-0.0722	HOMO-2	LUMO+6
		2.70	0.016	0.0975	0.8002	0.0085	-0.0133	HOMO-6	LUMO+2
		2.70	0.012	0.3964	0.0222	-0.0641	0.2196	HOMO-2	LUMO+8
				0.3421	-0.2981	-0.3207	-0.0464	HOMO-2	LUMO+7
				0.0902	0.0569	-0.1804	-0.0968	HOMO-2	LUMO+6
		2.71	0.074	0.0975	0.8002	0.0085	-0.0133	HOMO-6	LUMO+2
		2.72	0.012	0.2784	0.0825	-0.1816	0.1138	HOMO-1	LUMO+11

				0.2761	0.1428	0.2408	0.1233	HOMO-1	LUMO+12
7	2.81	2.81	0.017	0.3484	-0.0604	-0.2882	-0.1058	HOMO-25	LUMO+1
				0.3202	0.0409	-0.0488	-0.0695	HOMO-28	LUMO
				0.0929	0.0165	-0.0478	-0.0461	HOMO-26	LUMO+1
				0.0842	0.2555	-0.1495	-0.0055	HOMO	LUMO+44
		2.81	0.064	0.3804	0.7467	0.515	-0.1447	HOMO-2	LUMO+12
				0.2607	0.4493	-0.2629	-0.0097	HOMO	LUMO+44
		2.85	0.019	0.5951	-0.5996	0.05	0.0106	HOMO	LUMO+46
				0.1283	0.1519	0.1067	0.0401	HOMO-3	LUMO+12
		2.85	0.016	0.4285	-0.2775	-0.1949	-0.0733	HOMO-3	LUMO+12
				0.1562	0.0946	0.1289	0.1059	HOMO-3	LUMO+11
				0.1383	-0.2889	0.0241	0.0051	HOMO	LUMO+46
		2.87	0.014	0.2517	0.171	-0.0203	0.1059	HOMO-10	LUMO+2
		2.90	0.017	0.8463	-0.3712	-0.1365	0.0422	HOMO-13	LUMO+2
				0.0157	-0.0214	-0.0313	0.0147	HOMO	LUMO+48
		2.98	0.014	0.3289	-0.0108	0.356	-0.0817	HOMO-2	LUMO+22
				0.2457	0.0297	0.1165	-0.076	HOMO-4	LUMO+16
				0.0998	0.0192	0.2452	0.0324	HOMO-2	LUMO+21
		3.00	0.012	0.2765	-0.092	0.107	0.0033	HOMO-19	LUMO+2
				0.1066	-0.0134	-0.1412	0.0067	HOMO-1	LUMO+30

*The excited states with oscillator strength *f* stronger than 0.010 are considered (f ~ 0.010 is the average value of the oscillator strengths of all excited states in the region below 3.0 μm^{-1}).

Table C–7. MCD spectral data for the complex $Au_9(PPh_3)_8^{3+}$ (3): peak energies (μm^{-1}), value of *B*–term (B), dipole momentum (D) and transitions responsible for MCD peaks. Golden core symmetry D_{2h}.

Peak	Peak Max/Min (μm^{-1})	Excitation state (μm^{-1})	State	B	D	Contributions to transition dipole moment				Transitions	
						Weight	x	y	z	Occ.	Unocc.
1	1.33	1.33	2A	-24.80	0.298	2.2063	0.0477	-0.0115	HOMO	LUMO	2.2063
2	1.78	1.78	4A	64.31	0.617	0.1141	-0.0642	-3.2411	HOMO	LUMO+2	0.1141
						-0.0026	0.001	0.7516	HOMO-2	LUMO	-0.0026
3	2.00	1.99	12A	-40.25	0.329	0.3148	-0.0046	0.0018	1.3241	HOMO-2	LUMO
						0.0339	-0.0225	0.0126	0.6383	HOMO	LUMO+2
4	2.10	2.10	16A	-38.45	0.054	0.74	-0.2052	0.1567	0.4147	HOMO	LUMO+7
						0.1875	-0.8209	0.0061	-0.145	HOMO	LUMO+8
5	2.27	2.26	27A	-17.55	0.016	0.6387	0.7958	0.175	-0.0251	HOMO	LUMO+14
						0.3291	-0.3021	0.0313	0.1586	HOMO-3	LUMO+2
		2.27	29A	12.70	0.025	0.0181	0.2008	0.0301	0.0068	HOMO	LUMO+13

						0.0153	0.4005	-0.0155	0.0045	HOMO-2	LUMO+2
						0.8343	-0.1316	0.0324	-0.232	HOMO-4	LUMO+2
		2.31	31A	-38.58	0.333	0.393	-2.0125	0.0779	-0.0228	HOMO-2	LUMO+2
6	2.35	2.32	32A	22.26	0.027	0.7918	-0.22	-0.2504	-0.5944	HOMO	LUMO+17
						0.1125	0.0076	-0.0373	0.7716	HOMO-6	LUMO
		2.34	34A	34.67	0.186	0.2933	0.0123	-0.0599	1.2403	HOMO-6	LUMO
7	2.44	2.40	42A	29.40	0.025	0.8809	-0.7551	-0.1592	0.0644	HOMO	LUMO+23
						0.0346	0.3229	0.0149	-0.0004	HOMO	LUMO+25
		2.43	46A	-27.85	0.023	0.7018	-0.7148	-0.144	-0.2879	HOMO	LUMO+24
						0.2484	0.86	0.0397	-0.0011	HOMO	LUMO+25
		2.44	47A	-13.89	0.069	0.4705	-1.1813	-0.0545	0.0015	HOMO	LUMO+25
						0.2459	0.9827	-0.0948	0.036	HOMO	LUMO+28
		2.44	48A	-25.26	0.097	0.2117	-0.3957	0.1757	0.1565	HOMO	LUMO+27
						0.0336	0.3625	-0.035	0.0133	HOMO	LUMO+28
		2.46	49A	-14.29	0.131	0.6554	-0.6948	0.3086	0.2748	HOMO	LUMO+27
						0.0808	0.5614	-0.0541	0.0205	HOMO	LUMO+28
		2.48	52A	31.60	0.177	0.5585	0.3041	0.128	-0.2039	HOMO	LUMO+29
						0.2248	-0.9307	0.0897	-0.0341	HOMO	LUMO+28
						0.0449	-0.3615	-0.0167	0.0005	HOMO	LUMO+25
8	2.55	2.49	54A	-14.65	0.051	0.0486	0.4321	-0.0417	0.0158	HOMO	LUMO+28
		2.50	56A	-33.66	0.048	0.0903	-0.215	-0.0354	0.0368	HOMO	LUMO+31
						0.0791	0.1141	0.0481	-0.0765	HOMO	LUMO+29
						0.0351	0.367	-0.0354	0.0134	HOMO	LUMO+28
		2.52	60A	74.18	0.298	0.4455	-0.4752	-0.0783	0.0813	HOMO	LUMO+31
						0.1119	-0.652	0.0629	-0.0239	HOMO	LUMO+28
						0.0407	-0.3415	-0.0158	0.0004	HOMO	LUMO+25
						0.0155	0.3308	0.0035	-0.0055	HOMO-6	LUMO+2
						0.0146	-0.3714	0.0144	-0.0042	HOMO-2	LUMO+2
		2.60	76A	11.47	0.013	0.6065	0.2996	0.1059	0.038	HOMO	LUMO+35
						0.2542	0.0623	-0.4645	0.0226	HOMO-16	LUMO
						0.0278	0.0137	0.2849	-0.0914	HOMO-13	LUMO+1
9	2.80	2.70	102A	23.22	0.098	0.4432	-0.0234	0.0677	-0.232	HOMO-2	LUMO+8
	b>20					0.1764	-0.2139	-0.2301	-0.0333	HOMO-2	LUMO+7
						0.0503	0.0424	-0.1347	-0.0722	HOMO-2	LUMO+6
		2.70	104A	39.41	0.016	0.535	-0.2332	-0.0732	0.1949	HOMO-21	LUMO
		2.71	106A	-53.81	0.301	0.3896	-1.5977	-0.0169	0.0266	HOMO-6	LUMO+2
		2.73	114A	-29.01	0.030	0.3624	-0.2636	0.0192	-0.0479	HOMO-2	LUMO+9
		2.76	127A	21.87	0.022	0.4282	0.2072	-0.0233	-0.017	HOMO	LUMO+43
		2.81	147A	-27.99	0.249	0.3804	0.7467	0.515	-0.1447	HOMO-2	LUMO+12
						0.2607	0.4493	-0.2629	-0.0097	HOMO	LUMO+44

		2.93	199A	-28.87	0.006	0.649	0.3464	0.2404	-0.242	HOMO-4	LUMO+14
		2.93	201A	32.81	0.019	0.2167	0.1521	-0.1843	-0.1212	HOMO-2	LUMO+18
		2.96	213A	24.24	0.003	0.4194	0.1185	-0.037	0.182	HOMO-37	LUMO+1
						0.2988	0.1369	-0.1479	-0.1999	HOMO-39	LUMO
		3.00	236A	-24.55	0.043	0.2765	-0.092	0.107	0.0033	HOMO-19	LUMO+2
						0.1066	-0.0134	-0.1412	0.0067	HOMO-1	LUMO+30

*Each MCD peak was considered independently.

Appendix D - Supporting Information for "Optical Properties of Small Gold Clusters $Au_8L_8^{2+}$ (L = PH_3, PPh_3): Magnetic Circular Dichroism Spectra"

Figure D–1. Metal atom numbers for gold core Au_8^{2+}.

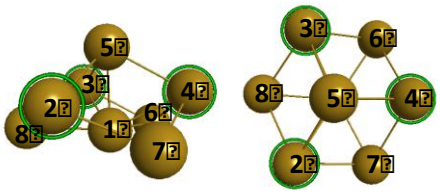

Table D–1. Geometry of gold core Au_8^{2+} in the crystal structure $Au_8(PPh_3)_8^{2+}$ and in the simulated $Au_8(PH_3)_8^{2+}$.

	Experiment[25]	Theory BP86/TZP.fc			
Atom #	$Au_8(PPh_3)_8^{2+}$	Bare Au_8^{2+}	$Au_8(PH_3)_8^{2+}$		
Structure #	1 "chair"		2a "half–chair"	2b "chair"	2d "half–chair"
Bond distance to central Au(1):					
1–2	2.795	2.869	2.750	2.768	2.783
1–3	2.735	2.869	2.755	2.768	2.784
1–4	2.731	2.869	2.757	2.768	2.755
1–5	2.583	2.710	2.680	2.637	2.664
1–6	2.683	2.813	2.752	2.760	2.806
1–7	2.678	2.813	2.752	2.760	2.808
1–8	2.730	2.813	2.794	2.760	2.752
Bond distance between equatorial Au atoms:					
2–3	4.430	4.297	4.787	4.447	3.525
3–4	4.174	4.297	4.035	4.409	4.725
4–2	4.394	4.297	4.253	4.395	4.735
6–7	4.650	4.748	4.396	4.762	4.909
7–8	4.692	4.748	4.983	4.785	4.734
8–6	4.667	4.748	4.934	4.791	4.717
Torsion angle:					
3–2–7–4	30.5°	24.4°	35.6°	32.4°	2.3°
6–7–2–8	30.2°	30.8°	13.0°	36.3°	53.7°
Bond distance Au–P:					
5–P	2.260	–	2.310	2.301	2.308
1–P	2.382	–	2.680	2.406	2.385

Figure D–2. Optical absorption and MCD spectra of $Au_8(PH_3)_8^{2+}$ (2b) using method GRAC/DZ.fc and GRAC/TZP.fc

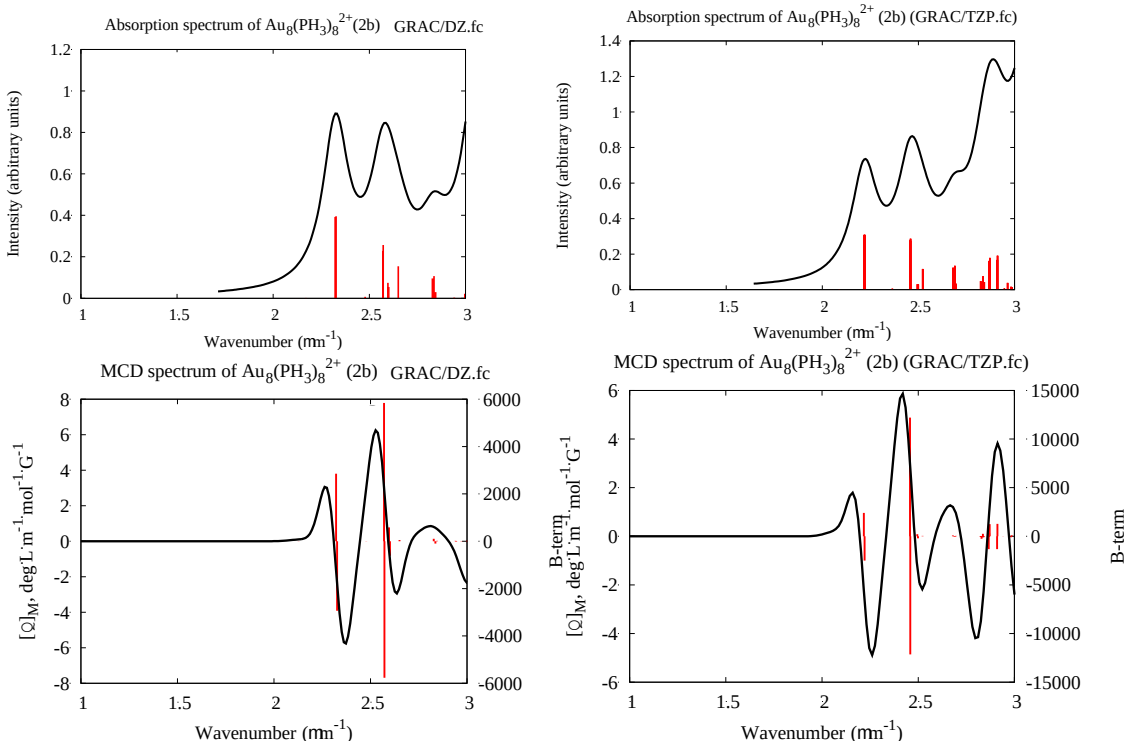

Figure D–3. Theoretical absorption spectra for $Au_8(PPh_3)_8^{2+}$ (1) using the LB94/DZ.fc level of theory in the gas phase.

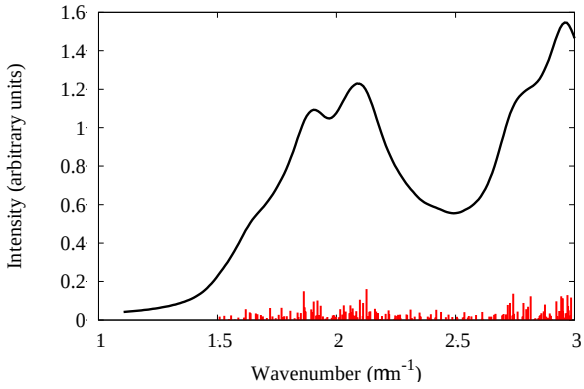

The optical absorption spectrum for the $Au_8(PPh_3)_8^{2+}$ (**1**) cluster was calculated by employing the asymptotically correct LB94 potential, which has previously been successfully used for investigation of spectroscopic properties of ligand–protected gold nanoparticles.[170, 193, 194] Comparison of the obtained theoretical results (**Figure S3**) with the experimental absorption

spectrum (**Figure 1a**)[26] for $[Au_8(PPh_3)_8](NO_3)_2$ shows a dramatic difference in the shape of the spectral lines. The intensity of the empirical absorption signal continuously increases with increasing energy, whereas the theoretical spectrum with LB94 has a significant minimum at 2.5 μm^{-1}. Analysis of the theoretical results showed that there are no significantly strong transitions in the region from 2.3-2.7 μm^{-1} (**Figure D–3**). This could be related to the use of the LB94 model potential, which can affect the response properties. Therefore, one of the important steps of this project is determination of a model potential/functional for calculation of optical properties that will give reasonable results and not be very time-consuming. To make a decision about the potential that will be best for the systems of interest, we have additionally tested SAOP, GRAC, B3LYP and CAMY–B3LYP functionals.

Because $Au_8(PPh_3)_8^{2+}$ (1) is a very large cluster, calculation of the absorption spectrum requires significant computational time. Thus, for initial testing of the quality of DFT functionals and model potentials, we choose the simple phosphine-stabilized gold cluster $Au_8(PH_3)_8^{2+}$ (**3**) with the gold core Au_8^{2+} structure from crystal data (**Figure 6–1**). The optical absorption spectra were calculated using LB94, SAOP, GRAC, B3LYP, and CAMY–B3LYP functionals. Also, solvent effects on the optical absorption spectra were included using the COSMO model with acetonitrile solvent. In the case of GRAC potentials, the IP (ionization potential) must be specified in the input file. For the $Au_8(PH_3)_8^{2+}$ (**3**) cluster, the first IP = 0.40 a.u. was calculated as the difference in the energy of $Au_8(PH_3)_8^{2+}$ and $Au_8(PH_3)_8^{3+}$ cations using the BP86/TZP.fc level of theory.

All obtained absorption spectra for the $Au_8(PH_3)_8^{2+}$ (**3**) structure with the considered functionals are blueshifted with respect to the experimental data obtained for $[Au_8(PPh_3)_8](NO_3)_2$ in acetonitrile at room temperature (**Figure D4**, **Table D–2**).[26] The smallest deviation was found for spectra that were calculated using the LB94 and GRAC methods. The most significant spectral shift was obtained for the functionals B3LYP and CAMY–B3LYP: in these cases, the first absorption peak position is blueshifted by 0.32 and 0.48 μm^{-1} with respect to the empirical data. The absorption spectra of the $Au_8(PH_3)_8^{2+}$ (**3**) cluster obtained from calculations with LB94, SAOP, B3LYP and CAMY–B3LYP exhibit the same dip that was observed in the optical absorption spectrum for the $Au_8(PPh_3)_8^{2+}$ (**1**) cluster with the LB94 method (**Figures D–1** and **D–3**). The dip occurs in the range of 3.05 – 3.44 μm^{-1} for B3LYP;

3.25 – 3.69 μm^{-1} for CAMY–B3LYP; 2.56 – 2.61 μm^{-1} for LB94; and 2.65 – 3.00 μm^{-1} for SAOP (i.e., no excitations were detected in these portions of the spectra).

Figure D–4. Theoretical absorption spectra for $Au_8(PH_3)_8^{2+}$ (3) cluster obtained with LB94, LB94 (COSMO), SAOP, GRAC, B3LYP and CAMY–B3LYP functionals.

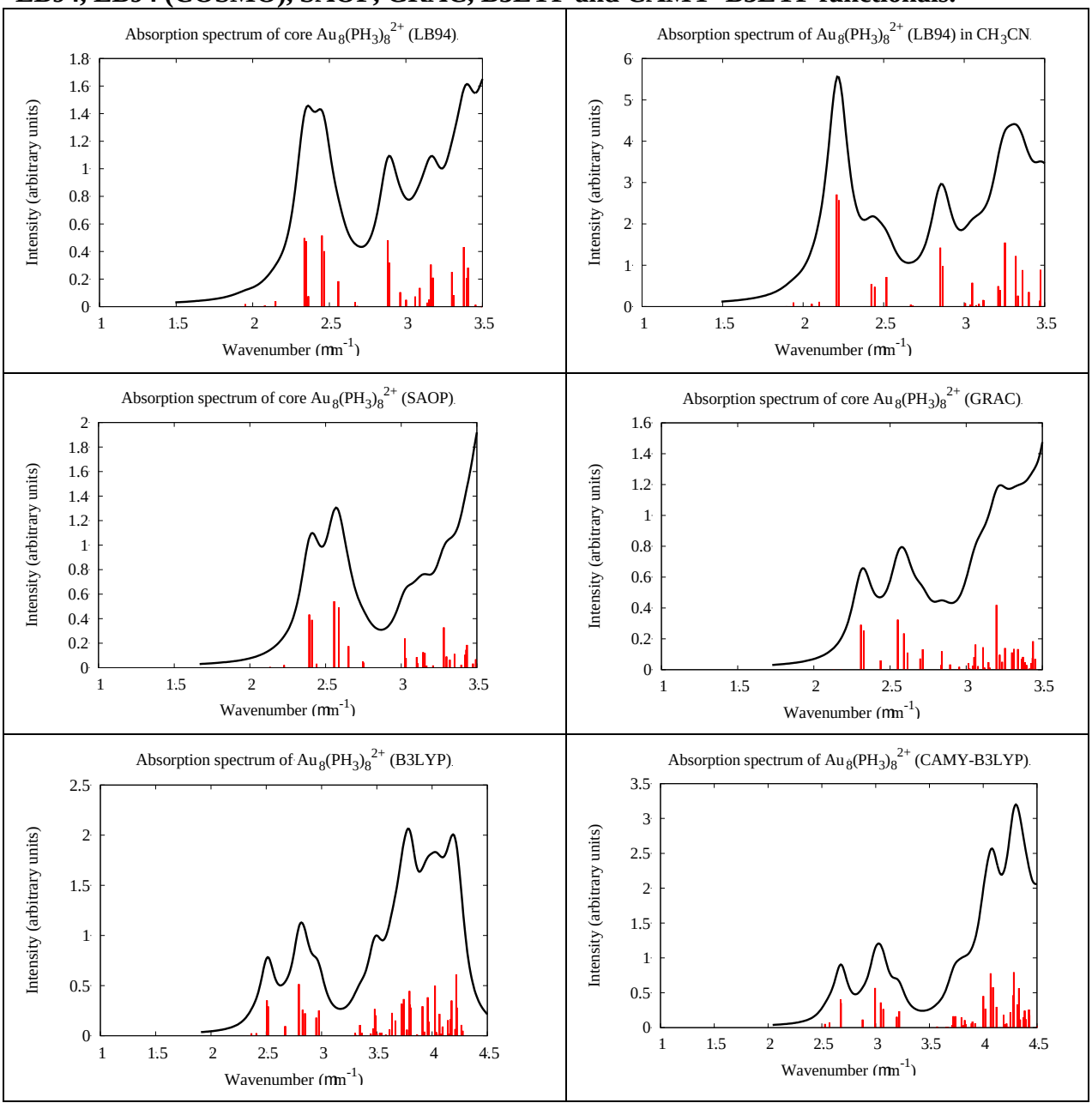

Table D–2. First peak position (μm^{-1}) of the experimental absorption spectrum[26] for $[Au_8(PPh_3)_8](NO_3)_2$ in acetonitrile and of the theoretical absorption spectra for $Au_8(PH_3)_8^{2+}$ (2b) structure using the LB94, SAOP, GRAC, CAMY-B3LYP and B3LYP functionals.

First peak position	Experiment[26]	LB94	LB94 (solvent)	SAOP	GRAC	CAMY–B3LYP	B3LYP
wavenumber (μm^{-1})	2.19	2.33	2.21	2.40	2.31	2.67	2.51

The absorption spectrum was also calculated using the LB94 functional with inclusion of solvent effects (**Figure D–4**). The spectrum calculated in CH_3CN redshifts with respect to the spectrum in gas phase. For example, the difference in the first peak position is 0.12 μm^{-1}. However, the overall shape of the spectra calculated in the gas and liquid phases are similar, including the dip. Solvent does not affect the presence of the dip.

The theoretical spectrum of $Au_8(PH_3)_8^{2+}$ (**3**) simulated with the GRAC approach does not exhibit a significant minimum (**Figure D–4**). Excitations that are responsible for the absence of the minimum in this absorption spectrum occur at 2.83 and 2.90 μm^{-1} and arise from electronic transitions from the HOMO–2 to the first three LUMO orbitals (LUMO, LUMO+1, and LUMO+2). Therefore, the GRAC/DZ.fc method gives us a reasonable agreement with experiment for the absorption spectrum and we will use it to calculate MCD spectra and investigate the optical properties for the system of interest.

Additionally, it should be notice that band assignments do not significantly dependent on the type of functional used in calculations.

Table D–3. Absorption spectrum data for the complex $Au_8(PPh_3)_8^{2+}$ (1): peak energies (μm^{-1}), oscillator strength (*f*) and transitions responsible for these peaks. Gold core symmetry is C_{3v}.

					Contributions to transition dipole moment			Transition	
no.	state #	Excitation state (μm^{-1})	*f*	Weight	x	y	z	from	to
I	3	1.89	0.03409	0.5512	1.5042	-0.1395	-0.0256	HOMO–1	LUMO
				0.2369	0.9713	-0.05	-0.1706	HOMO	LUMO+1
	4	1.91	0.04123	0.7432	0.0633	-1.9576	0.1031	HOMO–1	LUMO+1
II	5	1.99	0.02162	0.8883	1.0369	0.3772	-0.064	HOMO	LUMO+2
	6	2.04	0.03552	0.8032	0.3023	-1.3983	0.3628	HOMO–1	LUMO+2
III	10	2.11	0.01118	0.7288	-0.6731	-0.3936	-0.6747	HOMO	LUMO+5
	14	2.16	0.02131	0.4065	0.6043	0.242	0.0416	HOMO	LUMO+6

	17	2.20	0.02169	0.4244	-0.4028	0.0563	0.4262	HOMO–1	LUMO+7
				0.347	-0.0678	-0.509	0.5002	HOMO–1	LUMO+6
	18	2.22	0.01807	0.8275	0.7173	0.7554	0.327	HOMO	LUMO+9
	20	2.24	0.01819	0.6579	0.5955	-0.7819	-0.1803	HOMO	LUMO+10
	23	2.27	0.01262	0.7553	-0.1773	0.6373	0.2043	HOMO	LUMO+12
IV	25	2.29	0.01197	0.7234	0.0423	-0.4398	0.0837	HOMO–1	LUMO+11
	28	2.32	0.01287	0.3773	-0.1372	0.137	0.4605	HOMO	LUMO+14
				0.2333	-0.4645	-0.1667	0.126	HOMO–1	LUMO+12
	31	2.35	0.04936	0.484	0.2363	0.0742	-0.3701	HOMO–1	LUMO+13
				0.2097	0.378	0.0929	-0.1547	HOMO	LUMO+16
	35	2.41	0.02227	0.8005	-0.1786	0.9572	-0.5989	HOMO–1	LUMO+16
	38	2.44	0.0141	0.4073	-0.438	0.3653	0.051	HOMO	LUMO+18
	40	2.45	0.02004	0.7365	-0.6117	0.1541	-0.2341	HOMO	LUMO+19
V	41	2.47	0.0244	0.8129	-0.0191	1.1613	-0.1431	HOMO–2	LUMO+1
	48	2.53	0.01112	0.6747	0.3734	-0.9143	-0.0411	HOMO–1	LUMO+21
	52	2.55	0.06238	0.3179	-0.7041	0.2508	0.1197	HOMO–3	LUMO
	55	2.56	0.02757	0.3787	-0.3992	-0.8562	0.1155	HOMO–3	LUMO+1
	59	2.61	0.01468	0.8227	-0.0004	0.7858	-0.3834	HOMO–1	LUMO+26
	62	2.63	0.01457	0.5628	0.1299	-0.4446	0.3211	HOMO–2	LUMO+2
	63	2.63	0.01939	0.5516	0.0056	-0.3602	-0.2022	HOMO	LUMO+29
	64	2.64	0.01169	0.5529	-0.2798	-0.4369	-0.2324	HOMO	LUMO+30
	65	2.64	0.01447	0.6341	-0.4317	-0.1501	-0.2302	HOMO	LUMO+31
	75	2.71	0.02343	0.4301	-0.4037	-0.5138	0.1839	HOMO–2	LUMO+4
	81	2.74	0.01391	0.4627	0.1962	-0.3973	0.1766	HOMO–1	LUMO+33
	83	2.75	0.01896	0.3245	0.272	0.5465	0.0784	HOMO–2	LUMO+5
	84	2.75	0.02816	0.2622	-0.2443	-0.4909	-0.0704	HOMO–2	LUMO+5
	85	2.76	0.01176	0.1954	0.022	-0.2104	-0.1534	HOMO–1	LUMO+35
VI	88	2.77	0.01228	0.3317	-0.0287	0.2737	0.1995	HOMO–1	LUMO+35
	89	2.78	0.01401	0.418	0.2829	0.2074	0.0526	HOMO	LUMO+38
	90	2.79	0.01374	0.5924	0.3893	-0.8677	-0.0257	HOMO–2	LUMO+6
	92	2.79	0.02157	0.2206	-0.2372	0.5287	0.0157	HOMO–2	LUMO+6
	93	2.80	0.01326	0.7639	0.1701	0.2246	0.2034	HOMO–3	LUMO+3
	99	2.82	0.01179	0.8861	-0.0898	-0.3189	0.5346	HOMO–2	LUMO+8
	109	2.87	0.01101	0.3625	-0.1585	0.5131	0.0055	HOMO–2	LUMO+10
				0.352	0.7201	-0.0231	-0.1335	HOMO–6	LUMO
VII	112	2.88	0.01247	0.1712	0.5011	-0.0161	-0.0929	HOMO–6	LUMO
	115	2.89	0.02029	0.3596	0.351	0.2611	-0.0965	HOMO–2	LUMO+11

	116	2.89	0.01218	0.5493	-0.2196	0.1497	-0.2213	HOMO–3	LUMO+7
	118	2.90	0.01341	0.0822	-0.0692	-0.3851	0.0455	HOMO–6	LUMO+1
	119	2.90	0.02525	0.6904	0.4404	-0.3102	0.1264	HOMO–2	LUMO+12
	120	2.91	0.02556	0.1632	-0.0973	-0.542	0.064	HOMO–6	LUMO+1
	124	2.94	0.02052	0.8945	0.2484	-0.4297	-0.3339	HOMO–2	LUMO+13
	133	2.97	0.01713	0.2383	0.4226	-0.0447	-0.0338	HOMO–5	LUMO+3
	134	2.98	0.01509	0.563	0.6491	-0.0687	-0.0519	HOMO–5	LUMO+3
	137	2.99	0.02395	0.4911	-0.0354	-0.3734	0.2301	HOMO–2	LUMO+16

*****transitions with f >0.01

Table D–4. MCD spectral data for the complex $Au_8(PPh_3)_8^{2+}$ (1): peak energies (μm^{-1}), value of B–term, dipole momentum (D) and transitions responsible for MCD peaks. Gold core symmetry is C_{3v}.

						Contributions to transition dipole moment			Transition	
no.	state #	Excitation state (μm^{-1})	$B_{(direct)}$	D	Weight	x	y	z	from	to
I	1	1.83	-13.56	0.034	0.5069	0.2047	-1.4244	0.3175	HOMO	LUMO
					0.245	1.0054	-0.0518	-0.1766	HOMO	LUMO+1
					0.1788	-0.8719	0.0809	0.0149	HOMO–1	LUMO
	2	1.85	57.53	0.042	0.4157	1.3024	-0.0671	-0.2288	HOMO	LUMO+1
					0.3944	-0.1796	1.2498	-0.2786	HOMO	LUMO
	3	1.89	133.98	0.198	0.5512	1.5042	-0.1395	-0.0256	HOMO–1	LUMO
					0.2369	0.9713	-0.05	-0.1706	HOMO	LUMO+1
	4	1.91	-136.04	0.237	0.7432	0.0633	-1.9576	0.103	HOMO–1	LUMO+1
II	5	1.99	-117.36	0.119	0.8883	1.0369	0.3772	-0.064	HOMO	LUMO+2
	7	2.06	46.39	0.038	0.867	-0.406	-0.3113	-0.0892	HOMO	LUMO+3
III	9	2.11	-29.91	0.032	0.68	-0.7386	-0.0104	-0.0903	HOMO–1	LUMO+3
	10	2.11	22.79	0.058	0.7288	-0.6731	-0.3936	-0.6747	HOMO	LUMO+5
	11	2.13	-16.28	0.035	0.8252	-0.0668	-0.5164	0.3725	HOMO–1	LUMO+4
	12	2.15	18.04	0.015	0.4365	0.6281	0.2515	0.0432	HOMO	LUMO+6
	14	2.16	36.87	0.108	0.4065	0.6043	0.242	0.0416	HOMO	LUMO+6
	16	2.20	-26.59	0.035	0.4895	0.4333	-0.0605	-0.4585	HOMO–1	LUMO+7
					0.4348	-0.0761	-0.5707	0.5608	HOMO–1	LUMO+6
	20	2.24	31.39	0.089	0.6579	0.5955	-0.7819	-0.1803	HOMO	LUMO+10
	21	2.25	30.45	0.049	0.797	-0.7727	0.2204	0.2366	HOMO–1	LUMO+9
	22	2.26	-38.83	0.038	0.8883	0.1484	0.4941	-0.2542	HOMO	LUMO+11
	23	2.27	41.76	0.061	0.7553	-0.1773	0.6373	0.2043	HOMO	LUMO+12
IV										
	26	2.30	50.21	0.022	0.7979	0.324	-0.2976	-0.3725	HOMO	LUMO+13

	31	2.35	-77.05	0.230	0.484	0.2363	0.0742	-0.3701	HOMO–1	LUMO+13
	33	2.38	41.46	0.024	0.849	0.6757	0.1225	0.1839	HOMO–1	LUMO+15
	35	2.41	28.00	0.102	0.8005	-0.1786	0.9572	-0.5989	HOMO–1	LUMO+16
	39	2.45	64.39	0.013	0.963	-0.1979	-0.2208	0.1585	HOMO	LUMO+20
	40	2.45	-56.35	0.090	0.7365	-0.6117	0.1541	-0.2341	HOMO	LUMO+19
V										
	52	2.55	52.79	0.269	0.3179	-0.7041	0.2508	0.1197	HOMO–3	LUMO
	55	2.56	-46.46	0.118	0.3787	-0.3992	-0.8562	0.1155	HOMO–3	LUMO+1
	62	2.63	-52.32	0.061	0.5628	0.1299	-0.4446	0.3211	HOMO–2	LUMO+2
	63	2.63	82.06	0.081	0.5516	0.0056	-0.3602	-0.2022	HOMO	LUMO+29
	69	2.68	38.91	0.027	0.7996	-0.112	0.2986	0.2797	HOMO–1	LUMO+30
VI										
	90	2.79	-38.44	0.054	0.5924	0.3893	-0.8677	-0.0257	HOMO–2	LUMO+6
	92	2.79	52.83	0.085	0.2206	-0.2372	0.5287	0.0157	HOMO–2	LUMO+6
	115	2.89	45.87	0.077	0.3596	0.351	0.2611	-0.0965	HOMO–2	LUMO+11
VII	119	2.90	91.55	0.095	0.6904	0.4404	-0.3102	0.1264	HOMO–2	LUMO+12
	120	2.91	-121.41	0.096	0.1632	-0.0973	-0.542	0.064	HOMO–6	LUMO+1
	124	2.94	-52.86	0.077	0.8945	0.2484	-0.4297	-0.3339	HOMO–2	LUMO+13
	133	2.97	57.96	0.063	0.2383	0.4226	-0.0447	-0.0338	HOMO–5	LUMO+3
	137	2.99	37.30	0.088	0.4911	-0.0354	-0.3734	0.2301	HOMO–2	LUMO+16

*for bands I–III excited states with B>10, for another IV–VI

Figure D–5. Structure of $Au_8(PH_3)_8^{2+}$ isomers and the energy difference between them including ZPE (BP86/TZP.fc).

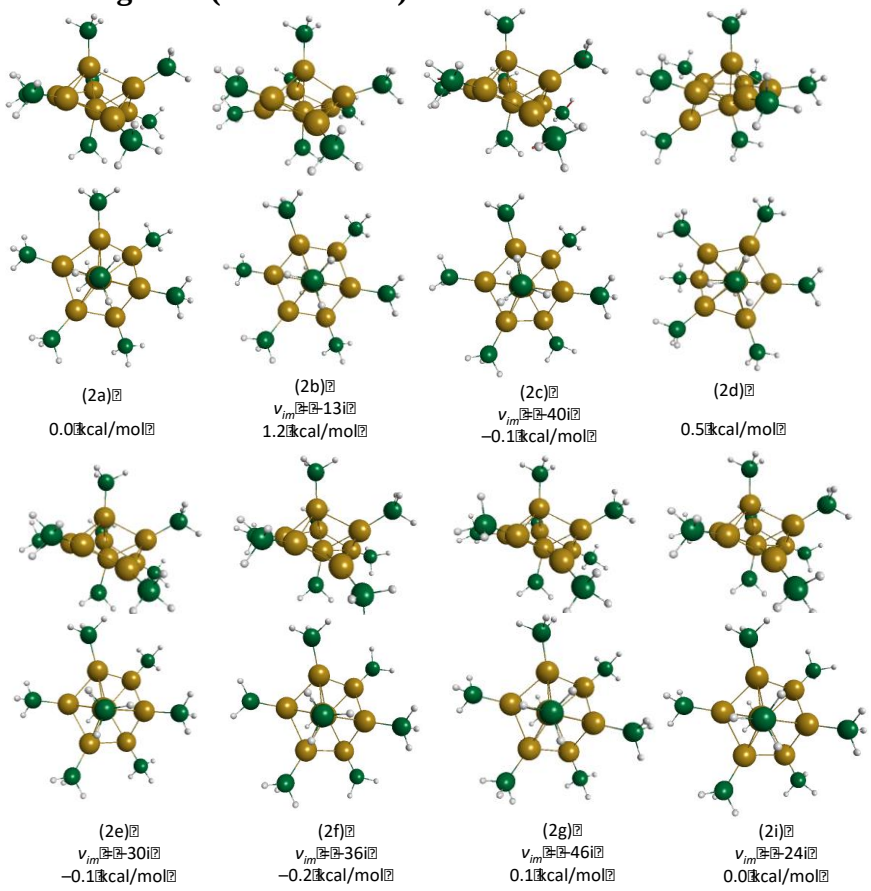

(*) – structures with negative values in Hess matrix (imaginary frequency).

Figure D–6. A) Empirical MCD spectrum of $Au_8(PPh_3)_8(NO_3)_2$ complex in acetonitrile;[26] and B) theoretical MCD spectrum of $Au_8(PPh_3)_8^{2+}$ (1).

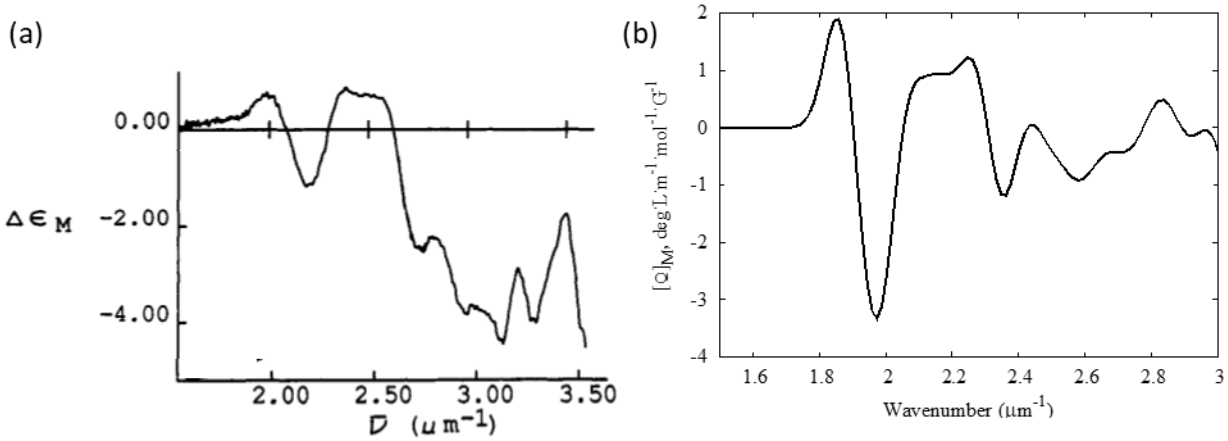

Table D5. Absorption spectrum data for the complex $Au_8(PH_3)_8^{2+}$ (2b): peak energies (μm^{-1}), oscillator strength (*f*) and transitions responsible for these peaks. Gold core symmetry is C_{3v}.

					Contributions to transition dipole moment			Transition	
no.	state #	Excitation state (μm^{-1})	*f*	Weight	x	y	z	from	to
I	5	2.32	0.1231	0.4128	1.4287	-1.2749	0.0077	HOMO–1	LUMO
				0.1189	-0.0937	-1.0618	0.0189	HOMO	LUMO+2
	6	2.33	0.1233	0.3514	1.2467	1.0724	-0.0071	HOMO–1	LUMO+1
				0.3367	0.1575	1.7851	-0.0318	HOMO	LUMO+2
II	8	2.57	0.0707	0.3975	0.5298	-0.5099	-0.3592	HOMO–1	LUMO+4
				0.2813	0.4014	-0.3889	0.2866	HOMO	LUMO+3
	9	2.57	0.0807	0.5011	0.515	0.4957	-1.1694	HOMO–1	LUMO+3
				0.292	0.4404	0.4421	0.9117	HOMO	LUMO+4
	10	2.60	0.0228	0.1148	0.2833	-0.2727	-0.1921	HOMO–1	LUMO+4
	11	2.60	0.0171	0.7479	-0.1781	-0.3122	0.3076	HOMO–1	LUMO+5
	12	2.65	0.0484	0.418	0.5192	0.5212	1.0748	HOMO	LUMO+4
				0.3095	-0.3988	-0.3839	0.9055	HOMO–1	LUMO+3
III	13	2.83	0.0305	0.7236	-0.3882	-1.0805	0.0789	HOMO–2	LUMO
	14	2.84	0.0341	0.6636	0.9289	-0.7413	-0.0632	HOMO–2	LUMO+1
	15	2.84	0.0093	0.6253	0.8655	0.2178	0.0878	HOMO–2	LUMO+2

Table D–6. MCD spectral data for the complex $Au_8(PH_3)_8^{2+}$ (2b): peak energies (μm^{-1}), value of B–term, dipole momentum (*D*) and transitions responsible for MCD peaks. Gold core symmetry is C_{3v}.

						Contributions to transition dipole moment			Transition	
no.	state #	Excitation state (μm^{-1})	$B_{(direct)}$	*D*	Weight	x	y	z	from	to
I	5A	2.32	2858.10	0.582	0.4128	1.4287	-1.2749	0.0077	HOMO–1	LUMO
					0.1189	-0.0937	-1.0618	0.0189	HOMO	LUMO+2
	6A	2.33	-2935.90	0.582	0.3514	1.2467	1.0724	-0.0071	HOMO–1	LUMO+1
					0.3367	0.1575	1.7851	-0.0318	HOMO	LUMO+2
II	8A	2.57	5844.10	0.302	0.3975	0.5298	-0.5099	-0.3592	HOMO–1	LUMO+4
					0.2813	0.4014	-0.3889	0.2866	HOMO	LUMO+3
	9A	2.57	-5766.40	0.344	0.5011	0.515	0.4957	-1.1694	HOMO–1	LUMO+3
					0.292	0.4404	0.4421	0.9117	HOMO	LUMO+4
	10A	2.60	585.78	0.096	0.1148	0.2833	-0.2727	-0.1921	HOMO–1	LUMO+4
	11A	2.60	-610.68	0.072	0.7479	-0.1781	-0.3122	0.3076	HOMO–1	LUMO+5

	12A	2.65	53.24	0.200	0.418	0.5192	0.5212	1.0748	HOMO	LUMO+4
					0.3095	-0.3988	-0.3839	0.9055	HOMO–1	LUMO+3
III	13A	2.83	102.9	0.118	0.7236	-0.3882	-1.0805	0.0789	HOMO–2	LUMO
	14A	2.84	-95.279	0.132	0.6636	0.9289	-0.7413	-0.0632	HOMO–2	LUMO+1
	15A	2.84	18.12	0.036	0.6253	0.8655	0.2178	0.0878	HOMO–2	LUMO+2

Table D–7. Absorption spectrum data for the bare Au_8^{2+}: peak energies (μm^{-1}), oscillator strength (*f*) and transitions responsible for these peaks. Gold core symmetry is C_{3v}.

					Contributions to transition dipole moment			Transition	
no.	state #	Excitation state (μm^{-1})	*f*	Weight	x	y	z	from	to
I	5A1	1.77	0.001875	0.9692	0	0	0.6596	HOMO	LUMO+1
	6E	1.83	0.005579	0.1695	1.6235	0	0	HOMO	LUMO+1
II	11E	1.98	0.008996	0.2796	-1.5513	0	0	HOMO	LUMO+2
III	19E	2.21	0.004241	0.0148	0.337	0	0	HOMO	LUMO+2
	26E	2.31	0.01945	0.124	6 -0.9590	0	0	HOMO	LUMO+2
	29E	2.36	0.005035	0.019	-0.3702	0	0	HOMO	LUMO+2
IV	39E	2.64	0.006355	0.3401	-0.5774	0	0	HOMO–6	LUMO+1
	49E	2.72	0.01958	0.2679	0.2698	0	0	HOMO–3	LUMO+2
				0.0878	-0.2887	0	0	HOMO–6	LUMO+1
				0.0813	-0.2634	0	0	HOMO–7	LUMO+1
				0.0115	-0.2683	0	0	HOMO	LUMO+2
				0.0114	-0.3453	0	0	HOMO	LUMO+1
	51A1	2.73	0.01054	0.767	0	0	0.5424	HOMO–8	LUMO+1
	56E	2.80	0.005257	0.8155	0.2678	0	0	HOMO–11	LUMO+1
	61E	2.83	0.02804	0.0277	-0.5273	0	0	HOMO	LUMO+1
				0.0153	-0.3029	0	0	HOMO	LUMO+2

Table D–8. MCD spectral data for the complex Au_8^{2+}: peak energies (μm^{-1}), value of *A*– and *B*–terms, dipole momentum (*D*) and transitions responsible for MCD peaks. Gold core symmetry is C_{3v}.

							Contributions to transition dipole moment			Transition	
no.	state #	Excitation state (μm^{-1})	A	B	*D*	Weight	x	y	z	from	to
I	3E	1.83	0.0132	-12.33	0.0670	0.1695	1.6235	0	0	HOMO	LUMO+1
	4E	1.92	0.0001	-0.86	0.0305	0.1279	-1.3758	0	0	HOMO	LUMO+1
II	5E	1.98	0.0675	26.86	0.0999	0.3386	2.2065	0	0	HOMO	LUMO+1
						0.2796	-1.5513	0	0	HOMO	LUMO+2

	7E	2.08	0.0032	5.93	0.0052	0.0789	-0.8023	0	0	HOMO	LUMO+2
	8E	2.21	0.0344	1.30	0.0421	0.0148	0.337	0	0	HOMO	LUMO+2
III	9E	2.25	-0.0499	-59.54	0.0317	0.0359	-0.5205	0	0	HOMO	LUMO+2
	11E	2.31	-0.0166	-65.68	0.1852	0.1246	-0.959	0	0	HOMO	LUMO+2
	13E	2.41	0.4947	-232.25	0.8394	0.2715	-1.3847	0	0	HOMO	LUMO+2
						0.1283	-1.2305	0	0	HOMO	LUMO+1
	14E	2.49	0.0459	-37.00	0.0264	0.0123	-0.2891	0	0	HOMO	LUMO+2
Iva	8A1	2.55	0.0000	-14.13	0.0610						
	15E	2.60	-0.0051	64.63	0.0286	0.1936	0.4389	0	0	HOMO–6	LUMO+1
	16E	2.64	-0.0319	34.96	0.0529	0.3401	-0.5774	0	0	HOMO–6	LUMO+1
	17E	2.64	0.0075	-40.75	0.0060	0.6252	-0.7415	0	0	HOMO–7	LUMO+1
Ivb	20E	2.72	-0.0385	-146.03	0.1578	0.2679	0.2698	0	0	HOMO–3	LUMO+2
						0.0878	-0.2887	0	0	HOMO–6	LUMO+1
						0.0813	-0.2634	0	0	HOMO–7	LUMO+1
						0.0115	-0.2683	0	0	HOMO	LUMO+2
	21E	2.75	-0.0396	60.24	0.0241	0.5332	-0.1516	0	0	HOMO–9	LUMO+1
	22E	2.76	-0.1075	-152.36	0.1051	0.1009	-0.1204	0	0	HOMO–1	LUMO+2
	23E	2.80	-0.0646	-176.20	0.0413	0.8155	0.2678	0	0	HOMO–11	LUMO+1
	24E	2.80	0.1937	615.52	0.2709	0.1975	-0.2284	0	0	HOMO–3	LUMO+2
	25E	2.83	0.2556	-356.55	0.2172	0.2621	-0.2617	0	0	HOMO–3	LUMO+2
						0.0277	-0.5273	0	0	HOMO	LUMO+1

Coordinates

Structure $Au_8(PPh_3)_8^{2+}$ (1)

Au	16.411314	7.847831	20.834447
Au	14.621029	6.511841	22.643830
Au	16.696230	10.566449	21.709449
Au	14.085369	9.034884	19.607491
Au	14.186289	11.637184	20.831724
Au	14.437290	9.191552	22.161268
Au	12.281508	7.680946	21.418334
Au	12.041771	10.383971	22.273879
P	14.592102	9.527763	24.513856
P	14.127525	13.790980	19.920702
P	18.666871	11.709194	21.945508
P	13.861935	8.898670	17.362461
P	14.802736	4.450548	23.686190
P	10.504688	6.402879	20.661615
P	18.071517	6.613900	19.780605
P	10.068717	11.370650	22.886880
C	10.931708	4.604576	20.492319
C	10.083625	3.619978	20.702886
H	9.223260	3.806139	21.059445

C	10.433336	2.338804	20.416515
H	9.782464	1.648156	20.455821
C	11.793299	2.027663	20.054341
H	12.062951	1.123926	19.942039
C	12.659927	2.999654	19.874658
H	13.561473	2.817027	19.633208
C	12.210968	4.310934	20.048726
H	12.805189	5.026889	19.857813
C	9.045484	6.226831	21.736065
C	7.711866	6.247132	21.197015
H	7.565566	6.480970	20.287368
C	6.649934	5.921578	22.008397
H	5.771472	5.905015	21.646223
C	6.844329	5.615784	23.347599
H	6.109686	5.341904	23.886649
C	8.132823	5.711008	23.906302
H	8.278971	5.572720	24.832794
C	9.187237	6.017159	23.044384
H	10.061478	6.079979	23.414980
C	9.823471	6.960719	19.085736
C	9.322834	6.040408	18.119938
H	9.440950	5.106481	18.246278
C	8.675980	6.507335	17.019378
H	8.331144	5.892317	16.382064
C	8.517323	7.834521	16.820042
H	8.081364	8.152023	16.039542
C	9.001860	8.743734	17.780224
H	8.869518	9.676143	17.653885
C	9.653140	8.302152	18.875169
H	9.995182	8.925578	19.504061
C	8.831512	11.264044	21.542343
C	9.120344	11.863976	20.307021
H	9.976888	12.250326	20.169451
C	8.210395	11.905768	19.315955
H	8.412121	12.370203	18.512995
C	7.026889	11.300293	19.447910
H	6.393206	11.332347	18.740407
C	6.732973	10.641001	20.590583
H	5.900648	10.188055	20.657965
C	7.628659	10.602744	21.696759
H	7.410698	10.145901	22.499719
C	9.000726	9.335423	24.377971
H	9.194652	8.785434	23.628354
C	8.432736	8.777764	25.573988
H	8.274610	7.841128	25.613293
C	8.113665	9.535396	26.646472
H	7.723344	9.147576	27.421357
C	8.378317	10.920901	26.581899
H	8.162137	11.467384	27.325900
C	8.946033	11.511047	25.447648
H	9.117859	12.446287	25.427995
C	9.260293	10.711358	24.344280
C	10.176289	13.122710	23.235297
C	9.029474	13.955501	23.170723
H	8.194837	13.592639	22.898391
C	9.126366	15.287262	23.499207

H	8.356904	15.837735	23.417788
C	10.284876	15.838337	23.934377
H	10.310396	16.748073	24.209518
C	11.431661	15.062890	23.976491
H	12.262020	15.445370	24.229170
C	11.348438	13.687441	23.633969
H	12.129335	13.149340	23.681698
C	15.197316	14.052180	18.543878
C	15.235977	13.118877	17.477009
H	14.807878	12.278269	17.575273
C	15.850571	13.400320	16.373641
H	15.797426	12.771617	15.663330
C	16.592139	14.582082	16.160267
H	17.091238	14.705101	15.360115
C	16.579874	15.511494	17.089567
H	17.027226	16.335737	16.940766
C	15.883930	15.287677	18.355772
H	15.888677	15.948962	19.038007
C	12.527853	14.462584	19.276649
C	12.425458	14.924084	17.965523
H	13.142962	14.851037	17.345054
C	11.166200	15.518638	17.611771
H	11.056077	15.848963	16.730200
C	10.127154	15.631812	18.476497
H	9.307887	16.029690	18.204165
C	10.288533	15.161192	19.751126
H	9.589636	15.252347	20.388440
C	11.469528	14.555540	20.099262
H	11.543964	14.183280	20.969603
C	14.557922	15.073257	21.171747
C	14.176647	16.366578	21.003294
H	13.681333	16.597997	20.228409
C	14.480924	17.363383	21.921363
H	14.160528	18.251879	21.814676
C	15.284029	16.997722	23.016308
H	15.574506	17.662493	23.631162
C	15.637891	15.740732	23.201606
H	16.088126	15.491447	23.998951
C	15.337389	14.697642	22.165620
H	15.687922	13.817076	22.221771
C	18.578235	13.090794	23.125803
C	18.950831	14.380224	22.819779
H	19.145409	14.625628	21.921363
C	19.036583	15.329405	23.858574
H	19.426199	16.180623	23.687313
C	18.558431	15.029666	25.124779
H	18.521481	15.699124	25.795784
C	18.132143	13.734153	25.394304
H	17.811082	13.497850	26.256223
C	18.182257	12.789415	24.372356
H	17.928209	11.896036	24.566077
C	19.340218	12.384494	20.467051
C	20.695995	12.851199	20.309828
H	21.293634	12.798712	21.045407
C	21.136261	13.360043	19.147502
H	22.026584	13.687427	19.085736

C	20.315783	13.417572	18.035712
H	20.655806	13.745225	17.213099
C	19.054328	13.014153	18.114323
H	18.493064	13.077963	17.350669
C	18.549956	12.503444	19.290687
H	17.643614	12.220086	19.315955
C	20.028573	10.670149	22.631674
C	20.881872	11.145322	23.594664
H	20.793537	12.030894	23.925955
C	21.894627	10.291732	24.083178
H	22.519589	10.616728	24.720492
C	21.980563	9.002460	23.645200
H	22.637651	8.419003	24.004566
C	21.090762	8.540362	22.656941
H	21.170435	7.654555	22.322843
C	20.128567	9.357162	22.182465
H	19.513686	9.032981	21.536728
C	16.258615	9.534689	25.273580
C	17.309873	8.850524	24.644688
H	17.152825	8.412413	23.816460
C	18.556892	8.806519	25.209006
H	19.249339	8.297268	24.801911
C	18.805617	9.523650	26.396600
H	19.683554	9.538930	26.761582
C	17.788964	10.202444	27.033914
H	17.960805	10.650481	27.853719
C	16.515763	10.233720	26.480827
H	15.820984	10.720317	26.907575
C	13.911864	11.114320	25.206198
C	14.598324	12.292679	24.933866
H	15.302070	12.292396	24.293744
C	14.266313	13.443943	25.573988
H	14.774790	14.228819	25.408342
C	13.217369	13.503858	26.455559
H	13.004011	14.311438	26.907575
C	12.490543	12.364145	26.663318
H	11.735220	12.387889	27.238866
C	12.844359	11.165697	26.040041
H	12.333679	10.380352	26.200072
C	13.694392	8.266732	25.509414
C	12.373793	7.940425	25.220236
H	11.951687	8.358623	24.481850
C	11.665470	7.041349	25.964237
H	10.769903	6.827070	25.725595
C	12.253830	6.442083	27.061990
H	11.753037	5.855290	27.617885
C	13.597460	6.712207	27.351168
H	14.037230	6.250199	28.055863
C	14.282777	7.650997	26.609974
H	15.171598	7.880930	26.854231
C	13.327487	3.946409	24.613805
C	12.092934	3.983393	24.001759
H	12.030031	4.302151	23.108957
C	10.953994	3.573931	24.644688
H	10.125598	3.553487	24.181442
C	11.013322	3.185907	25.981083

H	10.219640	2.941907	26.441521
C	12.225592	3.156993	26.635242
H	12.290014	2.872578	27.539274
C	13.347391	3.558497	25.933354
H	14.181265	3.567609	26.388178
C	16.162182	4.328889	24.866485
C	16.786309	5.503810	25.298848
H	16.537344	6.346920	24.939481
C	17.787277	5.408985	26.273068
H	18.195174	6.210453	26.579091
C	18.202874	4.238285	26.800888
H	18.860123	4.214986	27.485930
C	17.649594	3.091268	26.320796
H	17.948180	2.249901	26.646472
C	16.627274	3.142639	25.335346
H	16.263763	2.332520	24.998440
C	15.079944	3.030837	22.558677
C	14.414061	1.807009	22.704670
H	13.750065	1.695986	23.375675
C	14.735475	0.753337	21.851174
H	14.295395	-0.082013	21.957861
C	15.646471	0.892085	20.893799
H	15.837049	0.170437	20.307021
C	16.321606	2.107271	20.753421
H	16.954164	2.215715	20.051534
C	16.082414	3.125549	21.601302
H	16.606238	3.916527	21.545151
C	19.467328	7.510171	19.119426
C	19.426668	8.808356	18.790943
H	18.611026	9.273272	18.939743
C	20.491811	9.529943	18.249085
H	20.405386	10.454506	18.046942
C	21.711621	8.838638	18.007636
H	22.431299	9.269293	17.564043
C	21.828592	7.542347	18.431576
H	22.668221	7.102682	18.367003
C	20.739662	6.861401	18.950973
H	20.837183	5.950167	19.203653
C	18.789872	5.419738	20.907837
C	19.360272	4.183611	20.469859
H	19.280461	3.925473	19.560212
C	20.012998	3.383150	21.340200
H	20.345652	2.544424	21.042599
C	20.205388	3.770113	22.665364
H	20.714988	3.223860	23.252142
C	19.648569	4.946675	23.117380
H	19.743306	5.194418	24.029834
C	18.962063	5.758702	22.258269
H	18.593584	6.570921	22.583945
C	17.516480	5.622668	18.372618
C	18.108656	5.539665	17.196254
H	18.866132	6.095612	17.053068
C	17.722865	4.718268	16.160267
H	18.182605	4.732419	15.329232
C	16.655101	3.877688	16.368026
H	16.389300	3.255771	15.702636

C	16.001397	3.959753	17.533160
H	15.240081	3.409646	17.673537
C	13.037726	10.327880	16.657204
C	13.343110	10.847456	15.441534
H	14.040610	10.448442	14.936175
C	12.669100	11.947839	14.908099
H	12.916739	12.300716	14.060218
C	11.624964	12.525272	15.640870
H	11.153110	13.273892	15.295541
C	11.289404	11.994720	16.870578
H	10.566426	12.372355	17.356284
C	11.982782	10.931249	17.409628
H	11.759989	10.602321	18.271546
C	15.495920	8.833572	16.491558
C	16.414338	9.781625	16.789159
H	16.198912	10.431924	17.448933
C	17.647468	9.843373	16.182727
H	18.293033	10.487963	16.446637
C	17.011445	7.976864	14.868793
H	17.218033	7.340343	14.192173
C	15.776106	7.908939	15.528568
H	15.147277	7.230372	15.312386
C	12.938788	7.463992	16.710547
C	11.961298	7.552508	15.733519
H	11.712677	8.406839	15.399421
C	11.370434	6.469266	15.253428
H	10.734624	6.551897	14.551540
C	11.666938	5.209324	15.767210
H	11.202763	4.438460	15.463994
C	12.633371	5.112972	16.704932
H	12.889939	4.250459	17.013763
C	16.407084	4.823423	18.529841
H	15.909567	4.865098	19.338415
C	17.914564	8.936484	15.177624
H	18.736585	8.986470	14.703148
C	13.260096	6.221691	17.235559
H	13.892916	6.136257	17.940255

$Au_8(PH_3)_8^{3+}$ (2b)

Au	-0.01689500	-0.03230300	1.90070796
Au	1.36278200	-2.16535807	0.32713899
Au	-2.56036592	-0.05609700	0.32401201
Au	1.20526695	2.23441601	0.36111301
Au	-0.00326100	-0.00437400	-0.73470998
Au	-1.43581605	2.35728097	-0.77871197
Au	2.75616693	0.09932100	-0.78456300
Au	-1.31061995	-2.43658304	-0.71883202
P	2.24094391	4.17615700	1.18239403
P	5.03380823	0.19414000	-1.32051897
P	-4.78204203	-0.09808800	1.08576703
P	-2.39209008	-4.45684385	-1.20440698
P	-2.60158801	4.31801224	-1.31178498
P	2.55247998	-4.03474188	1.10563600
P	-0.01664400	-0.02941900	-3.13989711
P	-0.02218700	-0.04443700	4.20160913

H	-2.87488198	-5.24999189	-0.12755799
H	-1.67654896	-5.46033001	-1.91332805
H	-3.56901908	-4.42681217	-2.00136304
H	-3.14581108	5.09641314	-0.25356999
H	-3.75721693	4.22565508	-2.13473296
H	-1.91795397	5.34838676	-2.01372194
H	5.97756386	0.27579299	-0.26032001
H	5.61346722	-0.87996298	-2.04970193
H	5.50191784	1.27494204	-2.11690402
H	-5.81274223	-0.16465200	0.10883900
H	-5.28250313	0.99347299	1.84852397
H	-5.21686888	-1.15992498	1.92678201
H	3.72990799	-3.84079599	1.88013101
H	3.07853889	-4.93761015	0.14141400
H	1.90025795	-4.97815323	1.94714797
H	2.75113797	5.10595512	0.23539400
H	1.49306202	5.08095980	1.98596799
H	3.39249897	4.06307316	2.01005507
H	-0.59555399	-1.15989196	4.86916590
H	-0.69991398	1.00253606	4.88239622
H	1.22484696	0.01194700	4.88032389
H	0.63169903	-1.09343505	-3.82442999
H	-1.26182401	-0.07450500	-3.82478690
H	0.56731099	1.05541503	-3.84916902

$Au_8(PH_3)_8^{3+}$ (3)

Au	1.380367	1.987179	-0.578627
Au	2.753591	-0.114546	0.821684
Au	-1.134654	2.433506	0.730245
Au	-0.224303	-0.061676	-1.824329
Au	-2.595321	0.152431	-0.207751
Au	0.028803	0.016183	0.744726
Au	1.165254	-2.178720	-0.426665
Au	-1.396090	-2.250628	0.810315
P	0.065601	0.067393	3.149429
P	-4.869074	0.287175	-0.779355
P	-2.093905	4.521671	1.209306
P	-0.419703	-0.132868	-4.124643
P	5.007856	-0.225298	1.438082
P	2.196455	-4.087285	-1.343614
P	2.574352	3.712749	-1.649871
P	-2.599810	-4.190571	1.361406
H	0.765586	-0.137195	-4.908854
H	-1.165642	0.149003	3.855755
H	3.371307	4.571107	-0.843578
H	5.990523	-0.277608	0.412185
H	2.830696	-4.994970	-0.451600
H	-3.166777	-4.967348	0.313849
H	-5.807547	0.440584	0.277284
H	-2.621317	5.296197	0.139585
H	0.752377	1.121714	3.810458
H	0.636764	-1.025358	3.856567
H	-5.487806	-0.797845	-1.459762
H	-5.315257	1.345823	-1.618076
H	-1.287410	5.518901	1.823292

H	-3.209742	4.577262	2.088787
H	-1.117735	0.918196	-4.778688
H	-1.082054	-1.243979	-4.713051
H	5.446963	-1.325995	2.223611
H	5.553670	0.831969	2.216105
H	3.258473	-3.932397	-2.277412
H	1.412666	-5.024137	-2.073109
H	1.866027	4.708693	-2.378297
H	3.547046	3.385935	-2.635563
H	-3.747619	-4.076752	2.192994
H	-1.929841	-5.229507	2.063962

Au_8 (optimized core)

Au	0.000000	0.000000	-0.380717
Au	2.480849	0.000000	0.888809
Au	-1.240425	2.148479	0.888809
Au	-1.240425	-2.148479	0.888809
Au	0.000000	0.000000	2.329672
Au	-2.741121	0.000000	1.698206
Au	1.370561	-2.373881	1.698206
Au	1.370561	2.373881	1.698206

Appendix E - Supporting Information for "Theoretical Study of the Plasmon Resonance in AgNPs: MCD Spectroscopy"

Figure E-1. Optical absorption spectra of Ag_{10}^{+2} (T_d)

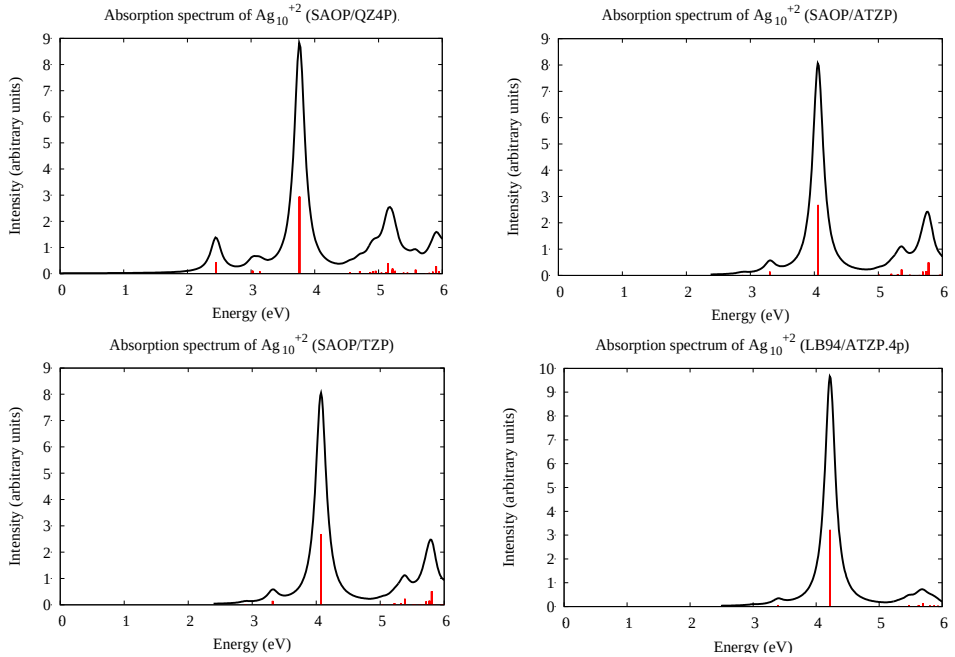

Figure E-2. Optical absorption spectra of Ag_{19}^{-1} (O_h)

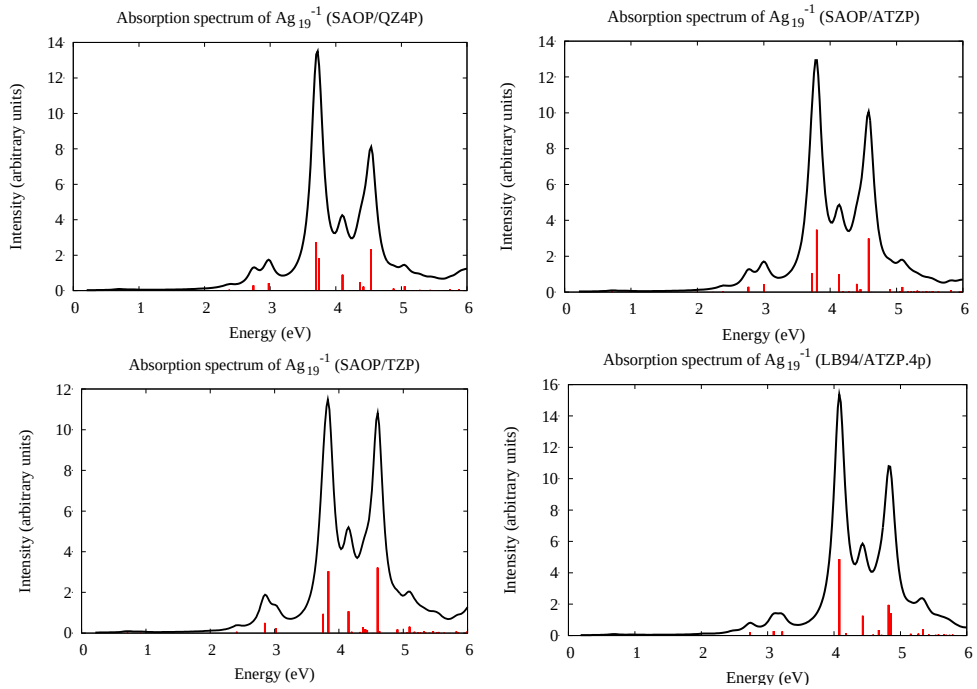

Figure E-3. Optical absorption spectra of Ag_{19}^{+1} (O_h)

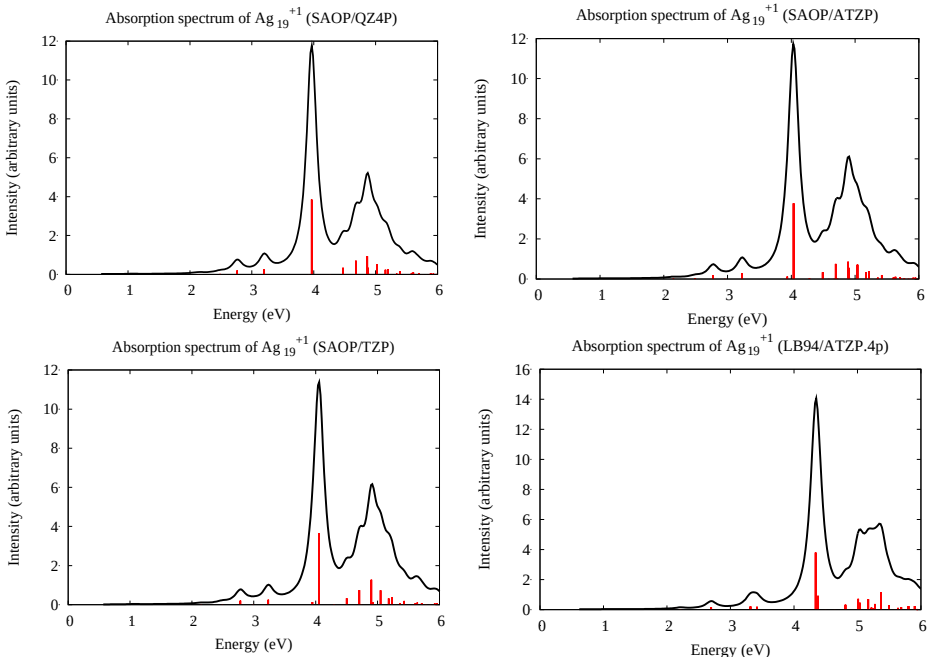

Figure E-4. Optical absorption spectra of Ag_{13}^{-5} (I_h)